

**Theory and Modelling of
Wavelength Tunable Laser
Transmitters With Enhanced
Tuning Range and Their
Modulation Performance**

Georgios Kyritsis

A thesis submitted for the degree of Doctor of Philosophy

School of Computer Science and Electronic Engineering

University of Essex

May 2015

ABSTRACT

The research that is described in detail in this thesis investigates key characteristics of the operation of Tunable Laser Diodes (TLDs), such as Continuous Wave (CW) operation, discontinuous, continuous and quasicontinuous wavelength tuning and direct Intensity Modulation (IM) (small-signal analysis). Two software simulation tools were used to model the TLDs and investigate their operation, Crosslight PICS3D and VPI (Virtual Photonics Incorporated). Two different Free-Carrier (FC) contributions to the refractive index change of the TLD during FC tuning were investigated, the FC plasma effect and the band-filling effect which uses the Kramers-Kronig (KK) relations (KK effect). It was found that the band-filling effect is heavily underestimated due to the lack of its investigation in published literature as it is the main contributor to the refractive index change instead of the plasma effect. Investigation on different types of wavelength tuning also took place. It was found that with careful design of the passive sections, such as the κL product, grating composition, section length and passive waveguide thickness the discontinuous, continuous and quasicontinuous tuning range can be enhanced greatly.

The issue of output power decrease during discontinuous tuning in bulk and Multiple Quantum Well (MQW) TLDs was also addressed and it was found that the power drop can be delayed at latter stages of the tuning range by carefully selecting the Lorentzian lineshape of the gain spectrum. A power stabilisation was realised with continuous tuning. A small-signal analysis of directly intensity modulated TLDs during discontinuous tuning was also made and was found that the increase of the resonance frequency depends mainly on the increase of the differential gain with the wavelength change.

ACKNOWLEDGEMENTS

In this point, the author wishes to thank exclusively his supervisor, Dr Nick Zakhleniuk, for the invaluable help he has offered throughout the course of this research. The explanation of important parts of the theory concerning semiconductor lasers, tunable laser diodes and optical networks in general as well as his support in all the stages of the research defines a contribution from his part, without which parts of the research would not have been completed properly. The author also wishes to thank Miss Celia Antoniou who greatly supported him at the final stages of the research and during the difficult period of writing this thesis, his family which always believed in him from the start and had a big influence in his life and all his friends.

List of publications

Journals

G. Kyritsis and N. Zakhleniuk, “Self-consistent simulation model and enhancement of wavelength tuning of InGaAsP/InP multi-section DBR laser diodes,” *IEEE J. Sel. Topics Quant. Electron.*, vol. 19, no. 5, pp. 1503311-1503311, Sep.-Oct. 2013.

Conferences

G. Kyritsis and N. Zakhleniuk, “Free-carrier refractive index contributions and tuning performance of InGaAsP laser diodes,” *International Conference on Superlattices, Nanostructures and Nanodevices (ICSNN)*, Dresden, Germany, July 2012 (Poster).

Proceedings

G. Kyritsis and N. Zakhleniuk, “Free-carrier refractive index contributions and tuning performance of InGaAsP laser diodes,” in *Proc. Abstracts ICSNN-2012*, Dresden, Germany, Jul. 22–27, 2012, pp. 263–264.

List of abbreviations

LASER	Light Amplification by Stimulated Emission of Radiation
TLD	Tunable Laser Diode
BL	Bit Rate-Distance
WDM	Wavelength Division Multiplexing
VPI	Virtual Photonics Incorporated
FC	Free-carrier
KK	Kramers-Kronig
MQW	Multiple Quantum Well
QD	Quantum Dot
FP	Fabry-Perot
DFB	Distributed Feedback
DBR	Distributed Bragg Reflector
WT	Widely Tunable
3S	Three-Section
4S	Four-Section
SG	Sampled Grating
SSG	Super-Structure Grating
VCSEL	Vertical Cavity Surface-Emitting Laser
EA	Electro-Absorption

VOD	Video On Demand
VoIP	Voice over IP
QCSE	Quantum Confined Stark Effect
SRH	Shockley-Read-Hall
TLLM	Transmission Line Laser Model
AR	Active Region
WG	Waveguide
CW	Continuous Wave
SMSR	Side Mode Suppression Ratio
SOA	Semiconductor Optical Amplifier
IVBA	Inter-Valence Band Absorption
IM	Intensity Modulation
AC	Alternating Current
DC	Direct Current
ROF	Relaxation Oscillation Frequency
NRZ	Non-Return to Zero
RZ	Return to Zero
XPM	Cross Phase Modulation
TOJ	Turn-On Delay Jitter
BER	Bit-Error Rate
SNR	Signal-to-Noise Ratio

Contents

1 Introduction	1
2 Literature review	10
2.1 Historical background of semiconductor lasers and TLDs.....	11
2.2 Applications of TLDs	19
3 Theory of semiconductor lasers	24
3.1 Electrons, holes, photons and phonons in semiconductors.....	25
3.2 Fermi levels and density of states in semiconductors.....	30
3.3 Doping in semiconductors	37
3.4 Rate equations and optical gain in semiconductors.....	39
3.5 The Fabry-Perot laser.....	50
3.6 Three-section tunable DBR laser	55
3.6.1 Free-carrier plasma effect	59
3.6.2 Band-filling effect.....	62
3.6.3 Thermal tuning.....	63
3.6.4 Quantum Confined Stark Effect.....	65
4 Physics and technology of tunable laser diodes	67
4.1 Introduction.....	68
4.2 Crosslight PICS3D.....	69
4.2.1 File structure	71
4.2.2 Carrier transport model	75

4.2.3	Optical model and field equations	78
4.2.4	Boundary conditions	80
4.3	VPI.....	81
4.3.1	Travelling-wave equations for optical fields	86
4.3.2	Rate equations for carrier density dynamics	88
4.3.3	Stimulated emission (gain) models	90
4.4	Conclusion	93
5	Different free-carrier contributions to the refractive index change in semiconductor materials and tunable laser diodes	95
5.1	Introduction.....	96
5.2	Device structure and parameters	100
5.3	Results and discussion	104
5.4	Conclusion	111
6	Design and optimisation of tunable laser diodes with enhanced tuning range	112
6.1	Introduction.....	113
6.2	Results and discussion	114
6.2.1	Effect of the κL product on the TLD discontinuous tuning performance.....	114
6.2.2	TLD passive section limitations on high carrier densities and electronic properties of the Bragg grating in discontinuous tuning.....	127
6.2.3	Effect of design parameters of the phase section on the continuous and quasi-continuous tuning performance	140
6.3	Conclusion	149

7 Investigation of power performance of bulk and multi-quantum-well tunable laser diodes with wavelength tuning and main limiting factors	151
7.1 Introduction.....	152
7.2 Results and discussion	160
7.3 Conclusion	181
8 Modulation and dynamics of tunable laser diodes and wavelength tunable transmitters	182
8.1 Introduction.....	183
8.2 Results and discussion	184
8.2.1 Device setup.....	184
8.2.2 Small-signal analysis of bulk TLDs during discontinuous tuning.....	199
8.3 Conclusion	207
9 Conclusions and future work	208
9.1 Overall conclusions.....	209
9.2 Recommended future work.....	212
References.....	214
Appendix.....	238

Chapter 1

Introduction

Throughout the centuries of human civilisation, interaction and communication between people everywhere in the globe was always one of the most significant parts of their culture. It helped them cooperate with each other to make their lives easier and form societies so that they would not face alone the dangers of a wild world. The main forms of communication in the first stages of civilisation were mainly oral (people speaking to each other over small distances), sonic (with the use of drums, trumpets and other acoustic devices over greater distances) and visual (with the use of smoke signals, fire beacons, moving flags or lit torches, reflecting mirrors, etc. over even greater distances).

As civilisation progressed and the centuries passed, a breakthrough in terms of human communication took place with the invention of writing, first by carving letters in stone and making marks in animal skin in a primitive form and later by using ink to write in scrolls and paper (typography, books). It quickly became one of the most popular means of communication over very long distances, also known as telecommunications, and together with the other three described above remained the only types of human communication for many centuries until the technological revolution that took place in the 19th century and onwards.

It was during this century that a breakthrough of extreme importance took place with the discovery and manipulation of electricity, which revolutionised the area of telecommunications up to that point. The most significant inventions of the time were the telegraph by Samuel F. B. Morse in 1838 and the telephone by Alexander Graham Bell in 1876, which used electrical signals to transmit information in long distances by using a copper cable [1] and completely changed people's lives in the way they communicated with each other. These new types of telecommunications were called *electrical communication systems* and were able to cover distances over 1000 km [2]. From that point and on the development of telecommunication systems became rapid compared to

the progress that took place in the previous centuries. The potential of these unique inventions opened new scientific paths and led to the idea of networking.

The realisation of this idea became apparent in the form of a worldwide telephone network when an increasing number of people started using the telephone in the years after the Second World War ended. This led to the need for greater bandwidth in the communication channel (copper cable) that was used and a significant growth in the transmitted information through that channel. Therefore, the transmission of electrical signals would have to take place at greater transmission rates or *bit rates* (bit / sec), however the copper cable during the 1940's could not support transmission frequencies of over 10 MHz because of its design issues and the losses it introduced which caused an additional problem to the whole situation [2].

For this reason, new types of telecom networks were initially developed in 1948 that could support bandwidths above 10 MHz. They were called *microwave systems* because their operation band was between 1 and 10 GHz and their evolution was so rapid that by 1975 they could achieve bit rates of 274 Mbps (Mbits/sec) with the use of coaxial cables instead of the copper wire pair [1]. The drawback of these systems though was that their repeater (device which retransmits the same signal it receives in a specific direction) spacing had to be up to 1 km. However, their Bit rate–Distance (BL) product (evaluates the performance of a system, where B is the bit rate and L is the repeater spacing multiplied together $B \times L$) was rather high (around 100 Mbps x km [2]) for the technology of the time and almost reached the fundamental transmission capacity of the copper cable.

It therefore became obvious that a transmission medium other than the copper cable had to be used in order the increasing demand for greater BL products to be satisfied. For this case, the idea of using optical waves instead of electrical signals for the transmission

of information in telecom networks was suggested because of their high travelling speed in a medium and high achievable BL products. Therefore, various optical network components (transmitter, transmission medium, receiver, amplifier, regenerator) began to be implemented in order to be used accordingly in an *optical network*.

The invention of the *LASER* (Light Amplification by Stimulated Emission of Radiation) in 1960 [3] brought closer the achievement of this goal as it is the ideal transmitter for optical networks. It is a device that generates monochromatic light (optical waves in the form of photons) with a highly concentrative beam which is very coherent and can be easily waveguided through a transmission medium. The idea of using gas lenses in order to confine light [4] was proposed during the 1960's as a transmission medium but it was not until 1966 that the invention of the *optical fibre* [5] made it the dominant medium for the new type of telecommunications, the *optical communications*.

Optical fibres became extremely popular as a transmission medium for optical networks because they could guide optical waves (light) in the same fashion as the copper cable could transfer electrical signals and radio frequency waves. However, in the early stages of their use in optical networks during the 1960's fibres introduced high losses of over 1000 dB/km in the wavelength region that optical signals were transmitted, which was their main disadvantage. This problem was finally solved after 1976 [6], when lasers started to operate near the wavelength region of 0.8-1 μm where the fibre losses were much lower and around 20 dB/km.

From that point and on this new type of systems, also called *lightwave systems*, which utilised lasers and optical fibres as the main type of transmitter and medium have dominated the area of telecommunications until today. Their main advantage compared with previous systems in the past years is their ability to transmit huge amount of data over very long distances with relatively low losses and thus achieving very high BL

products in terms of Tbps x km. They can historically be categorised in five generations according to the BL products and bit rates they achieved.

First generation (mid 1970's-1980): From 1975 these systems continued to evolve until they achieved in 1980 [7] a bit rate of 45 Mbps with a very long repeater spacing of 10 km compared to repeater spacings used by previous systems. Their operating wavelength was around 0.8 μm but further investigations showed that operating around the 1.3 μm wavelength region would reduce the losses introduced by the fibre as low as 1 dB/km.

Second generation (1980 - mid 1980's): In the early 1980's these systems could not manage to achieve bit rates higher than 100 Mbps while operating around the wavelength region of 1.3 μm because the *multimode* (guiding multiple wavelengths) fibres that were used for transmission at that time introduced high dispersion at that region [8]. A rapid increase in terms of bit rates took place though with the realisation of the *single-mode* (guiding only a single wavelength) fibre, when an extraordinary at that time bit rate of 1.7 Gbps (Gbits/sec) with a repeater spacing of 50 km was achieved in 1987 [1]. Further research showed that systems which were operating around the 1.5 μm wavelength region would achieve a minimum fibre loss of 0.2 dB/km [9] which later made it the most popular operating wavelength region.

Third generation (mid 1980's - 1990): The progress that was made during the mid 1980's led to the commercial achievement of a bit rate of 2.5 Gbps for these systems operating at 1.5 μm in 1990 [1] which could potentially reach the value of 10 Gbps in the following years. The drawback in their performance though was that they required a quite short for that time repeater spacing of 60-70 km and mainly the fact that high dispersion values were introduced by fibres in the 1.5 μm wavelength region. The realisation of the

dispersion-shifted fibres though which compensated the dispersion values in that region and the fabrication of *single-mode* lasers during that time led to the solution of that issue.

Fourth generation (1990's): During the 1990's these systems managed to achieve bit rates of 10 Tbps (Tbits/sec) and higher by using the Wavelength Division Multiplexing (WDM) technique and also used the newly developed *optical amplifiers* which amplified the optical signal strength and dramatically increased the repeater spacings to thousands of km. The main advantage of the WDM technique was that it could combine together many different transmitted wavelengths (each wavelength acting as one channel (signal) with a bit rate of up to 40 Gbps during the 1990's) into one main signal, so that when it is guided through the fibre the total capacity of the system would immediately increase to tens of Tbps. This breakthrough in terms of system capacity revolutionised optical communications and WDM became the most popular technique of transmission in optical networks increasing rapidly their capacity every 6 months. An indicative example of this is that these systems reached in 2000 a BL product higher than 25000 Tbps x km by combining 300 channels with a bit rate of 11.6 Gbps each while using a repeater spacing of 7380 km [10].

Fifth generation (2000's - today): During the last 17 years these systems have experienced significant growth in their evolution and they are estimated to reach bit rates as high as 160 Gbps for a single channel while operating in the wavelength region of 1.53 – 1.57 μm which includes the Short (S band), Conventional (C band) and Long (L band) wavelength window [1]. Significant success has been made in the area of amplifiers with the realisation of the *Raman* amplification technique and the area of fibres with the fabrication of the *dry fibre* which introduced very low losses in the 1.3 – 1.65 μm wavelength region [1]. Another record was also established in a 2010 experiment, when a

transmission of 640 WDM channels with a 12.5 GHz spacing spanned in both the C and L band with an overall bit rate of 64 Tbps was realised over 320 km [1].

All of the types of lightwave systems and optical networks that are mentioned above mainly use semiconductor lasers as the primary source of transmission. Single-mode lasers and especially the *Tunable Laser Diode* (TLD) have revolutionised the area of optical communications and their use in optical networks has been of paramount importance for the improvement and optimisation of the network performance. Their applications also cover a broad scientific spectrum and have been heavily investigated in published literature.

A historical background of semiconductor lasers and TLDs from the early years until recently and their applications is covered in Chapter 2. Published papers concerning these topics are reviewed and discussed.

Chapter 3 describes the basic theory of semiconductor lasers, such as multi-mode lasers and TLDs. The basic rate equations for photon generation are shown, the selection of lasing mode and the expression for gain at lasing conditions is described as well as various tuning mechanisms in the case of TLDs.

Chapter 4 concerns with the two different software packages that were used in this research, Crosslight PICS3D and Virtual Photonics Incorporated (VPI). A comparison between them is made and the advantages and disadvantages of each one is presented. The reason why they were used in this thesis is also given. The equations from semiconductor laser theory that these packages use in order to run all simulations are described in detail.

Chapter 5 investigates two different Free-Carrier (FC) contributions to the refractive index change of a bulk TLD with typical parameters during FC tuning. These contributions are the FC plasma effect and the band-filling effect which is calculated by

using the Kramers-Kroning (KK) relations (KK effect). It is shown that the band-filling effect instead of the plasma effect is the dominant contributor to the real part of the refractive index change, which also shapes the corresponding wavelength tuning performance of the device. This shows that the band-filling effect is heavily underestimated due to the lack of investigation of this effect in published literature as a contributor to the refractive index change. It is also found that the available refractive index change is not necessarily converted into the corresponding lasing wavelength shift due to design issues which are explained in Chapter 6.

Chapter 6 investigates the performance of a TLD similar to the one in Chapter 5 under different types of wavelength tuning. Some limitations in the tuning range due to the κL product are highlighted in the case of discontinuous tuning. It is shown that an optimisation of the device with careful design of the κL product and the grating composition enhances greatly the discontinuous tuning range. It is also found that the continuous and quasicontinuous tuning range can be increased by a careful selection of the phase section length and passive waveguide thickness.

Chapter 7 addresses the issue of output power decrease during discontinuous tuning in bulk and Multiple Quantum Well (MQW) TLDs. It is found that the power drop can be delayed at latter stages of the tuning range by carefully selecting the Lorentzian lineshape broadening function of the gain spectrum. It is also shown that the output power can be stabilised when the TLD is continuously tuned. The PICS3D simulation tool is used to simulate all TLDs in Chapters 5, 6 and 7.

Chapter 8 deals with the small-signal analysis of a directly intensity modulated TLD during discontinuous tuning. The VPI software simulation tool is used in all investigations here for a TLD model which has exactly the same parameters with the one in Chapter 7. Firstly, it is shown that the results from basic characteristics of laser

operation of the TLD in VPI are in excellent agreement with the ones of the TLD in PICS3D. When the TLD is directly intensity modulated during discontinuous tuning there are three parameters that affect its resonance frequency; the differential gain, the unmodulated output power and the lasing wavelength. A significant increase of the resonance frequency at the end of the tuning range is observed. It is concluded that this increase is caused mainly by the great increase of the differential gain with the wavelength change. The change of power and lasing wavelength during tuning is much smaller than the change of the differential gain and contributed little to the change of the resonance frequency.

Chapter 9 includes all the conclusions and some recommended work for the future.

Chapter 2

Literature review

2.1 *Historical background of semiconductor lasers and TLDs*

Semiconductor lasers were developed and had a rapid growth in the second half of the 20th century. The prediction of the existence of photons was first given by Einstein [11] in 1917 when he explained the photoelectric effect. He stated that not only spontaneous photon emission and absorption takes place, but also stimulated emission where a photon can stimulate an excited atom to emit a quantum of the same properties. In 1955, almost 50 years after Einstein's work, Gordon, Zeiger and Townes [12] made the first experiment of an electromagnetic wave amplification with the use of a NH₃-maser (Ammonia-Microwave Amplification by Stimulated Emission of Radiation). After three years in 1958, Shawlow and Townes [13] argued that this amplification can also happen for wavelengths of the optical region.

A few years after their findings, Maiman [3] was the first to fabricate a laser in 1960 with a ruby active medium and an emission wavelength of 694 nm. In addition, Javan [14] was able to fabricate a gas laser with a He-Ne (Helium-Neon) active medium in 1961. That was also the year that Fox [15] showed the oscillation of resonant lasing eigen-modes in a maser interferometer with a Fabry-Perot (FP) cavity, which characterised this kind of lasers as *multi-mode* lasers. 1962 was a year of historical significance for optical semiconductor devices, as the first semiconductor lasers with homo-junction structures grown on GaAs substrates were reported independently by Nathan [16], Hall [17] and Quist [18], confirming von Neumann's prediction in 1953 [19] that semiconductors can be used as optical amplifiers [which was the first idea of the Semiconductor Optical Amplifier (SOA)]. Holonyak [20] also reported in 1962 a semiconductor laser grown on a GaP substrate.

Four years later in 1966 Kao [5] suggested the possibility of optical fibre networks with a low loss and wideband optical glass fibre as a transmission medium. This led to the realisation that semiconductor lasers can be used as transmitters in optical fibre communications and research was then focused on the fundamental properties of semiconductor lasers. Such properties are their high-speed direct modulation investigated by Ikegami in 1967 [21] and Nishimura in 1970 [22], the mode competition investigated by Nishimura in 1971 [23] by developing a dynamics theory, the basics of optical beam theory demonstrated by Kogelnik in 1965 [24] and the potential for photonic integrated circuits shown by Miller in 1969 [25].

Important experiments conducted by Alferov [26] and Hayashi [27] in 1970 reported semiconductor lasers operating in Continuous Wave (CW) at room temperature. They used hetero-junctions instead of homo-junctions in a GaAlAs/GaAs device structure, leading to better photon and carrier confinement in the active region. The idea of hetero-junctions in the device structure of semiconductor lasers was first suggested by Kroemer in 1963 [28]. However, these early GaAlAs/GaAs lasers were using a gain-guiding waveguide with a FP resonator as an optical cavity as in Yonezu in 1973 [29]. Therefore, they were lasing in the multi-mode regime which made them unstable and unsuitable for optical fibre networks. As a result, research was focused on the realisation of lasers operating in a stable *single-mode* regime with a strong lasing wavelength selectivity. Such lasers, called single-mode lasers were the Distributed FeedBack (DFB) laser and Distributed Bragg Reflector (DBR) laser.

Kogelnik in 1971 [30] was the first to demonstrate single-mode operation with a DFB dye laser based on a periodic structure. One year later, he presented a couple wave theory which predicted single-mode operation in semiconductor DFB lasers [31]. Kaminow was the first to realise a DBR dye laser in 1971 [32]. In the field of

semiconductor lasers, Suematsu in 1973 [33] suggested a semiconductor laser with an active refractive index waveguide as an optical cavity which operated in a stable transverse single-mode regime. A year later [34], he made a general analysis of two distributed Bragg reflectors with a phase shift of $\pi/2$ between them in longitudinal single-mode lasers, which solved the problem of the operation of two modes in refractive-index coupled DFB lasers predicted by [31].

In 1973, Nakamura [35] was the first to realise an optically pumped GaAlAs/GaAs DFB laser. Streifer in 1975 [36] ensured single-mode operation with the use of external reflectors in DFB lasers and Nakamura in the same year [37] demonstrated CW operation at room temperature of a GaAlAs/GaAs DFB laser. Also in 1975, GaAlAs/GaAs lasers monolithically integrated with a wavelength selection filter and various optical components were developed by Reinhart [38] and Hurwitz [39], as well as Suematsu [40] who presented an Integrated Twin-Guide (ITG) laser with a single-mode pulsed operation.

Single-mode semiconductor lasers proved to be very useful for optical fibre communications and the next step for researchers during the 1970's was to find appropriate wavelength regions for optical transmission in optical fibres following Kao's proposal in 1966 [5]. Kapron in 1970 [6] managed to fabricate with chemical vapour deposition a low-loss silica fibre which became very industrially popular in optical fibre networks. In the early and mid-1970's, two other experiments of historical significance in optical communications took place. The first one from Keck in 1973 [41], showed that there is small attenuation in silica optical fibres around the long wavelength region of 1.5 μm . The second one from Payne in 1975 [42] demonstrated that there is zero material dispersion at the wavelength region of 1.3 μm . Therefore, research was shifted on the

finding of appropriate semiconductor materials of lasers in order to emit wavelengths in that regions.

In the following years, Hsieh [43] and Oe [44] in 1976 realised InGaAsP/InP Double Hetero-structure (DH) lasers in CW operation grown on InP substrates emitting at 1.1 μm and 1.3 μm , respectively. Itaya [45] and Yamamoto [46] also demonstrated in 1977 InGaAsP/InP lasers emitting at 1.3 μm . Two years later in 1979, Akiba [47], Kawaguchi [48], Kaminow [49] and Arai [50] realised InGaAsP/InP DH lasers operating at the long wavelength of 1.55 μm as well. In the same year of demonstration of lasers operating at 1.55 μm , Miya [9] reported a single-mode fibre with a very low attenuation of 0.2-dB/km at 1.55 μm .

After the realisation of DH lasers emitting at the long wavelengths of 1.3 μm and 1.5 μm during the 1970's, research was focused during the next decade on lasers with strong lasing mode selectivity which can be used as transmitters in fibre optic networks under direct modulation. The first operation of a directly modulated InGaAsP/InP DBR laser emitting at the 1.5- μm region was reported by Kawanishi in 1978 [51]. In 1980 Sakakibara and Utaka demonstrated InGaAsP/InP DBR-ITG lasers operating in the 1.3- μm region [52] and 1.5- μm region [53], respectively. The year later in 1981 directly modulated InGaAsP/InP DBR-ITG lasers emitting at 1.53 μm (Utaka [54]) and 1.55 μm (Utaka [55] and Tanbun-Ek [56]) were also reported.

Following the realisation of DBR lasers, Utaka in 1981 [57] and Matsuoka in 1982 [58] presented CW operation at room temperature of directly modulated InGaAsP/InP DFB lasers emitting at the 1.5- μm region. By increasing the laser operation temperature they also demonstrated thermal wavelength tuning which was the first notion of a new category of semiconductor lasers, the wavelength *tunable laser diodes* (TLDs). Three years later in 1984 Sekartedjo [59] demonstrated a phase-shifted DFB laser operating at

the 1.5- μm region and this type of semiconductor lasers became the most commonly used for long-haul optical networks.

Semiconductor lasers had a great improvement in their basic performance during the 1980's with the use of Multiple Quantum Wells (MQWs) in their active region. Van der Ziel [60] was the first to demonstrate a conventional MQW laser in 1975 with the use of optical pumping followed by Rezek in 1977 [61] who injected current into them instead. The idea of applying strain in the conduction and valence subbands of quantum wells in order to improve their optical gain was later proposed in 1983 by Osbourn [62]. Another idea for MQW semiconductor lasers with low threshold current and high efficiency with the use of band structure engineering was also proposed by Adams in 1986 [63].

In the following years, semiconductor lasers with a MQW active region benefited from the quantum well technology by showcasing higher speed, better temperature characteristics, higher output power and lower threshold currents than lasers with a bulk active region [64]. Many semiconductor lasers which are commercially available currently [65]–[69] and also appear in published literature use quantum wells in their active region in order to exploit all the advantages described above.

Further enhancement of the performance of semiconductor lasers came with the introduction of *quantum wires* and *Quantum Dots* (QD), which were proposed by Arakawa in 1982 [70]. Asada in 1986 [71] made an analysis that quantum dots could decrease the threshold current and yield higher gain when used in semiconductor lasers. Seven years later in 1993, Leonard [72] showcased the performance of self-assembled quantum dots on GaAs surfaces. A year later in 1994, Hirayama [73] was the first to achieve the operation of a tensile-strained InGaAs/InGaAsP/InP QD laser and Ohira in 2005 [74] was able to demonstrate the low-threshold and high-efficiency operation of a

quantum wire laser. The operation under 10 Gbps modulation of a QD laser which is insensitive to temperature changes was presented in 2004 by Otsubo [75]. Recent publications on QD lasers can be found in [76]–[79].

As was mentioned before, a new type of semiconductor lasers which emerged in the early 1980's was the wavelength tunable lasers. According to the published literature, Suematsu in 1980 [80] was the first to propose a Three-Section (3S) tunable DBR laser which, apart from the active (gain) section, it also had a phase tuning section responsible for continuous wavelength tuning and a tuning section with a wavelength selective Bragg reflector responsible for discontinuous wavelength tuning. Tuning was possible by injecting current through electrodes into the tuning sections which caused changes of the refractive index and in turn changes of the lasing wavelength with the use of the free-carrier plasma effect. In 1983, the first InGaAsP/InP tunable laser was realised by Tohmori [81]. A butt-joined built-in DBR laser with a phase tuning phase section was monolithically integrated into the tunable laser which performed a continuous wavelength tuning range of 0.4 nm.

Four years later in 1987, Murata [82] demonstrated a 3S tunable DBR laser lasing at 1.5 μm with electrodes on both the tuning sections which achieved a continuous range of over 5.8 nm. Other multi-section TLDs with considerable tuning ranges were also realised by Amann in 1989 [83], who presented a novel twin-guide TLD with continuous tuning range and by Öberg in 1991 [84], who achieved with a 3S TLD a 22 nm tuning range with the use of both the plasma effect and thermal tuning. Because of their wide tuning range (over 5 nm), TLDs such as the ones in [82]–[84] would be called Widely Tunable (WT) lasers. A typical example of the structure of a 3S TLD can be observed in Fig. 2.1. It should also be noted here that all the lasers that have been mentioned so far,

such as the FP, DFB and DBR laser as well as TLDs are also called *edge-emitting* lasers because of their lasing at the edges of their structure.

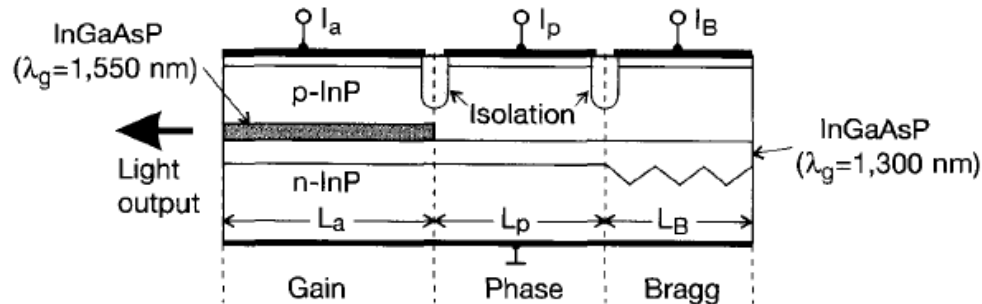


Fig. 2.1: A typical 3S TLD consisting of an active (Gain), Phase and Bragg section with length L_a , L_p and L_B , and injected with current I_a , I_p and I_B at its isolated top contact, respectively. The active section has an InGaAsP bulk active region (in grey) with bandgap wavelength $\lambda_g=1550$ nm and the passive sections have an InGaAsP waveguide region (white) with bandgap wavelength $\lambda_g=1300$ nm. The cladding and substrate are made of InP (After Ref. [85]).

After 1993, a breakthrough in terms of tuning range took place with the development of new types of gratings that, when introduced in WT lasers, would lead to wide tuning ranges of over 40 nm up to hundreds of nm. These new types of gratings were the Sampled Grating (SG) and the Super-Structure Grating (SSG). The lasers which implemented these types of gratings were Four-Section (4S) TLDs because they would consist of one grating section acting as a front mirror, a phase section and a gain section in the middle and another grating section acting as a rear mirror.

The first WT SG-DBR laser was demonstrated by Jayaraman and Coldren in 1993 [86], and it achieved a 57 nm discontinuous tuning range by carrier injection. In the same year [87], Tohmori realised the first WT SSG-DBR laser with carrier injection which could reach an impressive discontinuous tuning range of 103 nm. WT SG-DBR and SSG-

DBR lasers demonstrate wavelength tuning ranges which are one order of magnitude greater than the ones of WT DBR lasers with simple grating sections. Two reasons are responsible for this fact. The first one is that the tuning rates of the refractive index variations in the tuning sections of simple WT DBR lasers limit their overall tuning range. The second one is that WT SG-DBR and SSG-DBR lasers exploit the Vernier effect, as was explained by Coldren [86] who developed TLDs with wide tuning ranges for commercial use [88], [89]. Recent examples in published literature of WT SG-DBR and TLDs in general can be found in [90]–[94].

Another category of semiconductor lasers which is widely used today in telecom applications is the *surface-emitting* lasers, such as the Vertical Cavity Surface-Emitting Laser (VCSEL). Their key difference with edge-emitting lasers is that lasing now takes place at the (usually top) surface of the laser instead of the edges, therefore lasing is perpendicular to the plane defined by the active region. The main feature of VCSELs is that they have a very short cavity length which requires very high reflectivities of over 99% for an adequate optical feedback, which is provided by many layers (typically 20-40) of Bragg reflectors with alternating high and low refractive indices one on top of the other as is illustrated in Fig. 2.2. VCSELs are ideal for short and medium distance optical communication such as Ethernet and data links and single-mode VCSELs are especially useful for sensor applications.

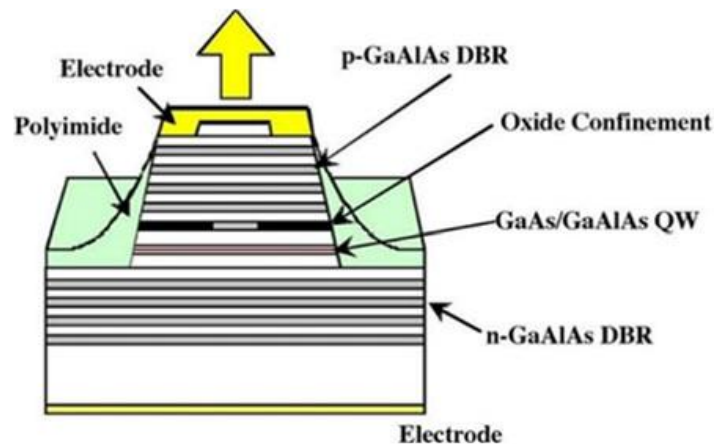


Fig. 2.2: A typical VCSEL with a GaAs/GaAlAs quantum well active region and GaAlAs Bragg reflectors (After Ref. [95]).

From a historical point of view, Koyama [95] was the first to realise the CW operation of a GaAs VCSEL at room temperature in 1988 followed by Lee in 1989 [96]. Other types of VCSELs operating with high performance were also extensively developed such as the WT VCSEL presented by Chang-Hasnain in 2000 [97]. A detailed review of the development of VCSELs throughout the 1980's until 2000 is given by Iga [98] and many recent publications of their operation in literature can be found in [69], [99]–[103].

2.2 Applications of TLDS

A tunable laser, as the name implies, is a type of laser, whose output radiation can be tuned across some range in the infra-red, visible and ultra-violet regions of the electromagnetic spectrum. It consists of an optical gain medium, a pumping process to stimulate the medium and a wavelength selective optical feedback. According to the

implementation of the optical feedback, a TLD can consist of two, three or four sections (one for the gain medium).

Depending on what they are used for, the tuning can take place on a specific value of a wavelength, producing only discrete ones, or over a wide continuous tuning range of wavelengths. The tuning mechanism is to inject current into the section which is responsible for the optical feedback and by varying the value of injection current to change the emitted wavelength in the optical output of the laser.

There are many types and categories of tunable lasers. Their lasing medium can be gas, liquid, and solid state. Among the types of tunable lasers are excimer lasers, CO₂ lasers, dye lasers (liquid and solid state), transition metal solid-state lasers, semiconductor crystal and diode lasers and free electron lasers [104].

Tunable lasers find applications in spectroscopy [105], metrology, photochemistry, atomic vapor laser isotope separation [106], [107] and, of course, optical communications. Some of their competitive advantages over other types of lasers and methods, according to each sector, are listed below;

In spectroscopy [108], TLDs can improve significantly the diagnostic investigations, by launching coherent high output powers into fibre-optic catheters. Their ability to tune quickly and accurately, allows accurate snapshots in constantly changing environments. In metrology [108], TLDs have improved the resolution, accuracy and precision of the output results, in comparison with those produced by helium-neon lasers, which were used by traditional metrology applications.

In optical communications, tunable lasers have many advantages, which, compared with other single-mode lasers, such as the DFB and DBR lasers, makes them more suitable transmitters for WDM systems [85]. The greatest advantage is, of course, the fact that a specific wavelength can be chosen for the emission light, by simply changing the

operation current that is injected into the section responsible for the optical feedback of the laser. This is not possible for normal single-mode lasers, because a different laser has to be constructed for each time light emission at a different nominal wavelength is required. This, however, is a more costly procedure in this specific case. The major problem with single-mode lasers, e.g. DFB lasers, is that their wavelength stability comes at the expense of tunability [109].

Other advantages of tunable lasers when they are used as transceivers in WDM networks, are that no wavelength planning is required before ordering, that they have simplified logistics, that the sparing costs for them can significantly be reduced and that they allow automated provisioning [110]. Tunable lasers have also been accepted as the best testing method in the manufacture of telecom components because they are faster, more accurate and lower in noise [108]. TLDs have reduced testing times of complex interleavers and multiplexers from hours to seconds [108], and are also widely exploited by networks and systems that use add-drop multiplexers, as well as systems that use technologies such as Video on Demand (VoD) and Voice over IP (VoIP) [110].

Referring to the matter of commercial availability of TLDs in the industry, a very informative example can be presented by the company Santec [111]. One of its devices is the tunable laser TSL-510, which can be seen in Fig. 2.3. The specifications of the device are as follows:



Fig. 2.3: The TSL-510 device of tunable laser by Santec [111].

The device comes with four different versions:

- Type A: Standard model with +10 dBm or more peak output power, +8 dBm or more full tuning range and 35 dB or more Signal to Noise Ratio (SNR)
- Type B: Low noise model with high SNR of 65 dB or more
- Type C: High wavelength accuracy model of ± 5 pm or less with built-in wavelength monitor
- Type D: Low noise (High SNR) and high wavelength accuracy model

All four types have the following specifications:

- 1) 130 nm tuning range within the emission wavelengths of 1260-1680 nm, which is split into three categories:
 - a) 1260-1360 nm
 - b) 1500-1630 nm
 - c) 1560-1680 nm
- 2) 100nm/s sweep speed
- 3) Mode-hop-free wavelength sweeps
- 4) <1 pm wavelength resolution (Fine tuning)
- 5) GPIB and USB interfaces with the industry standard SCPI command

Some of the applications of the TSL-510 tunable laser can be found in:

- Optical component characterisation
- Fibre optic transmission testing
- Fibre optic sensors

- Optical spectroscopy
- Photonic material characterisation

The previous discussion gives a general idea of how TLDs operate and are generally available and commercially applicable in the industry.

Chapter 3

Theory of semiconductor lasers

3.1 *Electrons, holes, photons and phonons in semiconductors*

The field of optoelectronics includes the science of optics and electronics in a single material or device [112]. The material that is chosen needs to allow both the propagation of light inside it as well as the flow of electrical current and permit these two to interact with each other. In the case of electrical conductivity, metals are the best candidates but are not suitable for light propagation. In the case of light propagation, glass and similar dielectric materials (like optical fibres) can allow and guide light waves inside them but are perfect electrical insulators.

There is one material type though that combines both features and can even be designed to permit the transformation of electrical current into light (which is the basic concept of a laser) and vice versa. This material type is the semiconductors and they are the most popular material for the fabrication of lasers with the widest range of applications in optical communications.

The flow of electrons is the reason for the conduction of electrical current. However, most electrons are not allowed to move freely as they are attached to single atoms in a specific quantised number of shells or discrete *energy levels* according to Bohr's atomic model [113]. There are some electrons though which are loosely bound to the outer shell of the atom and can be released to become free electrons or *conduction* electrons. When these electrons are released, the atoms that are left behind have a lack of electron and become positively charged or else *ions*. These atoms are also called *valence electrons* or *holes* because of this loss of electron in their outer shell and the fact that there is an empty space now in the outer shell than can be filled by another free electron.

The net charge however from this whole process in the semiconductor is zero, since free (conduction) electrons and ions (holes) have exactly the same number.

Apart from the free conduction electrons the valence electrons (holes) can also make a transition from one atom to another, therefore the positive charges can also move. In this way electrical current can be carried by both conduction and valence electrons, which are both also called *carriers* for this reason. Because of the discrete energy levels (shells) of the atom, these carriers are separated by an energy gap E_g . Therefore, in order for the valence electrons to become conduction electrons they need to receive a value of energy at least equal to the gap energy E_g . This gap energy is in the order of 1 eV in semiconductors.

The amount of energy that is required for a valence electron to become a conduction electron can be provided by light if it has a wavelength equal or shorter than the gap wavelength λ_g , which is defined as:

$$\lambda_g = \frac{hc}{E_g} = \frac{1240 \text{ nm}}{E_g \text{ (eV)}} \quad (3.1)$$

where h is the Planck constant and c is the speed of light in vacuum.

According to the wave-particle duality theory, light can be represented both as a wave produced by a combination of electromagnetic fields with a wavelength λ and as a series of particles produced by a stream of energy packets (quanta) called *photons*, which have an energy E_{ph} defined as:

$$E_{ph} = \frac{hc}{\lambda} = h\nu = \hbar\omega \quad (3.2)$$

where \hbar is the reduced Planck constant, ν is the frequency of the propagating photon and $\omega = 2\pi\nu$ is its angular frequency.

Therefore if a photon with an energy E_{ph} equal or greater than the gap energy E_g interacts with a valence electron, it can excite it to become a conduction electron and generate an electron-hole pair. The exact opposite though can also happen if a conduction electron becomes a valence electron (electron-hole recombination) by releasing energy equal to the gap energy in the form of light. The photon that is generated by this process will have an energy $E_{ph} = E_g$. The key physical mechanism which takes place in optoelectronic devices is this energy exchange and interaction between electrons and photons and will be described in more detail in section 3.4.

If the interaction between conduction and valence electrons is considered by the point of view of the atom, in the case of semiconductors the valence electrons belong to the outermost electron shell (energy level) of the atom which is fully occupied and no more electrons with the same energy are allowed. According to the number of electrons in the outermost shell of the atom semiconductors are categorised into types, so that type III semiconductors like Gallium (Ga), Aluminium (Al) and Indium (In), type IV semiconductors like Silicon (Si) and Germanium (Ge) and type V semiconductors like Nitrogen (N), Arsenic (As) and Phosphorus (P) have three, four and five electrons, respectively in the fully occupied outermost shell of their atom. Type III-V semiconductors is the most popular group for the fabrication of semiconductor lasers and are widely used in telecom applications.

To continue the previous discussion, when more than one atoms of the semiconductor are put together in a crystal lattice then the electrons of the atoms start to interact with each other and the valence energy levels are slightly separated forming as a result a *valence energy band* as is shown in Fig. 3.1.

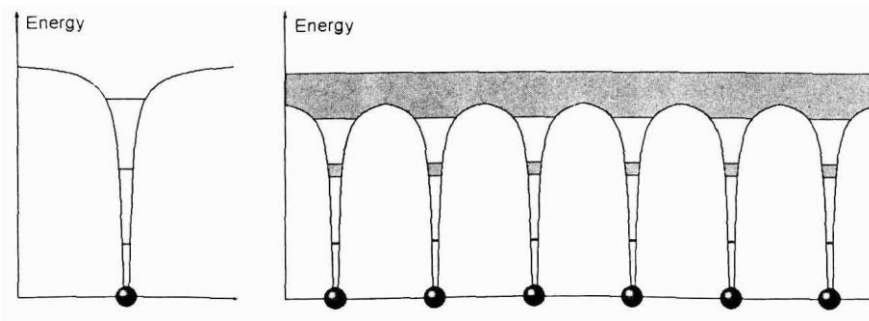


Fig. 3.1: A single atom and its electron energy levels (left) and the energy bands when many atoms are joined in a solid semiconductor crystal lattice (right) (After Ref. [112]).

Within this band it is possible that electrons can move and exchange places, however there can be no flow of charge there unless a hole (valence electron) is generated. The generation of holes can be achieved when electrons are excited in some way, by absorbing a photon for example as was described above, and move to the next higher energy band which is called the *conduction band*. The energy difference (gap) that exists between the conduction and valence band is therefore called the energy *bandgap*.

Initially, without any external excitation of electrons and holes in the lattice structure and with zero internal temperature $T=0$ K of the semiconductor the conduction band is completely empty of electrons and the valence band is fully occupied with electrons (system at equilibrium). Therefore, the electrical conductivity σ of the semiconductor is defined according to the concentration n of electrons in the conduction band and the concentration p of holes in the valence band as follows:

$$\sigma = en\mu_n + ep\mu_p \quad (3.3)$$

where e is the electron charge and μ_n and μ_p is the mobility of electron and holes, respectively.

The electron and hole concentrations change with the temperature of the semiconductor when there is no external energy supply. If the temperature rises, then the crystal lattice vibrates more strongly and more transitions of electrons from the valence band to the conduction band take place. Therefore, the conduction band starts filling with electrons while the valence band starts having a lack of electrons and a generation of holes takes place.

The vibrations of the crystal lattice are also called *lattice waves* and depending on the direction of the atom movement are classified into two categories. The first one is the *longitudinal* (L) waves where the oscillations of the atom are in the travel direction of the lattice wave. The second one is the *transversal* (T) waves where the oscillations of the atom are normal to the travel direction of the lattice wave. Depending on the relative movement of neighbouring atoms the lattice waves can also be classified into two additional categories. The first one is the *acoustic* (A) waves where the neighbouring atoms are moving in the same direction and the second one is the *optical* (O) waves where the neighbouring atoms are moving in the opposite direction in ionic crystals. When light passes through the crystal lattice and the electric field moves ions with different charges in different directions, then the optical waves interact directly with the incoming light waves.

The smallest portion of energy which is generated by the lattice vibrations is called a *phonon* and it can be considered to be a particle. Four types of phonons can therefore exist according to the above classification, LA, LO, TA and TO. During the crystal lattice vibrations electrons and holes can interact with phonons by generating and absorbing them, which in turn can cause changes in the electron-hole energy.

3.2 Fermi levels and density of states in semiconductors

As was discussed above, electrons can occupy bands with different energy or different energy levels. The probability that an electron (hole) exists in an energy level with energy E at a temperature T is given by the Fermi-Dirac distribution function $f_{n(p)}(E)$ which is a function of the energy E and is defined as:

$$f_{n(p)}(E) = \frac{1}{1 + e^{\frac{E - E_{F_{n(p)}}}{k_B T}}} \quad (3.4)$$

where $E_{F_{n(p)}}$ is the electron (hole) Fermi level energy and k_B is the Boltzmann constant ($k_B T \approx 25$ meV at room temperature $T=300$ K).

The electron (hole) Fermi level represents the highest energy state that an electron (hole) can occupy at $T=0$ K and it separates energy levels that are occupied by electrons from energy levels that are not occupied by electrons. The Fermi level for electrons and holes is the same at equilibrium in pure semiconductors and typically is set in the middle of its bandgap between the conduction and valence band as is shown in Fig. 3.2 (left).

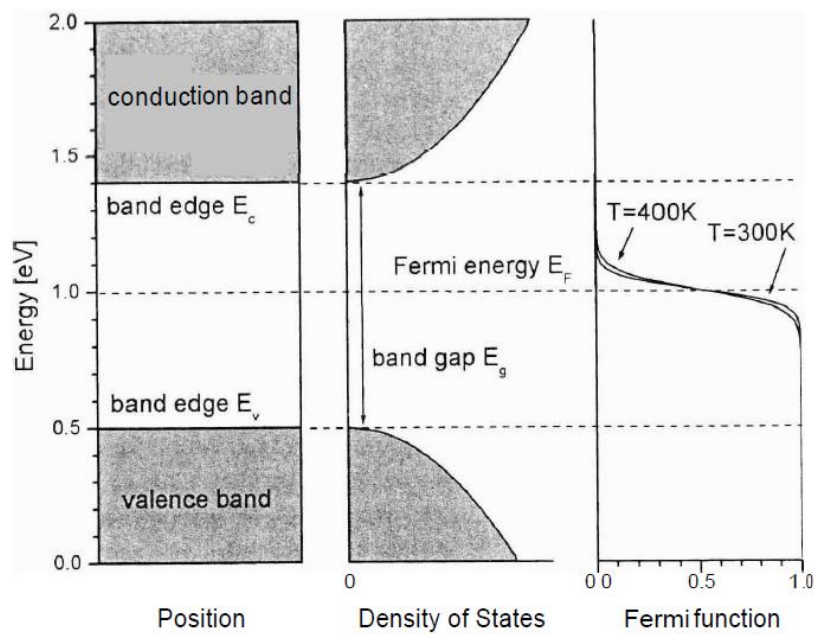


Fig. 3.2: Semiconductor conduction and valence band (left), density of states (middle), Fermi-Dirac function at different temperatures (right) and illustration of the Fermi energy at equilibrium (After Ref. [112]).

However, an increase in the temperature in the semiconductor leads to an increase of the amount of electrons that are excited and move from the valence to the conduction band. The number of possible energy states (levels) that an electron is allowed to jump to and make a transition when it is excited is called *density of (electron) states* $D(E)$. In bulk semiconductors, the density of states $D_c(E)$ and $D_v(E)$ in the conduction and valence band, respectively is a parabolic function of the transition energy E [shown in Fig. 3.2 (middle)] if electrons and holes are considered as (quasi-) free particles and is defined as:

$$\begin{aligned}
 D_c(E) &= \frac{1}{2\pi^2} \sqrt{\left(\frac{2m_n}{\hbar^2}\right)^3} \sqrt{E - E_c} \quad (E > E_c) \\
 D_v(E) &= \frac{1}{2\pi^2} \sqrt{\left(\frac{2m_p}{\hbar^2}\right)^3} \sqrt{E_v - E} \quad (E < E_v)
 \end{aligned}
 \tag{3.5}$$

where $m_{n(p)}$ is the electron (hole) effective mass in the semiconductor.

Apart from bulk semiconductor structures where particles are free to move in three dimensions (3D), there are other types semiconductor structures such as the *quantum well* and *quantum dot* which are widely used in the fabrication of semiconductor lasers with numerous applications and are described by the field of quantum mechanics.

A quantum well is a thin layer structure of a few nanometres thickness also called a *potential well* which is a region that has a minimum potential energy that can not be converted to any other type of energy. Because of this structure, the quantum well confines particles to two dimensions (2D) instead of three as in the bulk 3D structure and forces them to occupy a planar region. When the quantum well thickness becomes comparable to the de Broglie wavelength (explained below) of the carriers (electrons and holes) the effect of *quantum confinement* takes place which leads to discrete quantised energy levels also called *energy subbands*. The energy band structure of a typical quantum well is illustrated in Fig. 3.4 (left).

The de Broglie wavelength appears in this discussion because of the wave-particle duality which is one of the fundamental features of quantum mechanics. Thus, it is more appropriate to describe the behaviour of electrons within a semiconductor crystal by considering electrons as waves with a wave vector k and a wavelength λ which is called the *de Broglie wavelength* and is typically a few nanometres ($\lambda \sim \text{nm}$) in semiconductors.

The wave vector k is related to wavelength λ as $k = \frac{2\pi}{\lambda}$ and the de Broglie equation gives

for the wavelength λ in a semiconductor at temperature T :

$$\lambda = \frac{h}{p} = \frac{h}{\sqrt{3m_n k_B T}} \quad (3.6)$$

where $p = m_n u$ is the momentum of the electron and $u = \sqrt{\frac{3k_B T}{m_n}}$ is its velocity in the semiconductor.

The energy of the electron E_n in the semiconductor is therefore related to the wave vector k as follows:

$$E_n = \frac{\hbar^2 k^2}{2m_n} \quad (3.7)$$

As was mentioned above, the conduction and valence band of a semiconductor quantum well is split in a number of energy levels (states) or subbands each having a *quantum number* $m=1, 2, \dots$. The energy states at the bottom of the conduction band are n-like with zero orbital angular momentum and are isotropic in space. The energy states at the top of the valence band, however, are p-like with non-zero orbital angular momentum and are anisotropic in space with three independent states. These are the *Heavy-Hole* (HH) state, the *Light-Hole* (LH) state and the *Split-off* (SO) state. Most of the electron transitions take place between the conduction subbands and the HH and LH valence subbands, however there are also band to band transitions between the HH and LH band which is called *valence band mixing*. The SO valence subband is separated by a specific value of energy called the *split-off energy* (hence the name of the subband) from the HH and LH valence subbands and therefore is less important in the process of electron transitions.

Vertical transitions of electrons between subbands of the conduction and valence band are allowed only for subbands with the same quantum number. Electron transitions between subbands of different quantum number are therefore forbidden. This process is illustrated in detail in Fig. 3.3, where the “allowed” and “forbidden” electron transitions

between subbands of the conduction and valence (HH and LH) band with quantum numbers $m=1, 2$ are plotted as a function of the wave vector k of the electron.

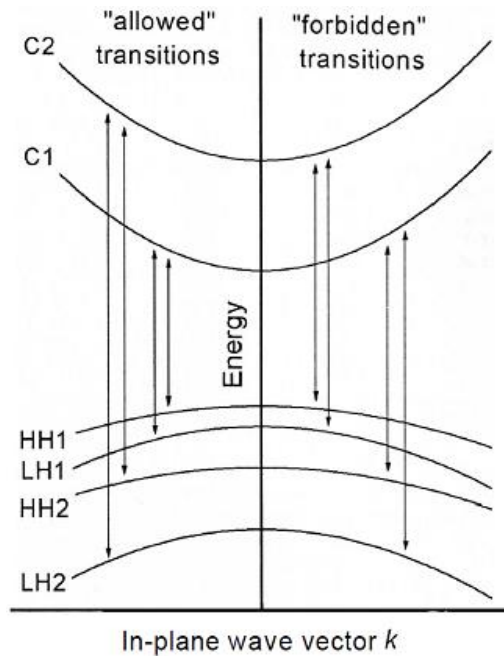


Fig. 3.3: Conduction (C1 and C2) and valence (Heavy-Hole HH1 and HH2 and Light-Hole LH1 and LH2) subbands (with quantum number $m=1, 2$) as a function of the wave vector k in a semiconductor quantum well and their allowed and forbidden transitions (After Ref. [112]).

The density of states for the conduction and valence subbands of a semiconductor quantum well depends on the number of subbands $n=1, 2, \dots$, it is inversely proportional to the quantum well thickness d_w and is defined as:

$$D_{c(v)}(E) = \sum_n \frac{m_{n(p)}}{\pi \hbar^2 d_w} \quad (3.8)$$

The quantum well density of states has a step-like behaviour which is illustrated in Fig. 3.4 (middle) as a function of transition energy E compared with the bulk density of states.

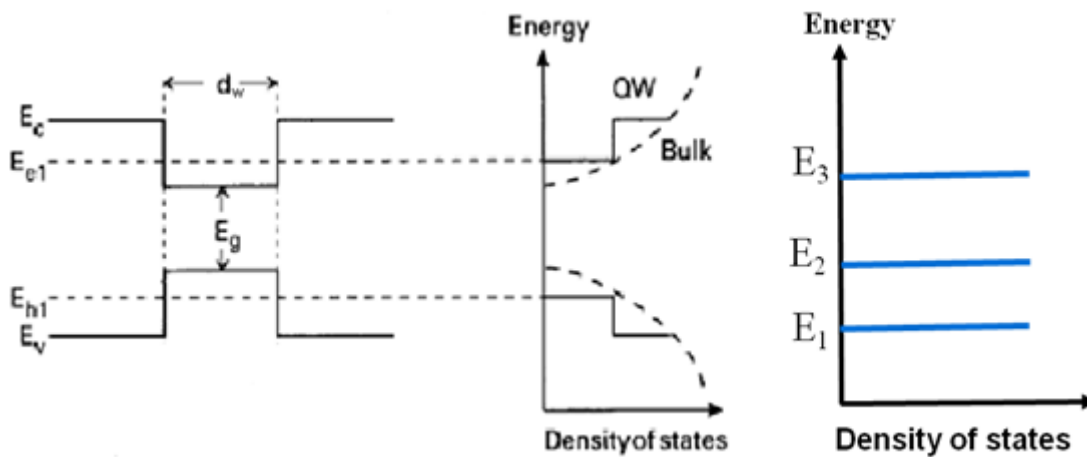


Fig. 3.4: Energy band structure of a quantum well of thickness d_w with bandgap energy E_g , conduction band energy E_c , conduction subband energy E_{c1} , valence band energy E_v , valence subband energy E_{v1} (left) and density of states as a function of energy for the case of a bulk (dotted line) and quantum well (solid line) semiconductor (middle) and the case of a semiconductor quantum dot (right) (After Ref. [85]).

The other semiconductor structure that was mentioned before and is widely used in the fabrication of semiconductor lasers is the quantum dot. It is a nanocrystal which is small enough to have quantum mechanical properties and is made of semiconductor materials. A fundamental property is that excitons (electron-hole pairs) in this structure are confined in all three spatial dimensions and the electronic states that emerge due to this confinement are quantised. The volume of a quantum dot is comparable to the de Broglie wavelength, therefore it can be described as a zero-dimensional box (0D) and in many respects it behaves like an *artificial atom*. The density of states of a quantum dot is illustrated in Fig. 3.4. (right) and is defined as a Dirac (delta) function $\delta(E-E_n)$ for each energy state $n=1, 2, \dots$ with energy E_n as:

$$\begin{aligned} \delta(E - E_n) &= \infty, & E &= E_n \\ \delta(E - E_n) &= 0, & E &\neq E_n \end{aligned} \quad (3.9)$$

In the three structures of semiconductor lasers (bulk 3D, quantum well 2D and quantum dot 0D) the concentration $n(E)$ and $p(E)$ of electrons and holes, respectively or else *carrier density* depends on the density of states of the conduction and valence band (and their subbands in the quantum well case) and is defined as a function of energy E as:

$$\begin{aligned} n(E) &= D_c(E)f(E) \\ p(E) &= D_v(E)[1 - f(E)] \end{aligned} \quad (3.10)$$

If Fermi statistics are taken into account, then the general expression for the electron and hole concentration n and p , respectively is:

$$\begin{aligned} n &= N_c F_{1/2} \left(\frac{E_{F_n} - E_c}{k_B T} \right) \\ p &= N_v F_{1/2} \left(\frac{E_v - E_{F_p}}{k_B T} \right) \end{aligned} \quad (3.11)$$

where $F_{1/2}$ is the Fermi integral of order one-half which is calculated by integrating the two equations in (3.10) and N_c and N_v is the effective density of states for the conduction and valence band, respectively and is defined as:

$$\begin{aligned} N_c &= 2 \sqrt{\left(\frac{m_n k_B T}{2\pi\hbar^2} \right)^3} \\ N_v &= 2 \sqrt{\left(\frac{m_p k_B T}{2\pi\hbar^2} \right)^3} \end{aligned} \quad (3.12)$$

The Fermi integral of order one-half can also be numerically evaluated by using the approximation:

$$F_{1/2}^{-1}(x) \approx e^{-x} + \frac{3}{4} \sqrt{\pi} \left[x^4 + 50 + 33.6x \left(1 - 0.68 e^{-0.17(x+1)^2} \right) \right]^{-\frac{3}{8}} \quad (3.13)$$

3.3 Doping in semiconductors

Doping in semiconductors takes place when impurity atoms are introduced in the semiconductor crystal lattice in order to increase the concentration of electrons and holes. When an impurity or *dopant* contributes a free electron in the crystal then it is called a *donor*. Donors have a concentration N_D and energy levels with energy E_D which are slightly below the conduction band as is illustrated in Fig. 3.5. In similar fashion when a dopant contributes a valence electron (hole) in the crystal then it is called an *acceptor*. Accordingly, many acceptors have a concentration N_A and energy levels with energy E_A which are slightly above the valence band as is shown in Fig. 3.5.

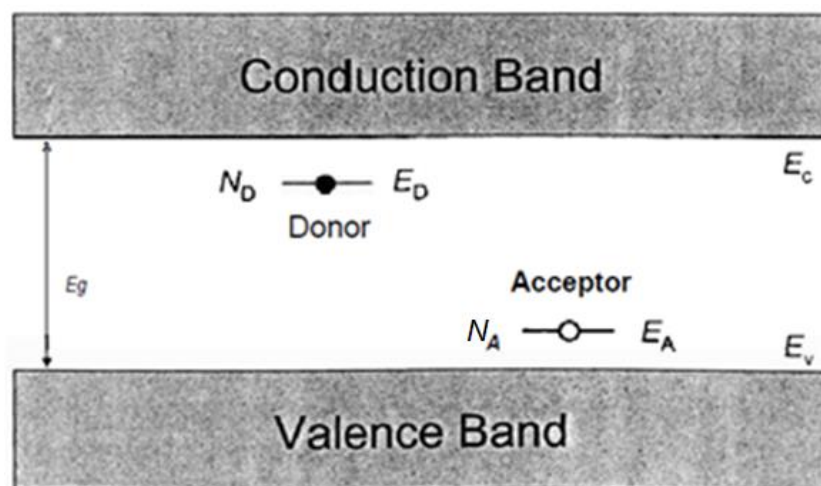


Fig. 3.5: Donor and acceptor levels between the conduction and valence band with energy E_c and E_v , respectively in a semiconductor with bandgap energy E_g (After Ref. [112]).

There are two types of doping in semiconductors, *n-doping* and *p-doping*. The process of n-doping takes place when donors become positively charged ions by releasing an electron into the conduction band, therefore providing an additional free electron to the

crystal. The process of p-doping takes place when acceptors become negatively charged ions by receiving an electron from the valence band, therefore providing an additional valence electron (hole) to the crystal. By this process the semiconductor (bulk case) becomes *degenerate* and the actual position of the Fermi level E_F is determined at thermal equilibrium by the *charge neutrality condition* which is:

$$n + n_A = p + p_D \quad (3.14)$$

where n_A is the concentration of the negatively charged ionised acceptors and p_D is the concentration of the positively charged ionised donors and is defined as:

$$n_A = N_A \frac{1}{1 + g_A e^{\frac{E_A - E_F}{k_B T}}}$$

$$p_D = N_D \frac{1}{1 + g_D e^{\frac{E_F - E_D}{k_B T}}}$$
(3.15)

where g_A and g_D is the degeneracy number of the acceptors and donors, respectively with typical values $g_A=4$ and $g_D=2$ [112].

When an external carrier injection or an absorption of light takes place in a degenerate semiconductor then non-equilibrium electron and hole concentrations are generated, which could be above the equilibrium level. The Fermi functions in (3.11) can still describe accurately the electron and hole concentrations, however the Fermi levels for electron and holes are not at the same level any more but are separated into two quasi-Fermi levels.

The quasi-Fermi level for electrons is not in the middle of the semiconductor bandgap any more (Fig. 3.2) but has a higher energy value and moves to a level slightly below the bottom of the conduction band. The quasi-Fermi level for holes is also not in the middle of the semiconductor bandgap (Fig. 3.2) but has a lower energy value and moves to a level slightly above the top of the valence band.

This process can be showcased in more detail in Fig. 3.6 for a case of a semiconductor double heterostructure laser under forward bias U . This type of laser has an undoped semiconductor material acting as an active region which is surrounded by two semiconductor materials (one of n-type and one of p-type) of higher bandgap energy so that carriers inside the active region are confined and cannot escape to the n-type and p-type regions and are forced to recombine.

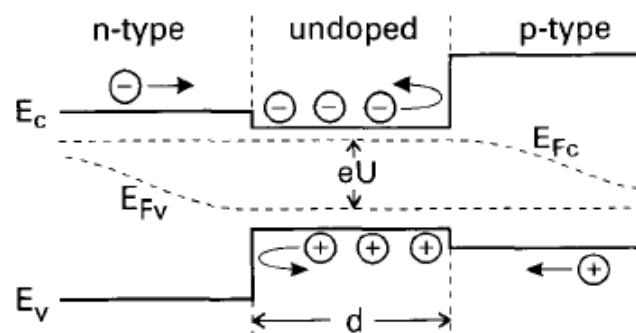


Fig. 3.6: A semiconductor double heterostructure laser under forward bias U with an undoped active region of thickness d between a n-type and p-type region, and a conduction band energy E_c , electron quasi Fermi level energy E_{Fc} , valence band energy E_v and hole quasi Fermi level energy E_{Fv} (After Ref. [85]).

3.4 Rate equations and optical gain in semiconductors

The generation of light relies on electrons and holes that are placed in various energy levels (bands) in a semiconductor material, such as a *p-n junction* structure or *double heterojunction* structure, and react (recombine) with each other [114]. This reaction is basically a transition from the levels (states) with higher energy to the levels with lower ones, or the opposite, and can be separated into four categories [114]:

1) *Spontaneous carrier recombination* (photon emission): It is the case when electrons from a higher energy level, with energy E_1 , jump spontaneously (without any external force or influence) to a lower energy level, with energy E_2 , where there is a gap (hole) that can be filled there. This procedure is followed by the generation of a photon with frequency ν that corresponds exactly to the difference between the energy levels $E_1 - E_2 = h\nu$, according to Planck, where h is the Planck constant. In this process we say that there is a recombination between electrons and holes or that the free charge carriers (electrons or holes) recombine to produce photons. The more the electrons make jumps per unit time to fill holes, the higher is the recombination rate and the more photons are generated, which is the fundamental physical process necessary (but not yet sufficient) for the lasing.

2) *Stimulated carrier generation* (photon absorption): In this case, an electron in a lower energy state, with energy E_2 , is hit (*stimulated*) by an incoming photon with frequency ν and causes it to jump to a higher energy state with energy E_1 , where $(E_1 - E_2) / h$ corresponds to the frequency of the photon as it was described above. In this case, the photon is absorbed as it gives all its energy to the jumping electron.

3) *Stimulated carrier recombination* (coherent photon emission): It is the exactly opposite case of 2), as now an incoming photon *stimulates* an electron in a higher energy state E_1 and makes it fall to a lower one E_2 , generating a new photon with a unique frequency $\nu = (E_1 - E_2) / h$. In this case, we will have two photons, the one that stimulated the electron and the generated one, with exactly the same characteristics and direction (coherent photons). This case is the most important condition for lasing, as it causes the chain generation of the photons, because each new photon can stimulate new electron-hole transition in turn.

4) *Nonradiative recombination*: In this case, electrons recombine with holes by jumping from higher to lower energy levels, but no photons are generated, because all the released energy becomes heat and is absorbed by the semiconductor material. The four categories of electronic transitions described above are illustrated in Fig. 3.7.

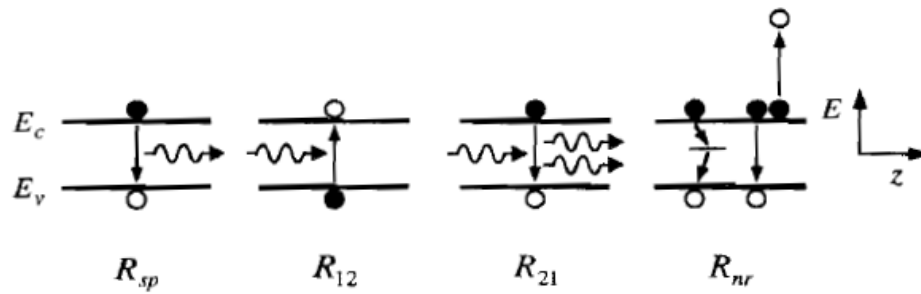


Fig. 3.7: The four categories of electronic transitions between the conduction and valence band with energy E_c and E_v , respectively. R_{sp} , R_{12} , R_{21} and R_{nr} is the spontaneous carrier recombination, stimulated carrier generation, stimulated carrier recombination and nonradiative recombination rate, respectively. z is the axis of photon propagation (After Ref. [114]).

After explaining the basic forms of electronic transitions, it is time to give the basic rate equations that describe mathematically this process. First of all, we should mention that every laser has a region where all carriers recombine to produce photon emission, as well as useful gain of photons that will contribute to lasing. This region is called the *active region*.

The first rate equation describes how the number of carriers are generated in the active section and how they recombine to produce photons. The generation of carriers in the case of semiconductor laser structures can be done by simply injecting current into the active region. This increases the amount of electrons and holes in the active region compared with the equilibrium state, which in turn increases the number of

recombination transitions. The carrier density inside the active region volume is defined as: $N = \text{number of carriers} / \text{volume}$. The resulting carrier density change per unit time is then defined by the balance or the rate equation as:

$$\frac{dN}{dt} = G_{gen} - R_{rec} \quad (3.16)$$

where G_{gen} is the rate of the electron injection into the active region and R_{rec} is the rate of recombination of the electrons per unit volume in the active region. But the number of injected electrons into the whole active region per second is $\eta_i I / e$, where I is the injection current, e is the electron charge and η_i is the current injection efficiency, which is the fraction of terminal current that generates carriers in the active region. So, G_{gen} can be written as the rate of injected electrons per unit volume:

$$G_{gen} = \frac{\eta_i I}{eV} \quad (3.17)$$

where V is the volume of the active region.

The rate of recombining electrons consists of the four types of recombination that were described above and is defined as:

$$R_{rec} = R_{sp} + R_{nr} + R_l + R_{st} \quad (3.18)$$

where R_{sp} is the spontaneous recombination rate, R_{nr} is the nonradiative recombination rate and R_{st} is the stimulated recombination rate for both stimulated photon absorption and emission. Finally, R_l is the rate of *carrier leakage* inside the cavity, as there are always carriers that escape from the active region before recombination takes place and do not contribute to the generation of light. The first three terms of the right side of (3.18) correspond to unstimulated recombination (*loss*) of carriers inside the cavity and can also

be described as the total carrier density N over the time these carriers remain in the cavity before they recombine, which is called *carrier lifetime* τ_c or

$$\frac{N}{\tau_c} \equiv R_{sp} + R_{nr} + R_l \quad (3.19)$$

It has been found that $R_{sp} \sim BN^2$, where B is called the *bimolecular or radiative recombination coefficient* and $R_{nr} + R_l \sim AN + CN^3$, where A is called the *linear or Shockley-Read-Hall recombination coefficient* and C is called the *Auger recombination coefficient*. So, (3.19) can be written as

$$\frac{N}{\tau_c} = AN + BN^2 + CN^3 = N(A + BN + CN^2) \quad (3.20)$$

or

$$\frac{1}{\tau_c} = A + BN + CN^2 \quad (3.21)$$

The rate of stimulated emission R_{st} represents the electron-hole recombination initiated by the present photons in the cavity that leads to the increasing generation of photons, which is a *gain process*. It is defined as $R_{st} = v_g g N_p$, where v_g is the group velocity of the emitted photons, N_p is the *photon density* and g is the gain process. The gain coefficient is defined as the relative amount of increased photon density ($\Delta N_p / N_p$) per unit length Δx , or mathematically as

$$g = \frac{1}{N_p} \frac{\Delta N_p}{\Delta x} = \frac{1}{v_g N_p} \frac{\Delta N_p}{\Delta t} = \frac{1}{v_g N_p} R_{st} \quad (3.22)$$

in accordance with the above expression. The laser cavity gain depends on the density of the carriers injected into the cavity.

From a quantum mechanical point of view gain takes place when an incoming photon in the cavity causes the transition of an electron from a higher to a lower energy band or else the stimulated recombination of an electron-hole pair. Therefore a second

photon is created which is coherent with the incoming one and the amplitude of the monochromatic wave is doubled. The second photon in turn can stimulate a new electron-hole pair in order to create a third photon and by repeating this process strong light amplification can be achieved.

The opposite process of light amplification is the photon absorption and the generation of new electron-hole pairs which leads to loss of light in the cavity. When more electrons exist in the conduction band with a higher energy level than in the valence with a lower energy level, then a carrier *population inversion* takes place which leads to gain instead of absorption. This inversion can be realised in a p-n junction structure when conduction band electrons are placed in the n-doped side and valence band holes are placed in the p-doped side.

By forwardly biasing the p-n junction with a low injection current the band to band absorption still dominates and the optical gain is negative ($g < 0$). By increasing the injection current, there comes a point where the stimulated emission and the absorption are equal and the gain is zero ($g = 0$). In this case the material becomes transparent or else reaches *transparency conditions* and the injection current which causes these conditions is called *transparency current*. With further increase of the injection current the stimulated emission dominates, there is strong light amplification and the gain becomes positive ($g > 0$).

The optical gain is proportional to the probability that a given photon causes an electron transition from a higher energy level j to a lower energy level i . This process as is already mentioned produces a new photon with energy $h\nu$ which must be equal to the transition energy $E_{ij} = E_j - E_i$ which is the energy difference between levels j and i . This

probability has been calculated in many publications [112] and the general expression for gain as a function of photon energy $E_{ij}=h\nu$ is given by:

$$g_{ij}(h\nu) = \frac{e^2 h}{2m_0^2 \epsilon_0 n' c} \frac{1}{h\nu} |M(E_{ij})|^2 D_r(E_{ij}) (f_j(E_j) - f_i(E_i)) \quad (3.23)$$

where m_0 is the electron mass, ϵ_0 is the dielectric constant of vacuum, n' is the real part of the complex refractive index $n = n' + in''$ of the semiconductor material, $|M(E_{ij})|^2$ is the transition matrix element (described in detail in [112]) which defines the strength of the transition between the energy levels j and i and is also the most important parameter for the calculation of gain, $f_j(E_j)$ and $f_i(E_i)$ is the Fermi function that gives the probability that the energy level E_j and E_i , respectively, is occupied by electrons and $D_r(E_{ij})$ is the density of allowed electron transitions between the two bands (levels) j and i and is defined in the case of a bulk semiconductor as:

$$D_r(E) = \frac{1}{\frac{1}{D_c} + \frac{1}{D_v}} = \frac{1}{2\pi^2} \sqrt{\left(\frac{2m_r}{\hbar^2}\right)^3} \sqrt{E - E_g}, \quad E > E_g \quad (3.24)$$

where m_r is the reduced effective mass which is defined as:

$$m_r = \frac{1}{\frac{1}{m_n} + \frac{1}{m_p}} \quad (3.25)$$

In the case of a quantum well with thickness d_w the reduced density of states for each subband is constant and defined as:

$$D_r^{2D} = \frac{m_r}{\pi \hbar^2 d_w} \quad (3.26)$$

The expression in (3.23) is valid in the case of a bulk semiconductor if the levels j and i are replaced with the conduction and valence band, respectively. The same

applies in the case of a quantum well where the gain is expressed as in (3.23) if the levels j and i are replaced with the subbands of the conduction and valence band, respectively. The gain spectrum of a bulk semiconductor and a quantum well for band to band electron transitions as a function of photon energy $h\nu$ is illustrated in Fig. 3.8.

As is seen in Fig. 3.8, the gain varies with photon energy and the reduced density of states defines the lower energy limit where the gain is positive. When the Fermi factor $f_j(E_j) - f_i(E_i) = 1$ or when $f_j(E_j) = 1$ at the upper energy level and $f_i(E_i) = 0$ at the lower energy level, then the gain reaches its maximum value. As the photon energy $h\nu$ increases however, the Fermi factor decreases until it becomes zero when the photon energy is equal to the quasi-Fermi level distance $\Delta E_{F_{ij}} = E_{F_j} - E_{F_i}$. At that point the gain is also zero. For higher photon energies after that point the gain becomes negative as the band to band absorption dominates. Therefore no band to band electron transitions can take place at photon energies higher than the difference between the Fermi level energies $\Delta E_{F_{ij}}$ of the levels j and i and the gain spectrum is limited according to this fact which is called the *Bernard-Duraffourd condition*:

$$E_g < h\nu < E_{F_j} - E_{F_i} \quad (3.27)$$

In Fig. 3.8 it can also be observed that the shape of the gain spectrum of the quantum well is rather sharp compared with the smooth shape of the gain spectrum of the bulk semiconductor because of the constant density of states for each subband of the quantum well. However, the shape of the quantum well gain spectrum can become smoother due to the intraband relaxation of the electron transitions in the quantum well which results to the transition energy broadening of the gain spectrum with the use of a lineshape broadening function (typically Lorentzian) as will be explained in Chapter 7.

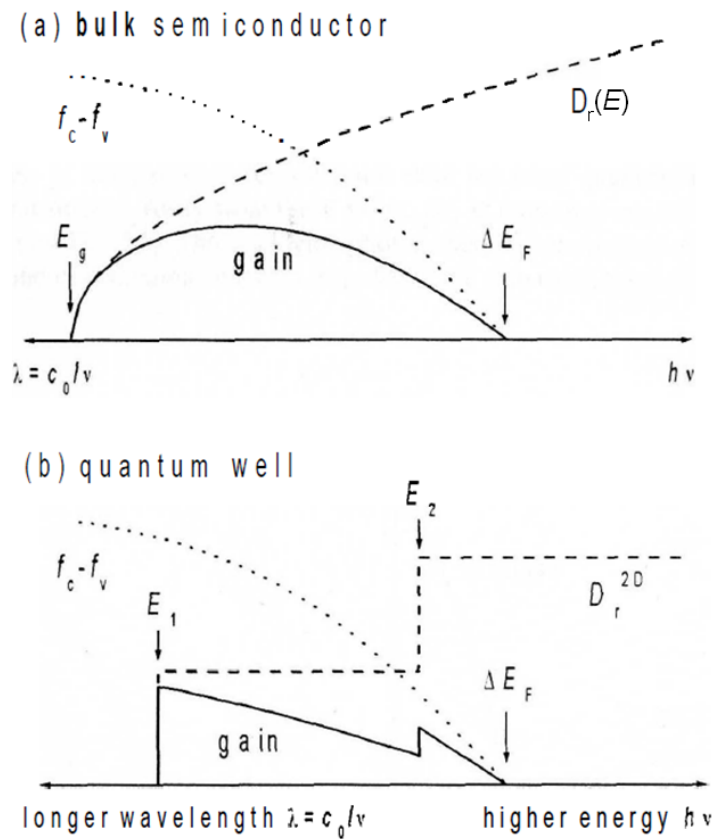


Fig. 3.8: Gain spectra, reduced density of states and Fermi level difference for band to band electron transitions as a function of photon energy $h\nu$ for (a) a bulk semiconductor from the conduction to the valence band and (b) a quantum well at different energy levels E_1 and E_2 (After Ref. [112]).

It is obvious that the expression of gain in (3.23) has a quite complex mathematical form which is not very useful for the expression of the rate equations, however it turns out that at or near the lasing state assuming that this happens at the gain peak the expression in (3.23) can be approximated by the linear function:

$$g = \alpha(N - N_{tr}), \quad (3.28)$$

where α is called *differential gain* equal to $\alpha = \frac{dg}{dN}$ and N_{tr} is the carrier density at transparency conditions ($g = 0$ at $N = N_{tr}$) or else *transparency carrier density*. So, the rate of stimulated emission can be written now as

$$R_{st} = v_g \alpha (N - N_{tr}) N_p \quad (3.29)$$

And (3.18) can be written as

$$R_{rec} = \frac{N}{\tau_c} + v_g \alpha (N - N_{tr}) N_p \quad (3.30)$$

As a result, the first rate equation that describes the recombination of electrons and holes ($N_{el} = N_{hol} \equiv N$) becomes:

$$\frac{dN}{dt} = \frac{\eta I}{eV} - \frac{N}{\tau_c} - v_g \alpha (N - N_{tr}) N_p. \quad (3.31)$$

In a working laser, after a certain current injection (pumping) point, the carrier density in a cavity is *clamped*, which means that it does not increase any more. This is the *steady state* for the laser. At the laser *threshold*, which is the condition just before the lasing operation starts, the stimulated recombination rate can be put to zero and (3.31) becomes

$$\frac{\eta I}{eV} - \frac{N}{\tau_c} = 0 \Rightarrow I_{th} = \frac{eV N_{th}}{\eta_i \tau_c}, \quad (3.32)$$

which defines the value of the injection current at threshold I_{th} if we know the carrier density at threshold N_{th} .

The second rate equation describes the generation and loss of photons inside the cavity. Physically it is the exact equivalent of the first rate equation, only instead of the electron density, one has to use the *photon density* N_p . So, the resulting rate of the photon generation inside the active region over time is described as:

$$\frac{dN_p}{dt} = \Gamma R_{st} - \frac{N_p}{\tau_p} + \Gamma \beta_{sp} R_{sp} = \Gamma v_g \alpha (N - N_{tr}) N_p - \frac{N_p}{\tau_p} + \frac{\Gamma \beta_{sp} N}{\tau_c} \quad (3.33)$$

where τ_p is the *photon lifetime*, which describes the photon loss process due to the internal optical losses in the cavity and the photon escape from the cavity through the mirrors, β_{sp} is the *spontaneous emission factor* and Γ is the *confinement factor*. The spontaneous emission factor is the reciprocal of the number of optical modes in the bandwidth of the spontaneous emission. The confinement factor is an electron-photon overlap factor in the active region and is defined as V / V_p , where V is the active region volume that is occupied by electrons and V_p is the cavity volume occupied by photons, which is usually larger than V .

The third rate equation describes how the phase of propagating photons changes in time and is as follows [41]:

$$\frac{d\phi}{dt} = \frac{1}{2} \alpha_H \left\{ \Gamma v_g \alpha (N - N_{tr}) - \frac{1}{\tau_p} \right\} \quad (3.34)$$

where $\alpha_H = \frac{\partial n' / \partial N}{\partial n'' / \partial N}$ is called the *linewidth enhancement factor* (or *alpha* or *Henry factor*) and it defines the additional linewidth broadening due to coupling between the real part n' and the imaginary part n'' (defines gain or absorption) of the refractive index $n = n' + in''$. It shows how wide the spectrum of a single mode will be in the frequency domain at the output of the laser. This equation is of a particular importance in the analysis of the laser operation in optical networks, as it describes such effects as e.g. the frequency chirping.

3.5 The Fabry-Perot laser

The general description of the FP laser cavity which defines the active region of the laser is shown in Fig. 3.9.

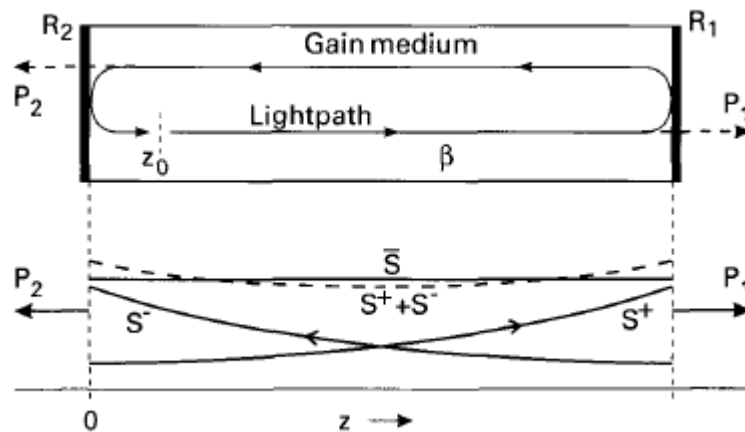


Fig. 3.9: A typical FP laser cavity (After Ref. [85]).

It consists of a homogenous and amplifying medium (gain medium) with a complex refractive index and two reflective facet mirrors on the right and the left side, with power reflectivities R_2 and R_1 respectively. As current starts to be injected inside the active region, the free electrons and holes (carriers) inside the cavity start to recombine and produce photons which propagate as a wave back S^- and forth S^+ inside the cavity. Each time they hit a facet, a small portion of light passes through the facet and the greatest portion gets reflected back to the cavity, according to the value of each facet. During this round trip of light, its gain always increases due to the amplifying cavity material [75].

In order to describe the mathematical form of the forward and backward wave, S^+ and S^- respectively, propagating along the $+z$ axis, we have to solve the general form of the wave equation:

$$\nabla^2 \vec{E}(\vec{r}, t) - \frac{n^2}{c^2} \frac{\partial^2 \vec{E}(\vec{r}, t)}{\partial t^2} = 0 \quad (3.35)$$

by which we denote for the wave $E(z, t)$ that propagates in the $+z$ axis and in time t :

$$E(z, t) = A_0 e^{i(\alpha t - \beta z)}, \quad z \geq 0 \quad (3.36)$$

where A_0 is the constant amplitude of the wave and $\beta = k_0 n$ is the propagation constant of the wave in the gain medium, where k_0 is the propagation constant (wave vector) of the wave in vacuum (also equal to $k_0 = \frac{2\pi}{\lambda_0}$, where λ_0 is the nominal wavelength in vacuum) and n is the refractive index of the gain medium.

The refractive index is complex because of the amplifying medium structure and is defined as $n = n' + in''$, where n' is responsible for the refraction of light inside the medium and $n'' = \frac{g_{net}}{2k_0}$ is responsible for the amplification (gain) or absorption (loss) of light inside the medium, where g_{net} is the net modal gain of the medium and is defined as $g_{net} = g_{mod} - \langle a_i \rangle$, where $g_{mod} = \Gamma g_m$ is the wavelength dependent modal gain caused by the active-medium material gain g_m and $\langle a_i \rangle$ stands for the average internal optical losses in the waveguide (e.g., scattering, absorption).

Depending on the value of g_{net} , there is amplification ($g_{net} > 0$) or absorption ($g_{net} < 0$) of light inside the cavity. So, β can now be written as:

$$\beta = k_0 n = k_0 n' + ik_0 n'' = k_0 n' + i \frac{g_{net}}{2} \quad (3.37)$$

Now that we have the general form of the wave propagating along the $+z$ axis and in time t , we can extract the form of the wave propagating forwards $S^+(z)$ along the $+z$ axis, which depends only on z and not time t as follows:

$$E^+(z, t) = A^+ e^{i(\omega t - \beta z)} = A^+ e^{-i\beta z} e^{i\omega t} = S^+(z) e^{i\omega t} \Rightarrow S^+(z) = A^+ e^{-i\beta z}$$

The same procedure can be followed in order to take the form of the wave propagating forwards $S^-(z)$ along the $+z$ axis:

$$E^-(z, t) = A^- e^{i(\omega t + \beta z)} = A^- e^{i\beta z} e^{i\omega t} = S^-(z) e^{i\omega t} \Rightarrow S^-(z) = A^- e^{i\beta z}$$

The steady-state oscillation condition requires that the field at any axial reference plain $z=z_0$, reproduces itself in magnitude and phase after one cavity roundtrip along the indicated lightpath. Therefore, this means that the complex cavity roundtrip gain must be unity, which can be expressed mathematically as

$$r_1 r_2 e^{-i2\beta L} = 1 \quad (3.38)$$

where the cavity length is denoted by L , and the mirror amplitude reflectivities r_1 and r_2 , are assumed to be real.

We can now derive the wave oscillating conditions of the FP cavity in order steady-state lasing to take place:

$$r_1 r_2 e^{-i2\beta L} = 1 \Rightarrow r_1 r_2 e^{-i2\left(k_0 n' + i \frac{g_{na}}{2}\right)L} = 1 \Rightarrow r_1 r_2 e^{-i2k_0 n' L} e^{g_{na} L} = 1$$

In order for the above equation to be valid, both $e^{-i2k_0 n' L} = 1$ and $r_1 r_2 e^{g_{na} L} = 1$ have to be valid.

Condition 1:

$$e^{-i2k_0 n' L} = 1 \Rightarrow \left. \begin{aligned} \cos(2k_0 n' L) &= 1 \\ \sin(2k_0 n' L) &= 0 \end{aligned} \right\} \Rightarrow 2k_0 n' L = 2m\pi \Rightarrow$$

$$\begin{aligned} \xrightarrow[n' \rightarrow \lambda_m]{} \frac{2\pi}{\lambda_m} n'(\lambda_m) L &= m\pi \Rightarrow \lambda_m = \frac{2n'(\lambda_m)L}{m}, \quad m=1, 2, \dots \\ \xrightarrow[k_0 = \frac{2\pi}{\lambda_m}]{} \end{aligned}$$

where m is an integer that defines the longitudinal mode number (or the number of *comb* modes), which equals the number of half-wavelengths that fit into the laser cavity of

length L and n' depends on the wavelength of each mode λ_m . This is the phase oscillation condition of the lasing modes.

Condition 2:

$$r_1 r_2 e^{g_{net} L} = 1 \Rightarrow \ln(e^{g_{net} L}) = \ln\left(\frac{1}{r_1 r_2}\right) \Rightarrow g_{net} = \frac{1}{L} \frac{1}{2} 2 \ln\left(\frac{1}{r_1 r_2}\right) = \frac{1}{2L} \ln\left(\frac{1}{r_1 r_2}\right)^2 = \frac{1}{2L} \ln\left(\frac{1}{r_1^2 r_2^2}\right) \Rightarrow$$

$$\begin{matrix} r_1^2 = R_1 \\ r_2^2 = R_2 \\ \Rightarrow \end{matrix} g_{net} = \frac{1}{2L} \ln\left(\frac{1}{R_1 R_2}\right)$$

This is the gain oscillation condition of the lasing modes as its solution gives the cavity gain peak wavelength λ_p .

So the two oscillation conditions are:

$$\left\{ \begin{array}{l} (1) \quad \lambda_m = \frac{2n'(\lambda_m)L}{m}, \quad m = 1, 2, \dots \\ (2) \quad g_{net} = \frac{1}{2L} \ln\left(\frac{1}{R_1 R_2}\right) \end{array} \right\} \quad (3.39)$$

In the FP laser m is usually very large $m \gg 1000$ for the lasing mode(s), so the distance between neighboring comb modes is very small. If we assume that the refractive index does not depend on the mode wavelength, then we can denote the mathematical expression of the mode spacing $\Delta\lambda_m$:

$$\Delta\lambda_m = \lambda_m - \lambda_{m+1} = \frac{2n'L}{m} - \frac{2n'L}{m+1} = \frac{2n'L}{m} \left(1 - \frac{1}{1 + \frac{1}{m}} \right)$$

Since $\frac{1}{m} \ll 1$, we can use the approximate formula $\frac{1}{1+x} \approx 1-x$, $x \ll 1$ and $\Delta\lambda_m$

becomes:

$$\Delta\lambda_m = \frac{2n'L}{m} \left(1 - \left(1 - \frac{1}{m} \right) \right) = \frac{2n'L}{m^2} = \left(\frac{2n'L}{m} \right)^2 \frac{1}{2n'L} = \frac{\lambda_m^2}{2n'L} = \lambda_m \left(\frac{\lambda_m}{2n'L} \right) \ll \lambda_m$$

Therefore, since $\frac{\lambda_m}{2n'L} \ll 1$, the mode spacing $\Delta\lambda_m$ around the m mode wavelength

$$\lambda_m \text{ is almost constant } \Delta\lambda_m = \frac{\lambda_m^2}{2n'L}.$$

In the case that $n'(\lambda_m)$ depends on λ_m , then $\Delta\lambda_m$ can be given by the complicated expression:

$$\Delta\lambda_m = \frac{\lambda_m^2}{2n'_g(\lambda_m)L} \quad (3.40)$$

where

$$n'_g(\lambda_m) = \left. \frac{d(k_0 n'(\lambda_m))}{dk_0} \right|_{\lambda_m} = n'(\lambda_m) - \lambda_m \left. \frac{dn'(\lambda)}{d\lambda} \right|_{\lambda=\lambda_m} \quad (3.41)$$

is the group refractive index, which includes the dispersion of $n'(\lambda_m)$ around λ_m .

The presentation of basic theory of light propagation in an optical cavity, which was done in this section treated the optical cavity as one material of refractive index n . However, in real devices where there is a laser core and claddings that surround it, the optical cavity is planar (slab) waveguide formed by a combination of materials (layers). Therefore in this case in all equations in this section the refractive index n has to be substituted with an *effective refractive index* n_{eff} which is an average of the refractive indices of the different laser materials.

The FP laser is the simplest type of laser which has only an optical cavity and lases in the multimode regime. However, this regime is not suitable for telecom applications and therefore single-mode lasers such as the TLDs are more preferable. In section 3.3 the basic theory of TLD operation is presented, however the principles of light propagation in an optical cavity are the same as in the case of the FP laser.

3.6 Three-section tunable DBR laser

A three-section tunable DBR laser consists, as the name implies, of three sections, which are the *Active section*, the *Phase section* and the *DBR (Bragg) section*, as it is shown in Fig. 3.10.

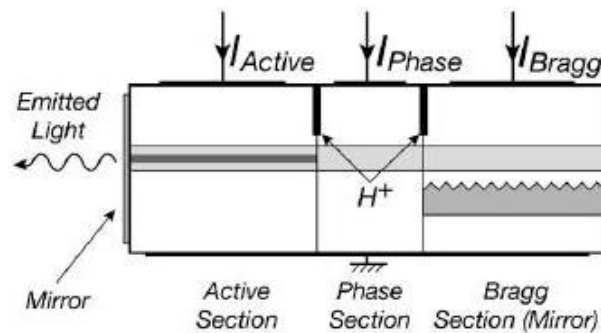


Fig. 3.10: A typical structure of a three-section tunable DBR laser (After Ref. [85]).

The active region is the area where all the emitted photons are generated. It has two facets (mirrors) with a certain value of reflectivity R , which are used for reflecting light back and forth, so that the gain process increases. The facet reflectivity R_l of the active section has a constant value while the the facet reflectivity of the DBR section is almost zero (anti-reflection coating). The lasing operation starts when a current is injected into the active region ($I_a = I_{Active}$). The procedure for the generation of lasing modes (gain condition) is the same as was described in section 3.2, however the optical cavity of the TLD is now a composite cavity formed by the active section, the phase section and the DBR penetration depth as will be explained below. Since tunable lasers are single-mode lasers, the selection of each mode takes place in the DBR section [85].

The DBR section consists of a material with steps with distance Λ between each step, which have the form of a pulse sequence and is called *grating*. The discontinuous

mode selectivity of the TLD is defined by the DBR grating which acts as a wavelength-selective mirror/reflector. The reflectivity coefficient R_g of the grating depends on the lasing wavelength and it substitutes R_2 in (3.39). Only wavelengths which serve a specific case are selected and reflected back to the active region, while the rest of them just pass through the laser and are absorbed. The reflected wavelengths are called *Bragg wavelengths* and are defined as:

$$\lambda_B = 2n'_{eff} \Lambda \quad (3.42)$$

where n'_{eff} is the real part of the effective refractive index n_{eff} .

The spectrum $R_g(\Delta\lambda)$ as a function of wavelength shift $\Delta\lambda = \lambda - \lambda_B$ of the lasing wavelength λ from λ_B is given by the following expression [85], [114]:

$$R_g(\Delta\lambda) = (\kappa L)^2 \frac{\tanh^2(\gamma L)}{(\gamma L)^2} \left[1 + (\Delta\beta L)^2 \frac{\tanh^2(\gamma L)}{(\gamma L)^2} \right]^{-1} \quad (3.43)$$

where L is the length of the DBR section, $\gamma = \sqrt{\kappa^2 - \Delta\beta^2}$, $\Delta\beta$ is the deviation of the propagation constant β of the wave, which leaves the active region and enters the DBR section, from the Bragg propagation constant β_0 , $\Delta\beta = \beta - \beta_0 = -(2\pi n_{gDBR} / \lambda_B^2) \Delta\lambda$, where n_{gDBR} is the group refractive index of the DBR material and κ is the coupling coefficient defined as $\kappa = 2\Gamma_g \Delta n'_g / \lambda_B$, where Γ_g is the optical confinement factor of the grating region and $\Delta n'_g = n'_1 - n'_2$ is the difference of the real parts of the refractive indices of the two materials n'_1 and n'_2 which form the grating.

The bandwidth $\Delta\lambda_{Rg}$ of the DBR reflectivity spectrum (3.43) is directly obtained from the above expressions as:

$$\Delta\lambda_{Rg} = \frac{\lambda_B^2}{\pi n_g} \sqrt{\kappa^2 + \left(\frac{\pi}{L}\right)^2} \quad (3.44)$$

As is seen, $\Delta\lambda_{Rg}$ is proportional to κ and inversely proportional to L . Depending on the value of the ratio $\frac{\kappa L}{\pi}$, $\Delta\lambda_{Rg}$ will be defined by either κ or L , or by both parameters, κ and L .

The gain oscillation condition of the TLD is now given as follows:

$$g_{net} = \frac{1}{2L_{eff,TLD}} \ln\left(\frac{1}{R_1 R_g(\Delta\lambda)}\right) \quad (3.45)$$

where $L_{eff,TLD} = L_a + L_p + L_{eff}$ is the effective length of the composite TLD cavity, L_a and L_p , is the length of the active and phase section, respectively and $L_{eff} = \frac{\tanh(\kappa L)}{2\kappa}$ is the DBR penetration depth.

In order for the TLD to achieve lasing conditions the most important condition is that the net gain is equal to the losses created by the two mirrors with reflectivities R_1 and $R_g(\Delta\lambda)$. These losses are called *mirror losses* a_m and therefore defined as in (3.45)

$$a_m = g_{net}.$$

The phase oscillation condition of the TLD states that the phase change $\Delta\phi$ must be an integer multiple of 2π after a complete roundtrip and is given as:

$$\frac{4\pi n'_{eff}(\lambda_m) L_{eff,TLD}}{\lambda_m} + \Delta\phi = 2\pi m, \quad m=1, 2, \dots \quad (3.46)$$

where ϕ is the phase of the grating reflection.

The mode spacing $\Delta\lambda_m$ of the three-section TLD is different than the one in (3.40) and is defined as:

$$\Delta\lambda_m = \frac{\lambda_B^2}{2(n'_{ga} L_a + n'_{gp} L_p + n'_{gDBR} L_{eff})} \quad (3.47)$$

where n'_{ga} , n'_{gp} , and n'_{gDBR} is the group refractive index of the active, phase and DBR section, respectively.

There are three types of wavelength tuning, the discontinuous, continuous and quasicontinuous tuning. Discontinuous (or DBR) tuning is achieved when current $I_{DBR}=I_{Bragg}$ is injected in the DBR section, which changes the effective refractive index and therefore the Bragg wavelength, which leads to a different emitted wavelength each time. This discontinuous (DBR) shift of wavelengths $\Delta\lambda_{DBR}$ takes place around some specific basic modes, which are called *comb modes* and are defined in the phase section.

The phase section is responsible for the determining of the comb modes. By injecting different values of current in this section, the total *roundtrip time* is changed, which is the time that the photons need to travel from the one side of the laser to the other. Therefore, the group velocity of the photons is changed as well, leading to a shift in the basic modes, as the propagating wavelength of these modes depends on group velocity. This is the case of continuous (or phase) tuning, however the wavelength shift happens only between the lasing mode and its sidemode periodically, so the maximum continuous wavelength range $\Delta\lambda_c$ is limited by the inter-mode distance.

In case both the DBR and phase section are injected with current simultaneously and $\Delta\lambda_B=\Delta\lambda_c$ then a wider continuous tuning range can be achieved. If however $\Delta\lambda_B \neq \Delta\lambda_c$, then several continuous wavelength ranges can be achieved in different discontinuous steps which is the case of quasicontinuous tuning.

The key element that makes TLDs different than the rest of the industrial lasers is their wavelength tuning ability. By inspecting equations (3.42) and (3.46) it is easy to conclude that by varying the real part of the effective refractive index n'_{eff} of the TLD structure both the Bragg wavelength (and in turn the lasing wavelength λ_m since λ_m is

always close to λ_B) and the comb-mode spectrum can be modified. The relation between the wavelength shift $\Delta\lambda$ from the initial lasing wavelength λ_0 and the change $\Delta n'_{eff}(\lambda_0)$ of the real part of the effective index of the TLD structure, which depends on λ_0 , is given by:

$$\frac{\Delta\lambda}{\lambda_0} = \frac{\Delta n'_{eff}(\lambda_0)}{n'_{g,eff}(\lambda_0)} \quad (3.48)$$

In practice always $\Delta n'_{eff} \ll n'_{eff}$ and as result $\Delta\lambda \ll \lambda_0$.

The change of n'_{eff} of the TLD can be achieved with numerous physical mechanisms. These physical mechanisms depend on the change of various physical parameters, such as the carrier density N of the tuning sections of the TLD (free-carrier plasma effect and band-filling effect), the temperature T of the TLD (thermal tuning) and the electric field E when applied to the TLD (quantum confined Stark effect). These methods are described in detail as follows:

3.6.1 Free-carrier plasma effect

The Free-Carrier (FC) plasma effect is the physical mechanism that is most frequently used for TLD tuning in the published literature. It is usually claimed that it provides the largest contribution to the wavelength tuning [85]. It takes place when electrons and holes are injected in a semiconductor, creating displaced free carriers in the energy bands. In presence of light the intraband free-carrier absorption, causes in turn a change $\Delta n'$ in the real refractive index n' of the semiconductor. The imaginary part of the refractive index n'' defines the gain/absorption of the material, which will be dealt with in section 3.3.2 in the investigation of the band-filling effect through the KK relations. In

calculating $\Delta n'$ due to the FC plasma effect, the simplest approach is to use the Drude classical model.

A general expression for the dielectric function of the bulk material which incorporates the effect of band structure and the effect of free carriers (electrons and holes) in the conduction and valence band is:

$$\varepsilon(\omega) = n'^2(\omega) = n_b^2 \left(1 - \frac{\omega_p^2}{\omega^2} \right) \quad (3.49)$$

where $n'(\omega)$ is the real part of the refractive index of the semiconductor with the free carriers present and n_b is the background refractive index which is related to the bandgap energy E_g of the material. This relation for light frequencies below the bandgap energy is approximately given by the Lorentz model (E_0 is a constant $E_0 \approx 19\text{eV}$, which is a typical value in most semiconductors materials as in [115]):

$$n_b^2 \approx 1 + \frac{E_0^2}{E_g^2} \quad (3.50)$$

The term in brackets in (3.49) describes the effect of free carriers on the refractive index of the material. Here ω is the angular frequency of the emitted light and ω_p is the plasma angular frequency. The plasma frequency depends on the concentration N of electrons and P of holes injected in an undoped semiconductor (with $N=P$, as is usually assumed [116]) as follows:

$$\omega_p^2 = \frac{e^2 N}{\varepsilon_0} \left(\frac{1}{m_n} + \frac{1}{m_p} \right) \quad (3.51)$$

where e is the electron charge, m_n and m_p is the electron and hole effective mass, respectively, and $\varepsilon = n_b^2$ is the static dielectric constant of the material.

In order to obtain an expression between the real part of the refractive index change $\Delta n'$ and the change of the injected carrier density ΔN , equation (3.49) needs to be transformed:

$$2n' dn' = -\frac{n_b^2}{\omega^2} \frac{d(\omega_p^2)}{dN} dN \quad (3.52)$$

Then using (3.51) and taking into account that $n' = n_b$ and $\omega = 2\pi \frac{c_0}{\lambda}$, where λ is the lasing wavelength in vacuum, one obtains for the refractive index change due to FC plasma effect:

$$\begin{aligned} dn' &= -\frac{n'}{2\left(2\pi \frac{c_0}{\lambda}\right)^2} \frac{e^2}{\varepsilon_0} \left(\frac{1}{m_n} + \frac{1}{m_p}\right) dN \Rightarrow \\ \Delta n' &= -\underbrace{\frac{e^2 \lambda^2}{8\pi^2 c_0^2 n' \varepsilon_0} \left(\frac{1}{m_n} + \frac{1}{m_p}\right)}_{\beta_{pl}} N = \beta_{pl} N \end{aligned} \quad (3.53)$$

The term β_{pl} is also called the plasma coefficient and it is negative so that n' and λ both decrease when the FC plasma effect is used for tuning.

The discontinuous wavelength shift $\Delta \lambda_{DBR}$ due to the change of the refractive index in the DBR section $\Delta n'_{DBR}$ is connected with the injected carrier density in the DBR section N_{DBR} and is derived from (3.48) and (3.53) as follows ($\Delta n'_{eff} = \Gamma_{DBR} \Delta n'_{DBR}$) [85]:

$$\Delta \lambda_{DBR} = \frac{\beta_{pl} \Gamma_{DBR} \lambda_B}{n'_{g,eff}} N_{DBR} \quad (3.54)$$

where β_{pl} is the FC plasma coefficient, Γ_{DBR} is the transverse confinement factor of the DBR section, λ_B is the Bragg wavelength and $n'_{g,eff}$ is the real part of the effective group index of the TLD.

3.6.2 Band-filling effect

One of the main features of semiconductors is that when they are injected with varying values of carrier density, a change of their gain takes place, which in turn causes a change in their refractive index at the peak gain energy. This happens because of the strongly asymmetric spectral shape of the gain curves of semiconductors. However, a change in gain corresponds to a change of the imaginary part of the refractive index as was shown in section 3.2. Therefore, in order to calculate the change $\Delta n'(\omega)$ of the real part of the refractive index $n'(\omega)$ (which depends on the angular frequency ω) from the gain change $\Delta g(\omega')$ at the gain peak angular frequency ω' , the Kramers-Kronig dispersion relation [117] can be used:

$$\Delta n'(\omega) = \frac{c}{\pi} P \int_0^{\infty} \frac{\Delta g(\omega')}{\omega'^2 - \omega^2} d\omega' \quad (3.55)$$

where P indicates a principal value integral, c is the speed of light in vacuum, ω' is the gain peak angular frequency and ω is the lasing angular frequency around ω' .

In Fig. 3.11, schematic plots are shown of the refractive index changes caused by the injection of two different carrier densities, where the upper plot displays the gain curves for the two carrier densities.

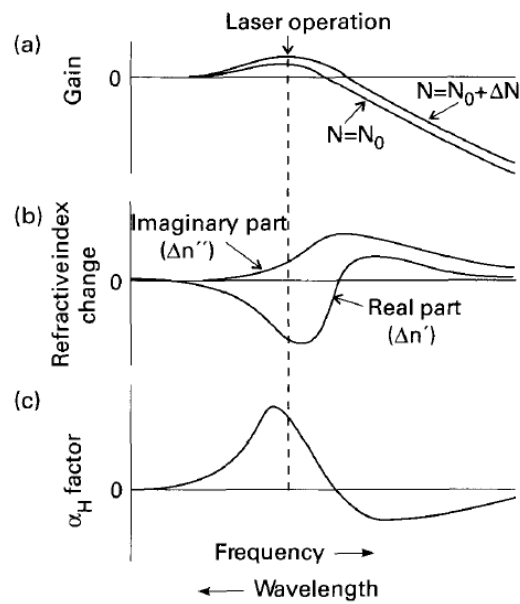


Fig. 3.11: (a) Spectral gain curves in a semiconductor for different carrier densities, (b) Changes in the real and imaginary part of the refractive index due to injected carrier density, (c) alpha factor a_H variation. All three are plotted versus frequency (wavelength) (After Ref. [85]).

3.6.3 Thermal tuning

Thermal tuning is the method where an increase in the temperature T of the laser, leads to an increase of the value of the emission wavelength. This happens because the Fermi-Dirac distribution and the bandgap energy in the laser cavity are sensitive to temperature changes. Therefore the gain peak wavelength λ_p and the refractive index n can be controlled by temperature changes.

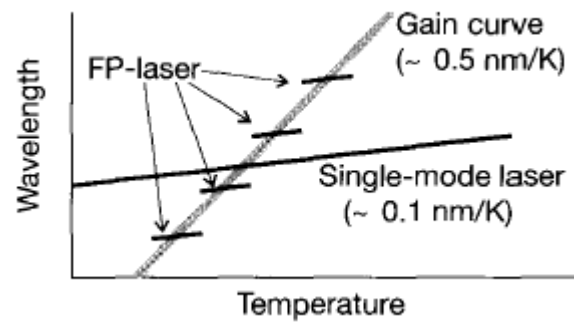


Fig. 3.12: Lasing wavelength vs Temperature for a 1500-nm InGaAsP/InP FP and single-mode laser and the gain of the active region (After Ref. [85]).

In Fig. 3.12, it is shown how the emission wavelength increases according to the increase of temperature in the case of a 1500-nm InGaAsP/InP multi-mode FP laser and in the case of 1500-nm InGaAsP/InP a single-mode DFB and DBR lasers. It can be seen that there is a change of about 0.5 nm/K for the FP laser and 0.1 nm/K for the DFB and DBR lasers. It can also be shown that the gain curve of the FP laser has some mode jumps when the temperature increases. Although for each longitudinal mode of the FP laser the increase of the emission wavelength is rather small (0.1 nm/K), on average there is a high temperature dependence of 0.5 nm/K. On the contrary, the wavelength of the DFB and DBR lasers increases by only 0.1 nm/K over the entire temperature range. This can be explained by the fact that the wavelength of each longitudinal mode of the FP laser and the mode of a single-mode laser are functions of the refractive index and do not depend explicitly on the gain curve.

3.6.4 Quantum Confined Stark Effect

The Quantum Confined Stark Effect (QCSE) takes place in multiple quantum well (MQW) structures in the laser cavity, when a strong electric field is applied, that leads to changes in the refractive index. This can be done by placing QW within a reversely biased p-n junction, in order the refractive index to be influenced by the applied electric field.

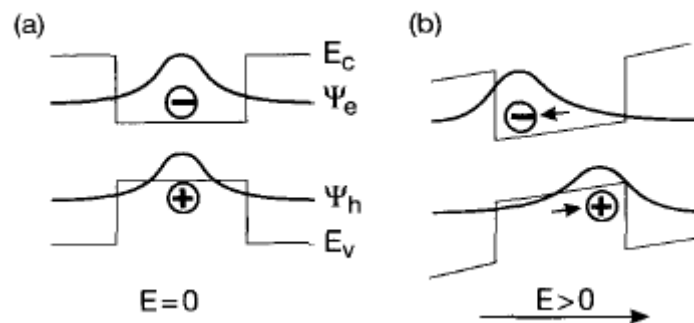


Fig. 3.13: (a) Application of an electric field to a QW structure, (b) Inclined band edges, displaced wavefunctions and reduced effective bandgap energy (After Ref. [85]).

An illustration of how the QCSE takes place is shown in Fig. 3.13, where the band edges and wave-functions for electrons and holes in a single QW are displayed, without the application of an electric field $E=0$ (a). When an electric field is applied $E>0$ (b), the band edges become inclined and the electron and hole wave-functions become displaced away from each other. Thus, the energy difference between the lowest-order wave-functions in the conduction and valence band will be reduced, which will result in the change of the effective bandgap energy and the element of the optical matrix. This will produce the built-in electron-hole dipole that will interact with the propagating light wave. A further increase of the applied electric field will change the dipole and lead to

the modification of the refractive index. It should be noted that significant effects on the refractive index are achieved only for photon energies near the bandgap energy, where absorption also occurs.

In Fig. 3.14 a comparison between the above discussed tuning mechanisms of TLDs is shown in terms of practically achievable performance and typical optical parameters.

Parameter	Plasma Effect	QCSE	Temperature
Δn	-0.04	-0.01	0.01
Γ	0.5	0.2	1
$\Delta\lambda_{\text{tune}}$	-8 nm	-1 nm	+5 nm
$f_{3\text{dB}}$	100 MHz	> 10 GHz	< 1 MHz
α_{II}	-20	-10	large
Heat generation	large	negligible	very large
Technology	moderate	demanding	simple

Fig. 3.14: Comparison of different physical tuning mechanisms used for TLDs (After Ref. [85]).

Chapter 4

Physics and technology of tunable laser diodes

4.1 Introduction

Two commercial software packages were used to obtain all the results of this research, Crosslight PICS3D and VPI. The reason for dealing with two separate software packages is that they deal with semiconductor devices from a completely different perspective. As it was already mentioned the scope of this thesis is to investigate different aspects of TLD operation as a stand-alone laser and its dynamic behaviour under small-signal modulation. PICS3D was chosen for the first part of this investigation, as it is a physics-based software designed to simulate very accurately laser diodes and related waveguide photonic devices (with good agreement to published experiments) based on detailed analysis of semiconductor and optical wave theory and equations.

VPI on the other hand, is designed to simulate various optical systems and their components (transmitters, amplifiers, fibres, regenerators, receivers, etc.) with also good agreement to published experiments as in the case of PICS3D. However, it does not take into account all physical and material parameters when it simulates semiconductor devices like PICS3D. VPI does allow though direct modulation of semiconductor lasers for both small-signal and large-signal analysis something that cannot be done in PICS3D. This is why it was chosen for the second part of the investigation of this thesis.

Together, both these packages, each from a different point of view, are able to simulate well all aspects of a semiconductor device and carry out various investigations concerning its operation. It should be noted though that these software packages are merely tools used in order to obtain results from the designed setups of this investigation. The design of the TLD models and optical networks presented in this thesis was done from scratch and in detail by the author and the selection of their parameters was done

carefully according to the published literature. This was a quite time-costly and tedious process as the setups had to work properly with reasonable parameters before the investigation described in Chapters 5, 6, 7 and 8 could take place. In sections 4.2 and 4.3 all the properties of the operation of these two software packages will be described. In section 4.4 a summary of the advantages and disadvantages of these two packages will be given.

4.2 *Crosslight PICS3D*

Crosslight PICS3D is a three dimensional (3D) simulation tool which is used in many publications (see list of publications in [118]) and can simulate very accurately optical transmitters (in our case TLDs) taking into account all physical models (both electrical and optical) and solving optical wave equations of semiconductor laser theory. All these models and equations will be described in the current and next sections and the accuracy of simulated results will be checked with the published literature. It will be shown that by importing parameters from published experiments the acquired results are in very good agreement with the experimental results.

Various semiconductor optoelectronic devices can be simulated by PICS3D, such as FP, DFB and DBR lasers, as well as VCSELs and multiple-section TLDs. PICS3D also gives a lot of options to the user to investigate parameters of the laser from the optical and electrical point of view, as it can show L-I (optical power vs current) and I-V (current vs voltage) characteristics, electron (carrier) and hole distributions, mode spectrums, band energy diagrams, Fermi levels, electric fields, plot material gain and

spontaneous emission spectrums and many other fundamental laser features, which help the user to observe in detail what happens inside the laser structure.

It also allows the user to design his laser model layer by layer, to choose the type of material and the material composition that he wants and the option to create gratings and bulk or quantum well layer structures. Some of its disadvantages though, is that it cannot provide output laser results in the time domain or allow large-signal direct laser modulation or simulation of other optical network components, such as fibres, optical switches, multiplexers, regenerators and photodiodes.

However, PICS3D provides reliable results when it is compared with experimental work from the published literature, even though it is a software simulation tool. To showcase this fact, the calculation of the change of the real part of the refractive index of a bulk GaAs material system (waveguide) as a function of photon energy when the system is injected with current is illustrated in Fig. 4.1. The design and material parameters of the bulk GaAs waveguide are borrowed and imported in PICS3D from the experimental work of [119].

The calculation of the change of the real part of the refractive index of the GaAs material due to the current injection was made according to the modified formula of the Kramers-Kronig relations which PICS3D uses [120] and is described in section 5.3 of Chapter 5. The solid line in Fig. 4.1 represents the change of the real part of the refractive index (real index change as is stated in the label of the y axis of Fig. 4.1) as is calculated in PICS3D and the dotted line represents the data obtained from [119]. It can therefore be concluded that the results obtained from PICS3D are in good agreement to those from the experimental work of [119].

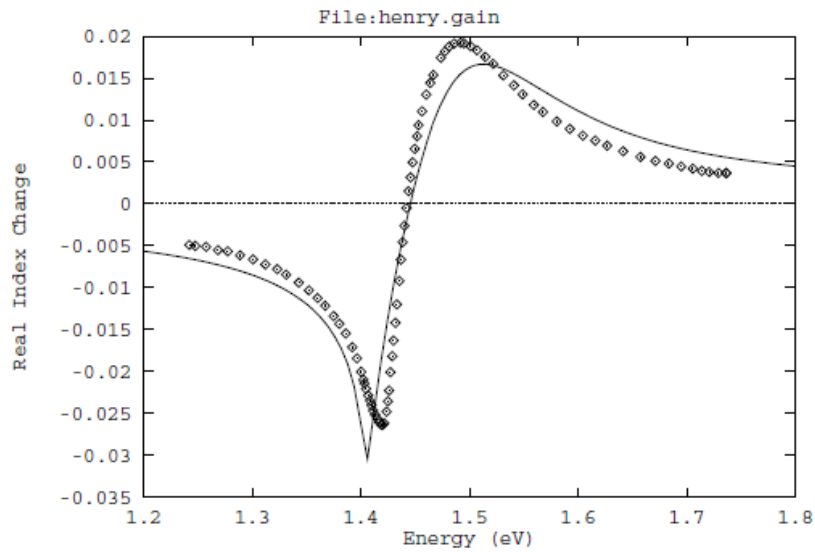


Fig. 4.1: Change of the real part of the refractive index of a bulk GaAs material under current injection as a function of photon energy in PICS3D and the experimental work of [119] (After Ref. [120]).

In section 4.2.1 a general description of how PICS3D is designed to run a simulation is given, together with a description of all the input and output files generated during this process. In sections 4.2.2-4.2.4 all the physical models used by PICS3D to simulate laser models are described in detail.

4.2.1 File structure

In Fig. 4.2 the file structure and the flow chart of a typical PICS3D simulation is shown as a series of boxes, where each file is described in detail below.

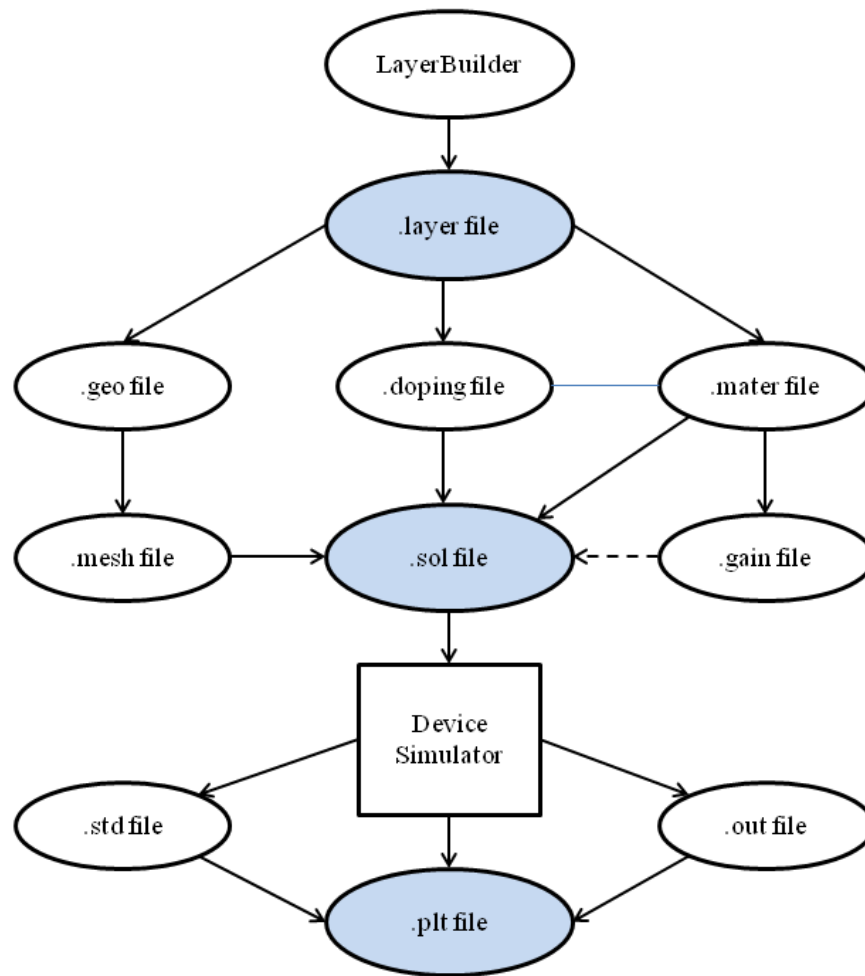


Fig. 4.2: File structure and flow chart of a typical PICS3D simulation.

1. The .layer file is the main file where the user defines the structure of the device. A device can be designed as one section corresponding to one .layer file or multiple sections, with each section corresponding to a separate .layer file. The .layer files of the multiple section device can then be linked together with a specific command in order to be treated by PICS3D as one device. As the name implies, the .layer file designs a device or a device section as a series of data blocks or *layers*, with each layer describing a specific region. These regions can be active regions, passive waveguides, gratings, n+ or p+ regions, barriers, QW regions and many others. The user can define the thickness of each layer, its material and

material composition, its doping (n+ or p+), the number of mesh points used to calculate all the spatial characteristics of the layer (the more mesh points the better the accuracy of the calculations) and whether the layer is an active or passive region. The length and width of the whole device or device section can also be specified, as well as the type of contact used for current injection. After any change made to the device structure the .layer file needs to be processed in order to generate the .geo, .doping and .mater files, the use of which is described in the steps 2, 3 and 4 below, respectively.

2. The .geo file is an input file which contains information about the device geometry and the initial mesh allocation. When it is processed, it generates the .mplt file, which is described in step 5.
3. The .doping file is an input file which contains about the doping of each layer and is used by the .sol file described in step 7.
4. The .mater file is another input file which contains information about the material and the material composition of each layer and is used by the .sol file.
5. The .mplt file is an input file designed to plot the mesh which is generated from the .geo file.
6. The .gain file is another important input file which is used to plot the material gain spectrum, spontaneous emission rate spectrum, quantum well subbands, and other

critical physical properties. It is very useful for the user to make estimations before the main simulation starts.

7. The .sol file is the main input file that defines the material properties and controls the bias and other conditions of the main equation solver. Different free-carrier contributions to the refractive index change can be defined as well as the accuracy of the solver. Various currents and biases can be controlled independently for different sections of a device.
8. The .std files are output files created in the form of .std 0001, .std 0002, etc., after every run of the .sol file. They contain numerical output data from the main equation solver and are used by the .plt file in order to plot diagrams in 2D and 3D graphics.
9. The .out files are output files created in the form of .out 0001, .out 0002, etc., after every run of the .sol file and have the same use as the .std files.
10. The .plt file is the main file used to plot all the data produced during a software run and are stored in the .out output files. It generates a Postscript .ps file which can either be opened with a Gnuplot platform or be converted to a .pdf file. The .plt file uses a set of commands to plot various electrical and optical properties of TLDs as a function of applied bias or injected current in any contact such as: I-V and L-I characteristics, lasing wavelength vs tuning current and optical power vs tuning current. It can also plot 2D and 3D spatial distributions of TLD electrical and optical properties such as: energy band diagrams (both for the conduction and

valence band including Fermi levels), electron and hole concentrations (carrier density) in linear and logarithmic form, refractive index change due to injected current, current densities, local modal gain or absorption in active or passive regions, electric fields, electric flux, intensity of the propagating optical wave inside the TLD. All the spatial distributions can be plotted as a cross-section of one axis vs the other two in 2D or across all axis in 3D. Lastly, the .plt file can plot the lasing mode spectrum of the optical cavity.

4.2.2 Carrier transport model

PICS3D uses the drift-diffusion model to simulate the transport of carriers in semiconductor devices and TLDs. The drift-diffusion model universally describes situations where excess carriers are introduced locally in an area, causing a condition of non-uniform carrier distribution, like in the injection of carriers from a junction [121]. Whenever there exists a gradient of carrier concentration or density, processes of drift and/or diffusion occur by which the carriers migrate from the region of high concentration toward the region of low concentration, to drive the system toward a state of uniformity. This description is very adequate for the conditions that exist in laser diodes. For example, in the cladding regions the carriers are mainly driven by the applied electric field, but once the carriers are injected into the central region (waveguide) of the active or passive sections, their transport there is mainly handled by diffusion.

The basic set of equations includes the Poisson's equation for the electrostatic potential V :

$$-\nabla\left(\frac{\epsilon_0\epsilon_s}{e}\nabla V\right)=N_D-N_A-n+p \quad (4.1)$$

where n is the electron density, p is the hole density, $N_{D(A)}$ is the donor (acceptor) doping density, e is the electron charge, ε_0 is the dielectric constant of vacuum, and ε_s is the relative dielectric constant of the material.

The electron and hole densities in semiconductors are defined by Fermi-Dirac distributions. Assuming parabolic density of states this yields [121] for the local free carrier densities:

$$n = N_c F_{1/2} \left(\frac{E_{Fn} - E_c}{k_B T} \right), \quad p = N_v F_{1/2} \left(\frac{E_v - E_{Fp}}{k_B T} \right) \quad (4.2)$$

where $N_{c(v)}$ is the effective density of states in the conduction (valence) band, $E_{Fn(p)}$ is the electron (hole) quasi-Fermi level, $E_{c(v)}$ is the conduction (valence) band energy, k_B is Boltzmann's constant, T is the temperature, and $F_{1/2}$ is the Fermi integral of order 1/2 [121]. The quasi-Fermi levels $E_{Fn(p)}$ and the band edge energies $E_{c(v)}$ are in general local functions of the coordinates. The spatial profiles of $E_{c(v)}$ are completely defined by the local electrostatic potential V .

In the quasi-Fermi levels approximation the local electron J_n and hole J_p current densities are given by simple equations:

$$J_n = n \mu_n \nabla E_{Fn}, \quad J_p = p \mu_p \nabla E_{Fp} \quad (4.3)$$

where $\mu_{n(p)}$ is the electron (hole) mobility. Note that the equations (4.3) are valid for both cases of degenerate and non-degenerate carrier statistics. The carrier mobilities in general depend on the local electric field strength [112]. However, in typical laser diode structures the transport is characterised by relatively weak electric fields and we ignore

this dependence. At the same time, the doping and the composition dependence of the mobilities in each layer are taken into account.

The equations (4.1) – (4.2) alone cannot provide solutions for all unknowns. The current continuity equations for the electrons and the holes must be added for a complete description of the carrier transport:

$$\frac{\partial n}{\partial t} = -R_n + \frac{1}{q} \nabla \cdot \vec{J}_n, \quad \frac{\partial p}{\partial t} = -R_p - \frac{1}{q} \nabla \cdot \vec{J}_p \quad (4.4)$$

where $R_{n(p)}$ is the electron (hole) recombination rate. Here we will use standard expressions [112] for the recombination rates which are the functions of the carrier density:

$$R_N = A_N N + B_N N^2 + C_N N^3 \quad (4.5)$$

where the coefficients A_N , B_N , and C_N describe Shockley-Read-Hall (SRH) recombination, spontaneous radiative recombination, and Auger recombination, respectively, of the electrons ($N \equiv n$) and the holes ($N \equiv p$). Note that these coefficients are different in each layer of the heterostructure, and in general they are different for electrons and holes.

However, when the high-density carriers are injected into the central region of each section, it is a good approximation to use $n \approx p$ (electroneutrality condition) in this region. Then each recombination mechanism in the central region can be described by a single coefficient which is the same for the electrons and holes. At the same time in case of vertical carrier leakage from the central region into the adjacent regions, the recombination of the minority leaked carriers is mainly described by the SRH mechanism, and the corresponding coefficients A_N are different for the electrons and holes. All these features are taken into account in our model.

The above set of equations (4.1) – (4.5) completely describes the 3D carrier transport in each layer of the structure, except the device contacts and the heterostructure's interfaces. At the contacts the transport is defined by the boundary conditions (discussed below in section 4.2.4), while at the heterointerfaces the PICS3D uses the thermionic emission model [121].

4.2.3 Optical model and field equations

The optical part of the TLD modelling concerns with the spatio-temporal solutions for the propagating electro-magnetic fields in a composite cavity. Under the scalar wave assumption the electric field with the frequency ω propagating along the cavity in the z -direction is written as:

$$E(t) = E_{\omega} \exp(-j\omega t), \quad E_{\omega} = E_{\omega}(z)\Phi(x, y) \quad (4.6)$$

The transverse modes $\Phi(x, y)$ describe the field distribution along the lateral x -direction and the transverse y -direction. The modes are obtained from the solution of the equation:

$$\left[\frac{\partial^2}{\partial x^2} + \frac{\partial^2}{\partial y^2} + \frac{\omega^2}{c^2} n^2(\omega, x, y, z) \right] \Phi(x, y) = \frac{\omega^2}{c^2} n_{eff}^2(\omega, z) \Phi(x, y) \quad (4.7)$$

Here $n(\omega, x, y, z)$ is a local complex refractive index, c is the speed of light in vacuum, and $n_{eff}(\omega, z)$ is the z -dependent effective refractive index which defines the z -dependent propagation constant $\beta(z) = \frac{\omega}{c} n_{eff}(\omega, z)$. As is seen from (4.7), the complex propagation constant $\beta(z)$ contains all information about optical properties of the structure.

Under the assumption of relatively weak z -dependence of n , the solution of equation (4.7) is obtained by the effective index method. The z -dependent part $E_\omega(z)$ is given by the equation:

$$\left[\frac{\partial^2}{\partial z^2} + \beta^2(z) \right] E_\omega(z) = f_\omega(z) \quad (4.8)$$

where $f_\omega(z)$ is the Langevin's noise source caused by the spontaneous emission contribution into the lasing mode. The function $f_\omega(z)$ is obtained by the averaging of the original Langevin's source $F_\omega(x, y, z)$ in the initial Maxwell's equations over the lateral directions using the obtained from equation (4.7) transverse modes [122], [123].

Equation (4.8) is the basic equation used for the optical field calculations in the PICS3D package. The effective refractive index $n_{eff}(\omega, z)$ and the complex propagation constant $\beta(z)$ in each section depend on the optical frequency (material and waveguide dispersion), on the section design (the waveguide geometry, material properties, gratings, etc.), and on the injected carrier density (FC effect) and the photon density (due to gain compression) [122].

In PICS3D, equation (4.8) is solved using the Green's function method [122], [123] to find the longitudinal modes and the intensity distributions along the TLD composite cavity. In the active section PICS3D uses the output from the carrier transport simulations to obtain the local gain. In passive sections the data from the electrical simulation are used to calculate the local values of the real and the imaginary parts of the refractive index. Thus, the lasing frequency tuning and possible wave gain/attenuation in passive sections are self-consistently described by the model. Since meshing of the electrical and the optical problems are different, the values from the electrical problem are linearly interpolated from the electrical mesh planes onto the optical mesh points [122].

4.2.4 Boundary conditions

The boundary conditions for electrical equations (4.1) and (4.4) refer to ohmic contacts and the abrupt heterointerfaces. In PICS3D ohmic contacts are implemented as simple Dirichlet boundary conditions, where the surface potential V_s and the electron and the hole quasi-Fermi levels E_{Fn}^s and E_{Fp}^s are fixed [122]. The quasi-Fermi potentials of the minority and the majority carriers at the electrodes are equal to each other and set to the applied bias $V_{applied}$ of the electrode:

$$E_{Fn}^s = E_{Fp}^s = -eV_{applied} \quad (4.9)$$

The potential V_s at the boundary is fixed at a value consistent with the charge neutrality condition $N_D - N_A - n + p = 0$. With the defined electrical potential V_s and the quasi-Fermi levels at the boundaries, one then can use equations (4.2) to calculate the boundary carrier densities n_s and p_s .

It should be pointed out that the charge neutrality assumption in the contacts implicitly assumes a high level doping in the vicinity of the contacts in order for the contacts to serve as an efficient injector. Otherwise, for low-doped regions near the contact there would be the induced carrier depletion (or the carrier accumulation) in these regions under high current injection levels. This would disturb the ohmic operation regime of the contacts, and the conditions (4.9) will become invalid. For typical laser structures this is not a problem as the cladding regions are usually heavily doped.

At the device heterointerfaces there is an abrupt change of the electrical properties. The equations (4.3) for the current densities become invalid here due to possible quasi-Fermi potential discontinuity. The current flow on both sides of the interface is described by the equations (4.3), however at the interface the carrier transfer is handled by

completely different physical mechanisms. In general, this may include various quantum tunnelling mechanisms and/or thermionic emission. A completely rigorous treatment of the interface carrier transfer is a very difficult problem due to non-linearity of the phenomena. The solution of this problem would require to find the quasi-Fermi levels on each side of the interface and then calculate the interface transfer current densities for the electrons and the holes and match them to the drift-diffusion current densities in (4.3). PICS3D uses a simplified approach in solving this problem. It assumes that the main interface transfer mechanism is the thermionic emission currents which are uniquely defined by the temperature and the carrier densities on each side of the interface. This approximation is reasonable for typical laser heterostructures.

Regarding the boundary conditions for the optical problem, they are the usual continuity conditions for the electromagnetic field components at each interface of the composite cavity.

4.3 VPI

Virtual Photonics Incorporated (VPI) (started as Virtual Photonics Pty Ltd) was founded in 1996 by Arthur Lowery [124] in order to create a program (VPI) that simulates optical circuits. The TLD models that are used in this thesis are based on the Transmission-Line model which was created by Johns [125] as a time-domain model to simulate microwave cavities. VPI has excessively been used in both the fields of academia and industry with a wide list of publications [126].

VPI allows the design of different types of optical networks, as it provides a full variety of components, such as lasers, fibres, amplifiers, regenerators, photodiodes, and

anything else that the user might need in order to create his own network. It also offers Bit-Error Rate (BER) and SNR calculations, eye diagrams, figures in the frequency and time domain, and gain figures. The user has the option to use a laser separately as a sole system to test its operation in the dynamic regime, to apply direct modulation and optical injection-locking to it, or use it as a transmitter in an optical network setup. It provides information mainly from the optical point of view of the laser, allowing the user to modify some key optical parameters, but it does not give any information about basic physics or electronic features of the laser, as in PICS3D. The laser structure here is more encrypted as it is presented as a closed box, where the user cannot see the internal layer structure of the laser or observe various physical elements, such as electron (carrier) and hole distributions, band energy diagrams, Fermi levels and the flow of current inside the device.

Therefore, the main disadvantage of VPI against PICS3D, is the fact that the user cannot have a very detailed laser setup, where he can control both its optical *and* electronic or physical aspects. The main equations that VPI uses to simulate semiconductor lasers are given in sections 4.3.1-4.3.3 and a description of how it works during a simulation is given in Chapter 8. Below follows a description of the models VPI uses to implement semiconductor devices and simulate their operation.

The TLDs which are used in all simulations presented in Chapter 8 are based on the Transmission-Line Laser Model (TLLM) of VPI which uses the Transmission-Line Model (TLM or Photonics TLM) method to describe all types of photonic devices. According to this method [127], both time and space are discretised with a time step Δt and spatial step $\Delta z = v_g \Delta t$, where v_g is the group velocity of the propagating wave in the modeled device. This spatial discretisation leads to the formation of nodes which recreate the modeled device and are considered as lumped *scattering nodes* which are connected

with each other with *transmission lines* of zero loss. All transmission lines have a signal delay of one time step Δt according to the chosen spatial step. In this way calculations (which is the *scattering* of incoming waves in order to produce outgoing waves) can be made for each scattering node independently from other nodes, with the use of information provided by adjacent nodes or previous iterations.

The spatial discretisation of a TLLM device which uses the TLM method is confined in only one dimension which is the axis of wave propagation z along the built-in waveguide of the device and is shown in Fig. 4.3. The device is divided in k sections, with each device section consisting of m smaller TLM sections of size $\Delta z = c\Delta t/n_{g,k}$, where c is the speed of light in vacuum and $n_{g,k}$ is the group refractive index of the k^{th} section. Each one of the m TLM sections contains a scattering node which represents the noise (spontaneous emission), loss (scattering and absorption), gain (stimulated emission) and grating-induced reflection (if any) that the propagating optical wave sustains as it passes through the section [128].

The scattering nodes of adjacent TLM sections are connected with transmission lines (which represent pure waveguide propagation delays) from where the output optical field from each TLM section is passed through with no changes to the adjacent TLM sections and is used at the next iteration as the input optical field for them. Each scattering node m generates output forward and backward propagating optical waves $E_{F,m}^{out}$ and $E_{B,m}^{out}$, respectively from its incident forward and backward propagating optical waves $E_{F,m}^{in}$ and $E_{B,m}^{in}$, respectively.

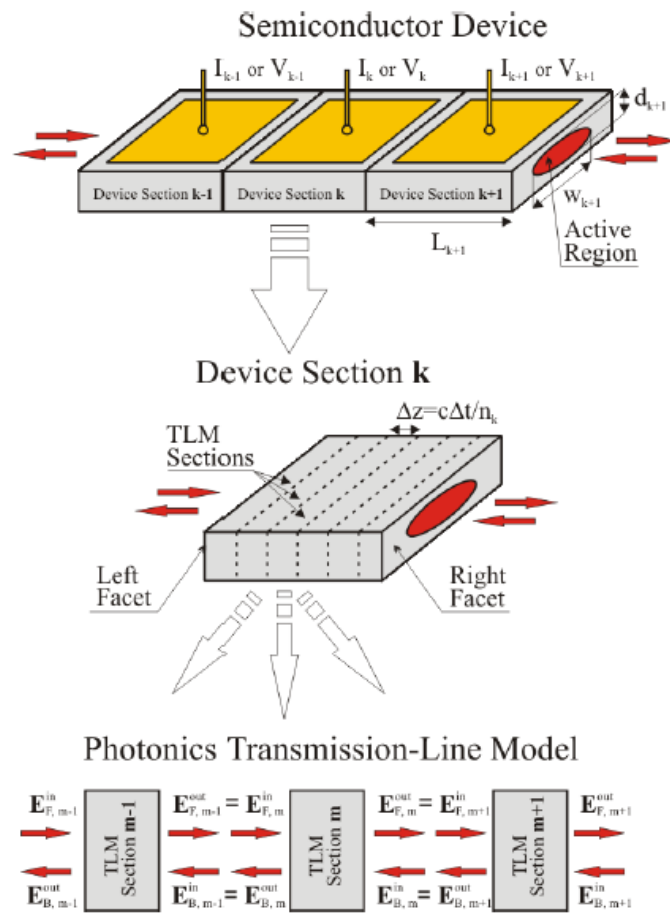


Fig. 4.3: A TLLM semiconductor device in VPI with k device sections and m scattering nodes (TLM sections) (After Ref. [129]).

Although VPI is a software simulation tool, it also provides reliable results when it is compared with experimental work. As an example of that, in Fig. 4.4 is presented a case where the design and material parameters of a three-section TLD in [82] are imported and used as TLLM device in VPI. The phase section is injected gradually with current from 0 to 40 mA while the DBR section remains inactive. The output frequency and power variation during phase wavelength tuning of the TLD in the time domain is illustrated in Fig. 4.5 and Fig. 4.6, respectively and the results are found to be in good agreement to those of [82].

Tunable Three-Section FP-Passive-DBR Laser

This shows the tuning characteristic of a 3-section laser. The left section is a Distributed Bragg Reflector (DBR). The middle section is a phase adjusting section, so that the Fabry Perot modes of the complete cavity are tuned to lie at the center of the DBR stopband. The right section is a gain section, which has a reflective right facet to form a Fabry Perot cavity with the DBR reflector.

This example shows the effect of tuning the phase section, by applying a current ramp which sweeps its carrier density and hence its index. The output frequency mode hops as the phase is tuned, and the output power fluctuates.

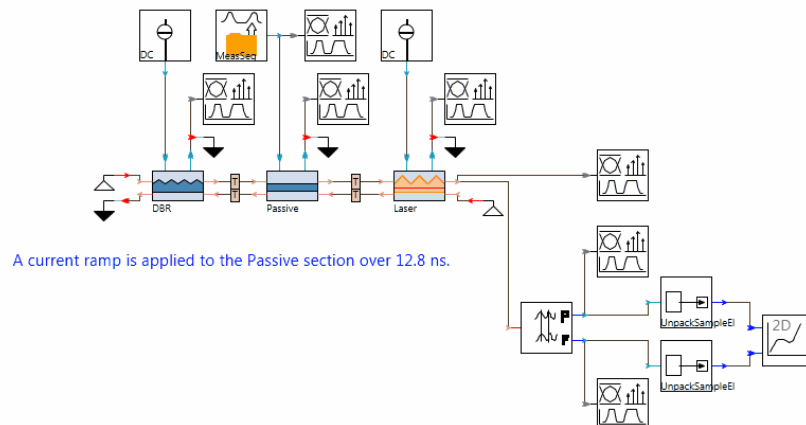


Fig. 4.4: A three-section TLD model in VPI according to [82] (After Ref. [129]).

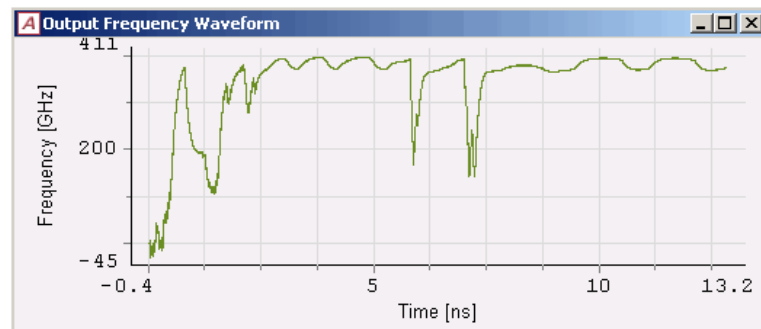


Fig. 4.5: TLD output frequency versus time during phase wavelength tuning (After Ref. [129]).

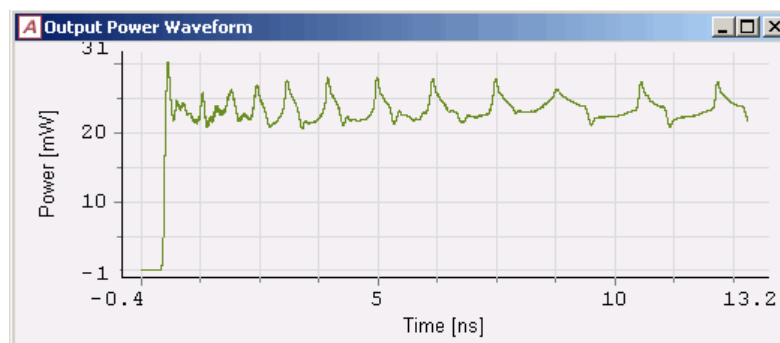


Fig. 4.6: TLD output power versus time during phase wavelength tuning (After Ref. [129]).

4.3.1 Travelling-wave equations for optical fields

VPI uses the travelling-wave equations for the propagation of the electro-magnetic field in the composite optical cavity of a TLLM device. The propagating electric field $\vec{E}(\vec{r}, t)$ along the axis of propagation z in time t inside the active region of the TLLM can be represented as a superposition of the forward and backward travelling optical wave with complex envelope amplitude $A(z, t)$ and $B(z, t)$, respectively as [129]:

$$\vec{E}(\vec{r}, t) = e^{j2\pi f_0 t} \left(\vec{F}(\vec{r}_\perp, f_0) A(z, t) + \vec{F}^*(\vec{r}_\perp, f_0) B(z, t) \right) \quad (4.10)$$

where f_0 is the frequency of the propagating wave in vacuum and $\vec{F}(\vec{r}_\perp, f_0)$ is the profile of the electric field which describes the fundamental mode(s) in the area between sections.

Amplitudes $A(z, t)$ and $B(z, t)$ are varying slowly in time but are rapidly oscillating along the propagation axis z so it is more useful to introduce in the calculations the amplitudes $a(z, t)$ and $b(z, t)$ which are slowly oscillating in both time t and along z and are defined as:

$$\begin{aligned} a(z, t) &= e^{j\beta z} A(z, t) \\ b(z, t) &= e^{-j\beta z} B(z, t) \end{aligned} \quad (4.11)$$

where $\beta = \frac{2\pi f_0}{c} n_{\text{eff}}(f_0)$ is the complex propagation constant and $n_{\text{eff}}(f_0) = n'_{\text{eff}}(f_0) + jn''_{\text{eff}}(f_0)$ is the complex effective refractive index which depends on the propagating wave frequency f_0 .

The travelling-wave equations can now be derived by substituting (4.10) and (4.11) into the Maxwell equations which gives for the forward and backward propagating wave

with complex amplitudes $a(z, t)$ and $b(z, t)$, respectively, which are slowly-varying in t and z [129]:

$$\begin{aligned} \left[\frac{1}{v_g} \frac{\partial}{\partial t} + \frac{\partial}{\partial z} \right] a &= \left[\frac{1}{2} (g(N) - a_{i,FC}) \right] a \\ \left[\frac{1}{v_g} \frac{\partial}{\partial t} - \frac{\partial}{\partial z} \right] b &= \left[\frac{1}{2} (g(N) - a_{i,FC}) \right] b \end{aligned} \quad (4.12)$$

where $v_g = c/n_g$ is the group velocity of the optical mode of the propagating wave, where c is the speed of light in vacuum and n_g is the group refractive index of the cavity, $g(N)$ is the optical gain in the active region which depends on the carrier density N which in turn varies in time according to the rate equations described in section 4.3.2 and $a_{i,FC} = a_i + a_{FC}N$ is the coefficient for the optical losses caused by the internal losses a_i of the cavity and Free-Carrier (FC) absorption which has a linear dependence with the carrier density N according to the coefficient a_{FC} .

The average photon density $S(t)$ in the active region of the TLLM device for a small amount of length Δz in time t can be determined by the amplitudes $A(z, t)$ and $B(z, t)$ of the forward and backward propagating optical fields, respectively and is defined as [129]:

$$S(t) = \frac{\Gamma}{E_{ph} v_g} \frac{1}{wd\Delta z} = \int_{z-\Delta z/2}^{z+\Delta z/2} |A(z, t) + B(z, t)|^2 dz \quad (4.13)$$

where $E_{ph} = hf_0$ is the photon energy for the frequency f_0 of the propagating wave in vacuum and Γ , w and d is the optical confinement factor, width and thickness of the active region, respectively.

4.3.2 Rate equations for carrier density dynamics

The processes of generation and recombination of electron-hole pairs in the active region of a TLLM device are governed in VPI by the rate equation responsible for the variation in time t of the density N of electrons and holes in the conduction and valence band, respectively which is assumed to be equal according to the charge neutrality condition. In the the case of a bulk active region this variation is defined by the first rate equation already described in section 3.4 as [129]:

$$\frac{dN}{dt} = \frac{\eta I}{eV} - R(N) - v_g g(N) S(t) \quad (4.14)$$

where I is the injection current into the active region, η is the current injection efficiency, e is the electron charge, V is the volume of the active region and $R(N) = AN + BN^2 + CN^3$ is the carrier density dependent recombination rate of carriers responsible for the spontaneous and non-radiative recombination of electron-hole pairs, where A is the non-radiative Shockley-Read-Hall or linear recombination coefficient, B is the bimolecular or radiative recombination coefficient and C is the non-radiative Auger recombination coefficient.

In the case of a MQW active region the generation and recombination of electron-hole pairs are described by two separate rate equations, one for the Separate Confinement Heterostructure (SCH) regions (two symmetrical regions before and after the MQW region which are used for better electronic and optical confinement) and one for the MQW region which are defined as [129]:

$$\frac{dN_{SCH}}{dt} = \frac{\eta I}{eV_{SCH}} - \frac{N_{SCH}}{\tau_{cap}} + \frac{N_{MQW}}{\tau_{esc}} \frac{d_{MQW}}{d_{SCH}} \quad (4.15)$$

$$\frac{dN_{MQW}}{dt} = \frac{N_{SCH}}{\tau_{cap}} \frac{d_{SCH}}{d_{MQW}} - \frac{N_{MQW}}{\tau_{esc}} - R(N_{MQW}) - v_g g(N_{MQW}) S(t) \quad (4.16)$$

where V_{SCH} is the volume of one SCH region, N_{SCH} and N_{MQW} is the carrier density of one SCH and MQW region, respectively, τ_{cap} and τ_{esc} is the carrier *capture* and *escape time*, respectively of the exchange of carriers between the SCH regions and the quantum wells (which also describes the capture and escape process, respectively of the confined electrons in the quantum wells and the unconfined electrons in the SCH regions) and d_{MQW} and d_{SCH} is the thickness of the MQW and one of the SCH regions, respectively.

In equation (4.15), the term $\frac{\eta I}{eV_{SCH}}$ defines the injection of carriers into the SCH regions, the term $\frac{N_{SCH}}{\tau_{cap}}$ defines the transport/dwell or *capture* of the carriers in the SCH regions and the term $\frac{N_{MQW}}{\tau_{esc}} \frac{d_{MQW}}{d_{SCH}}$ defines the thermionic emission or *escape* of the carriers from the quantum wells.

In equation (4.16), the term $\frac{N_{SCH}}{\tau_{cap}} \frac{d_{SCH}}{d_{MQW}}$ defines the injection or *capture* of carriers from the SCH regions into the quantum wells, the term $\frac{N_{MQW}}{\tau_{esc}}$ defines the thermionic emission or *escape* of the carriers from the quantum wells, the term $R(N_{MQW})$ defines the spontaneous and non-radiative recombination of the electron-hole pairs in the quantum wells and the term $v_g g(N_{MQW}) S(t)$ defines the stimulated gain and absorption processes in the quantum wells.

4.3.3 Stimulated emission (gain) models

Stimulated emission or gain in the active region of a TLLM device can be represented in VPI in five ways or models: 1) the flat gain model, 2) the linear gain model, 3) the logarithmic gain model, 4) the parabolic gain model and 5) gain modeling with information loaded by a data file.

In the flat gain model, the gain is frequency independent and only dependent on carrier density N . It is assumed to be flat around the region of the gain peak $g_{peak}(N)$ and is therefore defined as:

$$g(N) = g_{peak}(N) \quad (4.17)$$

In the linear gain model, the gain is frequency independent and only dependent on carrier density. The gain peak $g_{peak}(N)$ has a linear dependence on the carrier density and is therefore defined as [129]:

$$g_{peak}(N) = \alpha_{lin}(N - N_{tr}) \quad (4.18)$$

where α_{lin} is a constant coefficient called linear *differential gain* and N_{tr} is the transparency carrier density which are both specified by the user in VPI.

In the logarithmic gain model, the gain is frequency independent and only dependent on carrier density. The gain peak $g_{peak}(N)$ has a logarithmic dependence on the carrier density and is therefore defined as [129]:

$$g_{peak}(N) = \alpha_{log} \log\left(\frac{N}{N_{tr}}\right) \quad (4.19)$$

where α_{\log} is the constant coefficient logarithmic differential gain which is specified by the user in VPI.

In the parabolic gain model, the gain depends on both the frequency f and the carrier density N and has, as the name implies, a parabolic shape. It is defined in VPI as [129]:

$$g(f, N) = g_{peak}(N) \left(1 - \left(\frac{f - f_{peak}(N)}{\Delta f(N)/2} \right)^2 \right) \quad (4.20)$$

where $g_{peak}(N)$ has either a linear or logarithmic dependence on the carrier density, $f_{peak}(N)$ is the carrier density dependent frequency at the gain peak and $\Delta f(N)$ is the bandwidth of the gain spectrum which is the range of frequencies where the gain is positive.

According to [129], in the parabolic gain model for carrier densities greater than the transparency carrier density ($N > N_{tr}$), the gain is zero for frequencies lower than the bandgap frequency f_{gap} of the material of the active region ($f < f_{gap}$), positive for frequencies within the gain bandwidth ($f_{gap} < f < f_{gap} + \Delta f$) and negative for higher frequencies outside the gain bandwidth ($f > f_{gap} + \Delta f$). For carrier densities smaller than the transparency carrier density ($N < N_{tr}$), the gain is zero for frequencies lower than the bandgap frequency ($f < f_{gap}$) and negative for frequencies higher than the bandgap frequency ($f > f_{gap}$).

The bandgap frequency is found in the parabolic gain model in VPI with the use of a reference gain curve which is created by the user according to a reference carrier density N_{ref} , a gain peak frequency $f_{peak}(N_{ref})$ corresponding to N_{ref} and a gain

bandwidth $\Delta f(N_{ref})$ according to N_{ref} , all three also specified by the user. The bandgap frequency can therefore be defined as [129]:

$$f_{gap} = f_{peak}(N_{ref}) - \frac{\Delta f(N_{ref})}{2} \quad (4.21)$$

The gain curves of any carrier density and frequency can be recreated according to the reference gain curve and the gain bandwidth $\Delta f(N)$ and gain peak frequency $f_{peak}(N)$ of any gain curve dependent on any carrier density can therefore be defined as [129]:

$$\Delta f(N) = \Delta f(N_{ref}) \sqrt{\frac{g_{peak}(N)}{g_{peak}(N_{ref})}} \quad (4.22)$$

$$f_{peak}(N) = f_{peak}(N_{ref}) + \frac{\Delta f(N_{ref})}{2} \left(\sqrt{\frac{g_{peak}(N)}{g_{peak}(N_{ref})}} - 1 \right) \quad (4.23)$$

For the case where the carrier density of the gain curve is smaller than the transparency carrier density ($N < N_{tr}$, negative gain) then the gain peak $g_{peak}(N)$ is zero and the frequency dependent only gain is given by [129]:

$$g(f) = -g_{peak}(N_{ref}) \left(\frac{f - f_{gap}}{\Delta f(N_{ref})/2} \right)^2 \quad (4.24)$$

The gain curves for different carrier densities (smaller and greater than the transparency carrier density) which are based on the reference carrier density $N_{ref}=N_I$ are illustrated in Fig. 4.7.

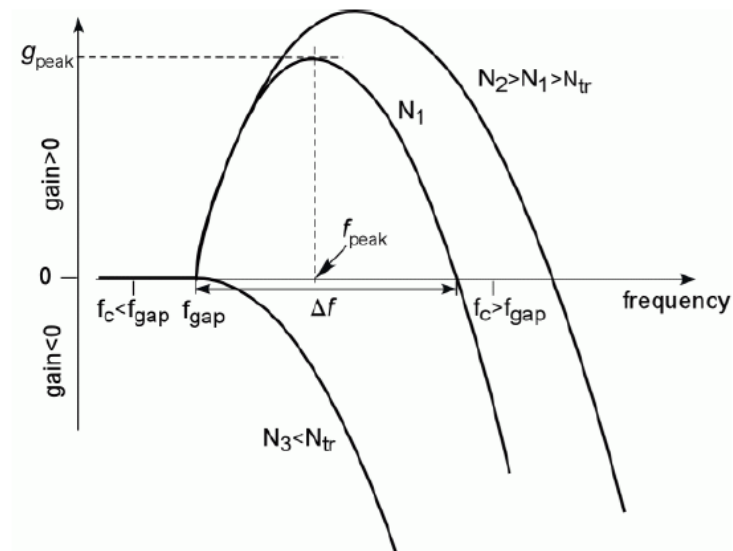


Fig. 4.7: Parabolic gain model in VPI for different carrier densities with $N_1=N_{ref}$ (After Ref. [129]).

For better accuracy of the parabolic gain model, the gain curve is approximated with the use of high-order Lorentzian functions. This is also what takes place in the case where the gain curve is given by a data file (from experimental or theoretical work) which is loaded as input in VPI. The software uses the raw data and then does an approximation with the use of high-order Lorentzian filters in order to recreate as accurately as possible the gain spectrum of the input data file which will be used in all simulations. The higher number of Lorentzians which are specified by the user the better the accuracy of the recreated gain spectrum.

4.4 Conclusion

The two different software packages which were used in this research, Crosslight PICS3D and VPI, were described in a comprehensive way. A comparison between them

was made and the advantages and disadvantages of each one were presented. The reason why they were used in this thesis was also given. The physical models based on semiconductor laser theory that are used for all calculations of the electric and optical problem in those packages were described in detail.

In this thesis, it is preferred to have a simulation software package that combines both the strengths of PICS3D and VPI but, unfortunately, there is no such software currently available. Therefore, it was decided first to create a TLD model and optimise its performance with proper results in PICS3D and then use these results to implement a TLD model in VPI which has exactly the same material and design parameters and exhibitS the same laser operation as in PICS3D, so that it can be simulated under direct Intensity Modulation (IM).

Chapter 5

**Different free-carrier contributions
to the refractive index change in
semiconductor materials and
tunable laser diodes**

5.1 Introduction

Wavelength tuning in TLDs is determined by three basic physical mechanisms, such as the free-carrier (FC) injection, the electro-optic effect, and the thermal tuning. Only the FC tuning mechanism will be taken into account in the investigations in this Chapter.

In the FC injection tuning, the lasing frequency shift is achieved by the FC contribution to the refractive index change Δn . It is the most common method of wavelength tuning, particularly in the telecom applications of TLDs. Since in semiconductor lasers the carrier density in the active section remains constant (clamped), the injection current change above the threshold does not yield any contribution to the FC refractive index change.

As a result of this, a typical design of a TLD consists of one or more passive sections which, together with the active section, make a composite optical cavity. The FC refractive index change in passive sections in its turn is caused by various physical phenomena, such as the Burstein-Moss effect (band-filling), band renormalisation (band shrinkage), the plasma effect, etc. The band-filling effect shows a spectral dependence of the refractive index change due to the change of gain when current is injected into a semiconductor laser or waveguide. The plasma effect shows that the refractive index change depends linearly on the change in carrier density when current is injected into a semiconductor laser or waveguide. There are plenty of theoretical publications that discuss in detail these contributions to the FC refractive index change for various semiconductor materials [130]–[134] as well as the relevant experimental works [119], [135]–[142].

However, in the majority of these papers a semiconductor material was used, which was usually a waveguide instead of a semiconductor laser. The main issue in question was the refractive index change due to the plasma effect which was considered to be the most usual and popular contribution to Δn . This reason was that the plasma effect is the easiest contribution to Δn to investigate because one simply injects current into a semiconductor material and just observes the linear change of its refractive index due to the change in injected carrier density.

However, the band-filling effect which is another major contributor to Δn was left out of the investigations of half of the above mentioned papers [130], [132], [135], [136], [138], [141], [142], because it is more complex to measure experimentally or calculate theoretically through the Kramers-Kronig relations. Therefore, the contribution from the band-filling effect is investigated only in a few publications in the published literature [119], [131], [133], [134], [137], [139], [140]. Among them, the experimental work in [119] for a GaAs laser and the theoretical work in [131] for an InGaAsP waveguide material show that the contribution from the band-filling effect to the refractive index change is actually greater than the contribution from the FC plasma effect. It is also stated in [131] that the predictions that were made for the refractive index change are in good agreement with the available experimental data for the InGaAsP material.

Therefore, it is very difficult to distinguish the FC contributions to Δn of both the plasma and band-filling effect in a semiconductor material, let alone a semiconductor laser such as the TLD, where different FC contributions to Δn affect the overall wavelength tuning. The main reason is because a comprehensive analysis of real TLD devices is a very challenging problem. A useful and most often used approach is to investigate the optical and the carrier transport problems separately. In this case, the FC injection problem is firstly solved in a device lasing at a fixed (i.e. not tuned) frequency,

which allows to establish the relationship between the injection current and the average carrier density in each passive section of the cavity. Then one uses the relationships between the carrier density and the refractive index change (which must be known a priori) and assigns the corresponding refractive index change to each passive section. Next, the pure optical problem is solved for the TLD lasing spectrum, which is now tuned due to the above inputted refractive index modification in the passive sections of the composite cavity. However, in real devices this is not what usually takes place.

Typically, the injected carriers have spatially inhomogeneous transverse distributions across each section. This in turn results in an inhomogeneous distribution of the local refractive index change, which is seen by the light propagating in a composite waveguiding cavity. In addition, in monolithic multi-section TLDs the sections are not completely isolated from each other and this may also influence the longitudinal carrier distributions (horizontal current leakage) making the corresponding refractive index profile more inhomogeneous. At high injection currents, when the vertical leakage effects become important, the situation becomes even more complex. Thus, the only adequate approach to the tuning problem in TLDs is to investigate the tuning performance of an operating device self-consistently for charge carrier transport and photon field propagation, including the real refractive index change (tuning) in the passive sections under the FC injection.

In terms of wavelength tuning, there are numerous recent theoretical models which demonstrate wide tuning ranges and are in agreement with the experimental data. In these cases, WT SG DBR lasers have been used. Representative examples are the theoretical models of [143], [144], [145] which have demonstrated tuning ranges of 40 nm, 47.3 nm, and 100 nm, respectively. However, all these works, except [144], do not model devices self-consistently, but use the refractive index change (due to plasma effect only) as an

input parameter.

In this Chapter, to the best of the author's knowledge, the first comprehensive numerical model of TLD operation is presented with wavelength tuning based on simultaneous consideration of optical and transport phenomena in a complex multisection device. A 3-D simulation model of a three-section InGaAsP/InP TLD operating at 1550 nm CW with a bulk optical cavity is developed by using the Crosslight PICS3D software. The effect of not only the plasma effect but also the band-filling effect (which is usually not investigated in published literature) to Δn of the TLD is investigated and measured in detail by the sophisticated solver of PICS3D for each effect separately and for both effects combined.

In section 5.2, the simulated device structure and its parameters are described in detail. Section 5.3 includes all the acquired results from the investigations, which are explained in a comprehensive way. The two main FC contributions to Δn is the plasma effect and the changes in the interband transitions (band-filling effect), which are calculated by using a modified formula of the Kramers-Kronig (KK) relations (KK effect) in PICS3D. The results show that the KK (band-filling) effect is heavily underestimated by the lack of investigation in published literature as it is the main contributor to Δn , a statement which is also supported by the experimental work of [119] and the theoretical work of [131]. Section 5.4 includes all the conclusions that can be made from all the investigations of this Chapter.

5.2 *Device structure and parameters*

The setup which is used in our simulations is a typical 3S TLD with a bulk $\text{In}_{0.61}\text{Ga}_{0.39}\text{As}_{0.84}\text{P}_{0.16}$ optical cavity operating at 1550 nm. Its structure is shown in Fig. 5.1, and a complete set of design and material parameters is given in TABLE I. These were typical parameters taken from both simulation and experimental data in the published literature and various textbooks and are widely used for the design of TLDs. The reason was that it was very difficult to find a single published paper on TLD operation either by experiment or even simulation which presented a complete set of design and material parameters for a single TLD structure. Therefore the parameter values that we used cannot be linked unfortunately to any experimental TLD or TLD model, which means we could not recreate the results of their investigations.

However, as was shown in Chapter 4, when PICS3D uses a complete set of experimental data as input, it does produce results which are in very good agreement with those from the setup of the experimental paper it borrowed the data from. We can therefore trust that PICS3D will produce adequate and valid results when we use typical parameters according to literature in our TLD model. It should be noted here that PICS3D is a very complex software tool which requires very careful selection of parameters in order for its solver to work properly and simulate the TLD model. The results from all the investigations in Chapters 5, 6 and 7 which use this PICS3D TLD model have come from tedious and meticulous trial-and-error work in order to finalise a properly working model and be able to optimise its performance. A description of the TLD model structure follows:

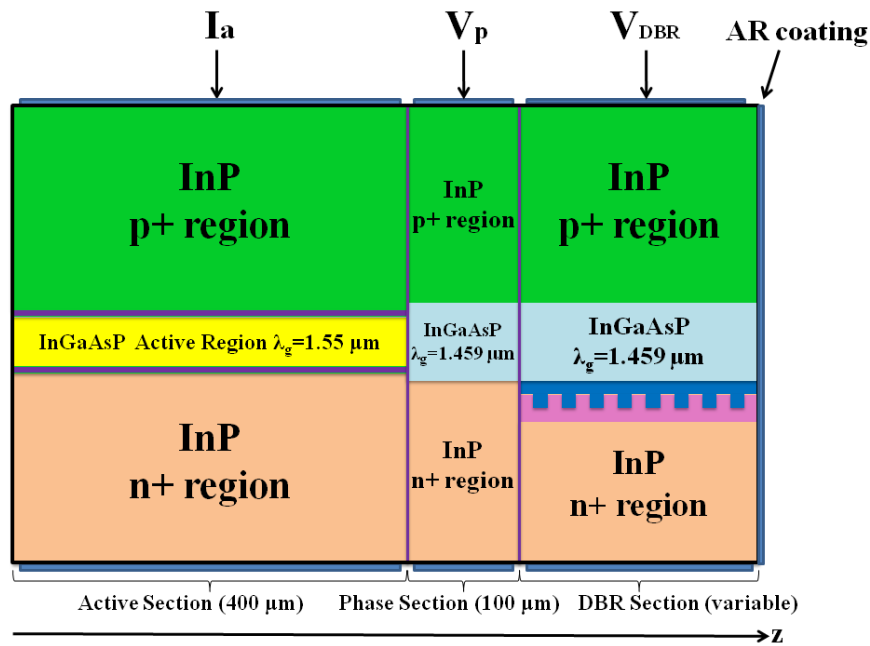


Fig. 5.1: The three-section TLD model.

The structure of the bulk TLD that was used in PICS3D is shown in two dimensions (y and z), with y being the axis of device thickness and z being the axis of photon propagation. It consists of three sections, each section of which consists of multiple layers of different colour. The total length of the device is $800 \mu\text{m}$, the total width, which is the same for all sections and layers, is $1.5 \mu\text{m}$ and the total thickness, again the same for all sections but not for all layers, is $3.33 \mu\text{m}$.

Each section has its own bottom and top contact for injecting currents and applying voltages. Although the separate pair of contacts to each section would minimise horizontal current leakage between sections, it is difficult to practically make individual bottom contacts to each section, as this would require removal of the substrate and local ion implantation in the n -layer. The main reason to use the separate bottom contacts in our model is to get around of the PICS3D's embodiment of the bias setup. In order to avoid spurious currents between top contacts, in PICS3D the common bottom contact

must always be pre-biased [120]. This means that there is a small current injection into each section. We found that the pre-biasing has no effect on the AR operation, but it decreases the available range of FC refractive index change in the passive sections. Our set up allows circumventing the latter problem at no physical cost.

TABLE I
STRUCTURE AND MATERIAL PARAMETERS

Symbol	Parameter Name	Value	Units
R_a	Left facet reflectivity	0.3 (z=0)	-
R_r	Right facet reflectivity	10^{-4} (z=800 μm)	-
w	TLD width	1.5	μm
d_a	Active region thickness	0.18	μm
d_p	Waveguide region thickness of phase section	0.38, 0.58	μm
d_{DBR}	Waveguide region thickness of DBR section	0.38	μm
d_g	Grating region thickness	0.2	μm
$E_{g,a}$	Active region bandgap	0.7986	eV
$E_{g,p}$	Waveguide region bandgap of passive sections	0.85	eV
κ	Coupling coefficient	180	cm^{-1}
$\langle \alpha_i \rangle$	Average internal losses	5	cm^{-1}
A	Linear recombination	1×10^8	s^{-1}
B	Bimolecular recombination	2×10^{-10}	$\text{cm}^3 \text{s}^{-1}$
C	Auger recombination	3.5×10^{-29}	$\text{cm}^6 \text{s}^{-1}$

N_n	Doping of the n+ region	1×10^{18}	cm^{-3}
N_p	Doping of the p+ region	1×10^{18}	cm^{-3}
N_{th}	Threshold carrier density	1×10^{18}	cm^{-3}

The active section (AR) of the TLD (400 μm length) is on the left side, the phase section (variable) is in the middle, and the DBR section (variable) is on the right side.

In the active section, the pink layer is doped with electrons, which makes it the n-layer of n-doping (electron doping= $1 \times 10^{18} \text{ cm}^{-3}$) and has a thickness of 1.5 μm . The yellow layer in the middle is the bulk active layer (active region) or the optical cavity, where all the photon generation takes place and has a total thickness of 0.18 μm . The green layer is doped with holes, which makes it the p-layer of p-doping (hole doping= $1 \times 10^{18} \text{ cm}^{-3}$) and has a thickness of 1.55 μm . Exactly below and above the AR, there are two purple layers of thickness of 0.05 μm each. These are barriers that are put there for better optical confinement and are also called the Separate Confinement Heterostructure (SCH) regions. They also enhance the potential barriers and improve carrier confinement in the optical cavity preventing possible vertical electron leakage from the AR into the p^+ region under high injection.

In the phase section, the pink layer is the n-layer (1.5 μm thickness and electron doping= $1 \times 10^{18} \text{ cm}^{-3}$), the light blue layer is a passive waveguide (WG) of no doping and the green layer is the p-layer (1.45 μm thickness and hole doping= $1 \times 10^{18} \text{ cm}^{-3}$).

In the DBR section, the pink layer is the n-layer (1.3 μm thickness and electron doping= $1 \times 10^{18} \text{ cm}^{-3}$). The grating layer consists of two InGaAsP materials (blue and purple), with one etched into the other, one of bigger refractive index and one of smaller refractive index. The light blue layer is a passive WG of no doping (0.38 μm thickness)

and the pink layer is the p-layer (1.45 μm thickness and hole doping= $1 \times 10^{18} \text{ cm}^{-3}$). The WG layer of the passive sections is an $\text{In}_{0.66}\text{Ga}_{0.34}\text{As}_{0.74}\text{P}_{0.26}$ quaternary with a bandgap wavelength $\lambda_{gp} \approx 1.46 \mu\text{m}$. The refractive index of each layer and their spectral dependence on the photon energy are calculated according to the Adachi model [146].

5.3 Results and discussion

The main focus of the investigation here is on the effect of different FC physical mechanisms on the refractive index change and on the tuning performance of the TLD. This effect is investigated in PICS3D for each mechanism separately as well as for all mechanisms combined together. In the case of the plasma effect, PICS3D uses the equations from the theory presented in Chapter 3. However, in the case of the KK effect, PICS3D uses a modified version of the KK relations which is presented as follows:

As was already mentioned in section 3.6.2 with the use of (3.55), the KK relations allow to calculate the refractive index change $\Delta n'$ due to the change Δg in the gain of the material around the photon energy E under the free carrier injection, since gain is related to the imaginary part n'' of the refractive index $g = (4\pi / \lambda)n''$. The index change is now given as:

$$\Delta n'(E) = -\frac{c_0 \hbar}{\pi e} \int_0^\infty \frac{\Delta g(E') - \Delta g(E)}{(E' - E)(E' + E)} dE' \quad (5.1)$$

Equation (5.1) is a modified version of the Kramers-Kronig formula, which was at first suggested in [119] and is later used in PICS3D [120]. It is the one which is taken into account by the optical solver in order to calculate comprehensively the KK effect. However, some helpful modifications can be introduced in order for the software to carry

out effectively numerical integration in equation (5.2). This is necessary because the integral in (5.2) is numerically difficult to compute due to the integrand's singularity at $E=E'$ [119]. For this, the integral in (5.2) is separated into three parts by the PICS3D solver, as is suggested in [120]:

$$\begin{aligned} \Delta n'(E) = & -\frac{c_0 \hbar}{\pi e} \int_0^\infty \frac{\Delta g(E') - \Delta g(E)}{(E'-E)(E'+E)} dE' \\ & -\frac{c_0 \hbar}{\pi e} \int_{E+\varepsilon}^\infty \frac{\Delta g(E') - \Delta g(E)}{(E'-E)(E'+E)} dE' \\ & -\frac{c_0 \hbar}{\pi e} \int_{E-\varepsilon}^{E+\varepsilon} \frac{\Delta g(E') - \Delta g(E)}{(E'-E)(E'+E)} dE' \end{aligned} \quad (5.2)$$

where ε is a small number.

As $E \rightarrow E'$, the integrand of the third term approaches the finite limit $\frac{1}{2E} \frac{d\Delta g(E)}{dE}$ [119].

Therefore, it may now be written as:

$$-\frac{c_0 \hbar}{\pi e} \frac{dg}{dE} \int_{E-\varepsilon}^{E+\varepsilon} \frac{1}{E'+E} dE'$$

It is visible that the integrand of the integral is no longer singular and can now be easily evaluated by the optical solver, in order to give accurate results concerning the KK effect. We can now proceed to the presentation of the acquired results from the investigations in this Chapter.

In the laser setup used in this Chapter, the AR is activated by injecting current in the top contact. During the passive section tuning, it operates at a given value of injected current $I_a=15$ mA, which provides the output power of 5.4 mW, as can be seen in the L-I characteristic in Fig. 5.2. The threshold current I_{th} of this laser is $I_{th}=5.31$ mA. The band profile of the AR under the 15 mA injection is shown in Fig. 5.3. It is interesting to observe that the quasi-Fermi level of the electrons E_{Fn} is continuous at all interfaces, while for the holes E_{Fp} has a discontinuity at the cladding interface. This indicates that the

electron injection into the AR is completely controlled by the drift-diffusion transport, while the hole injection is controlled by the thermionic emission.

In the current investigation only the case of DBR tuning is presented, where bias V_{DBR} is applied to the top contact of the DBR section from 0 V until the maximum value of $V_{DBR}=1.5$ V is reached. This voltage corresponds to an equivalent value of the DBR current I_{DBR} of around $I_{DBR} \approx 140$ mA, as is shown in the I-V characteristic of the DBR section in Fig. 5.4. The phase section remains inactive during all simulations that concerned tuning with a value of $V_p=0$ V of applied bias. Since each section in our model has a separate pair of the top and bottom contacts and can be driven completely independently, it is more convenient in the simulation of tuning to apply the bias to the passive section rather than specifying the injection current value.

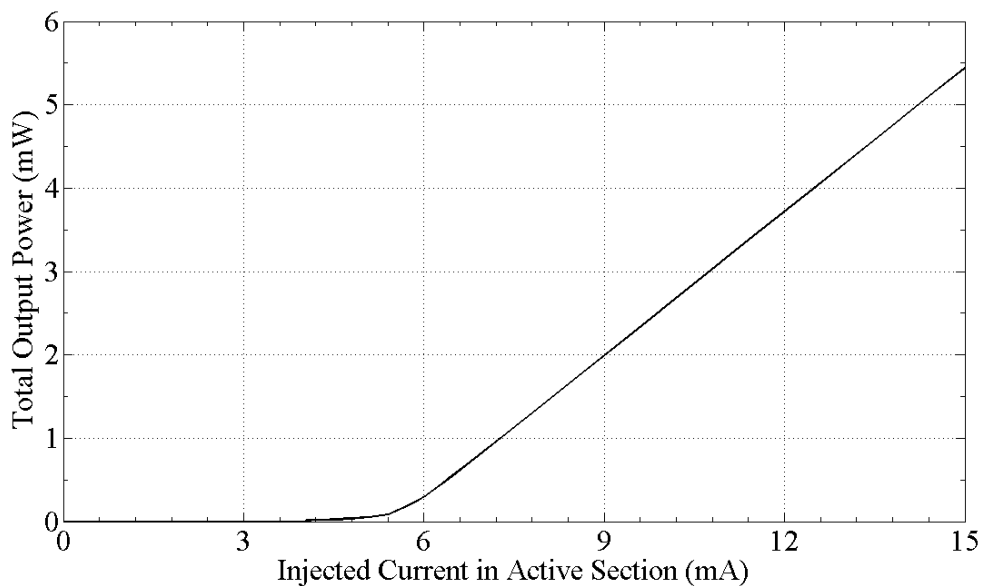


Fig. 5.2: L-I characteristic of the TLD.

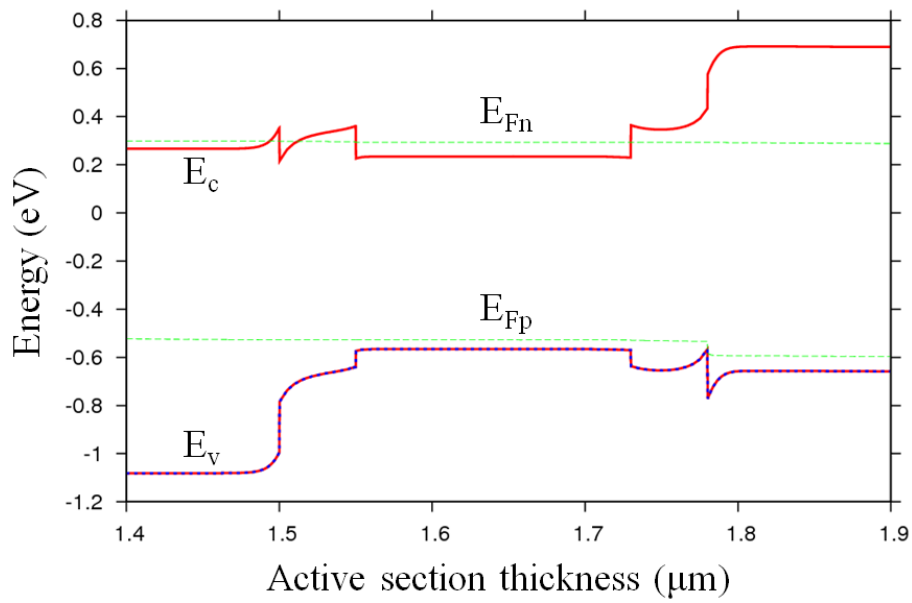


Fig. 5.3: Band structure profile of the active section under 15 mA injection.

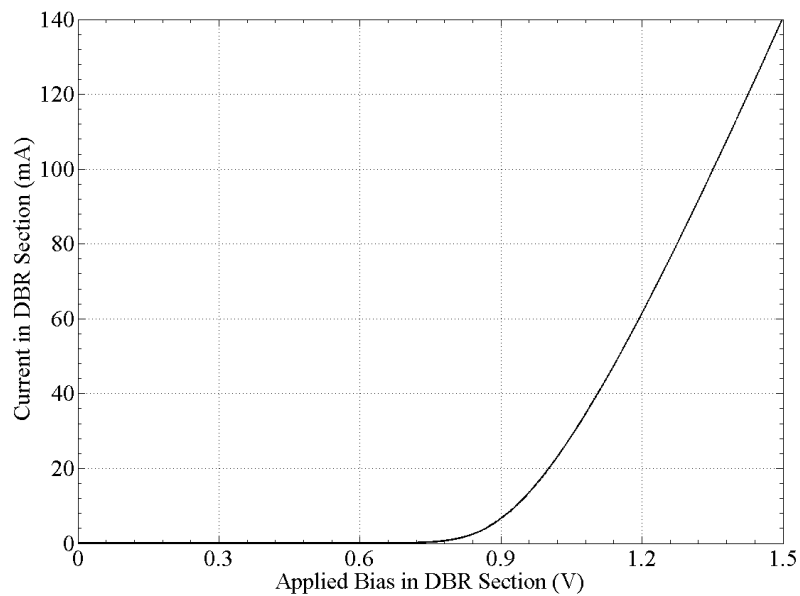


Fig. 5.4: I-V characteristic of the DBR section.

The PICS3D simulator has the option of activating and deactivating various FC contributions to the real part of the refractive index change $\Delta n'$. In this investigation, three cases are taken into consideration. The first one takes place when only the plasma effect is a contributor to $\Delta n'$ during tuning the DBR section. The second one takes place when only

the KK effect is activated as a contributor to $\Delta n'$ and the third one when both contributions are activated. The effect of all three cases on the output wavelength change is also investigated.

The main results are shown in Fig. 5.5, which demonstrates the contribution to $\Delta n'$ from the plasma effect (red line, number 1) and from the KK effect (blue line, number 2) separately, as well as when they are combined together (black line, number 3). The index change is plotted as a function of injection current (bias). The initial value of refractive index n' is around $n' \approx 3.4025$, before tuning starts by applying bias to the DBR section. It remains constant until 0.6 V of the applied bias, and then begins decreasing with further increase of the bias. At the final bias $V_{DBR} = 1.5$ V, n' reaches the value of $n' \approx 3.3805$ in the case where only the plasma effect is activated ($\Delta n'_{(plasma)} \approx -0.022$), the value of $n' \approx 3.3685$ when only the KK effect is activated ($\Delta n'_{(KK)} \approx -0.034$), and the value of $n' \approx 3.3465$ for the combined effect ($\Delta n'_{(plasma \& KK)} \approx -0.056$). As can be seen, a quite large $\Delta n'/n' \approx 1.65\%$ has been achieved, particularly in the case where both effects are contributing.

As is seen from Fig. 5.5, the contribution to $\Delta n'$ from the KK effect is almost double the contribution from the plasma effect for the same range of applied biases. It can also be observed that the plasma effect requires higher values of applied bias than the KK effect in order to achieve the same value of n' . Therefore it is concluded from the above observations that the KK effect gives a dominant contribution to $\Delta n'$, which is also supported by the experimental work of [119] and the theoretical work of [131].

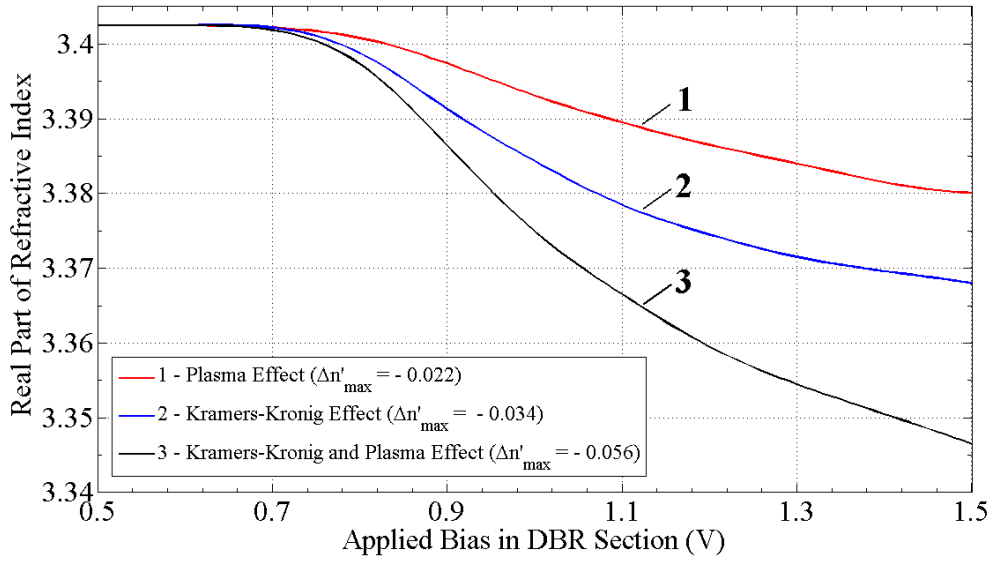


Fig. 5.5: Real part of refractive index in WG region of the DBR section as a function of the DBR bias.

In Fig. 5.6, the corresponding wavelength tuning of the DBR section is shown, when each effect is activated separately and when both are activated together. As in Fig. 5.6, the red line (number 1) shows the tuning curve when only the plasma effect is activated, the blue line (number 2) when only the KK effect is activated and the black line (number 3) when both are activated. The initial value λ_0 of the emitted wavelength λ of the TLD for all three cases, without any tuning of the passive sections ($V_p=0$ V, $V_{DBR}=0$ V), is around $\lambda_0 \approx 1.5502$ μm . In all three cases λ remains constant as n' is decreasing, until the required value of n' is reached, which causes the mode jump to a shorter wavelength. The size of this jump is defined by the inter-mode distance $\Delta\lambda_m$, which for our device was $\Delta\lambda_m=0.7$ nm.

As can be observed in Fig. 5.6, the plasma effect gives a blue wavelength shift $\Delta\lambda_{(plasma)}$ of around $\Delta\lambda_{(plasma)} \approx 6.2$ nm since the last wavelength jump happened at $\lambda_{(plasma)} \approx 1.544$ μm . The KK effect gives a blue wavelength shift $\Delta\lambda_{(KK)}$ of around

$\Delta\lambda_{(KK)} \approx 9.2$ nm since the last wavelength jump happened at $\lambda_{(KK)} \approx 1.541$ μm . The combined effect when both mechanisms are activated gives a blue wavelength shift $\Delta\lambda_{(plasma \& KK)}$ of around $\Delta\lambda_{(plasma \& KK)} \approx 10.2$ nm since the last wavelength jump happened at $\lambda_{(plasma \& KK)} \approx 1.540$ μm .

It is also visible that the KK effect requires smaller values of V_{DBR} than the plasma effect in order to give the same wavelength jumps and achieve the same tuning range. It is also shown that the wavelength tuning saturates for the KK effect at around $V_{DBR} \approx 1.3$ V, although the refractive index continues decreasing with further bias increase (see Fig. 5.5). The wavelength tuning continues for the plasma effect contribution even after $V_{DBR} = 1.5$ V and it saturates at a much greater value of V_{DBR} .

The same observations can be made for the tuning curve of the combined effect, where the wavelength jumps happen at smaller bias values and the tuning saturates much earlier than in the case of each effect separately. From the above, it can be concluded that the KK effect gives the main contribution to the output wavelength tuning and defines the tuning behaviour of the DBR section.

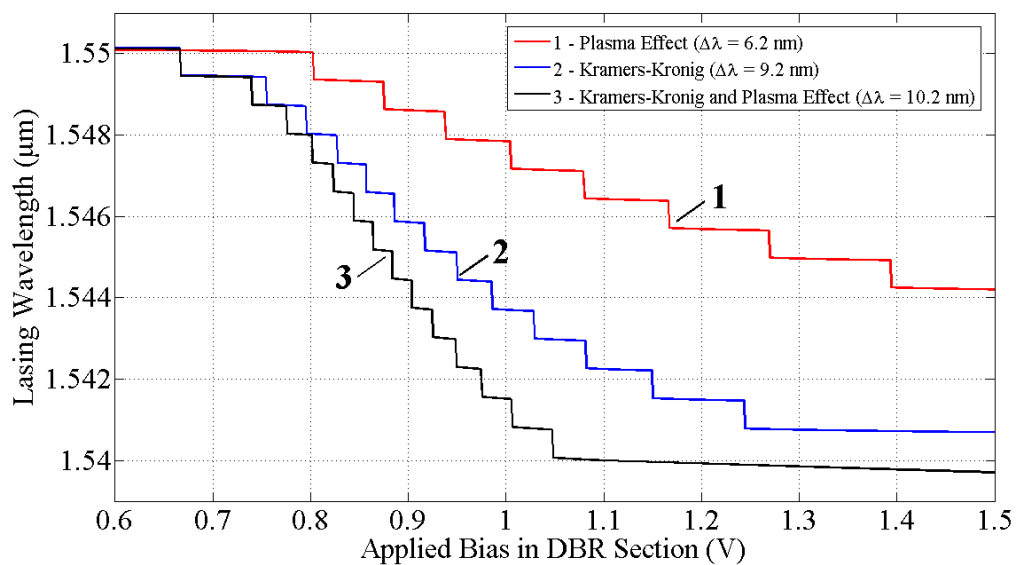


Fig. 5.6: Lasing wavelength as a function of current (bias) in the DBR section.

In the case where both effects are activated, wavelength tuning saturates at around $V_{DBR} \approx 1.1$ V, although the refractive index is still changing with further bias increase (actually more than 50% of available $\Delta n'$ is not converted into the corresponding wavelength tuning). The reason for such behaviour has to do with the design of the TLD and will be discussed in Chapter 6.

5.4 Conclusion

Different FC contributions to the real part of the refractive index change were investigated, as well as their effect on the output lasing wavelength of the device. The FC contributions in question were the plasma effect and the inter-band optical transitions which were calculated by using the KK relations (band-filling effect). The contribution of each effect was investigated separately by activating one effect each time as well as when they acted together. It was shown that the band-filling effect instead of the plasma effect is the dominant contributor to the real part of the refractive index change, which also shapes the corresponding wavelength tuning performance of the device. This shows that the band-filling effect is heavily underestimated due to the lack of investigation of this effect in published literature as a contributor to the refractive index change, a statement which is also supported by the experimental work of [119] and the theoretical work of [131]. It was also found that the available refractive index change is not necessarily converted into the corresponding lasing wavelength shift due to design issues which will be explained in Chapter 6.

Chapter 6

Design and optimisation of tunable laser diodes with enhanced tuning range

6.1 Introduction

The maximum achievable tuning range is one of the most important goals in the modelling and fabrication of TLDs for telecom applications. Indicatory of this is the fact that there are many publications available in literature which concern TLDs with a wide tuning range. In Shi [147] for example, the dynamic range of a sampled-grating (SG) DBR laser is discussed, where the achieved tuning range was 50 nm. Another theoretical model in Dong [143] simulates a WT SG-DBR laser, which uses a travelling-wave model with a digital filter approach. The time-domain traveling-wave method and the frequency-domain transfer-matrix method are both integrated in a single process. One of their results was to achieve a tuning range of 47.3 nm. It was also claimed that their theoretical data were in agreement with the experimental data of Mason [148], where a continuous tuning range of 41 nm was reached. As part of their experiment, they used a four-section buried-ridge SG-DBR laser with an integrated ElectroAbsorption (EA) modulator and a bulk active section.

In another experiment in Akulova [149], similar tuning range results of 40 nm are found, when in a similar fashion a SG-DBR laser is implemented, which is integrated with a SOA and an EA modulator. It was also managed to achieve an error-free 2.5 Gbps transmission over a 350 km standard single-mode fibre span. Finally, in Kim [150] a new TLD structure has been implemented, where a SG-DFB laser diode is monolithically integrated with a SG distributed Bragg reflector, which can give a continuous tuning range of up to 27 nm.

The main focus of the investigation in this Chapter concerns the effect of specific material and design parameters of a TLD model on the discontinuous wavelength tuning

and how to achieve the maximum tuning range by optimising these parameters. The parameters in question are the composition of the materials which form the Bragg grating of the TLD and the length L of the DBR section. It is shown that different material compositions and different lengths L have strong effect on the Bragg reflectivity spectrum and the DBR tuning range. Investigations on how to enhance the tuning range by optimising specific design parameters of the simulated TLD are also made. Continuous and quasicontinuous tuning ranges are also presented in the optimised setups. All the TLD models in this Chapter are designed with the use of the Crosslight PICS3D software.

Section 6.2 includes all the acquired results from the various investigations, which are explained in a comprehensive way. Section 6.3 includes all the conclusions made during the investigations.

6.2 *Results and discussion*

6.2.1 **Effect of the κL product on the TLD discontinuous tuning performance**

The setup and parameters of most of the simulated devices in this section is the same with the one described in Chapter 5. In all the simulated TLDs during the DBR section tuning the AR operates at a fixed injection current $I_a=15$ mA which provided the output power between 4.5 mW and 5.5 mW in various simulated TLDs.

We have already investigated the refractive index change in the DBR section due to different FC contributions in Chapter 5. In all our simulations in this Chapter both contributions are always activated. This means that only their combined effect on the wavelength change is calculated here. The real part of the refractive index in the WG

region of the DBR section is plotted as a function of the DBR bias in Fig. 6.1. Fig. 6.2 shows the corresponding wavelength tuning of the DBR section. A DBR tuning range of $\Delta\lambda \approx 10$ nm has been achieved in this device.

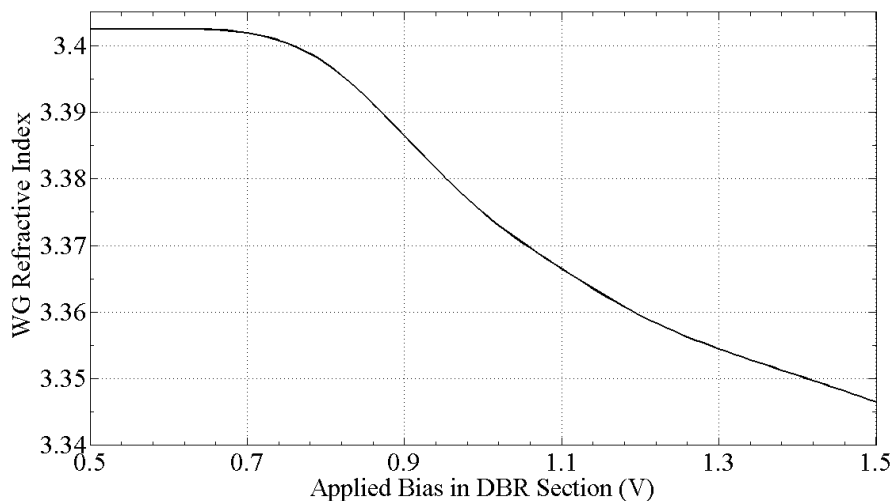


Fig. 6.1: Real part of refractive index in WG region of the DBR section as a function of the DBR bias.

As it was observed in Chapter 4 the tuning performance of the TLD is not optimal. It was seen that the wavelength tuning saturates at around $V_{DBR}=1.05$ V, although the refractive index is still changing with further bias increase and more than 50% of the available $\Delta n'$ is not converted into the corresponding wavelength shift. This also happens in spite of the fact that more longitudinal modes are still available for further wavelength hops, as is shown in the lasing modes spectrum in Fig. 6.3 for this case. An expansion of this observation will be given in this section.

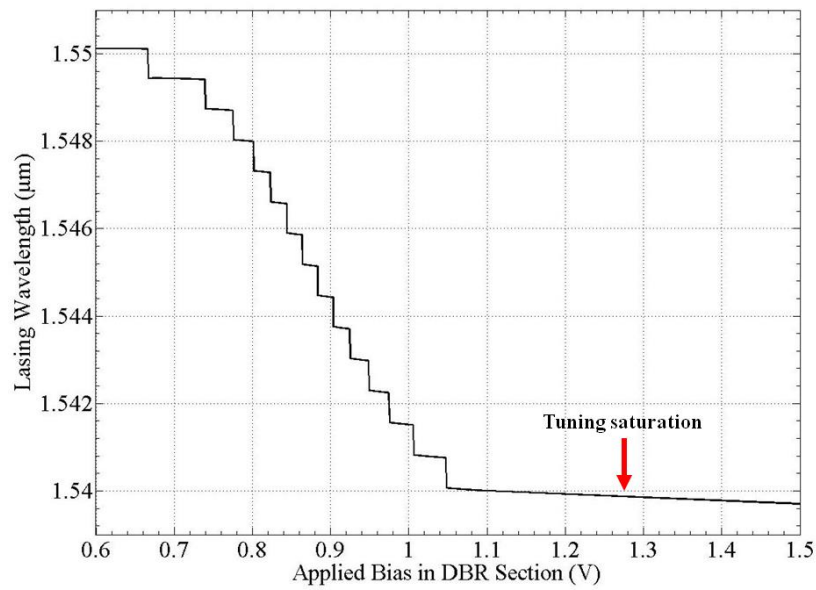


Fig. 6.2: DBR wavelength tuning in a TLD with $\kappa=180 \text{ cm}^{-1}$ and $L=300 \text{ }\mu\text{m}$.

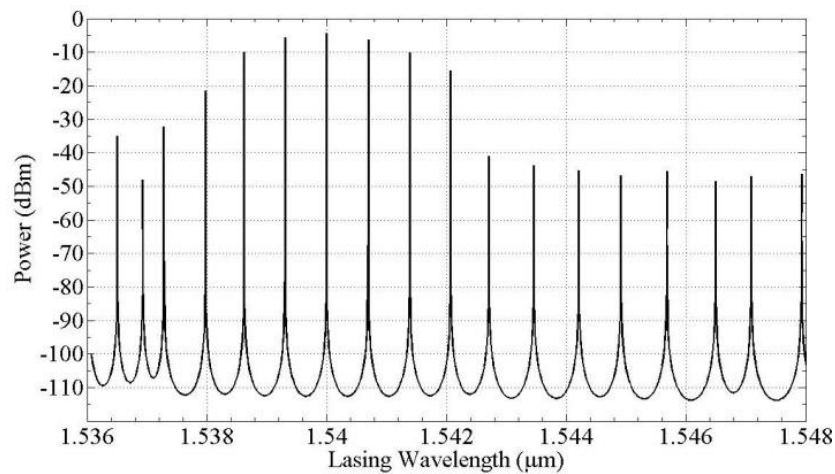


Fig. 6.3: Lasing spectrum of the TLD with $\kappa=180 \text{ cm}^{-1}$ and $L=300 \text{ }\mu\text{m}$ taken at the DBR section bias $V_{DBR}=1.1 \text{ V}$.

In order to understand the underlying physical reason of such an unusual behaviour of the lasing wavelength we have to inspect the comb mode spectrum in Fig. 6.3, taken at the point of the tuning saturation ($V_{DBR}=1.1 \text{ V}$), and also consider in detail the DBR reflectivity spectra as was discussed in section 3.3.

In Figs. 6.4 and 6.5, $R_g(\Delta\lambda)$ spectra are shown as a function of the wavelength deviation from the Bragg wavelength, $\Delta\lambda = \lambda - \lambda_B$, for different values of κ and the DBR section length L . For all curves in these figures the Bragg wavelength, as an example, was chosen to be $\lambda_B = 1.550 \mu\text{m}$ and the group index of the DBR section was $n_{gDBR} \approx 3.4$.

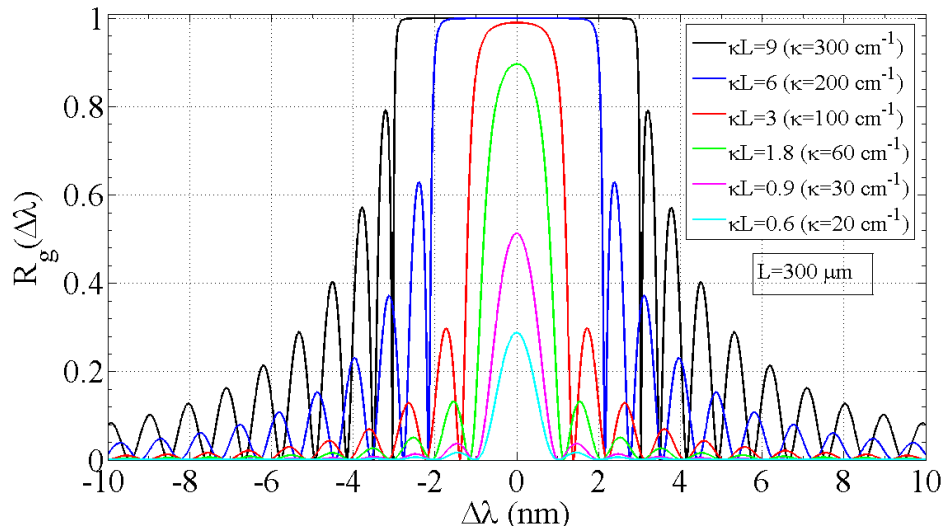


Fig. 6.4: DBR reflectivity spectra for various κ and $L=300 \mu\text{m}$, $\lambda_B=1.55 \mu\text{m}$.

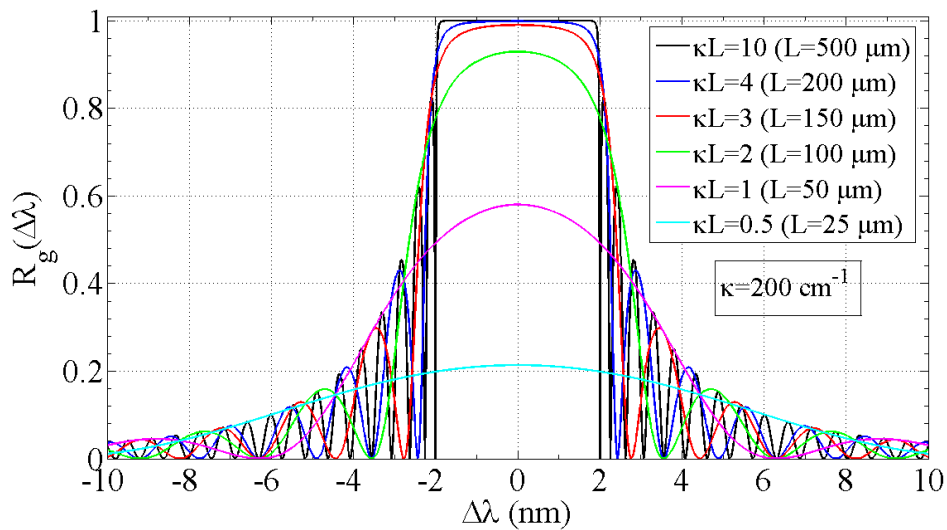


Fig. 6.5: DBR reflectivity spectra for various L and $\kappa=200 \text{cm}^{-1}$, $\lambda_B=1.55 \mu\text{m}$.

The tuning behaviour of the TLD strongly depends on the shape of the $R_g(\Delta\lambda)$ dependence. For our simulated device the length of the DBR section was $L=300\ \mu\text{m}$ and the grating consisted of $\text{In}_{0.8}\text{Ga}_{0.2}\text{As}_{0.44}\text{P}_{0.56}$ and $\text{In}_{0.93}\text{Ga}_{0.07}\text{As}_{0.16}\text{P}_{0.84}$ materials. They have refractive index difference of $\Delta n'_g = 0.0853$ which corresponds to the value of the coupling constant $\kappa=180\ \text{cm}^{-1}$. This results in $\kappa L=5.4$ and the reflectivity spectral width $\Delta\lambda_{R_g} = 4\ \text{nm}$ within which the reflectivity is almost 100%. Fig. 6.6 shows the DBR reflectivity spectra for this device (black curve). The Bragg wavelength in this device is $\lambda_{B1}=1.5518\ \mu\text{m}$. This value was chosen such that it corresponds to the lasing wavelength $\lambda_0=1.55\ \mu\text{m}$ (1.5502 μm , to be exact) at the beginning of the tuning, in agreement with the results shown in Fig. 6.2.

As can be seen from Fig. 6.3, there are roughly 6 modes next to the lasing mode at $\lambda=1.540\ \mu\text{m}$ within the spectral range $\Delta\lambda$ equal to the DBR reflectivity bandwidth, $\Delta\lambda = \Delta\lambda_{R_g} = 4\ \text{nm}$, since the comb mode spacing is $\Delta\lambda_m=0.7\ \text{nm}$. Also, all these modes have a very small Side Mode Suppression Ratio (SMSR) and are competing with each other in order to become the dominant lasing mode. This in turn makes it difficult to select a particular lasing mode from the competing modes at the tuning point. As a result of poor wavelength selectivity, the TLD is lasing in a multimode regime. It is also found that the SMSR deteriorates as the DBR bias (injection current) increases. A good discussion of the matter of SMSR in TLDs is given in [151].

It is interesting to note that the TLD tuning performance is very good at smaller biases, even though there was more than one cavity mode (actually, 4-6 modes) within the reflectivity bandwidth $\Delta\lambda_{R_g}$. This is in contrast with the usual requirement for the wavelength tuning that there must always be only one cavity mode within the reflectivity

bandwidth [85]. We explain this behaviour of the TLD tuning by the shape of the gain spectrum and the DBR reflectivity, and in particular by the mutual spectra positioning at the lasing wavelength.

As was shown in [152], [153] (see also [85] and [114]), for a good SMSR (i.e. for good mode selectivity in our case) the cavity gain for the lasing mode should exceed the gain of the nearest side mode by about 5 cm^{-1} . This condition is better satisfied at the longer lasing wavelength if the reflectivity spectrum is red-shifted with respect to the gain peak wavelength, as will be confirmed by the following simulations.

With the deeper tuning the lasing wavelength becomes shorter (blue-shifted) and the peak of the reflectivity spectrum moves towards the gain peak wavelength. If in addition the reflectivity spectrum is flat over a few comb modes, the SMSR will decrease and the wavelength selectivity will become more difficult to achieve. The deterioration of the tuning performance of the TLD with the tuning depth clearly shows that the separate consideration of the carrier injection transport problem and the optical problem may lead to wrong conclusions about the actual device tuning performance. As was already mentioned, the refractive index change will continue to increase with the injection current increase, but this will not be converted into the wavelength tuning.

In order to investigate how the tuning can be improved, we have considered different TLD designs. In particular, we will use such parameters of the DBR that the reflectivity bandwidth remains practically the same as in the previous device, $\Delta\lambda_{R_g} = 4 \text{ nm}$, but its spectral shape is changed. This case corresponds to the red curve in Fig. 6.6. Here the composition of the two grating materials ($\text{In}_{0.83}\text{Ga}_{0.17}\text{As}_{0.37}\text{P}_{0.63}$ and $\text{In}_{0.9}\text{Ga}_{0.1}\text{As}_{0.23}\text{P}_{0.77}$) corresponds to the refractive index difference $\Delta n'_g = 0.0411$ which gives the coupling constant $\kappa=89 \text{ cm}^{-1}$. The length of the DBR section was also chosen

shorter, $L=167 \mu\text{m}$. This results in $\kappa L=1.48$. The Bragg wavelength in this device is $\lambda_{B2} = 1.5504 \mu\text{m}$. The reflectivity bandwidth was kept the same, $\Delta\lambda_{R_g} = 4 \text{ nm}$. The reflectivity spectrum has now a much steeper peak around λ_{B2} and a smaller reflectivity peak value, $R_g=0.8$. This value of R_g is reasonable and does not considerably change the threshold current. The tuning curve and the lasing spectrum for this device are shown in Fig. 6.7 and Fig. 6.8, respectively.

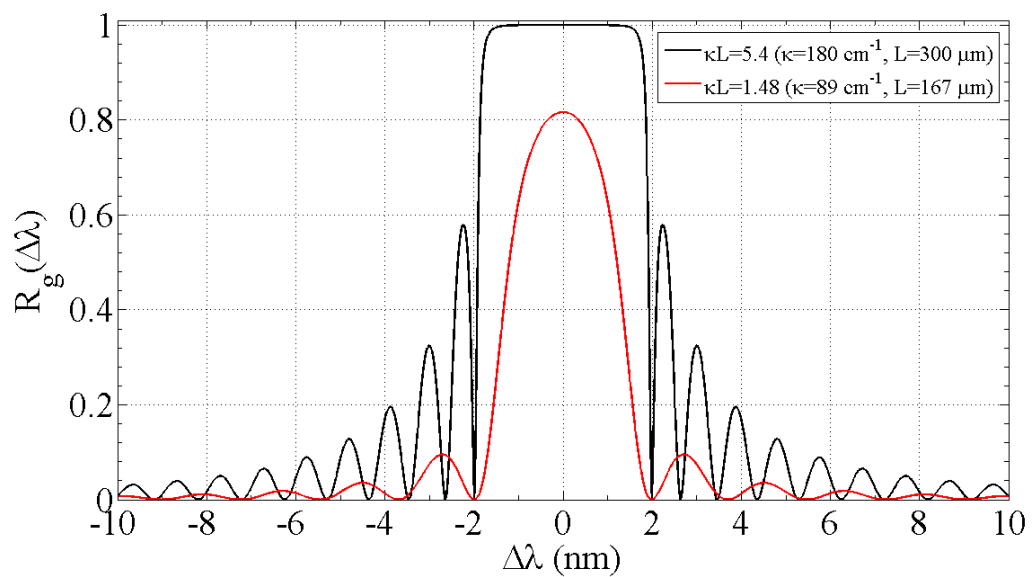


Fig. 6.6: DBR reflectivity spectra of two TLDS with $\Delta\lambda_{R_g} = 4 \text{ nm}$.

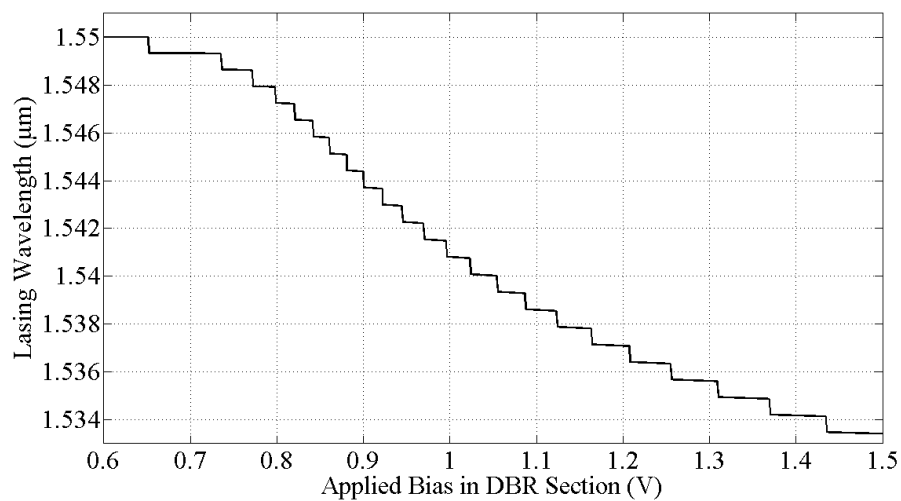


Fig. 6.7: DBR wavelength tuning in a TLDS with $\kappa=89 \text{ cm}^{-1}$ and $L=167 \mu\text{m}$.

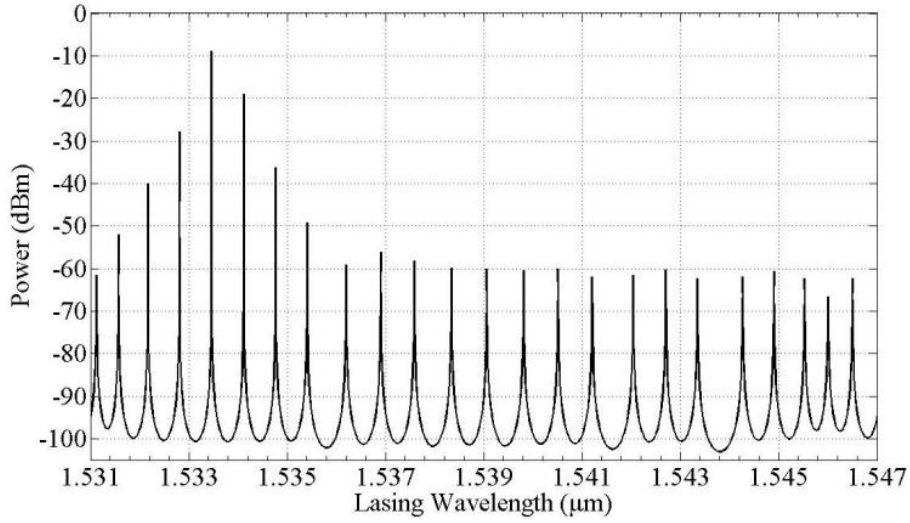


Fig. 6.8: Lasing spectrum of the TLD with $\kappa=89 \text{ cm}^{-1}$ and $L=167 \text{ }\mu\text{m}$ taken at the DBR section bias $V_{DBR}=1.5 \text{ V}$.

As can be seen in Fig. 6.7, the DBR tuning range is now increased from 10 nm to 17 nm for the same injection current. The tuning does not saturate, but further increases with the bias increase. Moreover, the cavity mode spectrum in Fig. 6.8 exhibits considerable improvement of the SMSR compared with the spectrum in Fig. 6.3. A single mode can now be selected even at higher DBR bias $V_{DBR}=1.5 \text{ V}$ ($V_{DBR}=1.1 \text{ V}$ for the device presented in Fig. 6.3). The neighboring modes are now well suppressed and the dominant lasing mode can be clearly distinguished, although the SMSR deteriorates at higher bias.

A physical explanation of why the steeper $R_g(\Delta\lambda)$ shape in the second design has improved the TLD's tunability (even though the reflectivity peak drops significantly) can be provided from the inspection of Fig. 6.9. Here the net gain g_{net} spectra of the AR is plotted together with the mirror losses a_m spectra of the composite cavity created by the left facet ($R_a=0.3$) and the DBR with wavelength-selective reflectivity $R_g(\Delta\lambda)$ for two TLDs with different parameters of the DBR sections: $\kappa L=5.4$ (black curve) and $\kappa L=1.48$

(red curve), respectively. Since we calibrated both devices to lase at $\lambda_0=1.55 \mu\text{m}$ at the beginning of the tuning, the Bragg wavelengths $\lambda_{B1,2}$ are slightly different for each device: $\lambda_{B1}=1.5518 \mu\text{m}$ for the first device (black curves) and $\lambda_{B2}=1.5504 \mu\text{m}$ for the second device (red curves). The mirror losses can be defined as in (3.45) [114]:

$$a_m = \frac{1}{2L_{eff,TLD}} \ln\left(\frac{1}{R_a R_s}\right)$$

where $L_{eff,TLD} = L_a + L_p + L_{eff}$ is the effective length of the composite TLD cavity and

$L_{eff} = \frac{\tanh(\kappa L)}{2\kappa}$ is the DBR penetration depth.

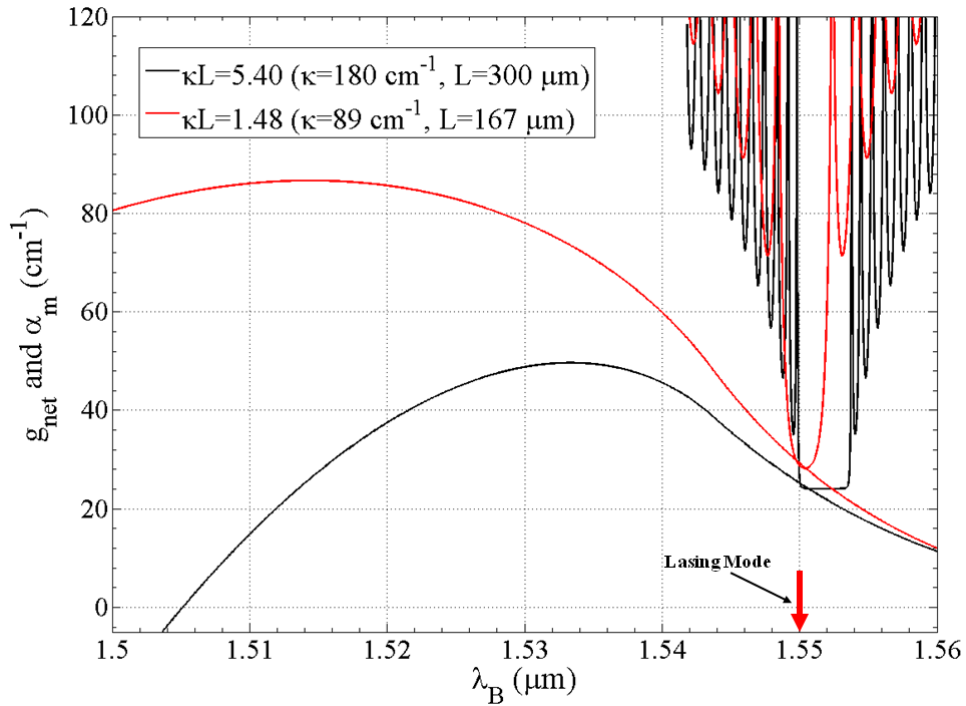


Fig. 6.9: Spectra of the net gain g_{net} and the cavity mirror losses a_m at the beginning of tuning (lasing wavelength $\lambda_0=1.55 \mu\text{m}$) for two TLDs with $\kappa L=5.4$ (black curve) and $\kappa L=1.48$ (red curve), respectively. The reflectivity bandwidth is kept the same (4 nm) for both curves.

It must be noted that the curves in Fig. 6.9 do not satisfy exactly the lasing condition (the net gain equals the mirror losses), since we do not have the exact values of the optical confinement factors. We use these factors as fitting parameters in Fig. 6.9 to satisfy the lasing condition at the beginning of tuning ($\lambda_0=1.55 \mu\text{m}$) as close as possible. However, Fig. 6.9 does correctly reflect the shapes and the mutual positions of the gain and the reflectivity spectra. Different Bragg wavelengths for the two simulated devices explain the shift of the mirror losses spectra in Fig. 6.9 with respect to each other (the spectra have different gain peak wavelengths).

The material gain spectra are directly calculated in PICS3D at the lasing threshold. The mirror losses $a_m(\lambda)$ were calculated separately using equation (6.1) and the parameters of the simulated device. Although the gain is clamped at the threshold carrier density N_{th} , this density is different for devices with different $R_g(\Delta\lambda)$. We first simulated both devices with no current injection into the phase and the DBR passive sections and have found that the corresponding threshold carrier densities were $N_{th}^{(1)}=1\times 10^{18} \text{ cm}^{-3}$ and $N_{th}^{(2)}=1.35\times 10^{18} \text{ cm}^{-3}$ for TLDs with $\kappa L=5.4$ and $\kappa L=1.48$, respectively.

These densities are then used in PICS3D to calculate the material gain spectra. The net gain spectra which are shown in Fig. 6.9 were calculated using the best estimates for the optical confinement factors. As is seen, the achieved gain - mirror losses balance is very good. The gain spectra are quite flat near the peak wavelengths $\lambda_{p1}=1.535 \mu\text{m}$ and $\lambda_{p2}=1.515 \mu\text{m}$.

As is seen from Fig. 6.9, even for the TLD with the flat $R_g(\Delta\lambda)$ spectrum ($\kappa L=5.4$) there is a strong asymmetry in the cavity mode selectivity. The neighboring cavity modes

within the reflection bandwidth which are located on the red side with respect to the lasing wavelength λ_0 will have larger difference between the mirror losses and the net gain, while the opposite is true for the comb modes on the blue side of the range with respect to λ_0 . Thus, the neighboring cavity modes which are red-shifted with respect to λ_0 will have larger SMSR compared with the blue-shifted modes. For the first device (black curves) the lasing condition is satisfied only for a single comb mode located practically at the very edge of the blue side of the reflectivity bandwidth. Inspection of the lasing spectrum at the beginning of the tuning shows that the SMSR is well above 30 dB for the nearest side mode in this device.

This asymmetry of the SMSR becomes even more important when the TLD is tuned, since actually not more than half of the comb modes within the $\Delta\lambda_{R_g}$ bandwidth will compete with each other and the mode selection is still possible. However, as the tuning becomes deeper, the tuned lasing wavelength approaches the region near the peak gain wavelength λ_p where both the gain and the mirror loss spectra are flat. The above asymmetry becomes weaker and thus more modes are now equally competing with the lasing mode. This makes the mode selection and further tuning more difficult.

The presented analysis of the tuning operation is in a qualitative and quantitative agreement with the results shown in Fig. 6.2 where the device with many cavity modes within the DBR reflectivity bandwidth is still tuning well at the beginning over the range of $\Delta\lambda \approx 10$ nm. As the lasing wavelength approaches the peak gain wavelength, the tuning saturates and the TLD enters the multimode lasing regime.

The tuning performance is very different in the second device ($\kappa L = 1.48$). Here the reflectivity spectrum has a sharp peak (no flat region) and the mirror losses increase rapidly away from the peak wavelength. Inspection of the lasing spectra (not presented

here) shows that the SMSR of the nearest mode is above 40 dB at the beginning of the tuning. As a result, the single mode selection in this device is considerably better. Another useful contribution to the improvement of the tuning stems from the blue shift of the material peak gain wavelength due to higher threshold carrier density. This considerably increases the tuning range as is shown in Fig. 6.7. Since even at the bias $V_{DBR}=1.5$ V the (tuned) lasing wavelength $\lambda=1.533$ μm is still considerably further away from the flat part of the gain spectrum (red curve in Fig. 6.9), the tuning does not saturate in this device.

We now investigate whether the tuning can be improved by reducing the reflectivity bandwidth $\Delta\lambda_{R_g}$. We again compare two devices which have almost the same peak reflectivities ($R_{peak} \approx 1$ and $R_{peak} \approx 0.8$) as before, but the reflectivity bandwidth is decreased twice to $\Delta\lambda_{R_g} = 2$ nm. The corresponding reflectivity spectra are shown in Fig. 6.10.

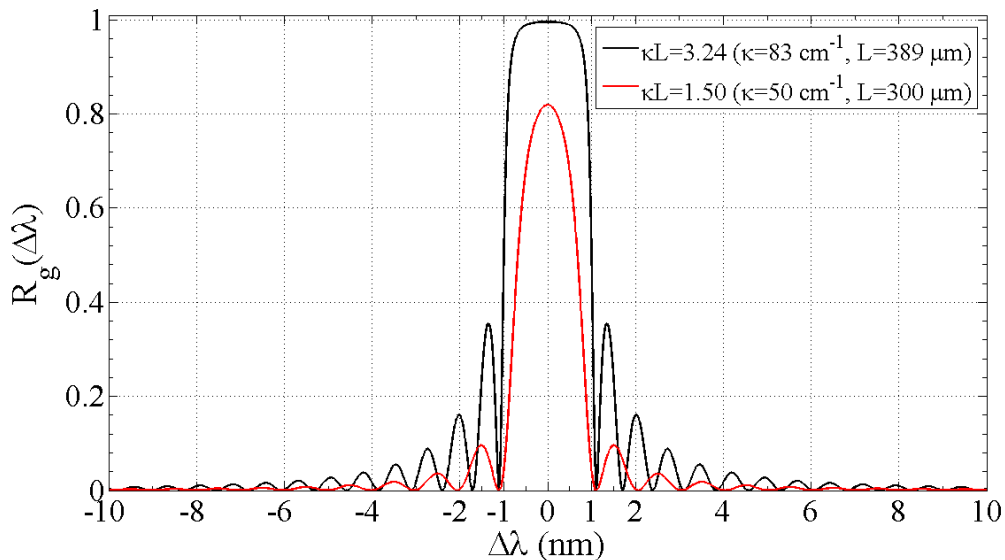


Fig. 6.10: DBR reflectivity spectra of two TLDS with $\Delta\lambda_{R_g} = 2$ nm.

The first device has the following DBR parameters: grating consists of $\text{In}_{0.84}\text{Ga}_{0.16}\text{As}_{0.36}\text{P}_{0.64}$ and $\text{In}_{0.89}\text{Ga}_{0.11}\text{As}_{0.24}\text{P}_{0.76}$ materials, $\Delta n'_g = 0.0389$, $\kappa = 83 \text{ cm}^{-1}$, $L = 389 \text{ }\mu\text{m}$, $\kappa L = 3.24$ (black curve in Fig. 6.10). In the second device the grating consists of $\text{In}_{0.85}\text{Ga}_{0.15}\text{As}_{0.34}\text{P}_{0.66}$ and $\text{In}_{0.88}\text{Ga}_{0.12}\text{As}_{0.26}\text{P}_{0.74}$ materials, $\Delta n'_g = 0.0253$, $\kappa = 50 \text{ cm}^{-1}$, $L = 300 \text{ }\mu\text{m}$, $\kappa L = 1.5$ (red curve in Fig. 6.10). The tuning performance of these TLDs is shown in Fig. 6.11 and 6.12, respectively. As is seen, the tuning range of the first device is increased from 10 nm to 17 nm due to better mode selectivity in the DBR with the narrower reflectivity bandwidth. The tuning range of the second device remains almost the same (17 nm) as in Fig. 6.7. Here the effect of the sharp reflectivity peak dominates the wavelength selection.

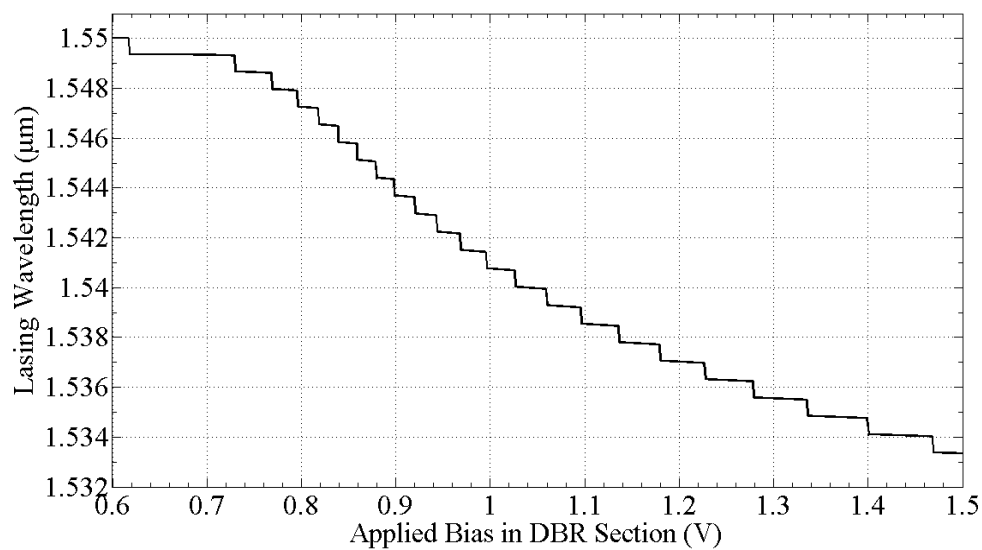


Fig. 6.11: DBR wavelength tuning in a TLD with $\kappa = 83 \text{ cm}^{-1}$ and $L = 389 \text{ }\mu\text{m}$.

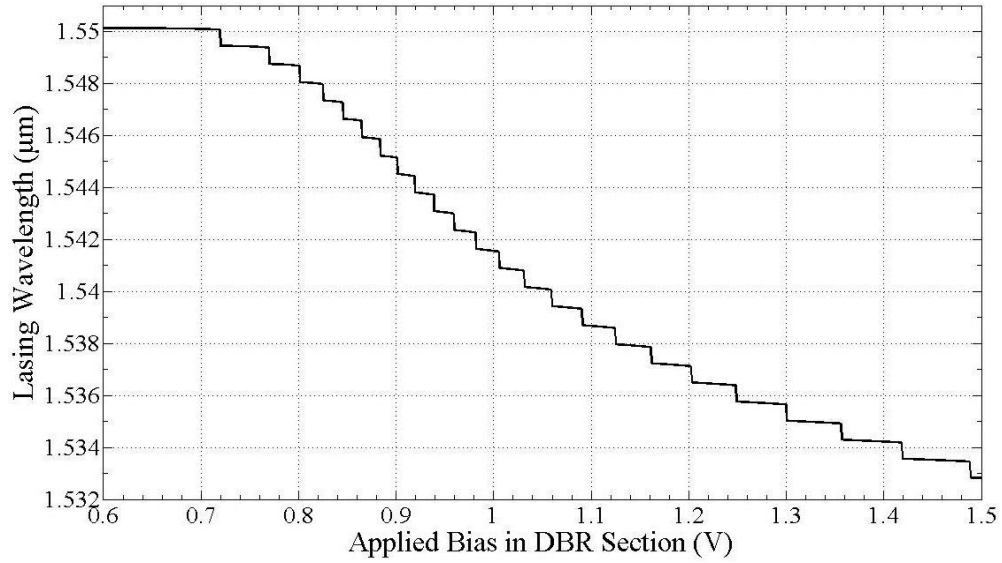


Fig. 6.12: DBR wavelength tuning in a TLD with $\kappa=50 \text{ cm}^{-1}$ and $L=300 \text{ }\mu\text{m}$.

It is obvious from the above analysis that the largest tuning range was achieved in the devices with smaller κL product ($\kappa L \approx 1.5$). This is because the reflectivity spectrum in this case is characterised by a sharp peak which improves the SMSR and allows to avoid the tuning saturation effect.

6.2.2 TLD passive section limitations on high carrier densities and electronic properties of the Bragg grating in discontinuous tuning

In this section we demonstrate that in the relatively optimised setup, a discontinuous tuning range of $\Delta\lambda_{discont} = 30 \text{ nm}$ can be achieved. This value is close to the record 22 nm continuous tuning obtained in the experimental work [84]. However, it is necessary to point out that in our device the 30 nm tuning is due to the forward current injection only, while in [84] the forward injection provides only 4 nm tuning (due to the FC plasma effect). A further 18 nm wavelength shift was due to the thermal tuning by

reverse biasing the Bragg section which results in a “soft breakdown” of the diode and efficient heating of the waveguide.

We start by investigating the case of extreme tuning in the device shown in Fig. 6.12 (grating consists of $\text{In}_{0.85}\text{Ga}_{0.15}\text{As}_{0.34}\text{P}_{0.66}$ and $\text{In}_{0.88}\text{Ga}_{0.12}\text{As}_{0.26}\text{P}_{0.74}$ materials, $\Delta n'_g = 0.0253$, $\kappa = 50 \text{ cm}^{-1}$, $L = 300 \text{ }\mu\text{m}$, $\kappa L = 1.5$, red curve in Fig. 6.10). In all the simulated TLDs in this section, during the DBR section tuning the AR operates at a fixed injection current $I_a = 15 \text{ mA}$ which provided the output power between 4.5 mW and 4.6 mW in the simulated TLDs.

The DBR section was designed to accommodate very high carrier densities. In practice the maximum carrier density in the passive sections is limited by four factors: (a) carrier leakage from the WG region into the adjacent layers (this mainly takes place for the electrons due to higher position of the electron quasi-Fermi level because of smaller electron density of states in comparison with the holes); (b) possibility of lasing in the passive section at high injection; (c) increased optical losses; (d) device overheating. Since Joule’s heating is not included in the current model, we have investigated the limitations (a), (b), (c) only.

Case (a) can be prevented by the extra potential barrier on the p-side of the central WG region. For simplicity, in order to investigate the high carrier density case, we have increased the conduction band discontinuity in the DBR section to $\Delta E_c = 0.8\Delta E_g = 0.4 \text{ eV}$. In all previous simulated devices we used $\Delta E_c = 0.4\Delta E_g = 0.2 \text{ eV}$, which is a typical value for InP/InGaAsP heterobarriers. The leakage current in all our devices was below 3% even at very high injection levels. By making this optimisation, we were able to bias the DBR section with a voltage as high as $V_{DBR} = 3.5 \text{ V}$ which corresponds to the injection current of $I_{DBR} \approx 700 \text{ mA}$ as is shown in the I-V characteristic in Fig. 6.13. This also gives

a carrier density value in the WG region of the DBR section of $N = 6.31 \times 10^{18} \text{ cm}^{-3}$. Most of the applied bias drop ($\sim 2.1 \text{ V}$) was in the p-InP region due to low hole mobilities. Another interesting observation is that at high currents in the passive DBR section, the electron injection is mainly controlled by the thermionic emission. This follows from a very large electron quasi-Fermi level discontinuity ($\Delta E_{Fn} \approx 0.2 \text{ eV}$), which is seen from the band profile inspection in Fig. 6.14.

The tuning curve of the TLD is shown in Fig. 6.15, and the 3D wave intensity distribution in the cavity is shown in Fig. 6.16. As one can see, the tuning range of $\Delta\lambda = 26 \text{ nm}$ at $V_{DBR} = 3.5 \text{ V}$ was achieved without any sign of saturation. Although the $I_{DBR} \approx 700 \text{ mA}$ current is too high, it is only the last few tuning steps which are mainly contributing to this value. If we restrict the tuning range to $\Delta\lambda = 22 \text{ nm}$ at $V_{DBR} = 2.4 \text{ V}$, the maximum required current is $I_{DBR} \approx 400 \text{ mA}$, which is a quite reasonable value.

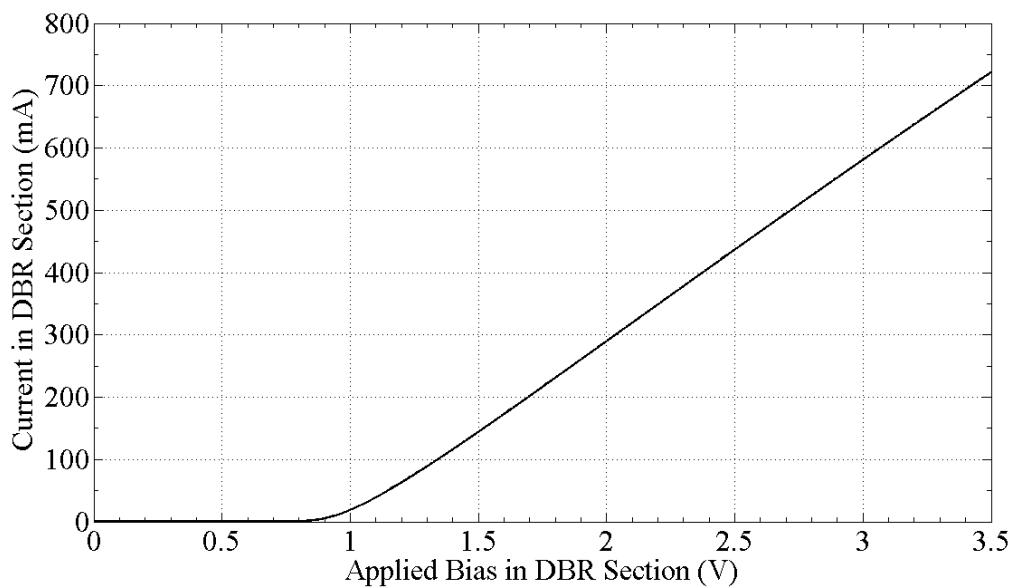


Fig. 6.13: I-V characteristic of the DBR section of the TLD with $\kappa = 50 \text{ cm}^{-1}$ and $L = 300 \text{ }\mu\text{m}$.

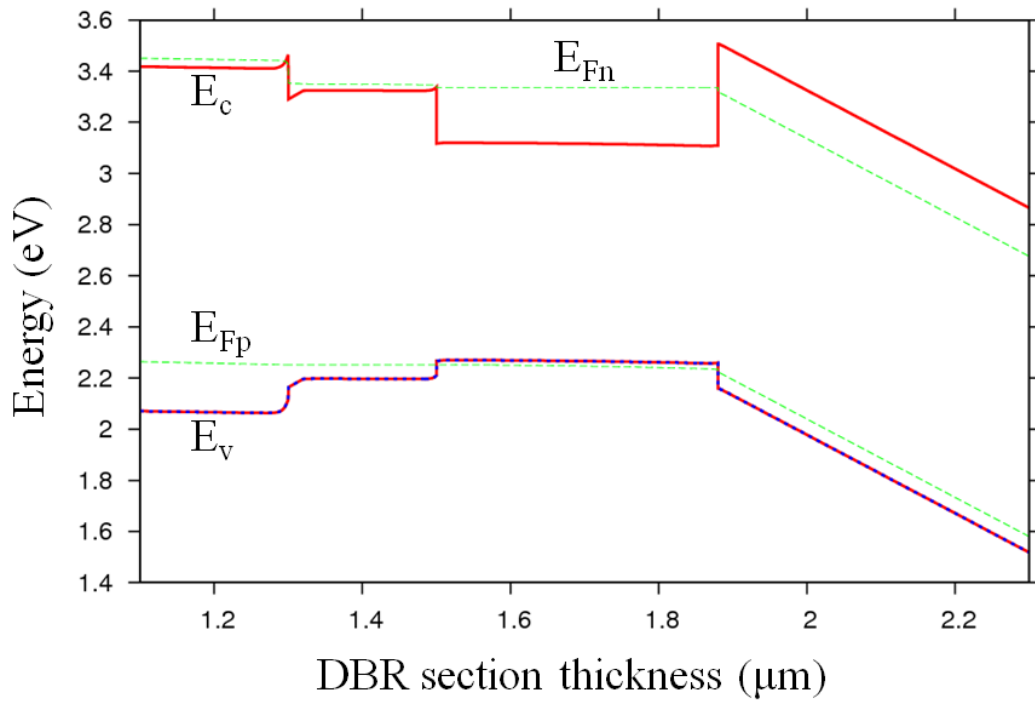


Fig. 6.14: Band structure profile of the DBR section of the TLD with $\kappa=50 \text{ cm}^{-1}$ and $L=300 \text{ }\mu\text{m}$ taken at bias $V_{DBR}=3.5 \text{ V}$.

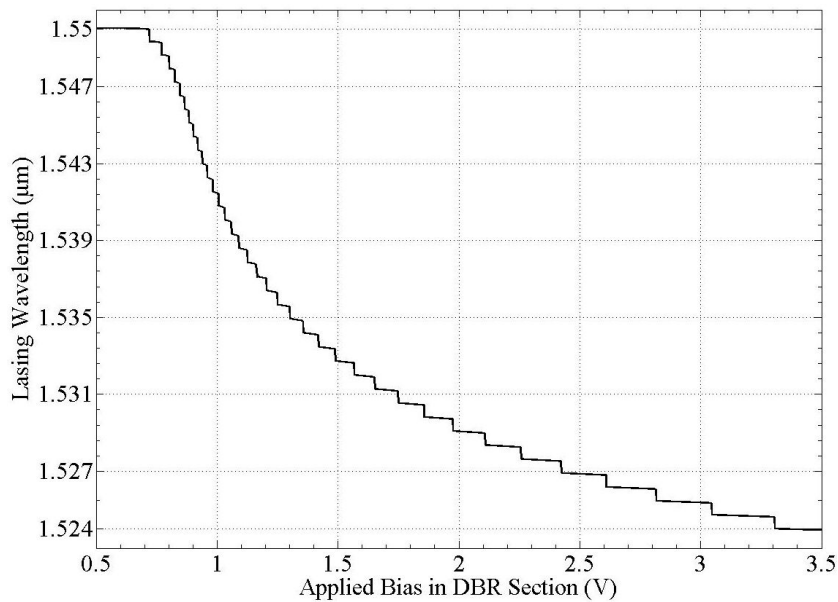


Fig. 6.15: DBR wavelength tuning performance of the TLD with $\kappa=50 \text{ cm}^{-1}$ and $L=300 \text{ }\mu\text{m}$ at high injection levels.

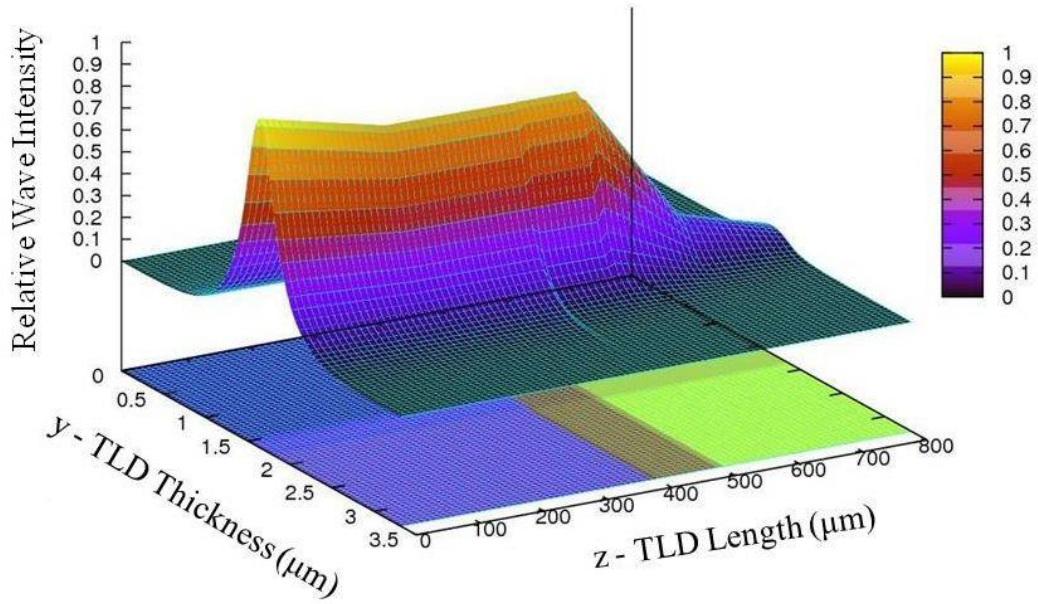


Fig. 6.16: 3D intensity distribution in the TLD with $\kappa=50 \text{ cm}^{-1}$ and $L=300 \text{ } \mu\text{m}$ at bias $V_{DBR}=1.5 \text{ V}$.

Case (b) is also not a problem even at extremely high carrier densities, provided that the external facet of the DBR section has antireflection coating and the λ_B wavelength is at least 10 nm away from the bandgap wavelength λ_{gp} of the passive section (in our devices $\lambda_B \approx 1.55 \text{ } \mu\text{m}$ and $\lambda_{gp} \approx 1.46 \text{ } \mu\text{m}$).

Case (c) requires special consideration. Since the FC tuning always blue-shifts the lasing mode λ_m , the deeper is tuning the closer is λ_m to λ_{gp} , and thus the higher optical losses are. This can be shown in Fig. 6.17, where the optical losses in the WG region of the passive sections are increasing with the tuning depth. On the other hand, in TLDs one cannot choose too big difference between the passive and the active region bandgaps, as this decreases the FC refractive index change $\Delta n'$ at the lasing wavelength, [130], [131], due to spectral dependence of $\Delta n'$.

We have discovered a very subtle effect which can counterbalance the optical losses with the tuning depth. The effect can be understood in Fig. 6.18 from inspection of the g_{net} and α_m spectra of the TLD described in case (a). As is seen, the FC tuning always moves the DBR reflectivity up the ascending gain spectrum curve. This in turn results in an increase of the gain of the next lasing mode ($dg/d\lambda > 0$). This would increase the lasing mode power if the losses remain the same. If the passive section optical losses also increase, the two effects may in principle counterbalance each other.

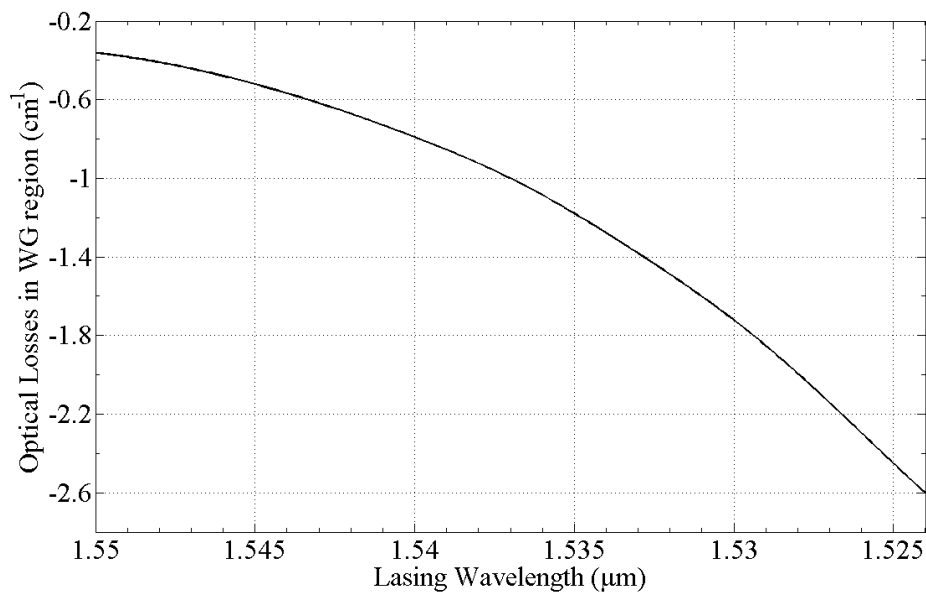


Fig. 6.17: Optical losses in the WG region of the passive sections at different lasing wavelengths for the TLD with $\kappa=50 \text{ cm}^{-1}$ and $L=300 \text{ }\mu\text{m}$.

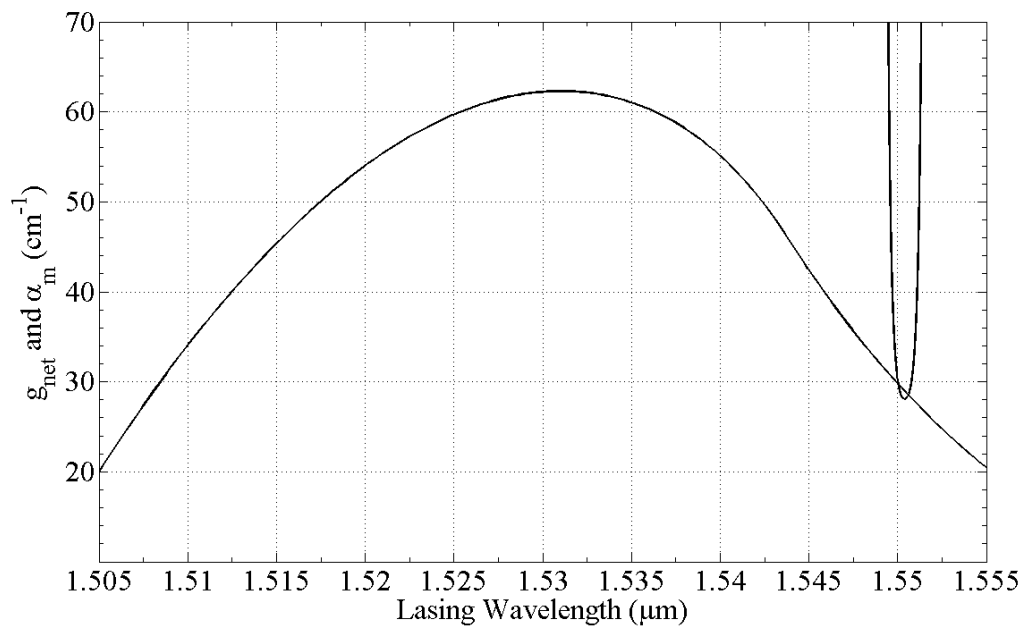


Fig. 6.18: Spectra of the net gain g_{net} and the cavity mirror losses a_m at the beginning of tuning (lasing wavelength $\lambda_0=1.55 \mu\text{m}$) for the TLD with $\kappa=50 \text{ cm}^{-1}$ and $L=300 \mu\text{m}$.

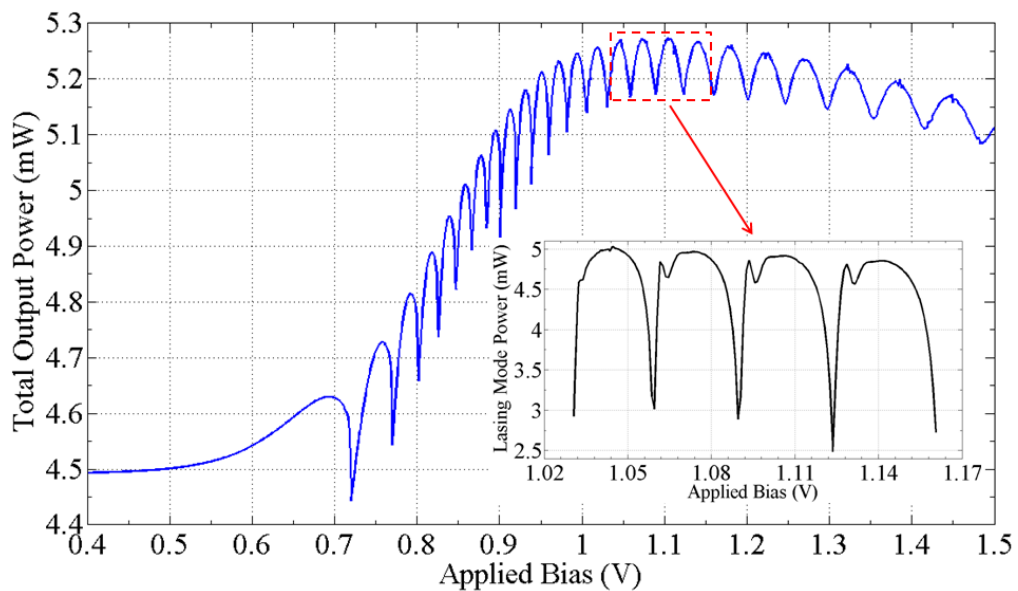


Fig. 6.19: The output power of the TLD as a function of the DBR section bias. The main curve shows the total power variation and the insertion shows the power variation for a few lasing modes. The TLD is the same as in Fig. 6.15.

Fig. 6.19 shows the power variation in the TLD with the DBR tuning. Initially, the power P increases from 4.5 mW to 5.27 mW due to the lasing mode gain increase, as was explained above. As the lasing modes are further blue-tuned, the optical losses increase, the gain variation $dg/d\lambda$ flattens, and the two effects compensate each other. For even deeper tuning, an increase in the optical losses in the passive section dominates, and the output power decreases from 5.27 mW to 5.1 mW.

For the above described case of extreme tuning (tuning range of $\Delta\lambda=22$ nm at $V_{DBR}=2.4$ V), the power continues to decrease with further wavelength blue-shift from 5.27 mW to 4.69 mW (with a power change ΔP of $\Delta P = 5.27 - 4.69 = 0.58$ mW) as is shown in Fig. 6.20. This means that the power decreases quite considerably by $\Delta P/P \approx 11\%$.

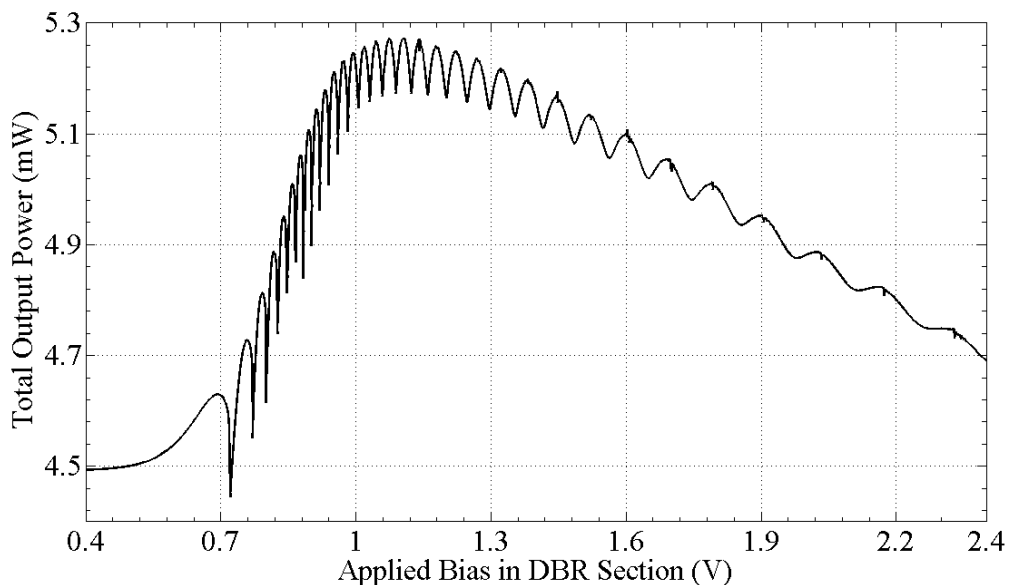


Fig. 6.20: The output power of the TLD with $\lambda_{gp}=1.46$ μm as a function of the DBR section bias.

Another proof of the interaction between the lasing mode gain and the increasing optical losses with the tuning depth can be found by the inspection of the threshold

current of different lasing wavelengths of the tuning range ($\Delta\lambda=22$ nm) taken at different positions of g_{net} when the TLD is in CW operation.

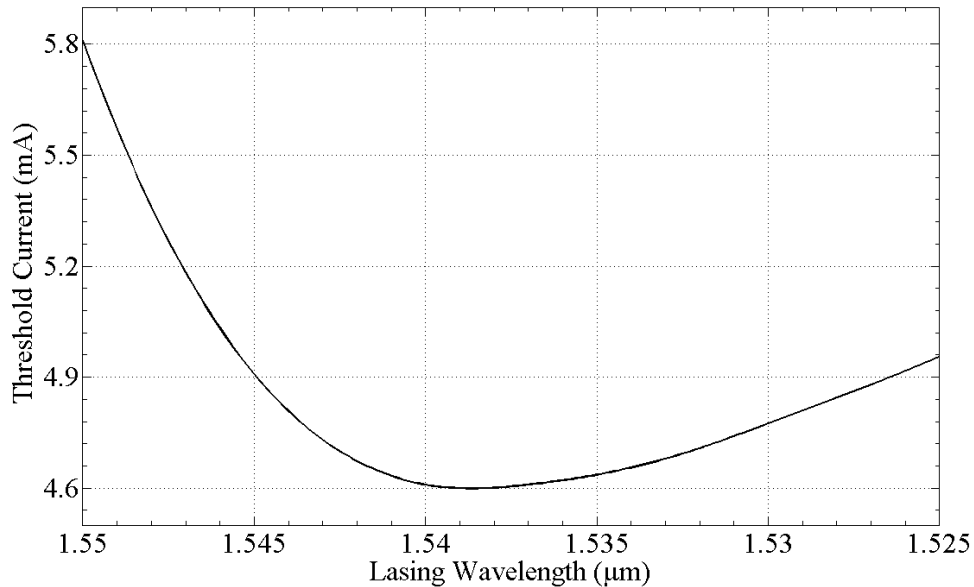


Fig. 6.21: Threshold current of different lasing wavelengths of the $\Delta\lambda=22$ nm tuning range for the TLD with $\kappa=50$ cm⁻¹ and $L=300$ μm.

As is shown in Fig. 6.21, the threshold current decreases from 5.8 mA to 4.6 mA for a range of wavelengths from $\lambda_0=1.55$ μm until $\lambda=1.539$ μm, as the lasing mode gain increase dominates the optical losses increase (less current needed to achieve lasing conditions). It then reaches its minimum value of 4.6 mA at $\lambda=1.539$ μm, when the gain variation $dg/d\lambda$ flattens and the two effects compensate each other. At longer wavelengths, the threshold current starts increasing again from 4.6 mA to 4.96 mA until the last $\lambda=1.525$ μm of the tuning range, as the increase in the optical losses in the passive section dominates (more current needed to achieve lasing conditions).

One way to resolve this problem is by selecting a λ_{gp} to be far enough away from λ_m so that the optical losses are neglectable during extreme tuning and the power can

stabilise. To illustrate this effect, two TLDs were designed with $\lambda_{gp}=1.4 \mu\text{m}$ and $\lambda_{gp}=1.3 \mu\text{m}$, respectively. The power variation in the TLDs with the extreme DBR tuning is shown in Fig. 6.22 and Fig. 6.23, respectively. The rest of the design parameters were kept the same as the TLD in Fig. 6.19. As can now be observed in Fig. 6.22, the power drop with the wavelength blue-shift has improved considerably for $\lambda_{gp}=1.4 \mu\text{m}$ (from 5.35 mW to 5.1 mW only, with $\Delta P/P \approx 4.7\%$). However, the distance of λ_{gp} from λ_m during extreme tuning was not enough to eliminate the effect. This was done in the latter case of $\lambda_{gp}=1.3 \mu\text{m}$, where the power has now stabilised around 5.4 mW with the wavelength blue-shift, as is shown in Fig. 6.23.

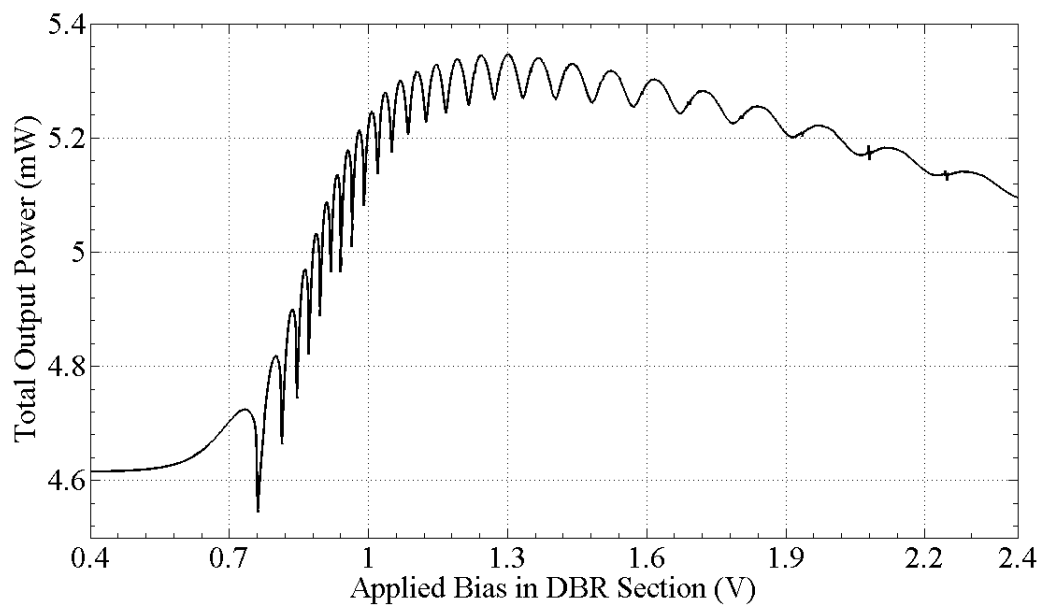


Fig. 6.22: The output power of the TLD with $\lambda_{gp}=1.4 \mu\text{m}$ as a function of the DBR section bias.

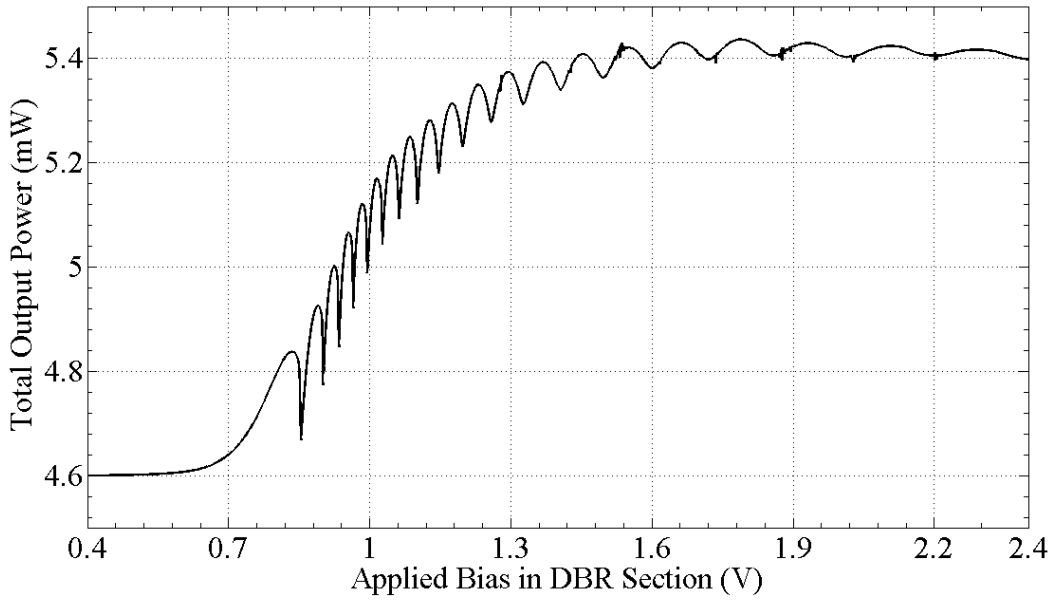


Fig. 6.23: The output power of the TLD with $\lambda_{gp}=1.3 \mu\text{m}$ as a function of the DBR section bias.

Unfortunately, as was mentioned above, the drawback for using WG bandgap wavelengths well away from the AR bandgap wavelength is that it reduces the available $\Delta n'$ range, which in turn reduces the $\Delta\lambda$ range. It was indeed found that $\Delta n' \approx -0.078$ and $\Delta\lambda \approx 22 \text{ nm}$ for the TLD with $\lambda_{gp}=1.46 \mu\text{m}$, $\Delta n' \approx -0.065$ and $\Delta\lambda \approx 18 \text{ nm}$ for the TLD with $\lambda_{gp}=1.4 \mu\text{m}$, and $\Delta n' \approx -0.055$ and $\Delta\lambda \approx 14 \text{ nm}$ for the TLD with $\lambda_{gp}=1.3 \mu\text{m}$, for the same $V_{DBR}=2.4 \text{ V}$. Therefore, it is concluded that there is a trade-off between the maximum achievable wavelength tuning range and the smallest possible output lasing power decrease with the tuning depth in a TLD. It is important that the curves in Fig. 6.18 can be engineered by varying λ_{gp} and stabilising the power within the required tuning range, but the effect cannot be eliminated completely.

With the above insight into the passive section limitations, we have optimised the TLD design in order to further increase its tuning. This was achieved by improving the *electronic* properties of the Bragg grating. We keep the same value of $\kappa L=1.5$ as in the

TLD in Fig. 6.15, but change the material composition of the grating layers to: $\text{In}_{0.66}\text{Ga}_{0.34}\text{As}_{0.74}\text{P}_{0.26}$ and $\text{In}_{0.68}\text{Ga}_{0.32}\text{As}_{0.69}\text{P}_{0.31}$. Note that this requires very careful composition selection as $\Delta n'_g = 0.0253$ must remain the same. The simulated TLD was biased up to a maximum value of $V_{DBR}=3.5$ V as in the previous case of Fig. 6.15. The tuning curve of the TLD is shown in Fig. 6.24.

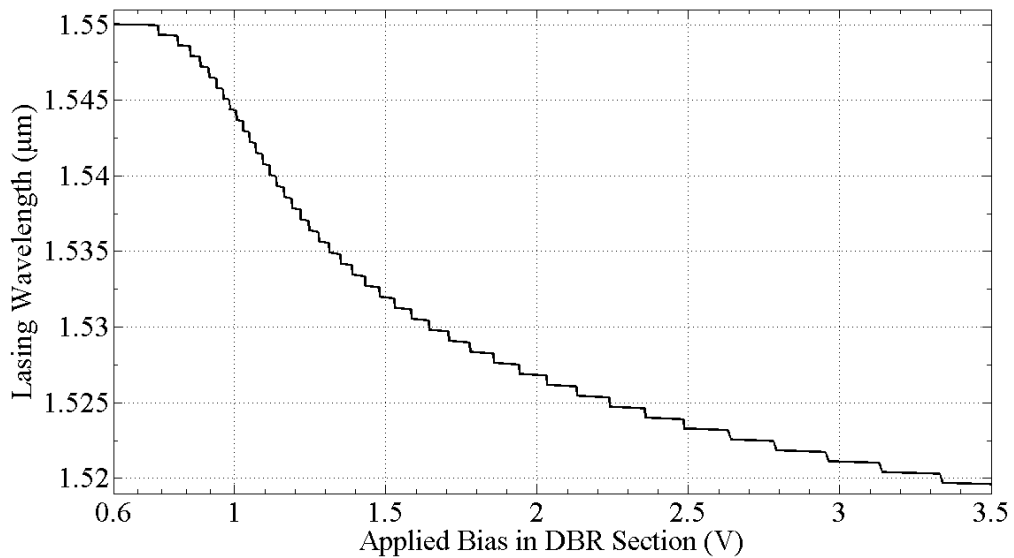


Fig. 6.24: DBR wavelength tuning performance of the optimised TLD with $\kappa=50$ cm^{-1} and $L=300$ μm at high injection levels.

As can one see, the tuning range of $\Delta\lambda=30$ nm was achieved this time with this optimisation, which is 4 nm bigger than that of Fig. 6.15. If we restrict the applied bias to a reasonable value of $V_{DBR}=2.4$ V ($I_{DBR}\approx 400$ mA), we also get quite a high tuning range of $\Delta\lambda=26$ nm, which is also 4 nm bigger than that of Fig. 6.15 for the same DBR bias. It is impressive that the optimised TLD needs only around 50% of the injected current required for the TLD in Fig. 6.15 ($I_{DBR}\approx 700$ mA) in order to achieve the same tuning range of $\Delta\lambda=26$ nm.

The main physical reason for such large improvement of $\Delta\lambda$ in comparison with Fig. 6.15, is the increased transverse overlap between the optical wave and the injected carriers. The effective bandgap of the grating in the TLD in Fig. 6.14 was $E_{g,\text{eff}}\approx 1.12$ eV, and for the optimised TLD $E_{g,\text{eff}}\approx 0.86$ eV (shown in Fig. 6.25) due to different grating material compositions. As a result, the injected FC density in the grating region of the optimised TLD is about an order of magnitude higher. Taking into account that the grating thickness ($0.2\ \mu\text{m}$) is comparable to the WG thickness ($0.38\ \mu\text{m}$), this means that the propagating mode in the optimised TLD has considerably better overlap with the region of the FC refractive index change. The latter effect is responsible for the tuning range increase.

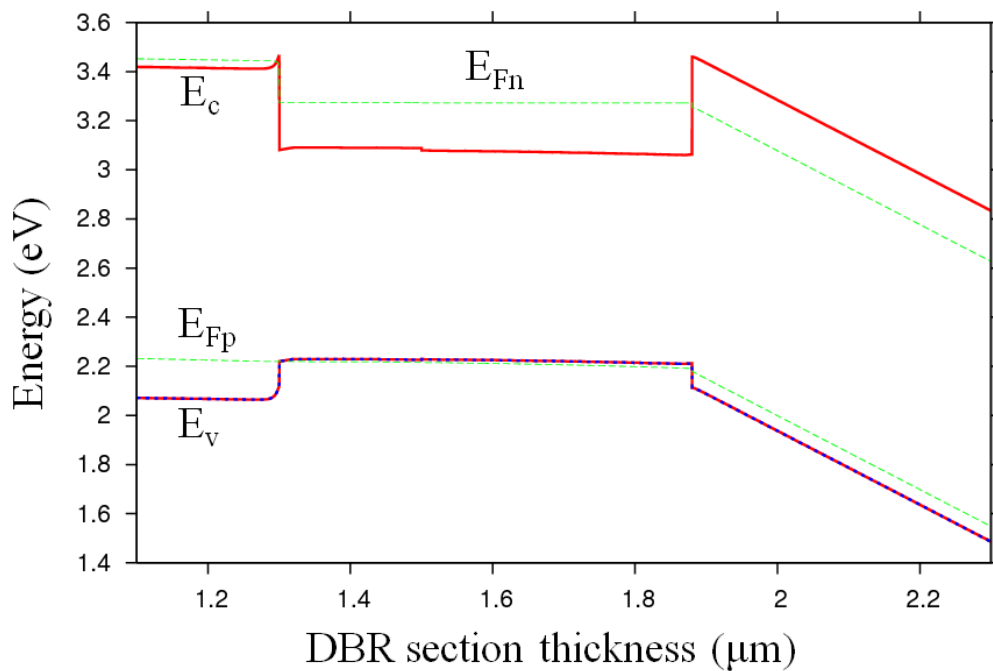


Fig. 6.25: Band structure profile of the DBR section of the optimised TLD with $E_{g,\text{eff}}\approx 0.86$ eV taken at bias $V_{\text{DBR}}=3.5$ V.

It is interesting to note that this effect does not necessarily lead to a bigger $\Delta n'$ or N in the WG region of the optimised TLD for the same $V_{\text{DBR}}=3.5$ V. It was found that

$\Delta n' \approx -0.082$ and $N = 5.43 \times 10^{18} \text{ cm}^{-3}$ for the optimised TLD, while for the TLD in Fig. 6.15 they were $\Delta n' \approx -0.091$ and $N = 6.31 \times 10^{18} \text{ cm}^{-3}$, for the same $V_{DBR} = 3.5 \text{ V}$. This is also visible by a careful observation of the DBR band structure of the optimised TLD, where the quasi-Fermi level E_{Fn} has a slightly smaller energy value than the E_{Fn} in Fig. 6.14.

A possible explanation of this result would be that the grating region in the optimised TLD is now treated as an “effective” WG region with $N \approx 5 \times 10^{18} \text{ cm}^{-3}$ as is seen in Fig. 6.14. This means that the amount of injected carriers in the DBR section will now be distributed homogenously in a wider area, the WG region ($d_{DBR} = 0.38 \text{ }\mu\text{m}$) and the grating region ($d_g = 0.28 \text{ }\mu\text{m}$) in a total area of $0.58 \text{ }\mu\text{m}$. Therefore, there will be fewer carriers for the same amount of injected current ($I_{DBR} \approx 700 \text{ mA}$). In the TLD in Fig. 6.14, most of the injected carriers were distributed in the WG region ($N = 6.31 \times 10^{18} \text{ cm}^{-3}$), leaving the grating region with a carrier density of only $N \approx 1 \times 10^{17} \text{ cm}^{-3}$.

Our grating design is different from usual designs in which the grating consists of InP and the WG quaternary, and thus have the same problem of poor overlap between the lasing mode and the FC index change, as our TLD in Fig. 6.15. The drawback of our optimised design is that it is more difficult to fabricate, but it is capable to considerably increase $\Delta\lambda$.

6.2.3 Effect of design parameters of the phase section on the continuous and quasi-continuous tuning performance

In this section we investigate the effect of different design parameters of the TLD phase section, such as the thickness d_p of the WG region and the section length L_p , on the

continuous and quasi-continuous tuning behaviour. We report a continuous range of $\Delta\lambda_{cont} = 10$ nm and a quasi-continuous range of $\Delta\lambda_{quasicont} = 26$ nm in the optimised design.

The TLD that is used here is the same as the one described in section 6.2.2 and shown in Fig. 6.24 with the following parameters: grating consists of $\text{In}_{0.66}\text{Ga}_{0.34}\text{As}_{0.74}\text{P}_{0.26}$ and $\text{In}_{0.68}\text{Ga}_{0.32}\text{As}_{0.69}\text{P}_{0.31}$ materials, $\Delta n'_g = 0.0253$, $\kappa = 50 \text{ cm}^{-1}$, $L = 300 \text{ }\mu\text{m}$, $\kappa L = 1.5$, $d_p = 0.38 \text{ }\mu\text{m}$, $L_p = 100 \text{ }\mu\text{m}$. The AR is driven at a constant current of $I_a = 15 \text{ mA}$ during tuning. At first, the tuning behaviour of the phase section is investigated, so the DBR section remains inactive with $V_{DBR} = 0 \text{ V}$. The phase section is driven at a maximum bias of $V_p = 2.5 \text{ V}$, which gives an injection current of $I_p \approx 143 \text{ mA}$ and its tuning behaviour is shown in Fig. 6.26.

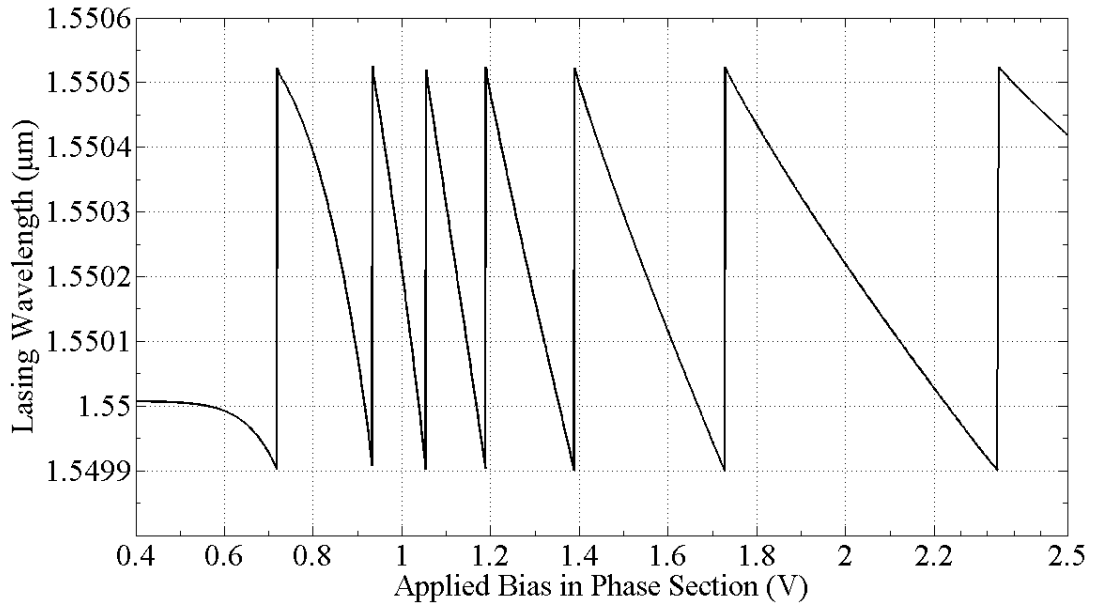


Fig. 6.26: Phase wavelength tuning performance of the TLD with $d_p = 0.38 \text{ }\mu\text{m}$ and $L_p = 100 \text{ }\mu\text{m}$.

As can be seen in Fig. 6.26, there are 6 continuous tuning ranges which cover the whole inter-mode distance of $\Delta\lambda_m \approx 0.6$ nm until the last bias value of $V_p=2.5$ V. This means that a continuous range of at least $6 \times 0.6 = 3.6$ nm can be achieved with this TLD, which is rather small.

In order to improve the continuous range of the TLD, we take into consideration the observations made in section 6.2.2 for the improvement of the DBR wavelength tuning range. As was discussed there, the selection of a grating effective bandgap close to the WG bandgap led to a wider region of injected carriers (grating + WG region). This, in turn, increased the transverse overlap between the optical wave and the injected carriers in this region and improved the discontinuous tuning range.

For this reason, we increased the thickness of the WG region of the phase section to $d_p=0.58$ μm . This led to an increase of the transverse optical confinement factor of the phase section $\Gamma_{p,xy}$ from $\Gamma_{p,xy}=0.654$ in the TLD in Fig. 6.26 to $\Gamma_{p,xy}=0.822$ in the new TLD. All the other design parameters of the TLD remained the same as the one in Fig. 6.26. The tuning behaviour of the phase section of the TLD for the same $V_p=2.5$ V is shown in Fig. 6.27.

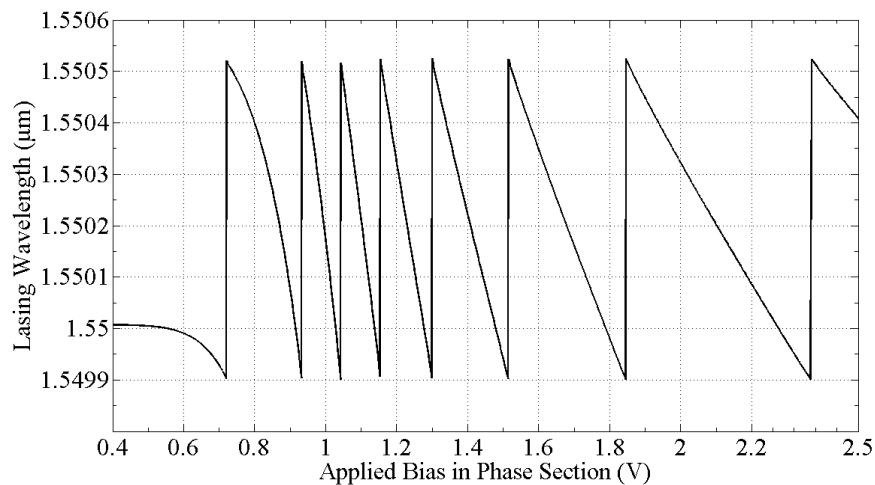


Fig. 6.27: Phase wavelength tuning performance of the TLD with $d_p=0.58$ μm and $L_p=100$ μm .

As can be seen now in Fig. 6.27, the number of continuous tuning ranges (wavelength changes) has increased from 6 to 7 compared with Fig. 6.26, which means that a continuous range of at least $7 \times 0.6 = 4.2$ nm can be achieved with this TLD. Another proof of the increased optical overlap in the WG region of the TLD with $d_p=0.58$ μm compared with the one with $d_p=0.38$ μm can be observed in Fig. 6.28 and Fig. 6.29, respectively. In these figures, the spatial wave intensity distribution of the phase section is plotted in the direction of section thickness.

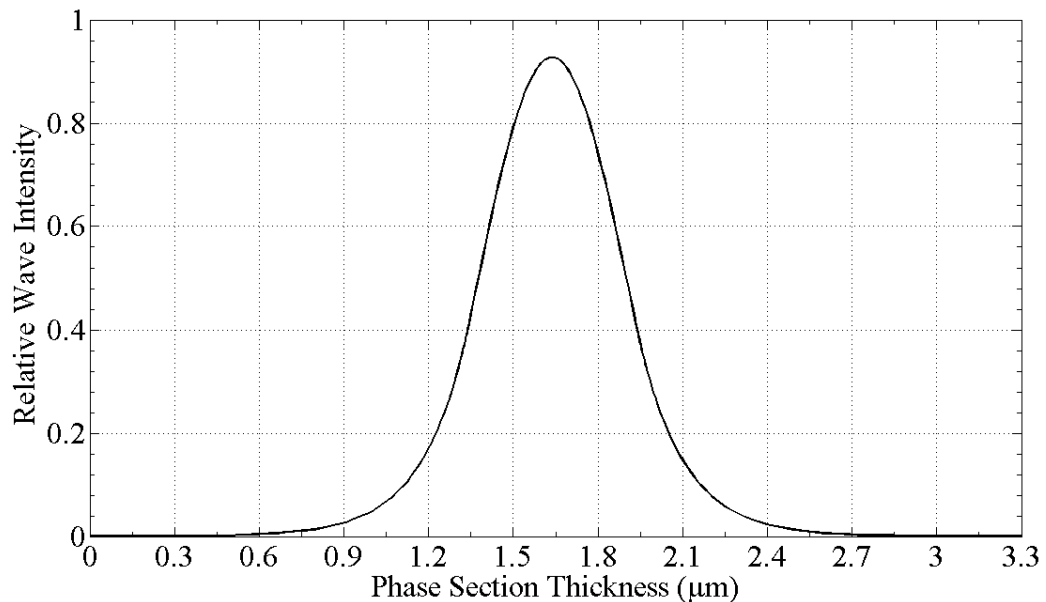


Fig. 6.28: Wave intensity distribution in the TLD with $d_p=0.58$ μm and $L_p=100$ μm at bias $V_p=2.5$ V.

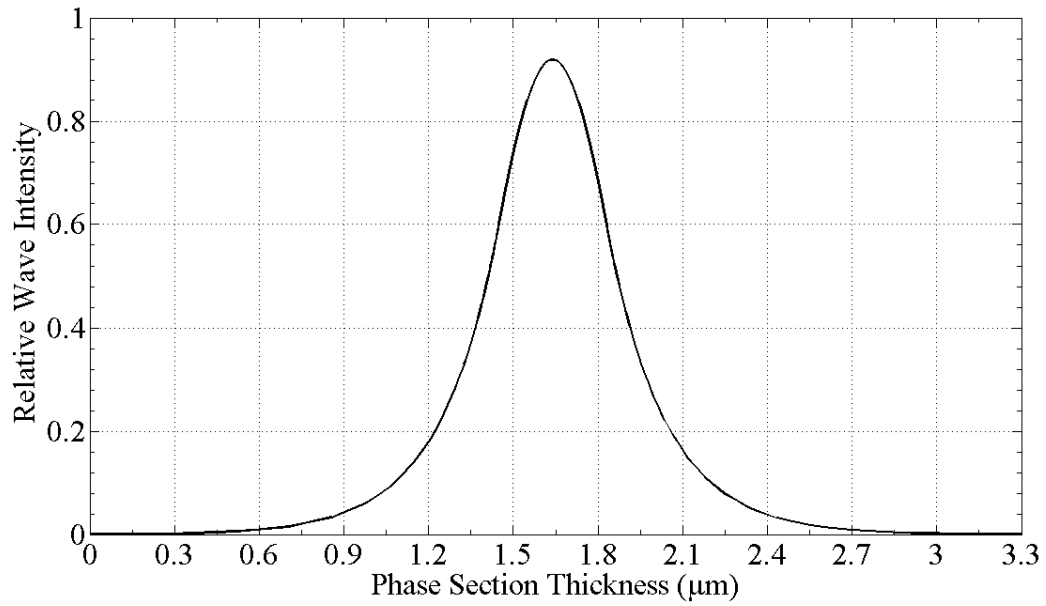


Fig. 6.29: Wave intensity distribution in the TLD with $d_p=0.38 \mu\text{m}$ and $L_p=100 \mu\text{m}$ at bias $V_p=2.5 \text{ V}$.

Again, it was found that this effect does not lead to a bigger $\Delta n'$ or N in the WG region of the TLD with $d_p=0.58 \mu\text{m}$ for the same $V_p=2.5 \text{ V}$. The values for the TLD with $d_p=0.58 \mu\text{m}$ were $\Delta n' \approx -0.07$ and $N = 4.27 \times 10^{18} \text{ cm}^{-3}$, while for the TLD with $d_p=0.38 \mu\text{m}$ they were $\Delta n' \approx -0.078$ and $N = 5 \times 10^{18} \text{ cm}^{-3}$, for the same $V_p=2.5 \text{ V}$.

Further investigations showed that the continuous range of 4.2 nm can be improved considerably by increasing the phase section length. The thickness of the WG region was kept the same at $d_p=0.58 \mu\text{m}$ and the phase section length is now given a value of $L_p=300 \mu\text{m}$. With this modification, for the same number of continuous tuning ranges (7), the required refractive index change and carrier density in the WG region of the phase section has decreased considerably at $\Delta n' \approx -0.023$ and $N = 1 \times 10^{18} \text{ cm}^{-3}$, respectively. The required value of applied bias has also decreased at $V_p=1.08 \text{ V}$ which corresponds to a value of injected current of $I_p \approx 17 \text{ mA}$.

This means that for the same values of N , $\Delta n'$ and V_p as in the TLD with $d_p=0.58$ μm , $L_p=100$ μm , the number of accessible continuous tuning ranges will inevitably increase. The corresponding injection current for $V_p=2.5$ V was measured to be $I_p \approx 430$ mA, which is within reasonable limits as was also stated for $I_{DBR} \approx 400$ mA during extreme DBR tuning in section 6.2.2. The tuning behaviour of the phase section of the TLD for the same $V_p=2.5$ V is shown in Fig. 6.30.

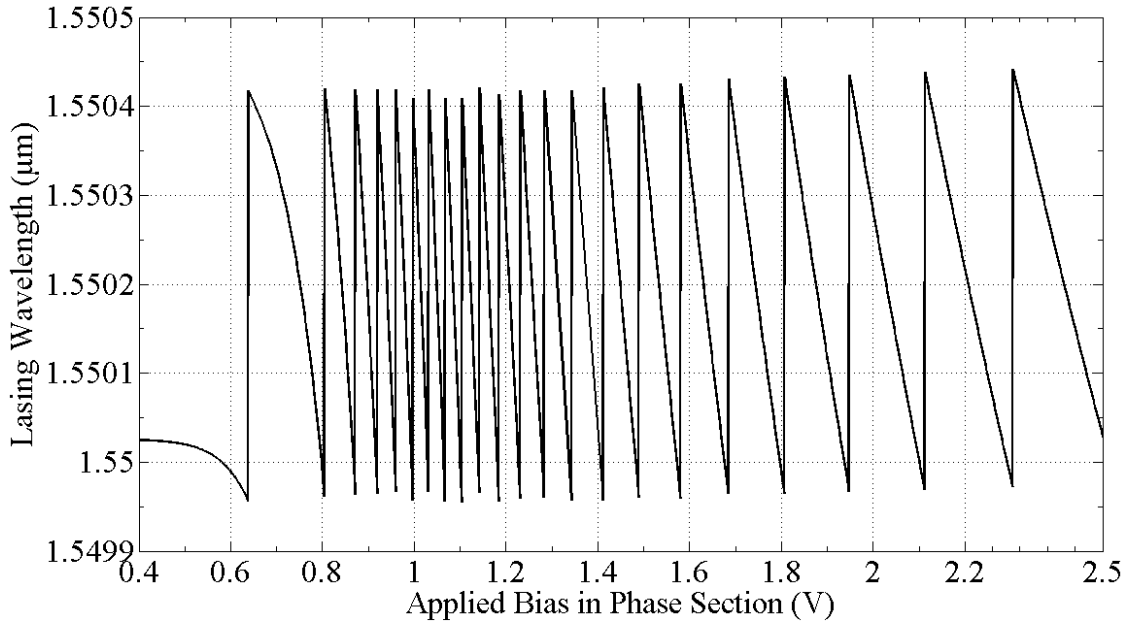


Fig. 6.30: Phase wavelength tuning performance of the TLD with $d_p=0.58$ μm and $L_p=300$ μm .

As can be observed in Fig. 6.30, the number of continuous tuning ranges has now increased considerably from 7 to 22 compared with Fig. 6.27. The main reason for this increase is that there is better longitudinal confinement of the optical wave across the TLD in Fig. 6.30. This can also be proved by calculating the longitudinal optical confinement factor $\Gamma_{p,z}$ of the phase section of the two devices in Fig. 6.27 and 6.30. Taking

into account that $\Gamma_{p,z} = \frac{L_p}{L_{tot}}$, where L_{tot} is the total TLD length, it was found that $\Gamma_{p,z}$ has

increased from $\Gamma_{p,z}=0.125$ ($L_p=100 \mu\text{m}$, $L_{tot}=800 \mu\text{m}$, Fig. 6.27) to $\Gamma_{p,z}=0.3$ ($L_p=300 \mu\text{m}$, $L_{tot}=1000 \mu\text{m}$, Fig. 6.30). It should also be noted that the increase of the cavity length of the TLD in Fig. 6.30, led to a smaller inter-mode distance of $\Delta\lambda_m \approx 0.47 \text{ nm}$ (also seen in Fig. 6.30). This means that a continuous range of at least $22 \times 0.47 \approx 10.34 \text{ nm}$ can be achieved with this TLD.

The achieved continuous tuning range was actually found to be $\Delta\lambda_{cont} \approx 11 \text{ nm}$ (from 1550-1539 nm) by simultaneous driving of the phase and DBR section of the TLD. It is shown in Fig. 6.31 as a function of V_p .

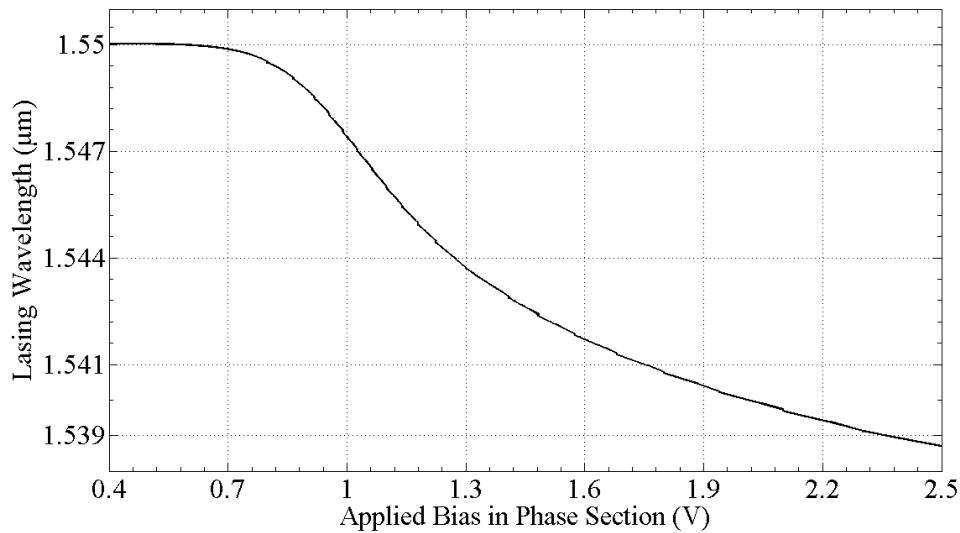


Fig. 6.31: Continuous wavelength tuning performance of the TLD with $d_p=0.58 \mu\text{m}$ and $L_p=300 \mu\text{m}$ for the $\Delta\lambda_{cont} = 1550\text{-}1539 \text{ nm}$ range.

It should also be mentioned that the range of wavelengths from $\lambda=1539 \text{ nm}$ to $\lambda=1524 \text{ nm}$ within the 26 nm discontinuous range, which was achieved in section 6.2.2, can also be accessed continuously. This can be done by splitting the 1539-1524 nm range into two 11 nm continuous tuning ranges, $\Delta\lambda_{cont} = 1539\text{-}1528 \text{ nm}$ and $\Delta\lambda_{cont} = 1535\text{-}1524 \text{ nm}$. The first $\Delta\lambda_{cont}$ range can be accessed by driving at first the DBR section, which blue

shifts λ until the value of $\lambda=1539$ nm is reached. Then by driving both passive sections all wavelengths until $\lambda=1528$ nm can be accessed continuously. The same can be done for wavelengths within the $\Delta\lambda_{cont} = 1535-1524$ nm range. The achieved ranges of $\Delta\lambda_{cont} = 1539-1528$ nm and $\Delta\lambda_{cont} = 1535-1524$ nm are shown in Fig. 6.32 and Fig. 6.33, respectively.

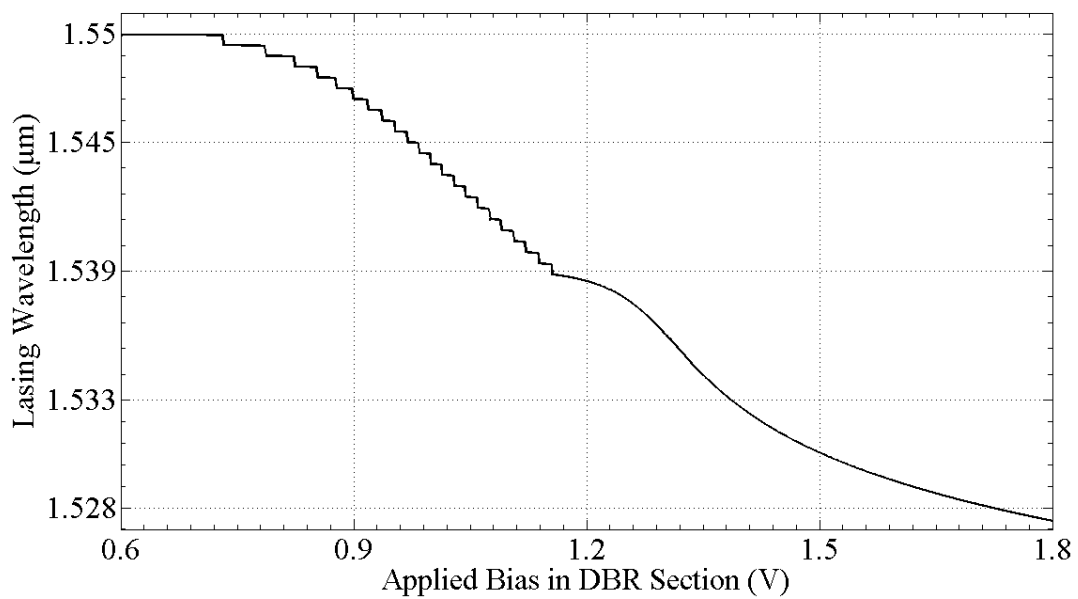


Fig. 6.32: Discontinuous and continuous wavelength tuning performance of the TLD with $d_p=0.58$ μm and $L_p=300$ μm for the $\Delta\lambda_{discont} = 1550-1539$ nm and $\Delta\lambda_{cont} = 1539-1528$ nm range, respectively.

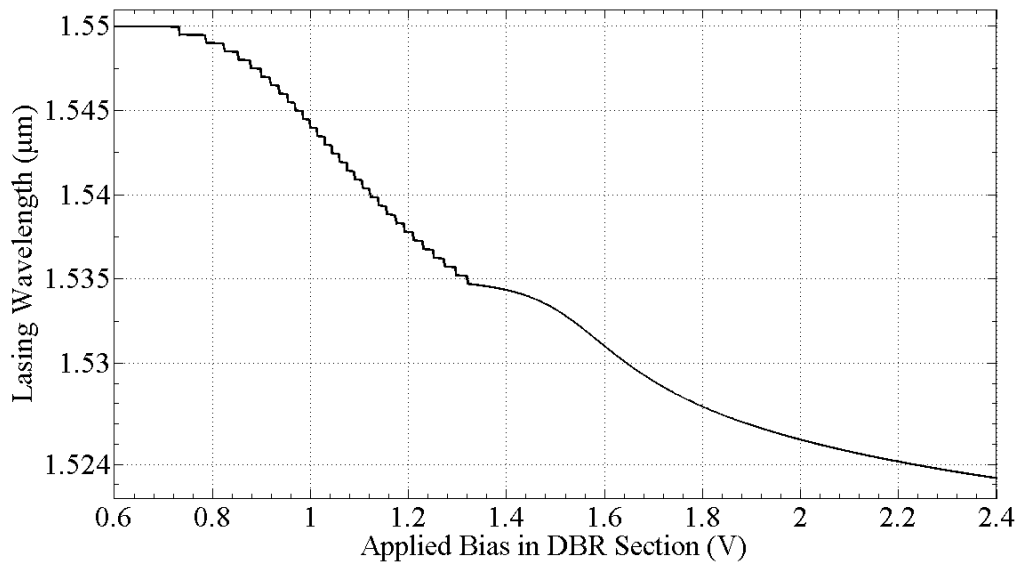


Fig. 6.33: Discontinuous and continuous wavelength tuning performance of the TLD with $d_p=0.58 \mu\text{m}$ and $L_p=300 \mu\text{m}$ for the $\Delta\lambda_{\text{discont}} = 1550\text{-}1535 \text{ nm}$ and $\Delta\lambda_{\text{cont}} = 1535\text{-}1524 \text{ nm}$ range, respectively.

A quasi-continuous tuning range of $\Delta\lambda_{\text{quasicont}} = 26 \text{ nm}$ was also achieved as is shown in Fig. 6.34.

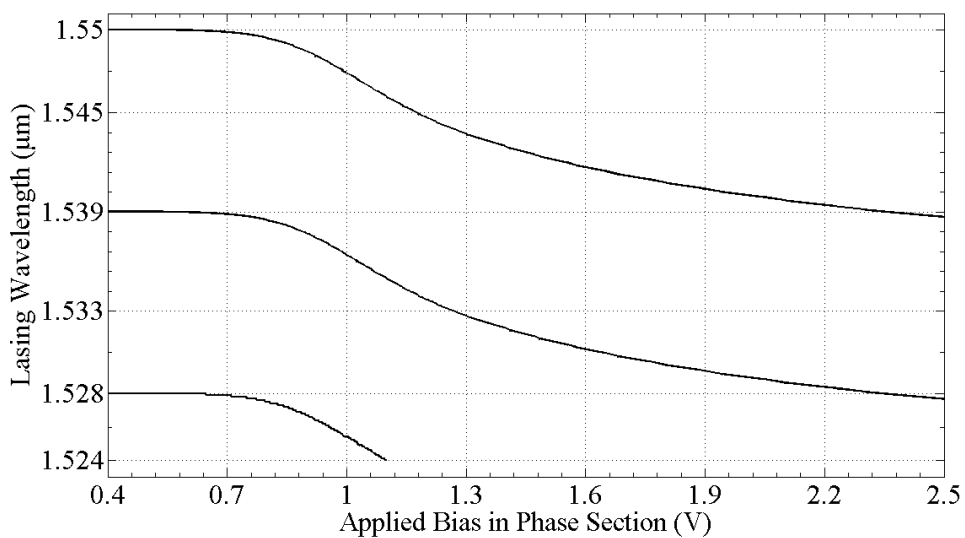


Fig. 6.34: Quasi-continuous wavelength tuning performance of the TLD with $d_p=0.58 \mu\text{m}$ and $L_p=300 \mu\text{m}$ for the $\Delta\lambda_{\text{quasicont}} = 1550\text{-}1524 \text{ nm}$ range.

6.3 Conclusion

A completely self-consistent model of a multi-section TLD was developed and applied to investigate the wavelength tuning performance by using the commercial Crosslight PICS3D software simulation tool. Both the optical and FC transport phenomena were modeled on the same footage for the calculation of the wavelength tuning. Strong effects of the DBR grating design and various material parameters on the FC tuning and lasing spectral purity were demonstrated and explained. In depth physical analysis of the FC tuning process and the TLD design optimisation were presented.

The analysis of the TLD operation suggested that the optimal design for the enhanced tunability is to use such κL products for the DBR section which resulted in the reflectivity spectrum with narrow bandwidth (covering 2-3 cavity modes) and sharp peak (i.e. without high reflectivity flat region) at the Bragg wavelength. The sharp peak was very important in order to avoid tuning saturation. By carefully tailoring the mutual positions of the gain spectra and the mirror reflectivity spectra, it was possible to considerably enhance the tuning range. The best performance of the TLD was achieved when the peak of the reflectivity is red-shifted with respect to the gain peak wavelength. In this case, good mode selection and reasonable (~ 10 nm) tuning was achieved due to asymmetry of the SMSR even for the DBR mirror reflectivities with a wide bandwidth covering many comb modes. However, the wavelength tuning of such devices would inevitably saturate as the lasing wave-length approached the gain peak wavelength. The saturation was avoided and the tuning range increased 2-3 times in the structures in which the DBR reflectivity had a sharp peak.

Further improvement was achieved by modifying *electronic* properties of DBR

grating and by modifying the length of the phase section and thickness of its passive waveguide. Even for a basic 3-section TLD a record high FC tuning $\Delta\lambda_{discont} = 30$ nm, $\Delta\lambda_{cont} = 11$ nm and $\Delta\lambda_{quasicont} = 26$ nm was reported. The obtained results should be useful for practical development of real TLDs. The model can further be extended to more complex multi-section integrated photonic devices.

Chapter 7

**Investigation of power performance
of bulk and multi-quantum-well
tunable laser diodes with
wavelength tuning and main
limiting factors**

7.1 Introduction

The TLD output power stability during wavelength tuning is one of the most important factors for adequate laser operation in optical transmission systems and is sought at all times. The main effect which disrupts this stability and usually leads to a power decrease is the existence of losses in the tuning sections. These losses are either internal losses of the tuning region medium or they are caused by Free-Carrier Absorption (FCA) and Inter-Valence Band Absorption (IVBA). The second type of losses produces even more problems because the losses vary during the wavelength tuning. This happens because both the FCA and IVBA are proportional to the carrier density in the tuning regions, which increases under the current injection.

The impact of absorption losses on the laser power performance is reported in many works in the published literature for all kinds of tunable lasers, such as tunable DFB lasers [154], Two Section (2S)-tunable DBR lasers [155]–[157], 3S-tunable DBR lasers [151], [158]–[165], WT DBR lasers with a two-wavelength DBR laser array [166], WT digital supermode (DS) DBR lasers [167], [168], WT DBR lasers using a digital concatenated grating with multiple phase shifts [169], WT lasers with an interleaved SG rear mirror [170], WT SG-DBR lasers [86], [149], [150], [171]–[174], and WT SSG-DBR lasers [175]–[177].

In order to compensate the power loss in the tuning sections the most common method is to inject more current into the gain section throughout the tuning procedure as in [159], [177]. Apart from this method, several other proposals for the compensation of absorption losses have been made in various publications, such as the integration of the active section of the laser with a SOA [149], [169]. An alternative approach was proposed

in [170], where the TLD used a SG rear reflector with interleaved connections for wavelength tuning and lasing mode selection. The other proposals include using the thermal tuning method (which has advantages of power and linewidth stability, as was first investigated in [161] and [163], although this tuning method is very slow), or inserting a thin layer of active material into the tuning regions in order to generate some gain there which would balance the absorption loss in these regions [160], or special bandgap engineering by selecting a tuning layer bandgap wavelength ($\lambda_g=1.48 \mu\text{m}$) very close to that of the active layer ($\lambda_g=1.56 \mu\text{m}$) so that the gain spectra of the active and the passive regions overlap due to the bandgap tail states in the tuning region providing an additional gain contribution to the emission spectrum [164].

However, most theoretical works are based on the rate equation model which reveals no actual information about the gain spectrum shape and its interaction with the cavity lasing mode during tuning [149]–[151], [154], [155], [157], [159]–[166], [168]–[177]. Some models [86], [156], [158], [167], assume for simplicity a broad flat gain spectrum. In real photonic devices though, the expression for the gain spectrum is more complex, especially in MQW lasers. There are some exceptions as in [175], which provides experimental data for the gain spectrum shape and in [157], where an approximate power expansion up to the cubic terms of the modal gain spectra was used for a particular two-section TLD design, and near 50% power decrease with tuning has been demonstrated.

In this Chapter it will be shown that, apart from losses due to FCA and IVBA, the TLD output power performance is also affected by the shape of the gain spectrum and the positioning of the DBR reflectivity in respect to this spectrum during discontinuous tuning. It will also be demonstrated that a power stabilisation could be achieved during continuous tuning, with specific gain spectrum shapes and a careful selection of tuning

currents. For this purpose, two 3-D simulation models of a 3S InGaAsP/InP TLD model operating at 1550 nm CW have been developed, one with a bulk optical cavity and one with a MQW optical cavity. A comparison of the power performance of these two models under discontinuous tuning will be made and the main differences highlighted. All the TLD models in this Chapter are designed with the use of the Crosslight PICS3D software.

One of the main factors which affects the shape of the gain spectrum is the intraband carrier relaxation due to various scattering mechanisms. This causes spectrum broadening and deforms and reduces its peak values [178], [179], [180]. The effect becomes particularly strong in the case of MQW lasers [181]–[184] where the gain spectrum shape broadens and smoothens despite the sharp step-like density of QW states. PICS3D allows to incorporate the intraband electronic relaxation model [120], [185] into the gain spectrum $G(\hbar\omega)$ of a MQW laser via a convolution integral:

$$G(\hbar\omega) = \int_{E'_g}^{\infty} g(E_{cv}) L(\hbar\omega - E_{cv}) dE_{cv} \quad (7.1)$$

where $G(\hbar\omega)$ is the gain coefficient as a function of photon energy $\hbar\omega$ which includes the effect of the intraband relaxation, $g(E_{cv})$ is the optical gain defined in (3.23) in section 3.4 and [186] without intraband relaxation which is caused by photon-induced transitions of electrons from a conduction subband with energy E_c to a valence subband with energy E_v in the quantum-well, $L(\hbar\omega - E_{cv})$ is a lineshape broadening function defined by the intraband relaxation effects, $E_{cv} = E_c - E_v$ is the carrier transition energy and E'_g is the bandgap between the two subbands. A simplified version of (7.1) can be applied to bulk lasers if the QW subbands are replaced with the conduction and valence bands of the bulk semiconductor, respectively, and $E'_g = E_g$ is the bulk bandgap.

Several theoretical methods have been developed to approximate the lineshape function, such as in [187] (and its simplified version in [188]), where it was shown using a density matrix approach that the electron state decay with time obeys initially a Gaussian and then an exponential dependence. Other approaches give a Lorentzian lineshape, as in [189], where the scattering rate out of a state depends on the position of the state in the band and the band filling. PICS3D uses a Lorentzian lineshape for a very accurate calculation of the gain spectrum (also described in Chapter 3) in accordance with the detailed studies of [185], [190]:

$$L(\hbar\omega - E_{cv}) = \frac{1}{\pi} \frac{\hbar / \tau_{in}}{(\hbar\omega - E_{cv})^2 + (\hbar / \tau_{in})^2} \quad (7.2)$$

where τ_{in} is the average intraband relaxation time. As we will show, a variation of τ_{in} results in a significant change in the MQW TLD tuning and the output power performance.

For comparison reasons we consider two different simulation setups. The first setup which is used in our simulations is a 3S TLD with a MQW AR operating at 1.55 μm . The AR contains 5 unstrained 7-nm thick $\text{In}_{0.56}\text{Ga}_{0.44}\text{As}_{0.94}\text{P}_{0.06}$ QWs and 6 unstrained 22-nm thick $\text{In}_{0.74}\text{Ga}_{0.26}\text{As}_{0.57}\text{P}_{0.43}$ barriers. The second setup is a 3S TLD with a bulk $\text{In}_{0.61}\text{Ga}_{0.39}\text{As}_{0.84}\text{P}_{0.16}$ AR also operating at 1.55 μm . A complete set of design and material parameters of the setup is given in TABLE II.

The waveguide (WG) layer in all the passive sections is an $\text{In}_{0.66}\text{Ga}_{0.34}\text{As}_{0.74}\text{P}_{0.26}$ quaternary with a bandgap wavelength $\lambda_{gp} \approx 1.46 \mu\text{m}$. The grating layer consists of an $\text{In}_{0.68}\text{Ga}_{0.32}\text{As}_{0.69}\text{P}_{0.31}$ material etched into the WG quaternary. Between the WG and the p^+ region in both the DBR and the phase section there is a 6-nm thick $\text{In}_{0.53}\text{Ga}_{0.4}\text{Al}_{0.06}\text{As}$ electron stopper layer with a bandgap wavelength $\lambda_{gb} = \lambda_{gp} \approx 1.46 \mu\text{m}$ in order to prevent

current leakage into the DBR p^+ region. The refractive index of each layer and their spectral dependence on the photon energy are calculated according to the Adachi model [146].

The device has a common bottom contact for all sections and three mutually isolated individual top contacts for each section. According to PICS3D's embodiment of the bias setup [120], the bottom contact should always be pre-biased in order to avoid spurious currents between the top contacts. We applied a $V_b = 0.3\text{ V}$ pre-bias bottom contact voltage to all simulated devices. The optical solver in PICS3D is switched on only at biases when the AR injection current is near the threshold current. Prior to this point, in order to avoid severe convergence problems, it is required first to apply a voltage (not a current) bias V_a to the top contact and solve the electrical problem only. Once the threshold is reached and the Fermi levels in the AR are clamped by the large stimulated recombination term, the electrical solver is switched to current biasing and the coupled 3D electrical and optical problems are solved self-consistently.

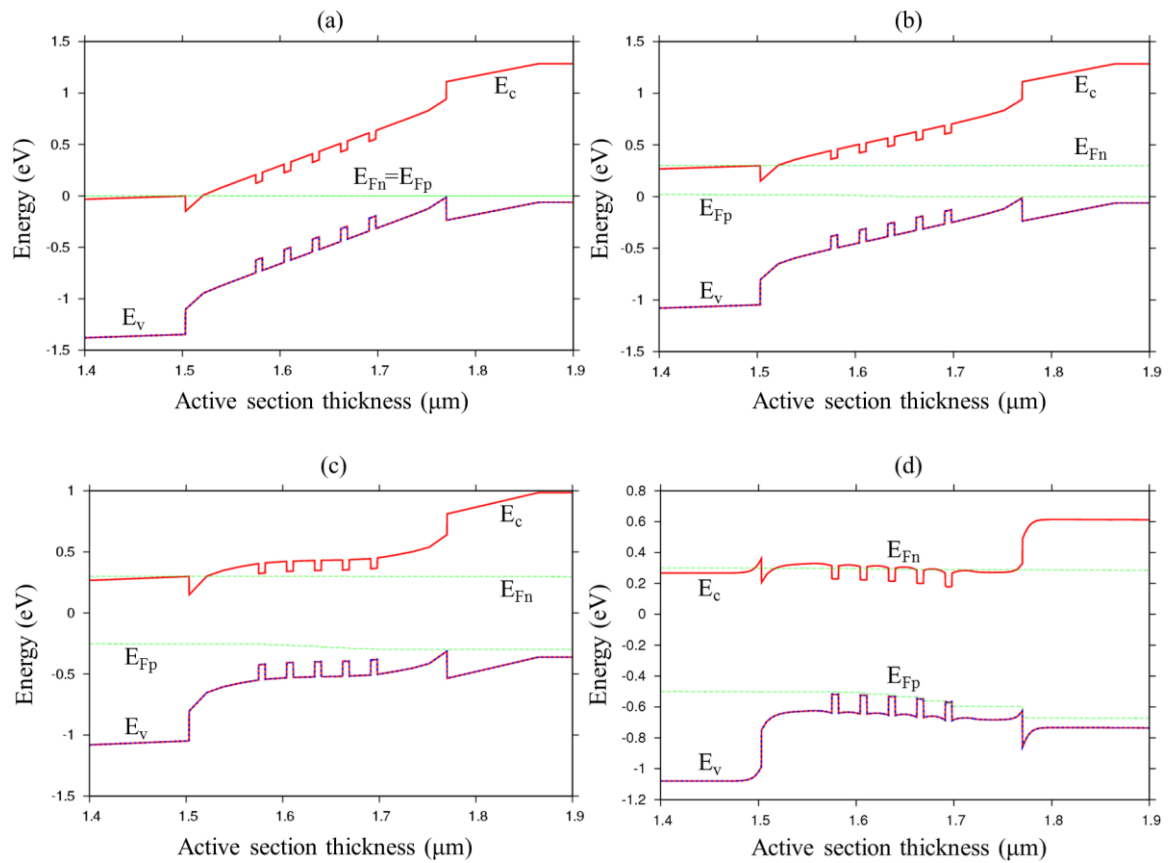
For all the investigated TLDs during the passive section tuning the AR operated at a fixed injection current $I_a = 15\text{ mA}$, almost double the threshold current $I_{th} \approx 7\text{--}8\text{ mA}$. The reported output power P_o when the passive sections were unbiased was around $P_o \approx 2\text{--}3\text{ mW}$. The band profile of the MQW AR (a) when the bottom and top contact are unbiased ($V_b = 0\text{ V}$ and $V_a = 0\text{ V}$) at equilibrium, (b) when only the bottom contact is under forward bias ($V_b = 0.3\text{ V}$ and $V_a = 0\text{ V}$) before threshold, (c) when both the bottom and top contact are under forward bias ($V_b = 0.3\text{ V}$ and $V_a = 0.3\text{ V}$) before threshold and (d) when the bottom contact is under forward bias and the top contact is under current injection ($V_b = 0.3\text{ V}$ and $I_a = 15\text{ mA}$) after threshold is shown in Fig. 7.1(a), 7.1(b), 7.1(c) and

7.1(d), respectively, where $E_{c(v)}$ is the conduction (valence) band energy and $E_{Fn(p)}$ is the electron (hole) quasi-Fermi level. The corresponding electron and hole concentration of the MQW AR under top contact injection current $I_a = 15$ mA after threshold is shown in Fig. 7.1(e). Wavelength tuning takes place by applying a forward voltage bias to the top contact of the corresponding passive section.

TABLE II
STRUCTURE AND MATERIAL PARAMETERS

Symbol	Parameter Name	Value	Units
R_a	Left facet reflectivity	0.3 (z=0)	-
R_r	Right facet reflectivity	10^{-4} (z=800 μm)	-
w	TLD width	1.5	μm
L_a	Active section length	400	μm
L_p	Phase section length	100	μm
L_{DBR}	DBR section length	300	μm
$d_{a,bulk}$	Bulk active region thickness	0.18	μm
$d_{a,MQW}$	Total MQW active region thickness	0.167	μm
d_p	Waveguide region thickness of phase section	0.58	μm
d_{DBR}	Waveguide region thickness of DBR section	0.38	μm
d_{gr}	Grating region thickness	0.2	μm
E_{ga}	Bulk active region bandgap	0.7986	eV
E_{gp}	Waveguide region bandgap of passive sections	0.85	eV

$\langle a_i \rangle$	Average internal losses	5	cm^{-1}
κ	DBR Coupling coefficient	50	cm^{-1}
A	Linear recombination	1×10^9	s^{-1}
B	Bimolecular recombination	2×10^{-10}	$\text{cm}^3 \text{s}^{-1}$
C	Auger recombination	3.5×10^{-29}	$\text{cm}^6 \text{s}^{-1}$
N_n	Doping of the n+ region	1×10^{18}	cm^{-3}
N_p	Doping of the p+ region	1×10^{18}	cm^{-3}



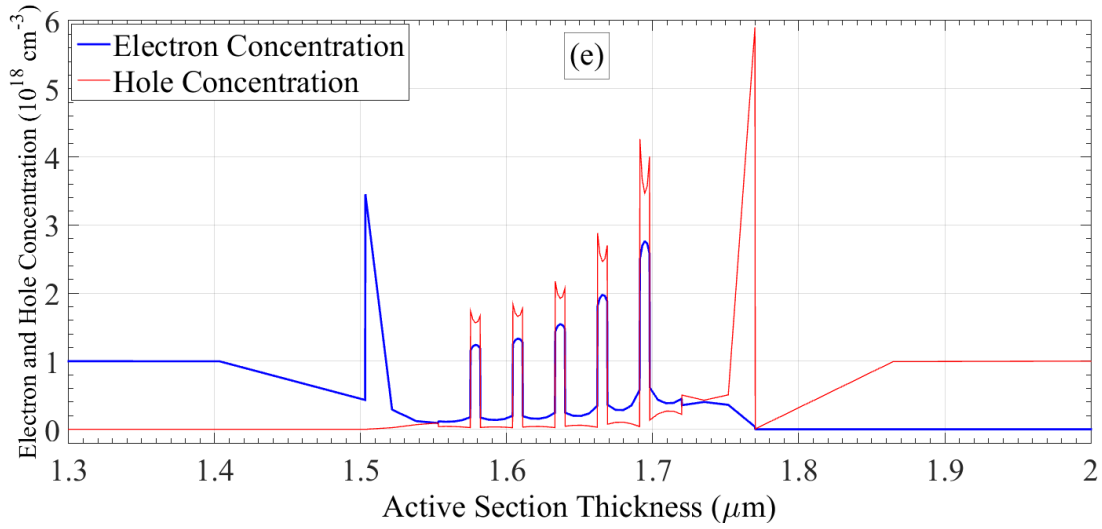


Fig. 7.1: Band structure profile of the MQW AR under forward bottom V_b and top contact V_a bias (a) $V_b = 0\text{ V}$ and $V_a = 0\text{ V}$, (b) $V_b = 0.3\text{ V}$ and $V_a = 0\text{ V}$, (c) $V_b = 0.3\text{ V}$ and $V_a = 0.3\text{ V}$, respectively before threshold and (d) under forward bottom contact bias $V_b = 0.3\text{ V}$ and top contact injection current $I_a = 15\text{ mA}$ after threshold. (e) Electron and hole concentration of the MQW AR under top contact injection current $I_a = 15\text{ mA}$.

The parameters in TABLE II are similar to those used for the TLD model described in section 6.2.2 and Fig. 6.24. Here the main investigation concentrates on how different intraband relaxation times of the Lorentzian broadening function of the MQW TLD affect its gain spectrum. In turn, the interaction of the gain spectrum with the mirror losses spectrum of the TLD will also be discussed. Subsequently, this interaction will mainly affect the TLD operation during wavelength tuning in terms of output power causing a variation that will be described in detail below. The acquired results will be compared with the case of a bulk TLD with exactly the same design parameters as the MQW TLD.

7.2 Results and discussion

PICS3D uses a self-consistent 3D laser model based on a drift-diffusion description of the carrier transport and traveling wave approach in describing the optical field in the cavity by a transfer matrix formalism. The interface carrier transport at the heterojunctions is described by the thermionic emission model. As is seen from Fig. 7.1(d), the hole quasi-Fermi level E_{Fp} discontinuity at the right heterobarrier clearly indicates that the hole injection is actually controlled by thermionic emission. In QW lasers the carrier transport across the QW regions is described in terms of the carrier capture/escape mechanism. PICS3D utilises a phenomenological model [114] in which a fraction of thermionic emission currents at each QW/barrier interface is captured/escaped into/from the QW. The heterojunction capture/escape coefficient γ is proportional to the microscopic scattering probability between the 3D and 2D states.

Different meshes are used for electrical and optical solvers. However, since the simulation of a TLD requires calculation of the local refractive index and modal gain as functions of the carrier density, these optical parameters are directly interpolated from the electrical mesh at every iteration of the Newton solver. As a result of this computational approach all PICS3D simulations of TLDs are carried out in a full 3D model [120].

We first investigate the case of discontinuous tuning of the MQW TLD. The QW capture/escape parameters were defined as $\gamma_e = 0.2$ and $\gamma_h = 0.05$ for the electrons and holes, respectively. The intraband relaxation time in the Lorentzian broadening function was at first chosen to be $\tau_{in}=1$ ps. We tune the DBR section by applying a voltage bias V_{DBR} to the contact varied from 0 V to a maximum value of 2 V, which corresponds to the

maximum injected DBR current $I_{DBR} \approx 400$ mA, as is seen from the I-V characteristic in Fig. 7.2.

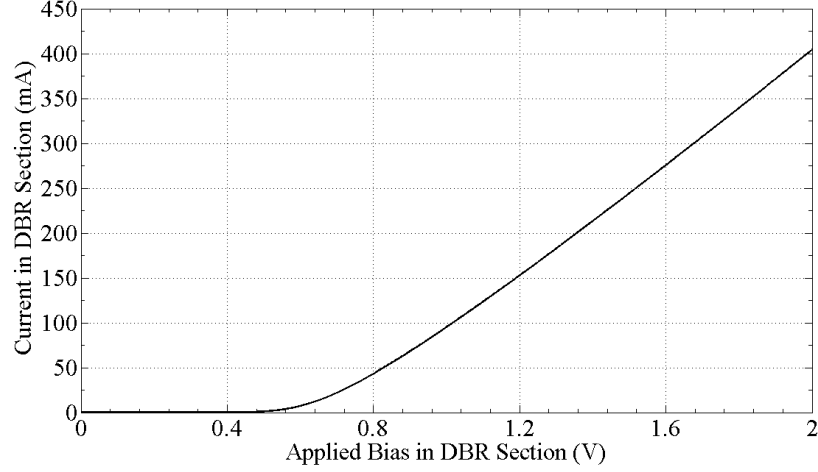


Fig. 7.2: Current-Voltage (I-V) characteristic of the DBR section.

The DBR carrier density at this bias was $N_{DBR} \approx 5.86 \times 10^{18} \text{ cm}^{-3}$. The phase section remained unbiased during this regime. The injected carriers cause a change $\Delta n'$ of the real part of the refractive index in the DBR WG region. The two main free-carrier contributions to the refractive index change in our TLD structures are the band filling effect and the plasma effect which are both activated in all our simulations with PICS3D. Fig. 7.3 demonstrates a record wavelength tuning range achieved in our TLD structure. At a maximum DBR bias we have obtained the total refractive index change of $\Delta n' \approx -0.086$, which results in a large wavelength tuning range of $\Delta \lambda = 32$ nm. The inter-mode distance $\Delta \lambda_m$ was measured to be $\Delta \lambda_m = 0.63$ nm.

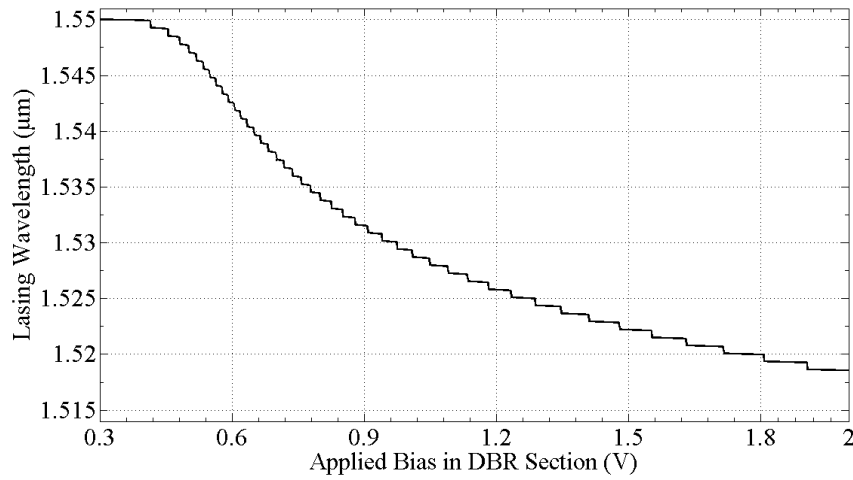


Fig. 7.3: DBR wavelength tuning performance of the MQW TLD with $\tau_{in}=1$ ps.

As can be easily observed, the injection levels that were used to achieve this tuning range are quite high. The main issue that can emerge here is the high carrier leakage from the WG into the adjacent layers (especially electrons), which can lead to Joule heating of the device. It was indeed found that the InGaAsP/InP structure (for the WG and p^+ region respectively) that was used initially led to leakage currents of over 73% for $V_{DBR}=2$ V. The main reason is that this structure has a band offset $\Delta E_c / \Delta E_g = 0.4$, which gives a conduction band discontinuity of only 0.2 eV (InGaAsP WG $E_g=0.85$ eV, InP $E_g=1.35$ eV) in our TLD. This discontinuity is not enough to prevent electron spillover during high injection.

For this reason we introduce a thin 6-nm thick InGaAlAs layer between the InGaAsP WG and the InP p^+ region, which can work as a potential barrier for electrons. The InGaAlAs/InP structure has a band offset $\Delta E_c / \Delta E_g = 0.72$, which increases the conduction band discontinuity to 0.36 eV (InGaAlAs $E_g=0.85$ eV) as it is shown in the band diagram of the DBR section in Fig. 7.4. As a result of this optimisation, the reported

leakage current was below 3% in all our devices even at very high injection levels ~ 400 mA.

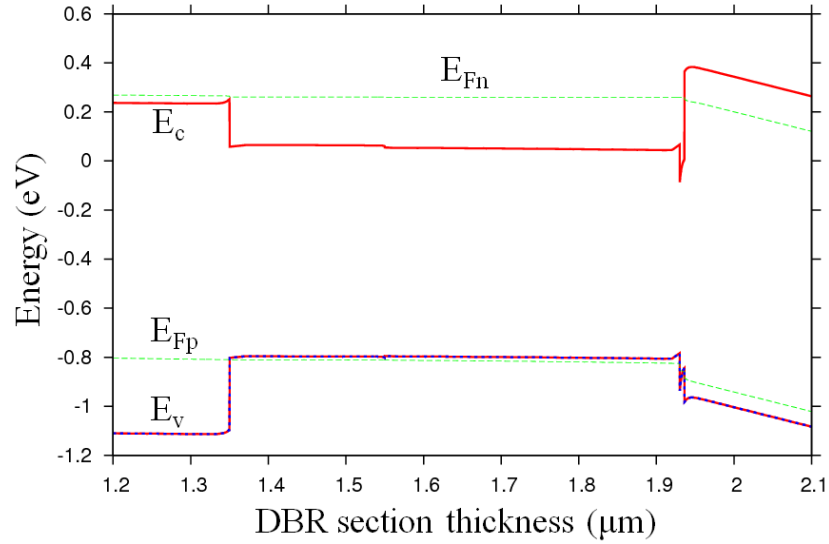


Fig. 7.4: Band structure profile of the DBR section under 400 mA injection.

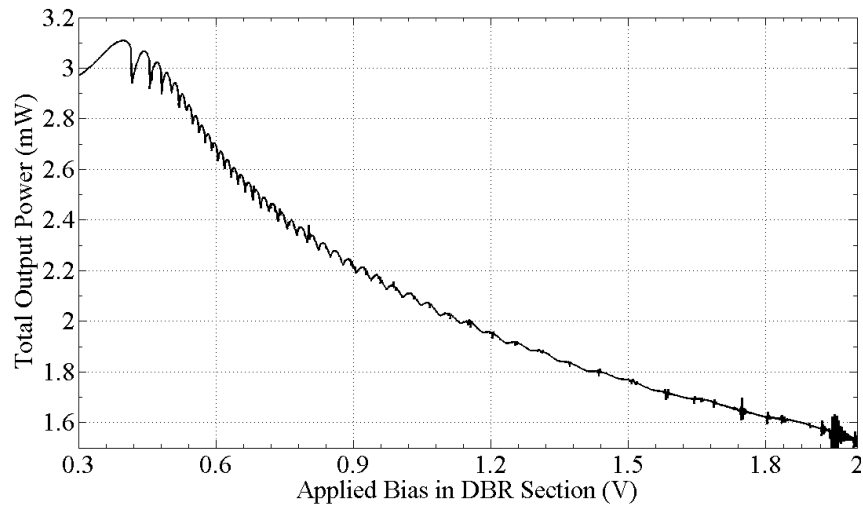


Fig. 7.5: The output power of the MQW TLD with $\tau_{in}=1$ ps as a function of the DBR section bias.

In Fig. 7.5 the reported output power of all modes of the TLD during tuning is plotted as a function of the applied DBR bias. As can be observed, a significant decrease (roughly half the initial value) of the output power takes place with deeper tuning. It will

be shown that this happens because of the interaction of the gain spectrum of the AR with the mirror losses and the increasing optical losses in the WG region of the passive sections during tuning. The WG optical losses are divided in two types.

The first type concerns losses caused by the absorption of a part of emitted photons from the AR in the WG region of the passive sections in the case where the passive sections are not under injection. The reason for this absorption is the ‘tail’ of the gain spectrum g_p of the passive sections which enters the tuning range region (1.55 μm -1.518 μm) of the gain spectrum of the AR. This happens because the calculation of gain in the passive sections in PICS3D is also done with the use of a Lorentzian broadening function as is the case of the gain in the AR. In our case the gain spectrum in the passive sections was already broadened by default in PICS3D with an intraband relaxation time $\tau_{in}=0.2$ ps causing the ‘tail’ of g_p to enter the tuning range region, a fact which has also been described in the theoretical study of [180]. It was also found that the ‘tail’ of g_p in the tuning range region is negative therefore the bandgap tail states of g_p would cause absorption to the lasing mode λ_m in that region. As λ_m is blue-shifted towards the bandgap wavelength $\lambda_{gp}=1.46$ μm of the passive sections during tuning, the negative gain values (absorption) of this ‘tail’ are increasing, which leads to increasing optical losses.

In the case where the passive sections are pumped, electrons and holes in the WG region start to recombine emitting photons with higher energy than the AR photons and the WG region expresses gain (no absorption, no losses). This gain is of small magnitude though and there is no lasing in the DBR section, because g_p has high values at much shorter wavelengths (at least 50 nm away from the tuning range region). During discontinuous tuning which is the case in our simulations, the pumped DBR section expresses gain in the WG region, however the losses described above are still present

because the phase section remains unpumped.

One way to reduce these losses is by selecting a shorter λ_{gp} so that the gain values of the ‘tail’ of g_p entering the tuning range region are smaller. Indeed, in this case the reported TLD power decrease during tuning was much smaller for the same $V_{DBR}=2$ V (shown in section 6.2.2). The drawback with this case though is that the available $\Delta n'$ is also decreased which in turn reduces the $\Delta\lambda$ range, as was stated in section 6.2.2.

A visualisation of the above discussion can be shown in Fig. 7.6, where the optical losses in the WG region of the passive sections are plotted for several different lasing wavelengths within the tuning range ($\lambda=1.55$ μm to $\lambda=1.518$ μm) for three different λ_{gp} ($\lambda_{gp}=1.4$ μm , $\lambda_{gp}=1.42$ μm and $\lambda_{gp}=1.46$ μm) when the passive sections are unpumped.

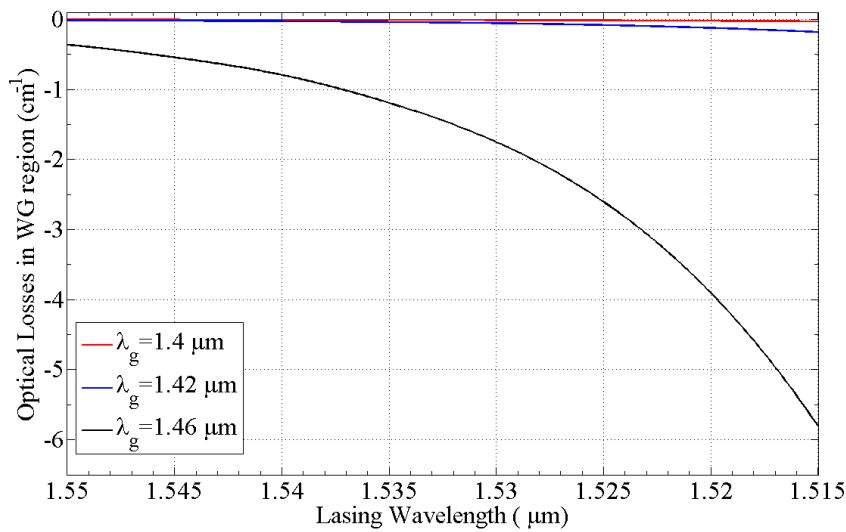


Fig. 7.6: Optical losses in the WG region of the passive sections at different lasing wavelengths.

The second type of optical losses concerns losses in the WG region of the passive sections which are caused by FCA and IVBA and are presented as a_{FC} and a_{IVBA} , respectively. PICS3D takes into account this type of absorption in all calculations successfully. They are directly proportional to the WG carrier density N and are defined

as [85]:

$$a_{FC} = \underbrace{\frac{e^3 \lambda^2}{4\pi^2 c^3 n \varepsilon_0} \left(\frac{1}{m_n^2 \mu_n} + \frac{1}{m_p^2 \mu_p} \right)}_{k_{FC}} N = k_{FC} N$$

and

$$a_{IVBA} = k_{IVBA} N$$

where $m_{n(p)}$ is the electron (hole) effective mass, $\mu_{n(p)}$ is the electron (hole) mobility, e is the electron charge, λ is the lasing wavelength in vacuum, c is the speed of light in vacuum, n is the WG refractive index, ε_0 is the dielectric constant of vacuum and k_{FC} and k_{IVBA} are constant coefficients for the FC absorption and IVBA, respectively. They have a value of $k_{FC} = 2 \times 10^{-19} \text{ cm}^2$ and $k_{IVBA} = 2 \times 10^{-18} \text{ cm}^2$ in all our simulations.

The main difference of this type of losses with the internal losses $\langle a_i \rangle = 5 \text{ cm}^{-1}$ is that they keep increasing with deeper tuning due to the increasing DBR carrier density, whereas the internal losses remain constant. Therefore, the WG FC and IVBA losses in the DBR section will have the value of $a_{FC} = 1.17 \text{ cm}^{-1}$ and $a_{IVBA} = 11.72 \text{ cm}^{-1}$, respectively, at the end of DBR tuning where the value of $N_{DBR} = 5.86 \times 10^{18} \text{ cm}^{-3}$ is reached ($V_{DBR} = 2 \text{ V}$). This additional $a_{FC} + a_{IVBA} = 12.89 \text{ cm}^{-1}$ is also a contributing factor to the ~50% power decrease of Fig. 7.5.

However, the FC and IVBA losses do not influence the TLD power behaviour during tuning as much as the losses caused by the interaction of the gain spectra of the AR and the passive regions which were described previously (first type of WG optical losses). This observation was made when we used the same TLD as in Fig. 7.5 for DBR tuning, but we deactivated a_{FC} and a_{IVBA} since this option is available in PICS3D. All the other parameters and features, including the passive region spectra and the internal losses

$\langle a_i \rangle = 5 \text{ cm}^{-1}$ remained the same. The TLD power behaviour during DBR tuning is shown in Fig. 7.7. As can be seen, the initial and final output power value has slightly increased by 0.1 mW compared with the ones in Fig. 7.5, due to the lack of FC and IVBA losses. However, the rate of the power decrease with deeper tuning is still roughly the same as the one in Fig. 7.5 (around 50%), which means that the power decrease is mainly influenced by λ_{gp} .

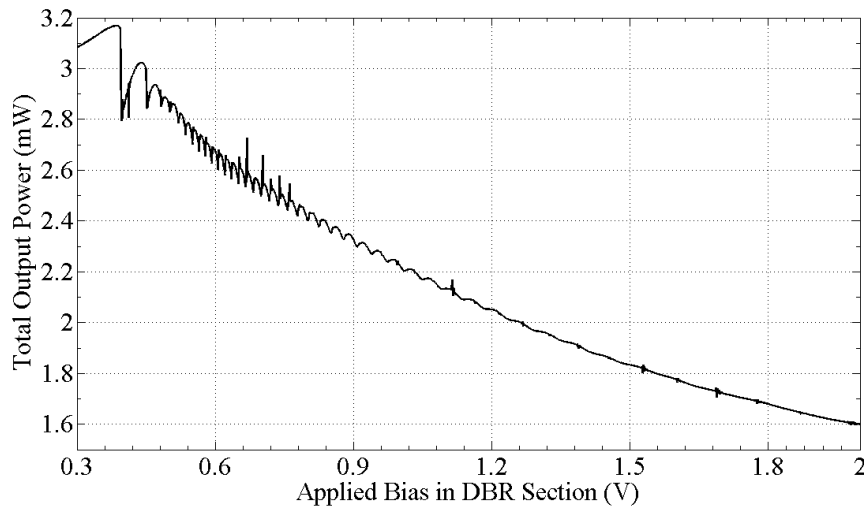


Fig. 7.7: The output power of the MQW TLD with $\tau_{in}=1 \text{ ps}$ and $a_{FC} = a_{IVBA} = 0 \text{ cm}^{-1}$ as a function of the DBR section bias.

Another major factor which influences the TLD power behaviour of Fig. 7.5 is the interaction of the lasing mode with the gain spectrum and the optical losses during tuning. This is illustrated in Fig. 7.8. Here the net gain g_{net} spectrum of the AR for a threshold carrier density $N_{th} = 1.86 \times 10^{18} \text{ cm}^{-3}$ at the beginning of tuning (initial lasing wavelength $\lambda_0 = 1.55 \text{ }\mu\text{m}$) is plotted together with the mirror losses a_m spectrum of the TLD as was described in section 6.2.1.

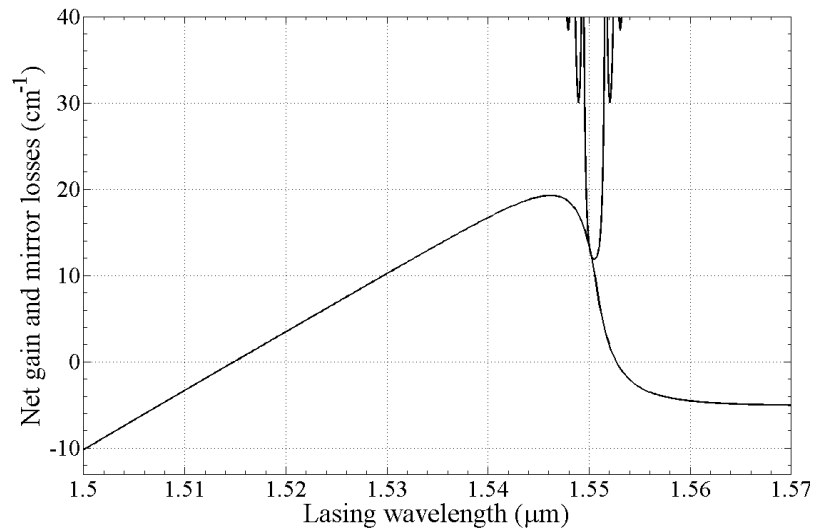


Fig. 7.8: Spectra of the net gain g_{net} and the cavity mirror losses a_m of the MQW TLD at the beginning of tuning (lasing wavelength $\lambda_0=1.55 \mu\text{m}$, $\tau_{in}=1 \text{ ps}$).

As is seen in Fig. 7.8, the FC tuning always moves the DBR reflectivity up the ascending gain spectrum curve. This in turn results in an increase of the gain of the next lasing mode ($dg/d\lambda > 0$). In the case where the increase of gain of the lasing mode is greater than the optical losses increase, an increase of the lasing mode power will also take place.

In similar fashion, a decrease of the lasing mode power will happen if the passive section optical losses increase with a greater rate than the lasing mode gain. If the lasing mode gain and the optical losses increase with the same rate, the two effects may in principle counterbalance each other and stabilise the lasing mode power around a specific value. These effects are depicted clearly in Fig. 7.5 and the power variation with DBR tuning can be explained more thoroughly.

Initially, the power P increases from 3 mW to 3.1 mW because the lasing mode gain increase is greater than the optical losses increase, as was explained above. As the lasing modes are further blue-tuned towards the gain peak, the gain variation $dg/d\lambda$

flattens. Therefore, the increase of both the lasing mode gain and the optical losses have roughly the same rate. This means that the two effects compensate each other and the lasing power stabilises around its maximum value of 3.1 mW.

For even deeper tuning (past the gain peak), the gain of the lasing mode will always decrease ($dg/d\lambda < 0$), which means that the increase in the optical losses in the passive sections will dominate. The result of this interaction was to significantly decrease the output power at the end of tuning by more than half the maximum power, from 3.1 mW to 1.5 mW ($\Delta P/P \approx 51.6\%$). It is therefore concluded that these output power variations mainly depend on the shape of the gain curve, which in turn is formed by τ_{in} . It will be later shown in this Chapter that this output power behaviour can be altered by changing the shape of the gain curve and the positioning of the mirror losses spectrum accordingly. However, a few more observations have to be made first about Fig. 7.5.

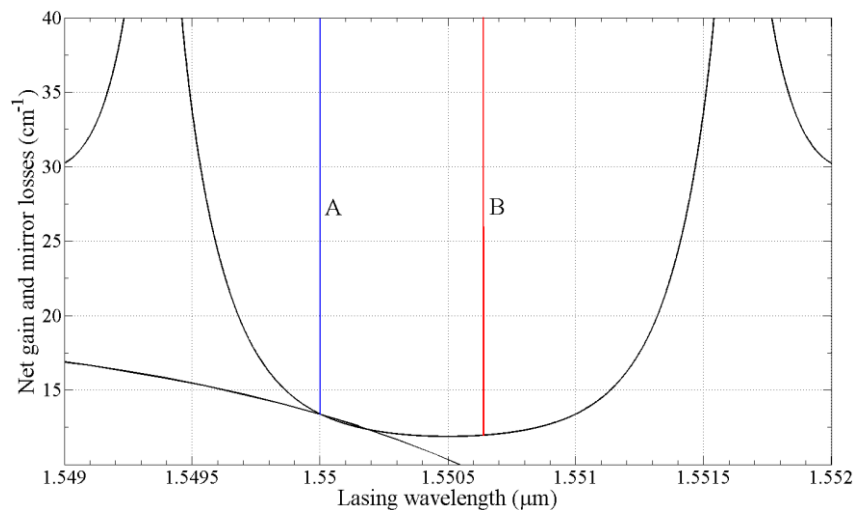


Fig. 7.9: Interaction of the cavity modes inside the a_m stopband with the net gain g_{net} of the MQW TLD at the beginning of tuning (lasing wavelength $\lambda_0=1.55 \mu\text{m}$).

Apart from the increase and decrease of output power in Fig. 7.5, numerous repeating power fluctuations, and in turn SMSR fluctuations, also take place. These

fluctuations happen in every wavelength change during Bragg tuning and can be explained by observing the positioning of the cavity modes inside the mirror losses spectrum and the interaction of these modes with g_{net} in Fig. 7.9. This interaction is shown at the beginning of tuning with an initial lasing wavelength at $\lambda_0=1.55 \mu\text{m}$, which is positioned at point A (blue line). As the a_m stopband is blue shifted during tuning the lasing mode λ_0 in point A moves towards point B (red line), where the wavelength change takes place ($\Delta\lambda_m=0.63 \text{ nm}$). The lasing mode experiences decreasing mirror losses as it approaches the bottom of the a_m stopband leading to an increase of its optical power and an increase of SMSR.

At the bottom of the a_m stopband the mirror losses are minimum, λ_0 reaches its maximum power and SMSR takes its highest value. As the a_m stopband is further blue shifted, the lasing mode experiences increasing mirror losses and its power starts to drop. When λ_0 reaches point B, it ceases to lase as the conditions for lasing are no longer suitable (not enough gain to compensate the mirror losses, minimum SMSR) and its power drops significantly. During the procedure of λ_0 moving from point A to point B its sidemode λ_m , which was positioned at shorter wavelengths, was moving towards point A with increasing power, since it experienced decreasing mirror losses. It reaches point A at the same time when λ_0 reaches point B and starts lasing. It then moves towards point B with the same power fluctuation as was described above for λ_0 .

Having described the power behaviour of the TLD in Fig. 7.5, we can return to the main problem of the TLD performance, which is the significant power loss almost at the beginning of tuning. This is clearly derived by observing Fig. 7.3 and 7.5, where the power loss starts at the first wavelength change at $V_{DBR}=0.42 \text{ V}$. The main reason why the

power drops so early during tuning is the proximity of the mirror losses spectrum to the gain peak as is shown in Fig. 7.8. Therefore, in order to delay this power reduction so that it starts at a shorter wavelength of the tuning range, we either need to change the gain spectrum shape or move the mirror losses spectrum at a longer initial wavelength.

By doing the second, the ascending part of the g_{net} curve will be longer during tuning and the power loss will start at a shorter wavelength compared with Fig. 7.5. Furthermore, a significant output power increase will also take place for the first few wavelength changes during tuning. Therefore, we attempted to red shift the mirror losses spectrum to the longest possible wavelength, so that λ_0 would be positioned at the bottom of the ascending part of the gain curve. However, it was found that not even a red shift of 1 nm was possible in order for tuning to commence at $\lambda_0=1.551 \mu\text{m}$. The reason is that instead of $\lambda_0=1.551 \mu\text{m}$, lasing actually took place at around $\lambda \approx 1.548 \mu\text{m}$. This happened because a sideband of the α_m spectrum interacted with the g_{net} spectrum as is shown in Fig. 7.10, for a threshold carrier density $N_{th} = 2 \times 10^{18} \text{cm}^{-3}$.

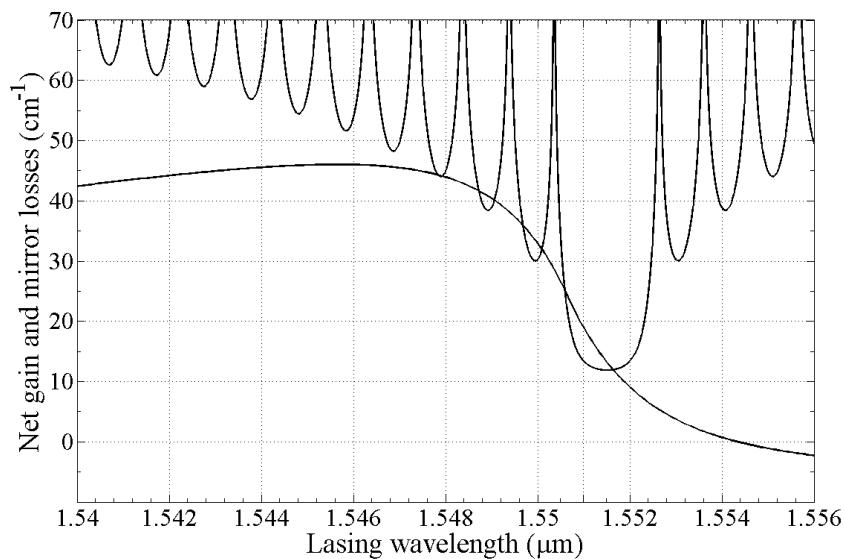


Fig. 7.10: Spectra of the net gain g_{net} and the cavity mirror losses α_m of the MQW TLD for the attempt to lase at $\lambda_0=1.551 \mu\text{m}$ ($\tau_{in}=1 \text{ps}$).

A careful observation of Fig. 7.10, shows that the mode inside the a_m sideband at $\lambda \approx 1.548 \mu\text{m}$ has a greater g_{net} value than the mode at the bottom of the a_m stopband at $\lambda_0 = 1.551 \mu\text{m}$, therefore the conditions for lasing are more suitable for the first one. The main reason of this jump to a lasing wavelength shorter than the wavelengths inside the a_m stopband is the steepness of the ascending part of the gain curve. This steepness creates very high mirror losses for the modes inside the a_m stopband as it is red shifted at longer wavelengths towards the bottom of the ascending part of the gain curve. The combination of very high mirror losses together with the very small values of g_{net} in that wavelength region will make it impossible for these modes to lase at any point.

To further support this argument we simulated the ‘ideal’ case of a TLD with exactly the same parameters as the one in Fig. 7.5, but with an unbroadened gain spectrum. In order to design this, we used a scattering time of $\tau_{in} = 10 \text{ ps}$ for the Lorentzian function, as scattering times of $\tau_{in} \geq 10 \text{ ps}$ yield a gain curve identical to the unbroadened one [191]. The interaction of the new g_{net} spectrum with the a_m losses for $N_{th} = 1.85 \times 10^{18} \text{ cm}^{-3}$ is shown in Fig. 7.11. It was found that lasing is impossible at $\lambda_0 = 1.55 \mu\text{m}$ because of the almost vertical steepness of the ascending part of the gain curve which causes wavelength jumps similar to the one in Fig. 7.10. The only region where lasing could actually take place was at the descending part of the gain curve past the gain peak at $\lambda_0 = 1.547 \mu\text{m}$. Therefore, it is easy to conclude that a power loss would immediately occur at the very beginning of the tuning range if DBR tuning was attempted. The slope of the descending part of the gain curve also indicates that a greater power reduction than the one in Fig. 7.5 would take place because of the fast decreasing gain values towards shorter wavelengths.

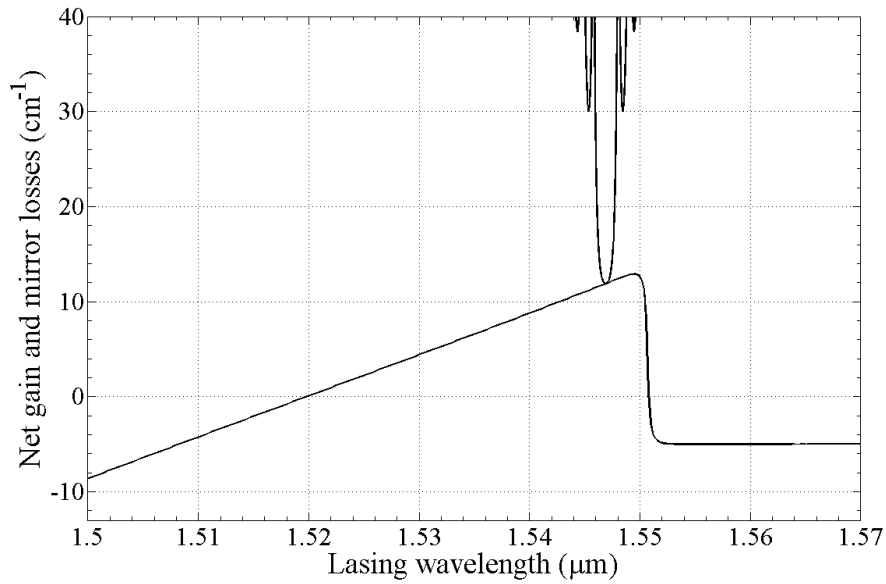


Fig. 7.11: Spectra of the net gain g_{net} and the cavity mirror losses a_m of the MQW TLD at $\lambda_0=1.547 \mu\text{m}$ ($\tau_{in}=10 \text{ ps}$).

The above discussion led to the conclusion that in order to take advantage of the positive effect of the ascending part of the gain curve on the TLD power behaviour, we need to use a broader gain spectrum, since a red shift of the a_m spectrum failed to provide adequate results.

Therefore, in order to broaden the shape of the gain curve we used a TLD with exactly the same parameters as the one in Fig. 7.5, but with a smaller scattering time of $\tau_{in}=0.1 \text{ ps}$. In this way, we were able to red shift the a_m spectrum by as many as 6 nm in order for tuning to commence at $\lambda_0=1.556 \mu\text{m}$. An attempt to further red shift the a_m spectrum in order lasing to happen at $\lambda_0=1.557 \mu\text{m}$ failed, with a jump at a shorter wavelength similar to the one in Fig. 7.10. However, the broadening of the gain spectrum improved the power behaviour of this TLD, as the power drop started at shorter

wavelengths of the tuning range as is shown in Fig. 7.12. There was also a significant power increase of 55% from 2 mW to 3.1 mW for the first six wavelength changes.

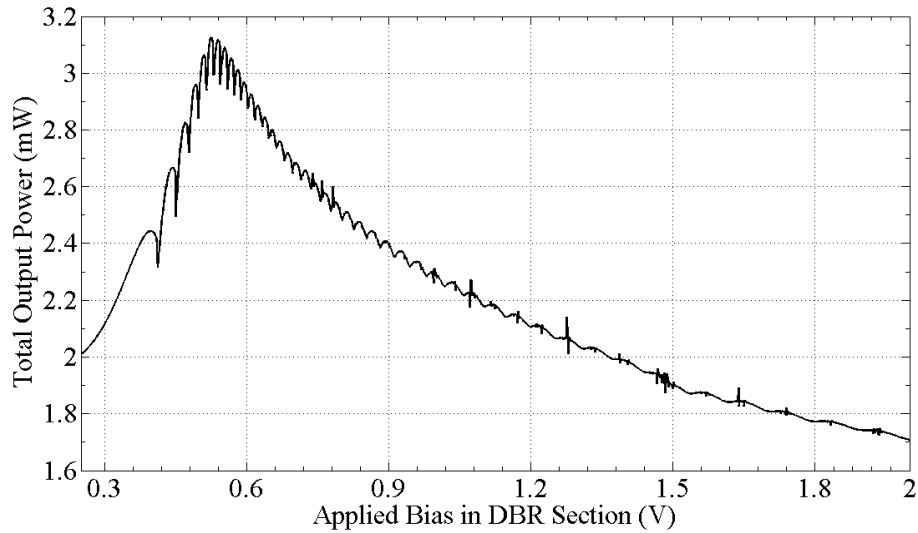


Fig. 7.12: The output power of the MQW TLD with $\tau_{in}=0.1$ ps as a function of the DBR section bias.

This is also explained by the fact that the a_m spectrum is now further away from the gain peak of the optimised TLD compared with the TLD in Fig. 7.8. The mutual positioning of the g_{net} spectrum taken at $N_{th} = 2.21 \times 10^{18} \text{ cm}^{-3}$ and the a_m spectrum of the optimised TLD at the beginning of tuning is shown in Fig. 7.13.

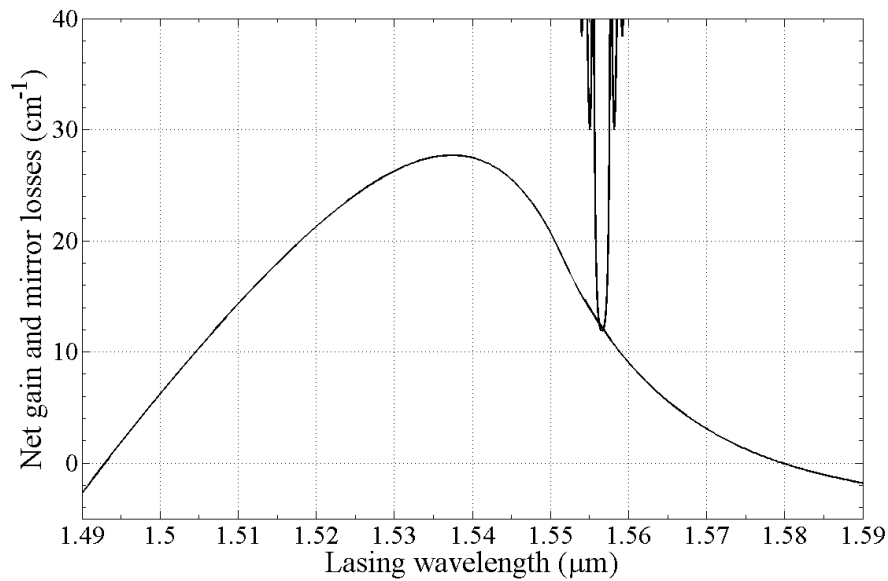


Fig. 7.13: Spectra of the net gain g_{net} and the cavity mirror losses a_m of the MQW TLD at the beginning of tuning (lasing wavelength $\lambda_0=1.556 \mu\text{m}$, $\tau_{in}=0.1 \text{ ps}$).

Further investigation on the issue of the effect of the gain shape on output power performance during discontinuous tuning was carried out in the case of a TLD with a bulk $\text{In}_{0.61}\text{Ga}_{0.39}\text{As}_{0.84}\text{P}_{0.16}$ active region. It has exactly the same parameters as the MQW TLD in Fig. 7.1 and Table II and is operating at $1.55 \mu\text{m}$ with a bandgap wavelength of $\lambda_g=1.553 \mu\text{m}$. The investigation led to the exactly opposite results than the ones acquired in the case of the MQW TLD in terms of the power performance for the same τ_{in} .

It was found that for a scattering time of $\tau_{in}=0.1 \text{ ps}$ a power reduction of 33% took place during DBR tuning, after roughly 10 wavelength changes, which is quite early in the tuning range. An initial non significant power increase of 3% also took place. The power performance of the bulk TLD is shown in Fig. 7.14. Two reasons are responsible for this power behaviour; (1) the selection of a small τ_{in} which significantly broadened the gain spectrum making it almost flat and (2) the proximity of the a_m spectrum to the gain peak. The smoothness of the ascending part of the gain curve especially, is the reason of

the very small power increase (3%) in the first part of the tuning range before the gain peak is reached. The interaction of the gain spectrum taken at $N_{th} = 1 \times 10^{18} \text{ cm}^{-3}$ with the a_m spectrum of the bulk TLD is depicted in Fig. 7.15.

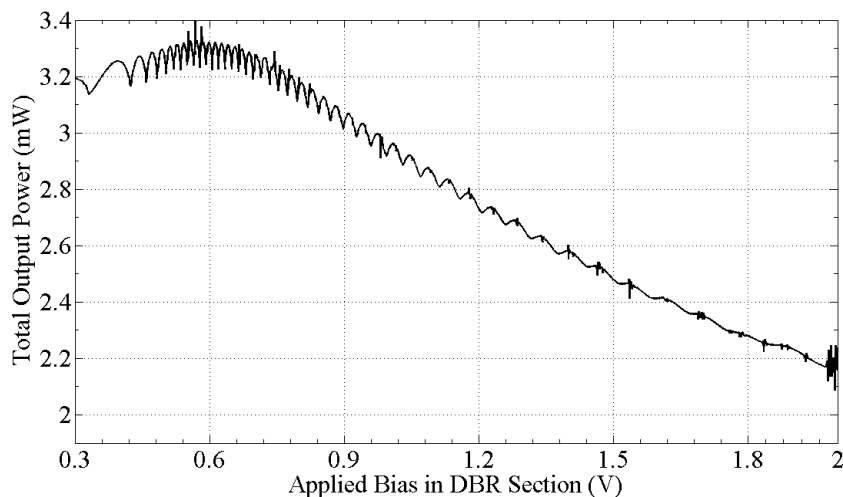


Fig. 7.14: The output power of the bulk TLD with $\tau_{in}=0.1$ ps as a function of the DBR section bias.

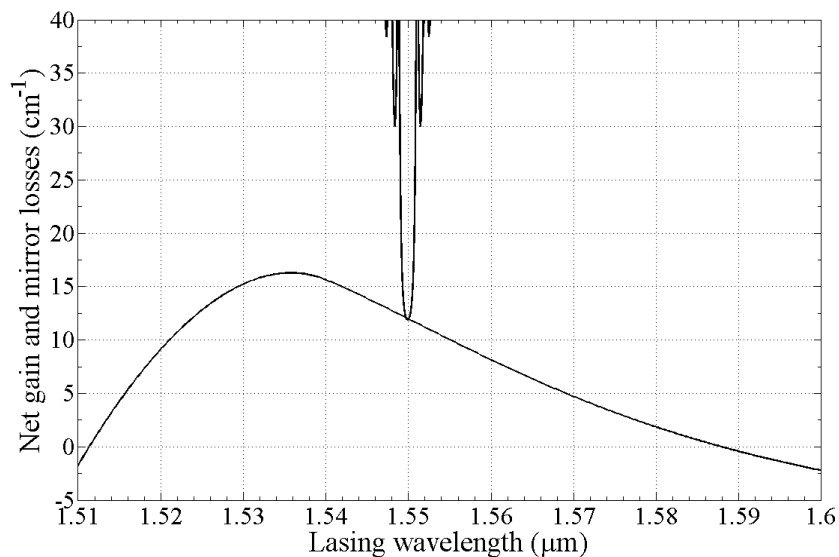


Fig. 7.15: Spectra of the net gain g_{net} and the cavity mirror losses a_m of the bulk TLD at the beginning of tuning (lasing wavelength $\lambda_0=1.55$ μm , $\tau_{in}=0.1$ ps).

The situation significantly improved when a higher $\tau_{in}=1$ ps was used for a bulk TLD identical to the one in Fig. 7.14. In this case, the gain spectrum became sharper and the a_m spectrum moved further away from the gain peak compared with the TLD in Fig. 7.15. The gain spectrum of the new bulk TLD taken at $N_{th} = 1.2 \times 10^{18} \text{ cm}^{-3}$ and its a_m spectrum is shown in Fig. 7.16.

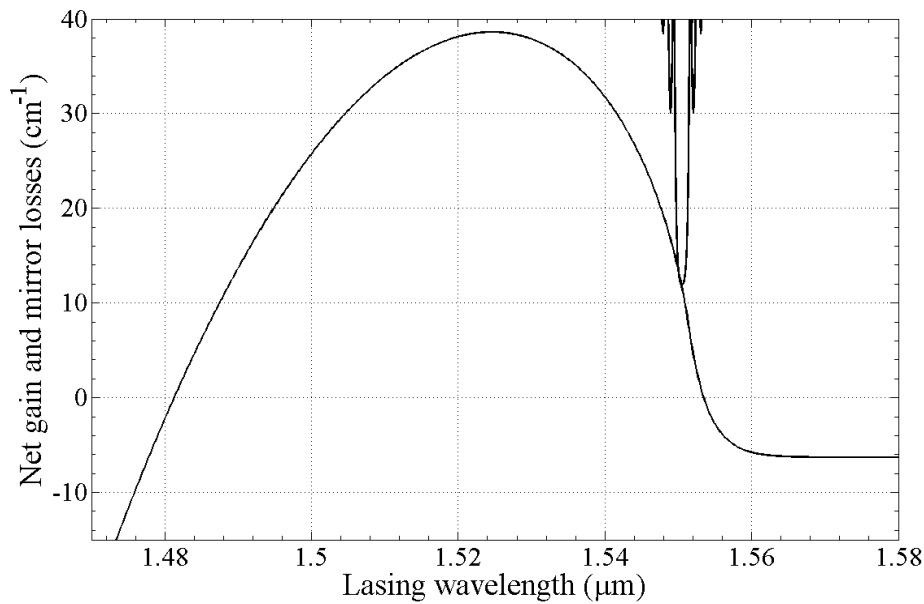


Fig. 7.16: Spectra of the net gain g_{net} and the cavity mirror losses a_m of the bulk TLD at the beginning of tuning (lasing wavelength $\lambda_0=1.55 \mu\text{m}$, $\tau_{in}=1$ ps).

As can be clearly observed in Fig. 7.16, the ascending part of the gain curve is now much steeper than the one in Fig. 7.15, which led to a quite substantial power increase of 75% of the TLD for the first 15 wavelength changes during tuning. It also delayed the following power drop to shorter wavelengths in the tuning range as is shown in the TLD power performance in Fig. 7.17.

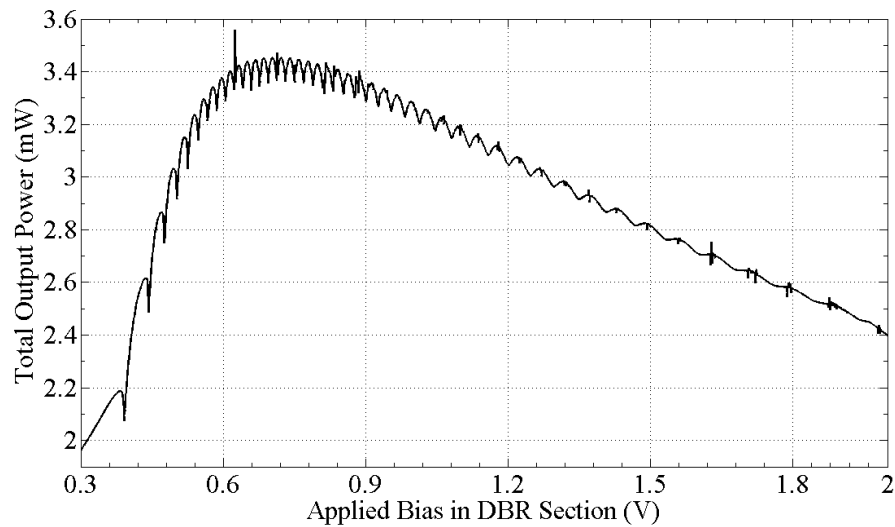


Fig. 7.17: The output power of the bulk TLD with $\tau_{in}=1$ ps as a function of the DBR section bias.

A red shift of the a_m spectrum in both TLDs with $\tau_{in}=0.1$ ps and $\tau_{in}=1$ ps failed with a result similar to the one in Fig. 7.10 because of the very small gain values close to the band edge ($\lambda_g=1.553$ μm). It should be kept in mind that the gain spectrums of the bulk TLDs are by definition broader than the ones of the MQW TLDs for the same τ_{in} because of the higher number of electron transitions from different subbands of the quantum wells in the AR.

It was shown in Fig. 7.17 that in the case of the bulk TLD with $\tau_{in}=1$ ps a significant power increase was achieved during discontinuous tuning. However, Fig. 7.17 also shows that a power drop of 30% at the end of the tuning range still takes place, which is a fact that also needs to be taken into account.

Further investigation on this matter showed that this power reduction can be eliminated completely in the case of continuous tuning. For this reason both passive sections of the TLD in Fig. 7.17 were driven simultaneously with a careful selection of applied bias for each one so that the wavelength changes caused by phase and DBR

tuning coincide. In order to limit possible leakage currents below 3% in the phase section, the same InGaAlAs layer between the WG and the p^+ region of the phase section was introduced, as the one in the DBR section.

Thus, the phase section was driven from 0 V to a maximum value of applied bias of $V_p=1.8$ V, which corresponds to a value of injected current I_p of $I_p \approx 125$ mA and a high carrier density N_p of $N_p \approx 5.3 \times 10^{18} \text{ cm}^{-3}$. The DBR section was driven to a maximum $V_{DBR}=0.6$ V, which corresponds to $I_{DBR} \approx 3.9$ mA and $N_{DBR} \approx 0.7 \times 10^{18} \text{ cm}^{-3}$. The achievable continuous tuning range as a function of the phase section bias was 5.7 nm as is shown in Fig. 7.18.

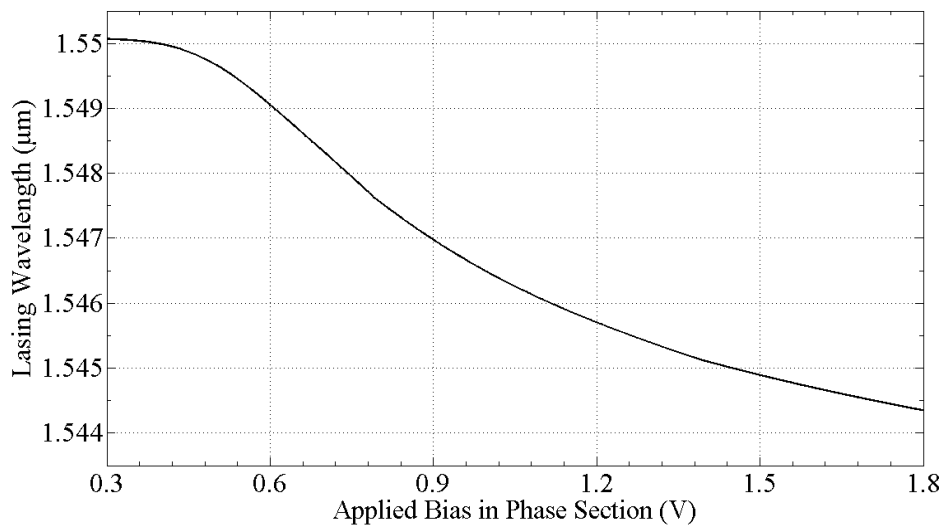


Fig. 7.18: Continuous wavelength tuning performance of the bulk TLD with $\tau_{in}=1$ ps.

However, the main improvement in terms of power performance is shown in Fig. 7.19, where a 40% power increase takes place, followed by a power stabilisation until the end of the tuning range. The power variation is plotted as a function of the phase section bias.

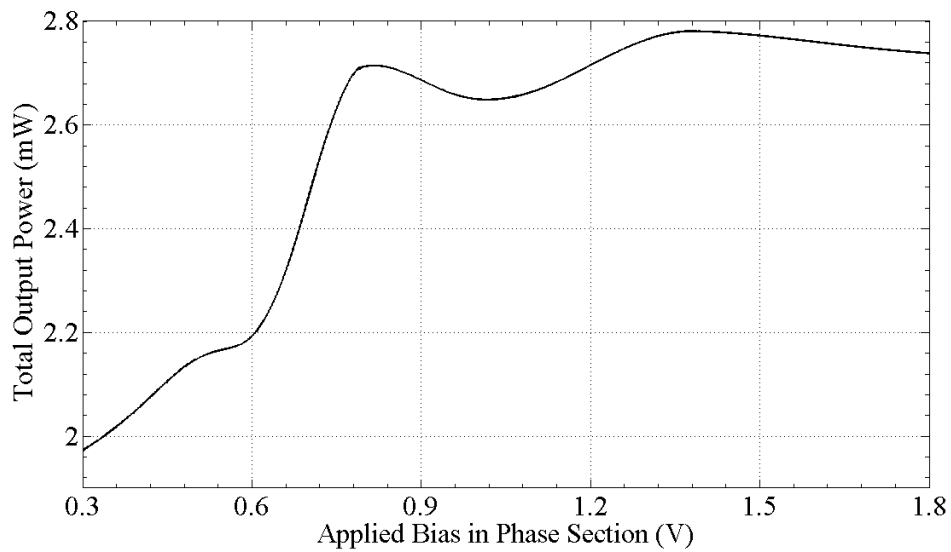


Fig. 7.19: The output power of the bulk TLD with $\tau_m=1$ ps as a function of the phase section bias.

The desired TLD power stabilisation in Fig. 7.19 happened for two reasons. The first one is the fact that the two passive sections are always pumped during continuous tuning. As it was discussed previously, this means that the passive WG regions will express a small amount of gain under injection, eliminating any kind of photon absorption in the form of optical losses which could reduce the TLD output power. The second reason is that during continuous tuning, the lasing mode is always positioned at the bottom of the a_m stopband, where it experiences minimum mirror losses and high SMSR. Thus, the increasing gain values of the ascending part of the gain curve will dominate in the interaction with the a_m spectrum and will eliminate the power loss and the power fluctuations in Fig. 7.17.

7.3 Conclusion

A model of two 3S TLDs, one with a bulk and one with a MQW optical cavity, was developed in order to investigate their output power behaviour during wavelength tuning by using the simulation software PICS3D. In the case of the MQW TLD, the monitored power variation during discontinuous tuning ($\Delta\lambda_{discont} = 32$ nm) consisted of a small power increase in the first few wavelength changes of the tuning range followed by a significant power decrease with deeper tuning. This variation was caused by the shape of the gain spectrum and its interaction with the mirror reflectivity spectrum and the increasing optical losses of the passive regions during tuning.

The shape of the gain spectrum of the TLD was formed by a Lorentzian lineshape broadening function which in turn was defined by the intraband relaxation time τ_{in} . By carefully selecting τ_{in} and the positioning of the mirror reflectivity spectrum in respect to the gain peak, the power increase could be significantly enhanced. The opposite results were acquired for the same relaxation times in the case of the bulk TLD due to the proximity of the mirror reflectivity spectrum to the band edge and the by default broader gain spectrum of its AR due to the lack of energy subbands compared with the case of the MQW TLD.

The significant power decrease was managed to be eliminated leading to an output power stabilisation with deeper tuning in the case of continuous tuning for the proposed optimised TLD setup.

Chapter 8

Modulation and dynamics of tunable laser diodes and wavelength tunable transmitters

8.1 Introduction

The term small-signal analysis refers to the direct Intensity (Amplitude) Modulation (IM or AM) or Frequency Modulation (FM) of a laser by injecting a small ($\sim 1\text{-}6\%$ of the threshold current) sine-wave Alternating Current (AC) on top of the Direct Current (DC) into its active region. The main reason for this process is the determination of a frequency of the modulated output power of the laser which is at resonance with the frequency of the sine-wave AC modulation injection current over a certain period of time. This frequency is called Relaxation Oscillation Frequency (ROF) and is calculated through a transfer function which takes into account the modulated output power of the laser and the AC modulation current.

Most papers in the published literature deal with ways to enhance as much as possible the ROF in single-mode semiconductor lasers [192]–[209]. The most common method is by increasing the DC injection current of the active region. In the case of 3S and 4S TLDs there are also various papers discussing this process [192], [195], [198], [199], [202], [203], [206]–[209], however most of them treat the TLD as a single-mode laser and no tuning is taking place with the exception of [206]. Therefore, the TLD performance under direct intensity modulation during tuning and the possible enhancement of its ROF during this process has not been thoroughly investigated in published literature.

In this Chapter, the main focus of the investigation concerns the small-signal analysis of directly intensity modulated TLDs during discontinuous tuning. This is done by injecting a small (~ 0.5 mA, 6% of the threshold current) modulation AC current on top of the DC current in the active section and by sweeping a number of frequencies with

a tiny step until a frequency is found where the TLD is at resonance with. It is found that the ROF can be significantly increased not by increasing the DC current of the active region as is usually suggested in literature, but by taking advantage of the increase of the wavelength dependent differential gain during discontinuous wavelength tuning.

All the investigations take place with the use of the VPI software for the case of a bulk TLD, all the device parameters of which are taken from the bulk TLD setup described in Chapter 7 with the use of PICS3D (same device structure, same optical and electronic parameters, same gain profile) and shown in Fig. 7.16 and 7.17. Some basic optical characteristics are plotted (L-I characteristic, carrier density, optical spectrums, optical power vs DBR current during DBR tuning), which are in good agreement with the ones acquired from PICS3D.

It is shown that in the small-signal analysis the ROF increases during DBR tuning mainly due to the significant increase of the wavelength dependent differential gain of the gain spectrum as the TLD is tuned to smaller wavelengths. The acquired results from all these investigations are described and explained in a comprehensive way in section 8.2 and all the conclusions made are included in section 8.3.

8.2 *Results and discussion*

8.2.1 **Device setup**

The TLD which is used in all the investigations of this Chapter is designed in VPI and is similar to the bulk TLD which was designed in PICS3D, used in Chapter 7 and

shown in Fig. 7.16 and 7.17. As a reminder, the structure and material parameters of the TLD designed in PICS3D are shown in Table III.

TABLE III
STRUCTURE AND MATERIAL PARAMETERS OF THE BULK TLD USED IN
PICS3D

Symbol	Parameter Name	Value	Units
R_a	Facet reflectivity at $z=0 \mu\text{m}$	0.3	-
R_r	Facet reflectivity at $z=800 \mu\text{m}$	10^{-4}	-
w	TLD width	1.5	μm
L_a	Active section length	400	μm
L_p	Phase section length	100	μm
L_{DBR}	DBR section length	300	μm
d_a	Active region thickness	0.18	μm
d_p	Waveguide region thickness of the passive sections	0.38	μm
d_{gr}	Grating region thickness	0.2	μm
E_{ga}	Active region bandgap	0.7986	eV
E_{gp}	Waveguide region bandgap of the passive sections	0.85	eV
a_{ia}	Internal losses of the active region	15	cm^{-1}
a_{ip}	Internal losses of the waveguide region of the passive sections	5	cm^{-1}

Γ_a	Confinement factor of the active region	0.34	-
Γ_p	Confinement factor of the waveguide region of the passive sections	0.822	-
κ	Coupling coefficient	50	cm^{-1}
A_a	Linear recombination of the active region	1×10^8	s^{-1}
B_a	Bimolecular recombination of the active region	2×10^{-10}	$\text{cm}^3 \text{s}^{-1}$
C_a	Auger recombination of the active region	3.5×10^{-29}	$\text{cm}^6 \text{s}^{-1}$
A_p	Linear recombination of the waveguide region of the passive sections	1×10^8	s^{-1}
B_p	Bimolecular recombination of the waveguide region of the passive sections	1×10^{-10}	$\text{cm}^3 \text{s}^{-1}$
C_p	Auger recombination of the waveguide region of the passive sections	1.5×10^{-29}	$\text{cm}^6 \text{s}^{-1}$

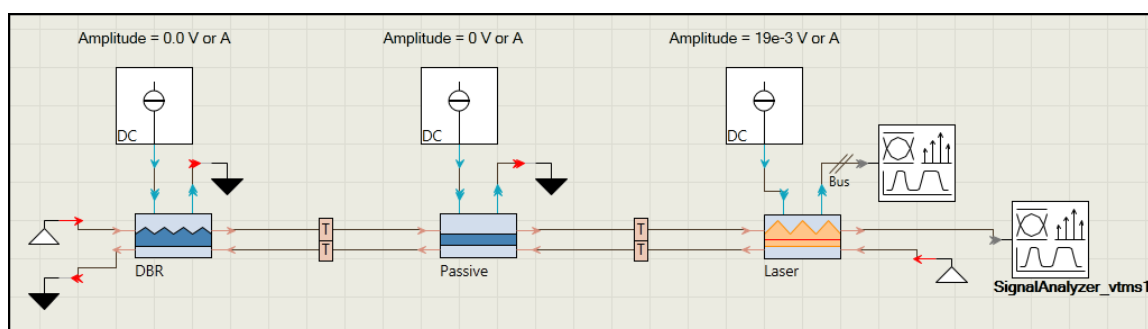


Fig. 8.1: The three-section TLD model in VPI.

The structure of the bulk TLD in VPI is shown in Fig. 8.1. It consists of three sections, the yellow and light-blue one on the right labeled “Laser” being the active

section, the grey and blue in the middle labeled “Passive” being the phase section and the grey and blue on the left labeled “DBR” being the DBR section. Each section is in fact a Transmission Line Laser Model (TLLM) of a semiconductor laser which can also be used as a separate device. However, when wired together with some modification of their optical parameters, they can act as a uniform TLD. The reason for choosing this structure is because there is no single component (box) in VPI which can act as a uniform three-section TLD. The TLD is shown in two dimensions, with y being the axis of device thickness and z being the axis of photon propagation and device length. The axis of propagation z moves now from right to left with $z=0 \mu\text{m}$ at the right facet of the active section and $z=800 \mu\text{m}$ at the left facet of the DBR section. Therefore the z axis moves in the opposite direction compared with the PICS3D TLD structure described in Chapter 5 (Fig. 5.1).

The active section of the TLD is a TLLM of a FP laser with a top input used for injecting current (connected with a DC source at steady-state or an AC source for modulation) and a top output used for plotting the carrier density when connected with a signal analyser. The right input can be used for optical injection but in this setup it is connected with a null source (white triangle). The right output used for plotting the optical signal in the time or frequency domain when connected with a signal analyser. The left input and output is connected with the right output and input of the phase section, respectively. The parameters of the active section are shown in Fig. 8.2.

Name:	Value	Unit
Device Structure		
DeviceSectionLength	400e-6	m
ActiveRegionType	Bulk	
ActiveRegionWidth	1.5e-6	m
ActiveRegionThickness	0.18e-6	m
CurrentInjectionEfficiency	0.95	
Optical Parameters		
NominalFrequency	$c / 1.553e-6$	Hz
EffectiveIndex	3.31	
GroupIndex	3.2	
PolarizationModel	TE	
InternalLoss	1500	1/m
InternalLossCarrierDependence	$2.2e-22$	m^2
ConfinementFactor	0.34	
OpticalCouplingEfficiency	1.0	
InterfaceReflectionCoefficient	0 0.3	
InterfaceReflectionPhaseLeft	0	deg
InterfaceTransmissionPhase	0.0	deg
DeviceSectionPhaseShift	0.0	deg
Nonlinear Parameters		
Grating Parameters		
GratingModel	NoGrating	
Gain Parameters		
GainShapeModel	File	
GainDataFile	ga1_08_15e24_VPI_42 ...	
Carrier Dynamics		
LinearRecombination	$1e8$	1/s
BimolecularRecombination	$2e-16$	m^3/s
AugerRecombination	$3.5e-41$	m^6/s
InitialCarrierDensity	$1.e+23$	$1/m^3$
Chirp Parameters		
ChirpModel	LinewidthFactor	
LinewidthFactor	5	
CarrierDensityRefIndex	0	$1/m^3$

Fig. 8.2: Parameters of the active section of the TLD in VPI.

The parameter NominalFrequency refers to the bandgap frequency $f_g = c/\lambda_g$ of the active region, where c is the speed of light in vacuum defined in the global parameters (shown later) and $\lambda_g = 1.553 \mu\text{m}$ is the bandgap wavelength of the active region, in order to provide an energy bandgap of $E_g = 1.24/\lambda_g = 0.7986 \text{ eV}$. The InternalLossCarrierDependence parameter is the $k_{FC} = 2 \times 10^{-19} \text{ cm}^2$ coefficient responsible for free-carrier absorption

which was used in Chapter 7. Unfortunately, VPI provides no option for IVBA losses therefore the $k_{IVBA} = 2 \times 10^{-18} \text{ cm}^2$ coefficient was simply added to the InternalLossCarrierDependence parameter ($k_{FC} + k_{IVBA} = 2.2 \times 10^{-18} \text{ cm}^2$) in order to take into account all losses as in the PICS3D TLD in Chapter 7. This value will be the same in all sections. The InterfaceReflectionCoefficient parameter defines the mirror reflectivities of each facet and the set of values [0 0.3] means that the left facet reflectivity is zero (all light is transmitted into the phase section with no reflection at the interface) and the right facet reflectivity R_a is 0.3. The GainShapeModel parameter defines the type of model used in VPI for the shape of the gain spectrum. If set to “File”, as in this case, then VPI takes straightforward the gain values needed for solving all equations at lasing conditions from a data file specified in the GainDataFile parameter. However, there are other types of gain models that can be specified as it will be discussed in the next subchapter. As a reminder, the gain spectrum of the VPI TLD which was imported from PICS3D is shown in Fig. 8.3.

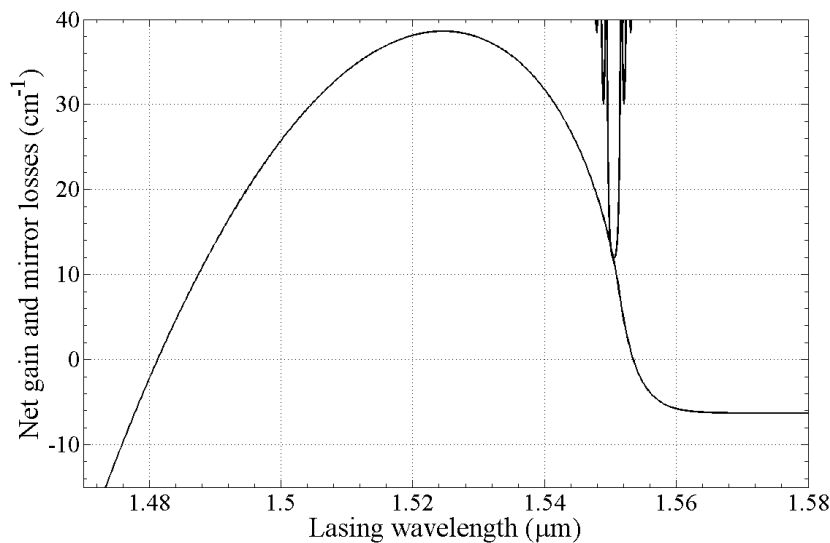


Fig. 8.3: Spectra of the net gain g_{net} and the cavity mirror losses a_m of the bulk TLD (VPI and PICS3D) at lasing wavelength $\lambda_0 = 1.55 \text{ μm}$.

The phase section of the TLD is a TLLM of a passive semiconductor device with zero gain and no grating, which is practically used as an optical waveguide. It has a top input used for injecting current (connected with a DC source for phase tuning) and a top output used for plotting the carrier density when connected with a signal analyser. However in this setup it is grounded (black triangle). The right input and output is connected with the left input and output of the active section. The left input and output is connected with the right output and input of the DBR section, respectively. The parameters of the phase section are shown in Fig. 8.4.

Parameters `ActiveRegionType`, `ActiveRegionWidth` and `ActiveRegionThickness` define the type, width and thickness of the passive waveguide of the phase section, respectively. The bandgap wavelength here is $\lambda_g=1.46 \mu\text{m}$, in order to provide an energy bandgap of $E_g = 1.24/\lambda_g = 0.85 \text{ eV}$. The `InterfaceReflectionCoefficient` parameter is zero for both facets which means that all light is transmitted from the active section into the DBR section and vice versa with no reflection at the interfaces. The `DifferentialIndex` parameter defines the coefficient of the FC plasma effect and will be discussed again when the TLD is tuned. This parameter has the same value in the DBR section as well.

Name:	Value	Unit
Device Structure		
DeviceSectionLength	100e-6	m
ActiveRegionType	Bulk	
ActiveRegionWidth	1.5e-6	m
ActiveRegionThickness	0.38e-6	m
CurrentInjectionEfficiency	1	
Optical Parameters		
NominalFrequency	c / 1.46e-6	Hz
EffectiveIndex	3.31	
GroupIndex	3.2	
PolarizationModel	TE	
InternalLoss	500	1/m
InternalLossCarrierDependence	2.2e-22	m ²
ConfinementFactor	0.822	
OpticalCouplingEfficiency	1.0	
InterfaceReflectionCoefficient	0.0	
InterfaceReflectionPhaseLeft	0	deg
InterfaceTransmissionPhase	0.0	deg
DeviceSectionPhaseShift	0.0	deg
Nonlinear Parameters		
NonlinearIndex	0.0	m ² /W
TwoPhotonAbsorption	0.0	m/W
EffectiveModeArea	1e-12	m ²
ConfinementFactorNonlinear	1.0	
Carrier Dynamics		
LinearRecombination	1e8	1/s
BimolecularRecombination	1e-16	m ³ /s
AugerRecombination	1.5e-41	m ⁶ /s
InitialCarrierDensity	1.0e+21	1/m ³
Chirp Parameters		
DifferentialIndex	-1.47e-26	m ³
CarrierDensityRefrIndex	0	1/m ³

Fig. 8.4: Parameters of the phase section of the TLD in VPI.

The DBR section of the TLD is a TLLM of a passive semiconductor device with zero gain but with an option of a grating. It practically works as a passive waveguide with Bragg reflection. It has a top input used for injecting current (connected with a DC source for DBR tuning), a top output used for plotting the carrier density when connected with a signal analyser (grounded in this setup), a left input connected with a null source (which

can also be used for optical injection) and a left output which is grounded. The right input and output is connected with the left output and input of the phase section, respectively. The parameters of the DBR section are shown in Fig. 8.5.

Name:	Value	Unit
Device Structure		
f DeviceSectionLength	300e-6	m
ActiveRegionType	Bulk	
f ActiveRegionWidth	1.5e-6	m
f ActiveRegionThickness	0.38e-6	m
f CurrentInjectionEfficiency	1	
Optical Parameters		
f NominalFrequency	c / 1.46e-6	Hz
[f] EffectiveIndex	3.31	
f GroupIndex	3.4	
PolarizationModel	TE	
f InternalLoss	500	1/m
f InternalLossCarrierDependence	2.2e-22	m ²
f ConfinementFactor	0.822	
[f] OpticalCouplingEfficiency	1.0	
[f] InterfaceReflectionCoefficient	1e-40	
[f] InterfaceReflectionPhaseLeft	0	deg
[f] InterfaceTransmissionPhase	0.0	deg
[f] DeviceSectionPhaseShift	0.0	deg
Grating Parameters		
GratingModel	Coupling	
GratingStopbandFrequencyDefinition	Absolute	
f GratingStopbandFrequency	c / 1550.3e-9	Hz
f GratingPhaseShift	0.0	deg
f IndexCoupling	5000	1/m
f IndexCouplingCarrierDependence	0	m ²
[f] IndexCouplingPhase	0.0	deg
f GainCoupling	0.0	1/m
f GainCouplingCarrierDependence	0	m ²
[f] GainCouplingPhase	0.0	deg
f CarrierDensityRefGrating	1.2e+24	1/m ³
Carrier Dynamics		
f LinearRecombination	1e8	1/s
f BimolecularRecombination	1e-16	m ³ /s
f AugerRecombination	1.5e-41	m ⁶ /s
f InitialCarrierDensity	1.0e+21	1/m ³
Chirp Parameters		
f DifferentialIndex	-1.47e-26	m ³
f CarrierDensityRefIndex	0	1/m ³

Fig. 8.5: Parameters of the DBR section of the TLD in VPI.

Parameters `ActiveRegionType`, `ActiveRegionWidth` and `ActiveRegionThickness` define the type, width and thickness of the passive waveguide of the DBR section, respectively. The bandgap wavelength here is $\lambda_g=1.46 \mu\text{m}$, in order to provide an energy bandgap of $E_g = 1.24/\lambda_g = 0.85 \text{ eV}$. The left facet reflectivity R_r is 10^{-4} and the right facet reflectivity is zero (all light is transmitted into the phase section with no reflection at the interface). The `GratingModel` parameter defines the design of the grating structure by VPI. If set to “Coupling” as in this case, then VPI uses the coupling coefficient to define the grating structure. The `GratingStopbandFrequency` parameter is the Bragg frequency $f_B=c/\lambda_B$ of the active region, where $\lambda_B=1.5503 \mu\text{m}$ is the Bragg wavelength. The `IndexCoupling` parameter is the coupling coefficient $\kappa=50 \text{ cm}^{-1}$.

In the following figures, some basic characteristics of the VPI TLD operating at steady-state will be shown in comparison with the same characteristics from the PICS3D TLD operation. Fig. 8.6 and Fig. 8.7 show the L-I characteristic of the VPI TLD and the PICS3D TLD, respectively. As can be seen the two curves are very similar which means that VPI recreates properly the TLD setup used in PICS3D.

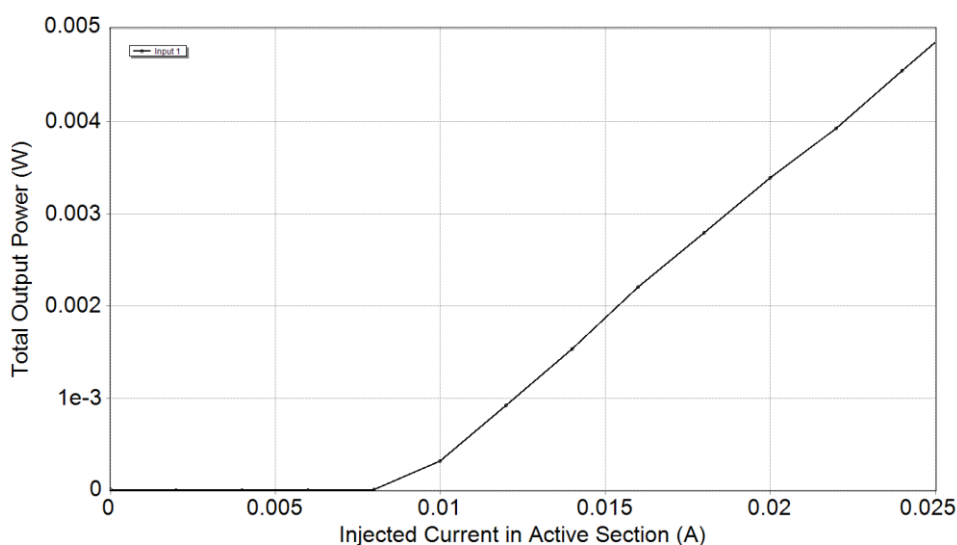


Fig. 8.6: Output power-Injected current (L-I) characteristic of the TLD in VPI.

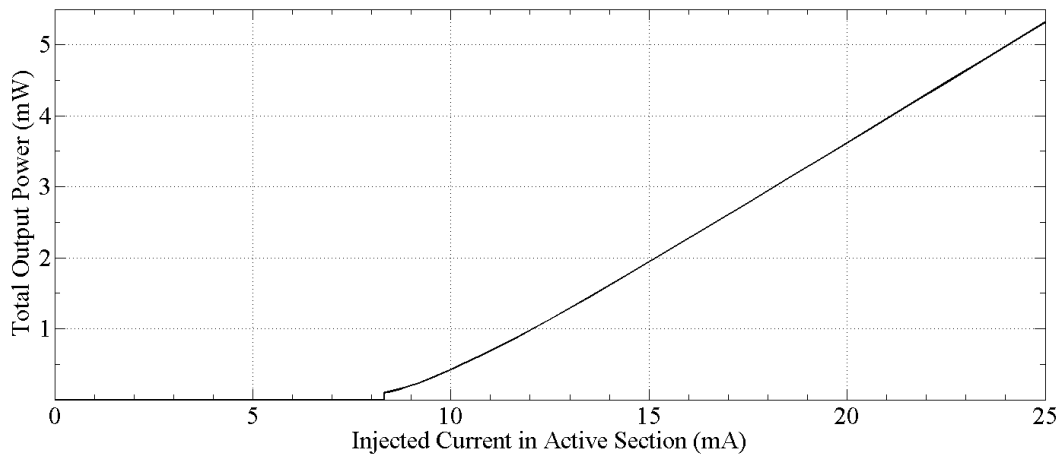


Fig. 8.7: Output power-Injected current (L-I) characteristic of the TLD in PICS3D.

The threshold current I_{th} was measured to be $I_{th} \approx 8.5$ mA for the VPI TLD which was very close to $I_{th} \approx 8.3$ mA for the PICS3D TLD. The threshold carrier density N_{th} was found to be $N_{th} \approx 1.2 \times 10^{18} \text{ cm}^{-3}$ for a lasing wavelength λ_0 of $\lambda_0 = 1.55 \text{ } \mu\text{m}$ which is exactly the same N_{th} for the PICS3D TLD for the same λ_0 . The threshold carrier density as a function of time is shown in Fig. 8.8.

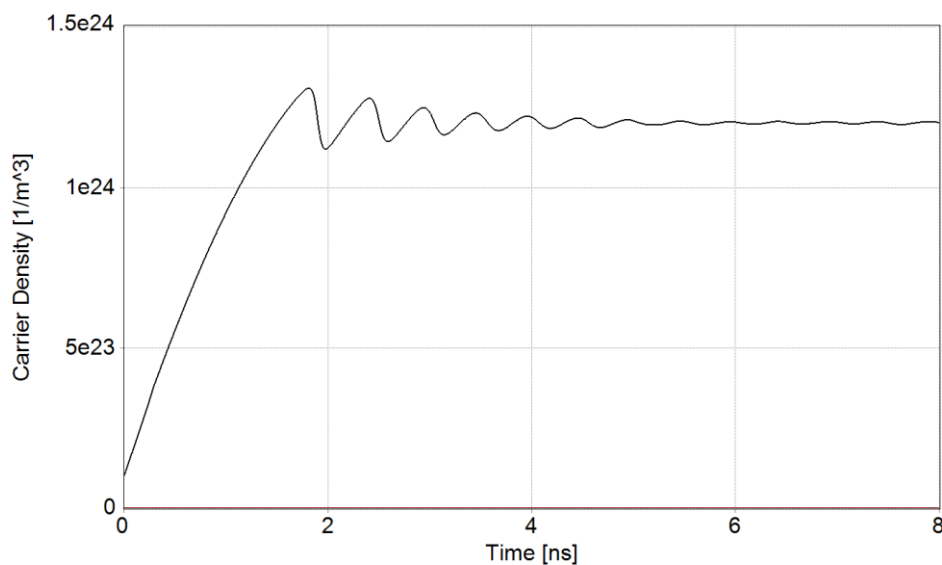


Fig. 8.8: Threshold carrier density as a function of time of the TLD in VPI.

The VPI TLD was free-running for 8 ns and at the start of the TLD operation a few oscillations can be observed until the TLD relaxes around the value of N_{th} . The time period (6 ns) of these oscillations is the turn-on delay of the TLD in order to achieve steady-state operation. The pulse response in the time domain of the VPI TLD for the same 8 ns is shown in Fig. 8.9 and the optical spectrum (wavelength domain) of the VPI TLD at $\lambda_0=1.55 \mu\text{m}$ is shown in Fig. 8.10.

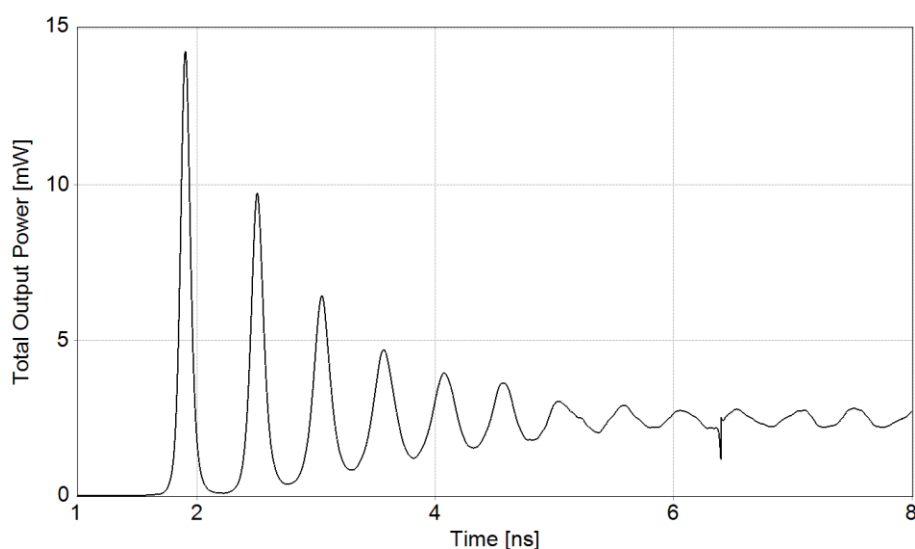


Fig. 8.9: Pulse response as a function of time of the TLD in VPI.

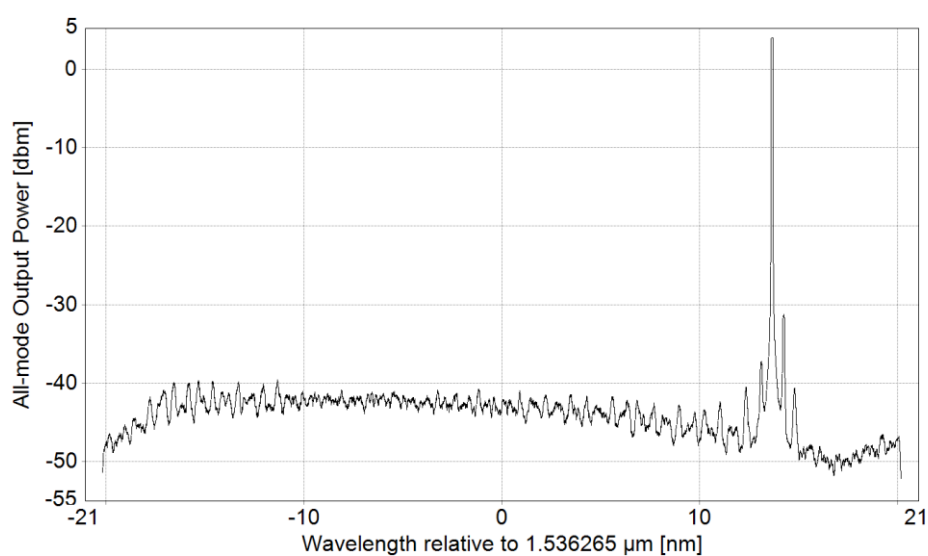


Fig. 8.10: Optical spectrum in the wavelength domain of the TLD in VPI at $\lambda_0=1.55 \mu\text{m}$.

The values of the x axis of Fig. 8.10 show the wavelength shift in nm from the center wavelength $\lambda_c=1.536265 \mu\text{m}$. The center wavelength is at the exact center of the optical spectrum (zero position) and its role will be explained later in the following subchapter. As can be seen, the lasing wavelength λ_0 is shifted by roughly 13.7 nm from λ_c , therefore $\lambda_0=1.55 \mu\text{m}$.

The VPI TLD performance under DBR tuning was also investigated. The DBR section was injected with a value of current I_{DBR} of $I_{DBR} \approx 400 \text{ mA}$, which corresponds to a DBR carrier density N_{DBR} of $N_{DBR} \approx 5.86 \times 10^{18} \text{ cm}^{-3}$ (same N_{DBR} for the PICS3D TLD for the same I_{DBR}). The DBR carrier density is plotted as a function of time in Fig. 8.11. The phase section is not injected with current ($I_p=0 \text{ mA}$) in all the investigations of this Chapter, therefore no phase tuning is taking place.

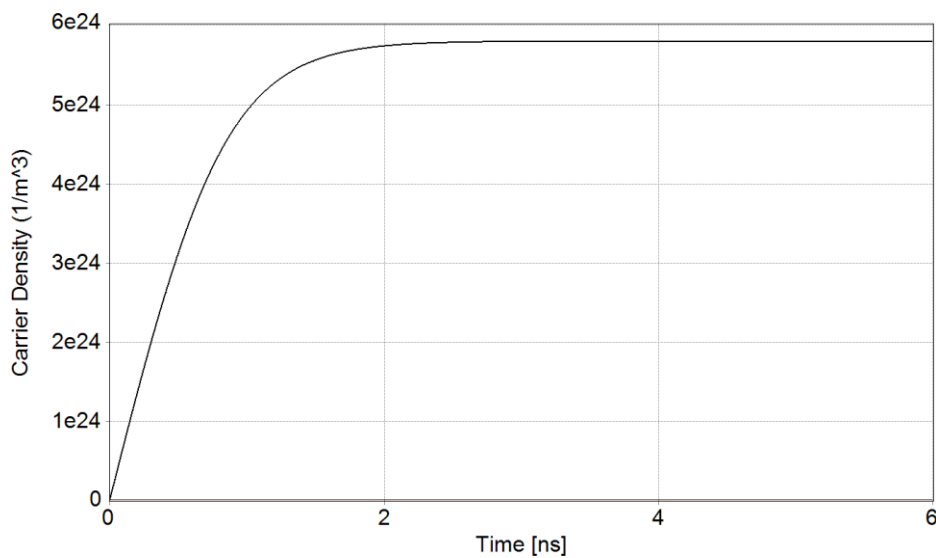


Fig. 8.11: Carrier density of the DBR section of the TLD in VPI as a function of time for $I_{DBR} \approx 400 \text{ mA}$.

The TLD is discontinuously tuned from the initial lasing wavelength $\lambda_0=1.55 \mu\text{m}$ to the lasing wavelength of $\lambda=1.518 \mu\text{m}$, which is a tuning range of $\Delta\lambda_{DBR}=32 \text{ nm}$ (as in the

case of DBR tuning of the PICS3D TLD). The wavelength shift $\Delta\lambda_{DBR}$ is connected with the injected carrier density in the DBR section N_{DBR} as in (3.54) $\Delta\lambda_{DBR} = (\beta_{pl}\Gamma_{DBR}\lambda_B / n'_{g,eff})N_{DBR}$, where β_{pl} is the FC plasma coefficient, $\Gamma_{DBR} = 0.822$ is the confinement factor of the DBR section, $\lambda_B = 1.5503 \mu\text{m}$ is the Bragg wavelength and $n'_{g,eff} = 3.4$ is the real part of the effective group index. Unfortunately, VPI considers the FC plasma effect as the only contribution to the refractive index change, which is responsible for wavelength tuning. However, in PICS3D the spectral dependence of the refractive index from the Kramers-Kronig relations was also present. Therefore, in order to include both contributions to $\Delta n'$ in VPI, the value of β_{pl} had to be increased from $\beta_{pl} = -0.7 \times 10^{-26} \text{ m}^3$ in PICS3D to $\beta_{pl} = -1.47 \times 10^{-26} \text{ m}^3$. This value is given to the DifferentialIndex parameter of both the phase and the DBR section.

The optical spectrum in the wavelength domain of the VPI TLD at $\lambda = 1.518 \mu\text{m}$ (shifted by roughly -18.2 nm from λ_c) is shown in Fig. 8.12. The inter-mode distance $\Delta\lambda_m$ was measured to be $\Delta\lambda_m = 0.63 \text{ nm}$ which was the same as in the PICS3D TLD.

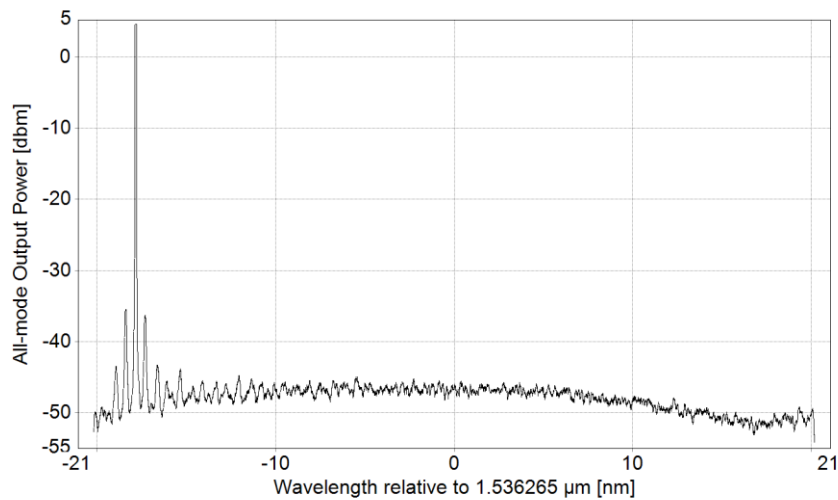


Fig. 8.12: Optical spectrum in the wavelength domain of the TLD in VPI at $\lambda = 1.518 \mu\text{m}$.

Fig. 8.13 shows the output power from all modes of the TLD during DBR tuning as a function of the injected DBR current. Again, as can be observed the power variation is very similar to the one of the PICS3D TLD during DBR tuning for the same value of I_{DBR} (shown in Fig. 8.14).

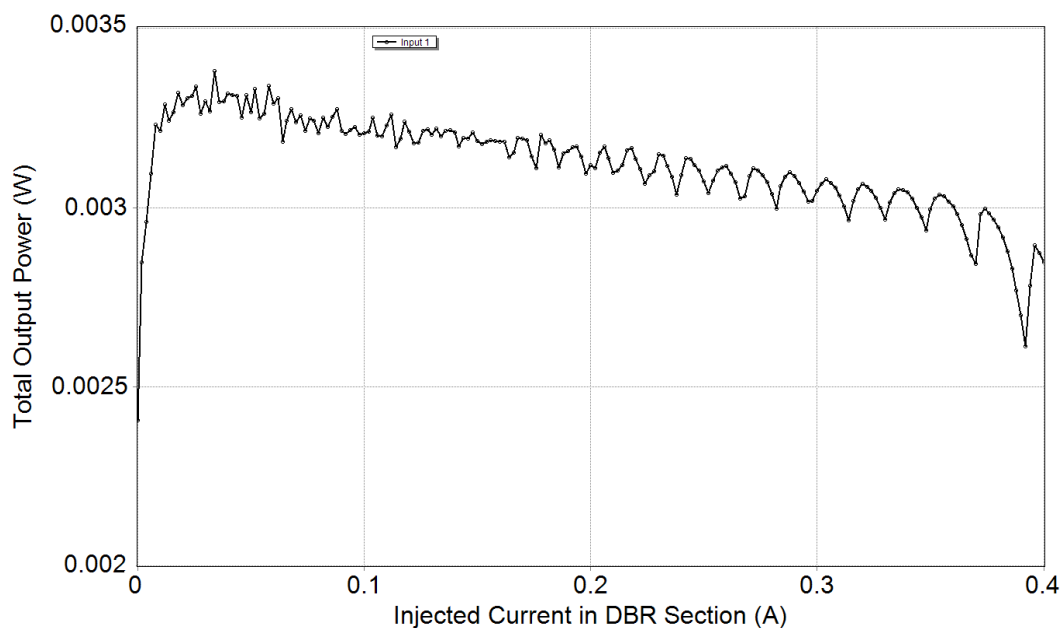


Fig. 8.13: The output power of the TLD in VPI as a function of the DBR section current.

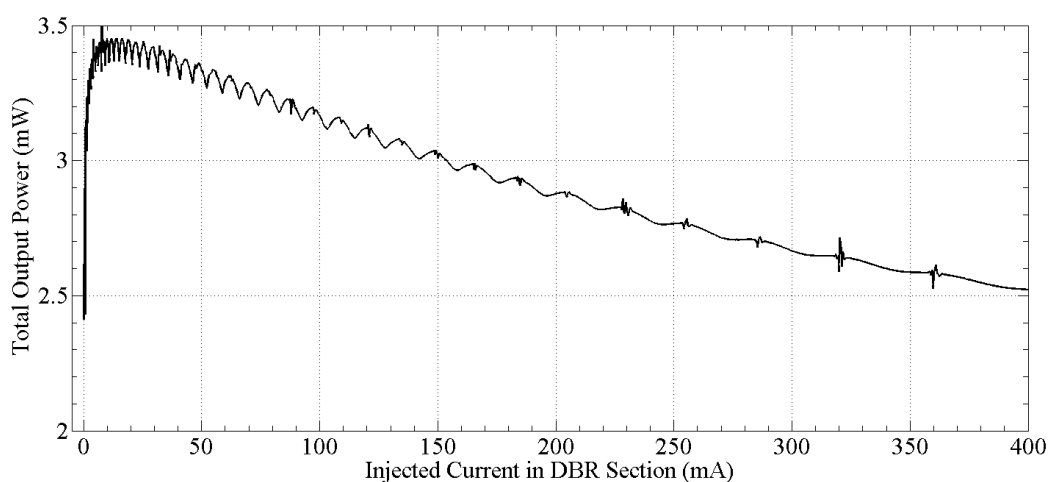


Fig. 8.14: The output power of the TLD in PICS3D as a function of the DBR section current.

It can be therefore concluded that the representation of the PICS3D TLD in VPI was done successfully with very similar results of laser operation.

8.2.2 Small-signal analysis of bulk TLDs during discontinuous tuning

The next part of the investigation in this Chapter is the performance of the TLD under direct intensity modulation with and without DBR tuning. The global parameters of the setup which was used in all simulations are shown in Fig. 8.15.

Name:	Value	Unit
Global		
f TimeWindow	32/10e9	s
i GreatestPrimeFactorLimit	2	
InBandNoiseBins	OFF	
BoundaryConditions	Aperiodic	
LogicalInformation	ON	
f SampleModeBandwidth	5120e9	Hz
f SampleModeCenterFrequency	$(c / (lo - (Gbw/2)))$	Hz
f SampleRateDefault	2560e9	Hz
f BitRateDefault	10e9	bit/s
DesignRules		
TrackingMode	None	
Player		
f Gbw	42e-9	m
f c	299792458	m/s
f lo	1.557e-6	m
f ModulationDepth	0.5e-3	
f ModulationFrequency	1e9	
f DUT_DC_Bias	19e-3	

Fig. 8.15: Global parameters of the IM setup in VPI.

The TimeWindow parameter defines the simulation time for which the setup is running (3.2 ns in this case). The SampleModeBandwidth parameter defines the range of frequencies in the frequency domain in which the simulation takes place and is also the inverse of the TimeWindow parameter ($\text{SampleModeBandwidth} = 1 / \text{TimeWindow}$). Its

value in this setup is 5.12 THz or 42 nm in the wavelength domain. It also defines the length ΔL of the sections in which the TLD is divided during a simulation (a kind of meshing as in the case of PICS3D). It therefore defines the accuracy of the obtained results and it is recommended to have a value of at least 5.12 THz or higher. The bandwidth of the imported gain spectrum is also 42 nm in the wavelength domain and it is defined by the Gbw parameter. The lo parameter defines the starting wavelength of the gain spectrum and has a value of 1.557 μm .

Therefore the wavelength range of the gain spectrum will be [1.557, 1.515] μm . The SampleModeCenterFrequency parameter defines the center frequency f_c of the SampleModeBandwidth which divides it in two equal parts as follows [-2.56, f_c , 2.56] THz. The value of f_c is $f_c = c/\lambda_{cg}$, where the c parameter defines the speed of light in vacuum and has a value of 299792458 m/s and $\lambda_{cg} = lo - (Gbw/2) = 1.536265 \mu\text{m}$ is the center wavelength of the gain spectrum in the wavelength domain. Therefore, it was chosen for the SampleModeBandwidth and the gain spectrum to have the same range in THz/nm and the same center frequency/wavelength in the frequency and wavelength domain, respectively. Fig. 8.16 shows the simulated setup for all investigations of the TLD performance under direct IM.

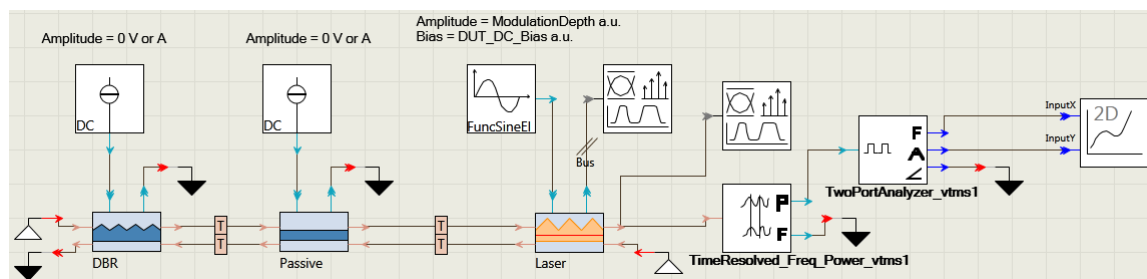


Fig. 8.16: The setup of the TLD under direct intensity modulation in VPI.

The three-section TLD is directly IM modulated as follows: A DC current I_{dc} is injected from the top contact of the active section with the component FuncSineEl. It is defined by the DUT_DC_Bias parameter and has a value of 19 mA $> 2I_{th}$ as is shown in the global parameters. On top of that current, an AC current is also injected to the active section by FuncSineEl. This is the modulation current I_{ac} which is defined by the ModulationDepth parameter and has a small value of 0.5 mA. The setup then uses a sweep function which modulates the TLD with a range of modulation frequencies starting from 0 GHz and increasing with a small frequency step until it reaches the value of 10 GHz. The frequency step f_s is reversely proportional to the TimeWindow and is defined as $f_s = 1/\text{TimeWindow} = (10/32) \times 10^9 = 0.3125$ GHz. The TLD is therefore swept with all these modulation frequencies until one frequency is found where it is in resonance. This frequency will be the ROF f_R in Hz of the TLD,.

The modulated output power P_m of the TLD is then measured with the TimeResolved_Freq_Power_vtms1 component and then passed to the TwoPortAnalyzer_vtms1 component. This component measures the root mean square (rms) value of P_m and it divides it with I_{ac} . It then sends this data from the 'A' (Amplitude) output port to the 2D component where they are plotted in the y axis. The TwoPortAnalyzer_vtms1 component also sends the modulation frequency bandwidth [0 : 0.3125 : 10] GHz from the 'F' (Frequency) output port to the 2D component where they are plotted in the x axis.

The IM response of the setup when the TLD is directly intensity modulated for the frequency bandwidth of [0, 10] GHz for the case of no tuning ($\lambda_0=1.55$ μm , $I_{DBR}=0$ mA) (black curve) is shown in Fig. 8.17.

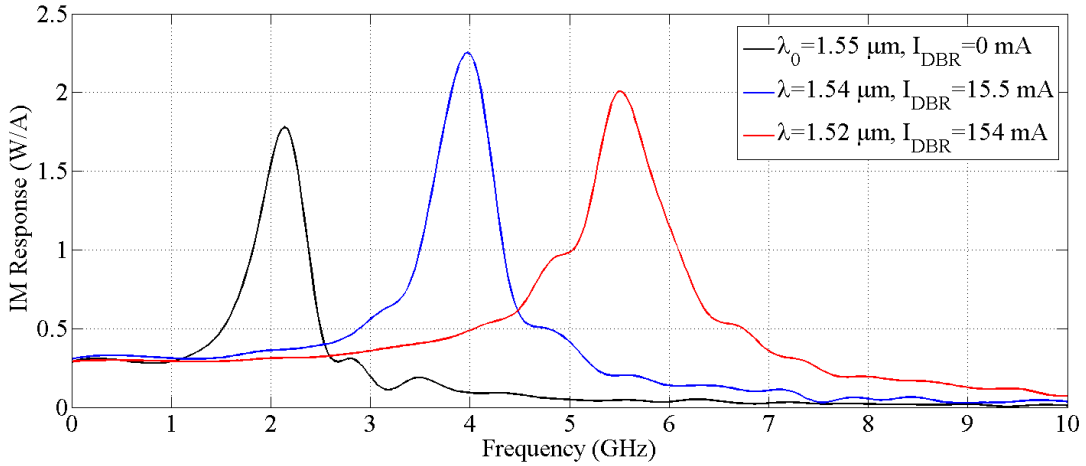


Fig. 8.17: IM responses of the TLD for $I_{dc}=19$ mA with ($\lambda=1.54$ μm , $\lambda=1.52$ μm) and without tuning ($\lambda_0=1.55$ μm).

The ROF was measured to be $f_R=2.19$ GHz. The unmodulated output power P_{dc} which corresponds to $I_{dc}=19$ mA was measured to be $P_{dc}=3$ mW. In order to check its accuracy this result was compared with the value of ω_R which can be obtained from the laser theory of small-signal analysis and is defined in rad/s as [114]:

$$\omega_R = \sqrt{\frac{\Gamma_a (\langle a_i \rangle + a_m)}{hVn_{ga}a_m} \alpha P_{dc} \lambda} \quad (8.1)$$

where Γ_a is the confinement factor of the active region, $\langle a_i \rangle$ are the average internal losses, a_m are the mirror losses, $h = 6.62606957 \times 10^{-34}$ m²kg/s is the Planck constant, $V = L_a w d_a$ is the volume of the active region, n_{ga} is the group index of the active region, $\alpha = \frac{dg}{dN}$ is the differential gain, P_{dc} is the unmodulated output power of the laser and λ is the lasing wavelength. The equation of ω_R refers to the dominant lasing mode of the laser so in principle it can be applied to both multi-mode and single-mode lasers, as in a TLD in this case.

The average internal losses are defined as:

$$\langle a_i \rangle = \frac{a_{ia}L_a + a_{ip}(L_p + L_{eff})}{L_{eff, TLD}}$$

where $L_{eff, TLD} = L_a + L_p + L_{eff}$ is the effective length of the composite TLD cavity and $L_{eff} = \tanh(\kappa L_d) / 2\kappa$ is the DBR penetration depth.

The term $(\Gamma_a(\langle a_i \rangle + a_m)) / hVn_g a_m$ in (8.1) is constant so the only terms that need to be measured every time are α , P_{dc} and λ . The differential gain was measured from the gain spectrum to be $\alpha = \frac{dg}{dN} = 1.67 \times 10^{-20} \text{ m}^2$, where the value dg was taken at $\lambda_0 = 1.55 \text{ }\mu\text{m}$ for a very small $dN = 0.01 \times 10^{18} \text{ cm}^{-3}$ around N_{th} which was measured as $N_{th} \approx 1.2 \times 10^{18} \text{ cm}^{-3}$.

Equation (8.1) now gives $f_R = \omega_R / 2\pi = 2.33 \text{ GHz}$ (transformation in Hz) which is in a 93% agreement with the measured one. Therefore, the obtained results from the VPI simulation are in very good agreement with the small-signal analysis theory of lasers.

The next investigation focused on the behaviour of the directly intensity modulated TLD under DBR tuning in the tuning range of $\Delta\lambda = 32 \text{ nm}$ ($[1.55, 1.518] \text{ }\mu\text{m}$ as was shown in Fig. 8.12). The DBR section was injected with a value of current of $I_{DBR} = 15.5 \text{ mA}$, which caused a wavelength shift of 10 nm with lasing taking place now at $\lambda = 1.54 \text{ }\mu\text{m}$. The IM response of the setup is plotted in Fig. 8.17 (blue curve) and the ROF was increased and measured to be $f_R = 4.69 \text{ GHz}$.

The unmodulated output power was also increased to $P_{dc} = 4 \text{ mW}$ as was expected from Fig. 8.13 since the gain peak was not yet reached (Fig. 8.3). The threshold carrier density was accordingly decreased to $N_{th} \approx 0.97 \times 10^{18} \text{ cm}^{-3}$ as less carriers are required to achieve lasing conditions because of the increase of the gain values (it should be noted that $\lambda = 1.54 \text{ }\mu\text{m}$ is still on the ascending part of the gain spectrum). The differential gain

was now increased greatly and measured to be $\alpha = 6.39 \times 10^{-20} \text{ m}^2$. Equation (8.1) now gives $f_R = 5.27 \text{ GHz}$ which is in a 88% agreement with the measured one. It can therefore be derived that the reason of the ROF increase is the increase of both α and P_{dc} . The decrease of λ did not affect the ROF increase as much because the rate of the increase $\frac{d\alpha}{d\lambda}$ and $\frac{dP_{dc}}{d\lambda}$ of α and P_{dc} , respectively during tuning was much greater than the rate of decrease $\frac{d\lambda}{\lambda}$ of λ .

The TLD was further tuned by injecting the DBR section with a value of current of $I_{DBR} = 330 \text{ mA}$, which caused a wavelength shift of 30 nm with lasing taking place now at $\lambda = 1.52 \text{ }\mu\text{m}$. The IM response of the setup is plotted in Fig. 8.17 (red curve) and the ROF was again increased and measured to be $f_R = 5.94 \text{ GHz}$.

The unmodulated output power was now decreased to $P_{dc} = 3.65 \text{ mW}$ as was expected from Fig. 8.13 since $\lambda = 1.52 \text{ }\mu\text{m}$ is now past the gain peak (Fig. 8.3). The threshold carrier density was accordingly increased to $N_{th} \approx 1.03 \times 10^{18} \text{ cm}^{-3}$ as more carriers are required to achieve lasing conditions because of the decrease of the gain values (it should be noted that $\lambda = 1.54 \text{ }\mu\text{m}$ is now on the descending part of the gain spectrum). The differential gain was still increased greatly and measured to be $\alpha = 12.04 \times 10^{-20} \text{ m}^2$.

Equation (8.1) now gives $f_R = 6.86 \text{ GHz}$ which is in a 87% agreement with the measured one. It can therefore be concluded that the main reason of the ROF increase is the increase of α . The decrease of λ and P_{dc} did not affect the ROF increase as much because now the rate of the increase $\frac{d\alpha}{d\lambda}$ of α during tuning was much greater than the rate of decrease $\frac{d\lambda}{\lambda}$ and $\frac{dP_{dc}}{d\lambda}$ of λ and P_{dc} , respectively.

This last conclusion can be more strongly supported if the same process described above (variable P_{dc}) is repeated and P_{dc} is kept stable (the same with $P_{dc}=3$ mW at $\lambda_0=1.55$ μm) during tuning by carefully adjusting I_{dc} at each wavelength shift. The TLD was again tuned to lase at $\lambda=1.54$ μm by injecting a current of $I_{DBR}=15.5$ mA in the DBR section. The power $P_{dc}=3$ mW was kept stable by adjusting the DC current to be $I_{dc}=15.5$ mA this time. The measured ROF was now $f_R=4.06$ GHz, with $N_{th} \approx 0.97 \times 10^{18} \text{ cm}^{-3}$ and $\alpha = 6.39 \times 10^{-20} \text{ m}^2$ remaining the same as before at $\lambda=1.54$ μm . Equation (8.1) now gives $f_R=4.57$ GHz which is in a 89% agreement with the measured one.

In similar fashion with the tuning process of variable P_{dc} , the TLD was further tuned to longer wavelengths at $\lambda=1.52$ μm by injecting a current of $I_{DBR}=330$ mA in the DBR section. The power $P_{dc}=3$ mW was kept stable by adjusting the DC current to be $I_{dc}=16.75$ mA this time. The measured ROF was now $f_R=5.46$ GHz, with $N_{th} \approx 1.03 \times 10^{18} \text{ cm}^{-3}$ and $\alpha = 12.04 \times 10^{-20} \text{ m}^2$ remaining the same as before at $\lambda=1.52$ μm . Equation (8.1) now gives $f_R=6.22$ GHz which is in a 88% agreement with the measured one.

The measured ROFs are plotted for the two cases of variable (black curve) and stable (blue curve) P_{dc} during tuning as a function of lasing wavelength in Fig. 8.18. The measured values of α during tuning as a function of lasing wavelength are shown in Fig. 8.19.

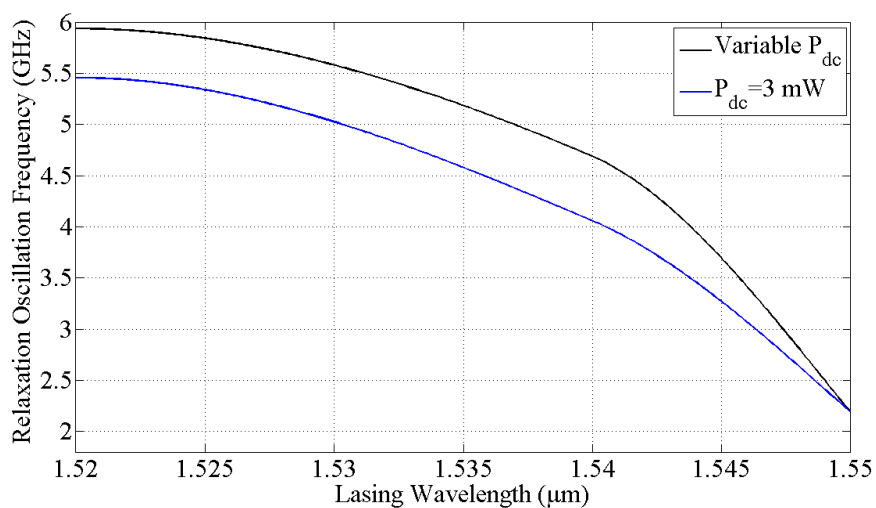


Fig. 8.18: ROFs for variable (black curve) and stable (blue curve) P_{dc} during tuning as a function of lasing wavelength.

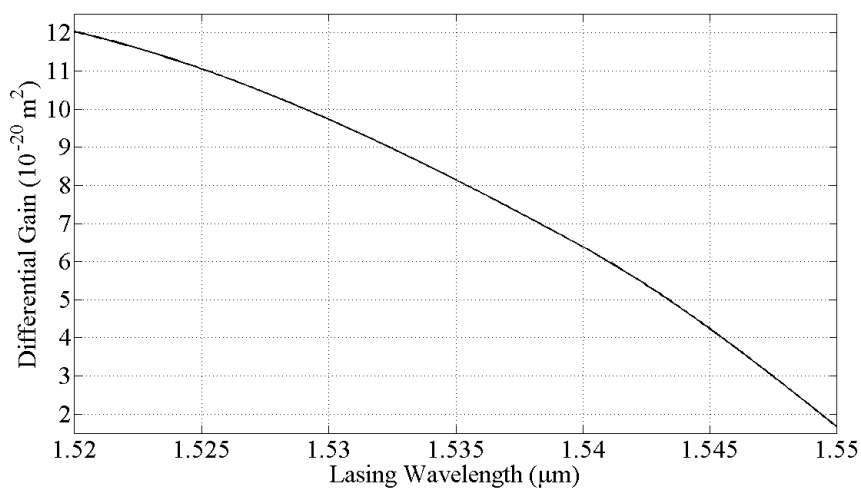


Fig. 8.19: Differential gain during tuning as a function of lasing wavelength.

It can easily be concluded by observing Fig. 8.18 and Fig. 8.19 that the rate of the increase of the differential gain dominates the performance of the TLD under direct intensity modulation during tuning and is the main reason for the increase of ROF during DBR wavelength tuning.

8.3 Conclusion

The performance of a bulk TLD in CW operation and under direct intensity modulation during discontinuous tuning has been investigated. The modeling of the TLD was done with the use of the commercial software simulation tool VPI. All the physical and material parameters of the VPI TLD were taken from the bulk TLD modeled with the use of PICS3D, described in Chapter 7 and shown in Fig. 7.16 and 7.17. The two TLDs had the same device structure, the same optical and electronic parameters and the same gain profile. Some basic optical characteristics were plotted (L-I characteristic, carrier density, optical spectrums, optical power vs DBR current during DBR tuning), which were in very good agreement with the ones acquired from PICS3D.

The TLD was directly intensity modulated during discontinuous tuning and it was shown that there are three parameters that affect its resonance frequency; the differential gain, the unmodulated output power and the lasing wavelength. A significant increase of the resonance frequency at the end of the tuning range was observed. It was proved that this increase was mainly caused by the great increase of the differential gain with the wavelength change. The change of power and lasing wavelength during tuning was much smaller than the change of the differential gain and contributed little to the change of the resonance frequency.

Chapter 9

Conclusions and future work

9.1 Overall conclusions

An overview of all the conclusions made Chapter by Chapter in this thesis is presented in this subsection.

In Chapter 5, different FC contributions to the real part of the refractive index change were investigated, as well as their effect on the output lasing wavelength of the device. The FC contributions in question were the FC plasma effect and the inter-band optical transitions which were calculated by using the Kramers-Kronig (KK) relations (band-filling effect). The contribution of each effect was investigated separately by activating one effect each time as well as when they acted together. It was shown that the band-filling effect instead of the plasma effect is the dominant contributor to the real part of the refractive index change, which also shapes the corresponding wavelength tuning performance of the device. This shows that the band-filling effect is heavily underestimated due to the lack of investigation of this effect in published literature as a contributor to the refractive index change, a statement which is also supported by the experimental work of [119] and the theoretical work of [131]. It was also found that the available refractive index change is not necessarily converted into the corresponding lasing wavelength shift due to design issues which will be explained in Chapter 6.

In Chapter 6, a completely self-consistent model of a multi-section TLD was developed and applied to investigate the wavelength tuning performance by using the commercial Crosslight PICS3D software simulation tool. Both the optical and FC transport phenomena were modeled on the same footage for the calculation of the wavelength tuning. Strong effects of the DBR grating design and various material parameters on the FC tuning and lasing spectral purity were demonstrated and explained.

In depth physical analysis of the FC tuning process and the TLD design optimisation were presented.

The analysis of the TLD operation suggested that the optimal design for the enhanced tunability is to use such κL products for the DBR section which resulted in the reflectivity spectrum with narrow bandwidth (covering 2-3 cavity modes) and sharp peak (i.e. without high reflectivity flat region) at the Bragg wavelength. The sharp peak was very important in order to avoid tuning saturation. By carefully tailoring the mutual positions of the gain spectra and the mirror reflectivity spectra, it was possible to considerably enhance the tuning range. The best performance of the TLD was achieved when the peak of the reflectivity is red-shifted with respect to the gain peak wave-length. In this case, good mode selection and reasonable (~ 10 nm) tuning was achieved due to asymmetry of the SMSR even for the DBR mirror reflectivities with a wide bandwidth covering many comb modes. However, the wavelength tuning of such devices would inevitably saturate as the lasing wave-length approached the gain peak wavelength. The saturation was avoided and the tuning range increased 2-3 times in the structures in which the DBR reflectivity had a sharp peak.

Further improvement was achieved by modifying *electronic* properties of DBR grating and by modifying the length of the phase section and thickness of its passive waveguide. Even for a basic 3-section TLD a record high FC tuning $\Delta\lambda_{discont} = 30$ nm, $\Delta\lambda_{cont} = 11$ nm and $\Delta\lambda_{quasicont} = 26$ nm was reported. The obtained results should be useful for practical development of real TLDs. The model can further be extended to more complex multi-section integrated photonic devices.

In Chapter 7, a model of 2 three-section TLDs, one with a bulk and one with a MQW optical cavity, was developed in order to investigate their output power behaviour

during wavelength tuning by using the simulation software PICS3D. In the case of the MQW TLD, the monitored power variation during discontinuous tuning ($\Delta\lambda_{discont} = 32$ nm) consisted of a small power increase in the first few wavelength changes of the tuning range followed by a significant power decrease with deeper tuning. This variation was caused by the shape of the gain spectrum and its interaction with the mirror reflectivity spectrum and the increasing optical losses of the passive regions during tuning.

The shape of the gain spectrum of the TLD was formed by a Lorentzian lineshape broadening function which in turn was defined by the intraband relaxation time τ_{in} . By carefully selecting τ_{in} and the positioning of the mirror reflectivity spectrum in respect to the gain peak, the power increase could be significantly enhanced. The opposite results were acquired for the same relaxation times in the case of the bulk TLD due to the proximity of the mirror reflectivity spectrum to the band edge and the by default broader gain spectrum of its AR due to the lack of energy subbands compared with the case of the MQW TLD.

The significant power decrease was managed to be eliminated leading to an output power stabilisation with deeper tuning in the case of continuous tuning for the proposed optimised TLD setup.

In Chapter 8, the performance of a bulk TLD in CW operation and under direct intensity modulation during discontinuous tuning has been investigated. The modeling of the TLD was done with the use of the commercial software simulation tool VPI. All the physical and material parameters of the VPI TLD were taken from the bulk TLD modeled with the use of PICS3D, described in Chapter 7 and shown in Fig. 7.16 and 7.17. The two TLDs had the same device structure, the same optical and electronic parameters and the same gain profile. Some basic optical characteristics were plotted (L-I characteristic,

carrier density, optical spectrums, optical power vs DBR current during DBR tuning), which were in very good agreement with the ones acquired from PICS3D.

The TLD was directly intensity modulated during discontinuous tuning and it was shown that there are three parameters that affect its resonance frequency; the differential gain, the unmodulated output power and the lasing wavelength. A significant increase of the resonance frequency at the end of the tuning range was observed. It was proved that this increase was mainly caused by the great increase of the differential gain with the wavelength change. The change of power and lasing wavelength during tuning was much smaller than the change of the differential gain and contributed little to the change of the resonance frequency.

9.2 *Recommended future work*

As part of future work, the author could give some recommendations on the areas on which further investigation can take place with the use of VPI:

- Small-signal analysis of a TLD with a MQW active region and investigation of the increase of ROF due to the huge increase of the MQW differential gain (indicator of MQW lasers) during tuning.
- Large-signal analysis (injection of electric rectangular pulses as an AC modulation current roughly twice the threshold current on top of the DC current in the active section) of both bulk and MQW TLDs during tuning as a stand-alone laser at various modulation speeds and for different bit generation formats [Non-Return to Zero (NRZ) and Return to Zero (RZ)].

- The use of the above TLD as a transmitter in an optical network at various bit rates and the investigation of the factors that limit its performance such as the effect of chirping of the TLD and attenuation, dispersion and non-linearities of the optical-fibre.
- Investigation of the enhancement of the modulation bandwidth in an optically injection-locked TLD (the effect of the external optical injection from the master laser into the modulated TLD on the maximal modulation speed).

The proposals below concern investigations in an optical network:

- Investigation of the effect of various intrinsic noise sources on the output bit stream of an optical network.
- The effect of Cross Phase Modulation (XPM) and the corruption that the optical fibre causes to the signal during transmission, due to its attenuation, dispersion and nonlinearities.
- The effect of intensity noise and Turn-On Delay Jitter (TOJ) on the general performance of the optical system. This can be estimated in terms of the power penalty of the system, eye diagrams of the received signal, and BER and signal-to-noise ratio (SNR) calculations. The sensitivity and other attributes of the photodiode that are used as a receiver can also be examined.

References

- [1] G. P. Agrawal, *Fiber-optic Communication Systems*. John Wiley & Sons, 2010.
- [2] G. E. Keiser, *Optical Fiber Communications*. McGraw-Hill, 2000.
- [3] T. H. Maiman, “Stimulated optical radiation in ruby,” *Nature*, vol. 187, no. 4736, pp. 493–494, Aug. 1960.
- [4] S. E. Miller, “Communication by laser,” *Sci. Am.*, vol. 214, no. 1, p. 19, 1966.
- [5] K. C. Kao and G. A. Hockham, “Dielectric-fibre surface waveguides for optical frequencies,” *Proc. Inst. Electr. Eng.*, vol. 113, no. 7, p. 1151, 1966.
- [6] F. P. Kapron, D. B. Keck, and R. D. Maurer, “Radiation losses in glass optical waveguides,” *Appl. Phys. Lett.*, vol. 17, no. 10, pp. 423–425, 1970.
- [7] R. J. Sanferrare, “Terrestrial Lightwave Systems,” *AT&T Tech. J.*, vol. 66, no. 1, pp. 95–107, Jan. 1987.
- [8] D. Gloge, A. Albanese, C. A. Burrus, E. L. Chinnock, J. A. Copeland, A. G. Dentai, T. P. Lee, T. Li, and K. Ogawa, “High-speed digital lightwave communication using LEDs and PIN photodiodes at 1.3 μm ,” *Bell Syst. Tech. J.*, vol. 59, no. 8, pp. 1365–1382, Oct. 1980.
- [9] T. Miya, Y. Terunuma, T. Hosaka, and T. Miyashita, “Ultimate low-loss single-mode fibre at 1.55 μm ,” *Electron. Lett.*, vol. 15, no. 4, p. 106, 1979.
- [10] G. Varella, F. Pitel, and J. F. Marcero, “Paper PD22,” in *Proc. Optical Fiber Commun. Conf.*, 2001.
- [11] A. Einstein, “Zur Quantentheorie der Strahlung,” *Phys. Zeitschrift*, vol. 18, pp. 121–128, 1917.
- [12] J. P. Gordon, H. J. Zeiger, and C. H. Townes, “The maser-new type of microwave

- amplifier, frequency standard, and spectrometer,” *Phys. Rev.*, vol. 99, no. 4, pp. 1264–1274, Aug. 1955.
- [13] A. L. Schawlow and C. H. Townes, “Infrared and optical masers,” *Phys. Rev.*, vol. 112, no. 6, pp. 1940–1949, Dec. 1958.
- [14] A. Javan, W. R. Bennett, and D. R. Herriott, “Population inversion and continuous optical maser oscillation in a gas discharge containing a He-Ne mixture,” *Phys. Rev. Lett.*, vol. 6, no. 3, pp. 106–110, Feb. 1961.
- [15] A. G. Fox and T. Li, “Resonant modes in a maser interferometer,” *Bell Syst. Tech. J.*, vol. 40, no. 2, pp. 453 – 488, Mar. 1961.
- [16] M. I. Nathan, W. P. Dumke, G. Burns, F. H. Dill, and G. Lasher, “Stimulated emission of radiation from GaAs p-n junctions,” *Appl. Phys. Lett.*, vol. 1, no. 3, pp. 62–64, 1962.
- [17] R. N. Hall, G. E. Fenner, J. D. Kingsley, T. J. Soltys, and R. O. Carlson, “Coherent light emission from GaAs junctions,” *Phys. Rev. Lett.*, vol. 9, no. 9, pp. 366–368, Nov. 1962.
- [18] T. M. Quist, R. H. Rediker, R. J. Keyes, W. E. Krag, B. Lax, A. L. McWhorter, and H. J. Zeigler, “Semiconductor maser of GaAs,” *Appl. Phys. Lett.*, vol. 1, no. 4, pp. 91–92, 1962.
- [19] J. von Neumann, “Notes on the photon-disequilibrium-amplification scheme (JvN), September 16, 1953,” *IEEE J. Quantum Electron.*, vol. 23, no. 6, pp. 659–673, Jun. 1987.
- [20] N. Holonyak and S. F. Bevacqua, “Coherent (visible) light emission from Ga(As_{1-x}P_x) junctions,” *Appl. Phys. Lett.*, vol. 1, no. 4, pp. 82–83, 1962.
- [21] T. Ikegami and Y. Suematsu, “Resonance-like characteristics of the direct modulation of a junction laser,” *Proc. IEEE*, vol. 55, no. 1, pp. 122–123, 1967.

- [22] Y. Nishimura, K. Kobayashi, T. Ikegami, and Y. Suematsu, "Hole-burning effect in semiconductor laser," in *Proc. Int. Quant. Electron. Conf.*, 1970, pp. 8–8.
- [23] Y. Nishimura, K. Kobayashi, T. Ikegami, and Y. Suematsu, "Axial-mode interactions in a semiconductor laser," *IECE Jpn. Tech. Rep. Quant. Electron.*, vol. QE71, no. 22, pp. 1–14, 1971.
- [24] H. Kogelnik, "On the propagation of Gaussian beams of light through lenslike media including those with a loss or gain variation," *Appl. Opt.*, vol. 4, no. 12, p. 1562, Dec. 1965.
- [25] S. E. Miller, "Integrated optics: An introduction," *Bell Syst. Tech. J.*, vol. 48, no. 7, pp. 2059–2069, Sep. 1969.
- [26] Z. I. Alferov, V. M. Andreev, E. L. Portnoi, and M. K. Trukan, "AlAs-GaAs heterojunction injection lasers with a low room-temperature threshold," *Sov. Phys. Semicond.*, vol. 3, no. 9, pp. 1107–1110, 1969.
- [27] I. Hayashi, M. B. Panish, P. W. Foy, and S. Sumski, "Junction lasers which operate continuously at room temperature," *Appl. Phys. Lett.*, vol. 17, no. 3, pp. 109–111, 1970.
- [28] H. Kroemer, "A proposed class of hetero-junction injection lasers," *Proc. IEEE*, vol. 51, no. 12, pp. 1782–1783, Dec. 1963.
- [29] H. Yonezu, I. Sakuma, K. Kobayashi, T. Kamejima, M. Ueno, and Y. Nannichi, "A GaAs-Al_xGa_{1-x}As double heterostructure planar stripe laser," *Jpn. J. Appl. Phys.*, vol. 12, no. 10, pp. 1585–1592, Oct. 1973.
- [30] H. Kogelnik and C. V. Shank, "Stimulated emission in a periodic structure," *Appl. Phys. Lett.*, vol. 18, no. 4, pp. 152–154, 1971.
- [31] H. Kogelnik and C. V. Shank, "Coupled-wave theory of distributed feedback lasers," *J. Appl. Phys.*, vol. 43, no. 5, pp. 2327–2335, 1972.

- [32] I. P. Kaminow, H. P. Weber, and E. A. Chandross, "Poly (methyl methacrylate) dye laser with internal diffraction grating resonator," *Appl. Phys. Lett.*, vol. 18, no. 11, pp. 497–499, 1971.
- [33] Y. Suematsu and M. Yamada, "Transverse mode control in semiconductor lasers," *IEEE J. Quantum Electron.*, vol. 9, no. 2, pp. 305–311, Feb. 1973.
- [34] Y. Suematsu and K. Hayashi, "General analysis of distributed Bragg reflector and laser resonator using it," in *Proc. Nat. Conv. IECE*, 1974, p. 1203.
- [35] M. Nakamura, A. Yariv, H. W. Yen, S. Somekh, and H. L. Garvin, "Optically pumped GaAs surface laser with corrugation feedback," *Appl. Phys. Lett.*, vol. 22, no. 10, pp. 515–516, 1973.
- [36] W. Streifer, D. R. Scifres, and R. D. Burnham, "Longitudinal modes in distributed feedback lasers with external reflectors," *J. Appl. Phys.*, vol. 46, no. 4, pp. 247–249, Apr. 1975.
- [37] M. Nakamura, K. Aiki, J. Umeda, and A. Yariv, "CW operation of distributed-feedback GaAs-GaAlAs diode lasers at temperatures up to 300 K," *Appl. Phys. Lett.*, vol. 27, no. 7, pp. 403–405, 1975.
- [38] F. K. Reinhart, R. A. Logan, and C. V. Shank, "GaAs-Al_xGa_{1-x}As injection lasers with distributed Bragg reflectors," *Appl. Phys. Lett.*, vol. 27, no. 1, pp. 45–48, 1975.
- [39] C. E. Hurwitz, J. A. Rossi, J. J. Hsieh, and C. M. Wolfe, "Integrated GaAs-AlGaAs double-heterostructure lasers," *Appl. Phys. Lett.*, vol. 27, no. 4, pp. 241–243, 1975.
- [40] Y. Suematsu, M. Yamada, and K. Hayashi, "A multi-hetero-AlGaAs laser with integrated twin guide," *Proc. IEEE*, vol. 63, no. 1, pp. 208–208, 1975.
- [41] D. B. Keck, R. D. Maurer, and P. C. Schultz, "On the ultimate lower limit of

- attenuation in glass optical waveguides,” *Appl. Phys. Lett.*, vol. 22, no. 7, pp. 307–309, 1973.
- [42] D. N. Payne and W. A. Gambling, “Zero material dispersion in optical fibres,” *Electron. Lett.*, vol. 11, no. 8, p. 176, 1975.
- [43] J. J. Hsieh, “Room-temperature operation of GaInAsP/InP double-heterostructure diode lasers emitting at 1.1 μm ,” *Appl. Phys. Lett.*, vol. 28, no. 12, pp. 283–285, 1976.
- [44] K. Oe and K. Sugiyama, “GaInAsP-InP double heterostructure lasers prepared by a new LPE apparatus,” *Jpn. J. Appl. Phys.*, vol. 15, no. 10, pp. 2003–2004, Oct. 1976.
- [45] Y. Itaya, Y. Suematsu, and K. Iga, “Carrier lifetime measurement of GaInAsP/InP double-heterostructure lasers,” *Jpn. J. Appl. Phys.*, vol. 16, no. 6, pp. 1057–1058, Jun. 1977.
- [46] T. Yamamoto, K. Sakai, S. Akiba, and Y. Suematsu, “Fast pulse behaviour of InGaAsP/InP double-heterostructure lasers emitting at 1.27 μm ,” *Electron. Lett.*, vol. 13, no. 5, p. 142, 1977.
- [47] S. Akiba, K. Sakai, Y. Matsushima, and T. Yamamoto, “Room temperature C.W. operation of InGaAsP/InP heterostructure lasers emitting at 1.56 μm ,” *Electron. Lett.*, vol. 15, no. 19, p. 606, 1979.
- [48] H. Kawaguchi, K. Takahei, Y. Toyoshima, H. Nagai, and G. Iwane, “Room-temperature C.W. operation of InP/InGaAsP/InP double heterostructure diode lasers emitting at 1.55 μm ,” *Electron. Lett.*, vol. 15, no. 21, p. 669, 1979.
- [49] I. P. Kaminow, R. E. Nahory, M. A. Pollack, L. W. Stulz, and J. C. Dewinter, “Single-mode C.W. ridge-waveguide laser emitting at 1.55 μm ,” *Electron. Lett.*, vol. 15, no. 23, p. 763, 1979.

- [50] S. Arai, M. Asada, Y. Suematsu, and Y. Itaya, "Room temperature CW operation of GaInAsP/InP DH laser emitting at 1.51 μm ," *Jpn. J. Appl. Phys.*, vol. 18, no. 12, pp. 2333–2334, Dec. 1979.
- [51] H. Kawanishi, Y. Suematsu, Y. Itaya, and S. Arai, " $\text{Ga}_x\text{In}_{1-x}\text{As}_y\text{P}_{1-y}$ - InP injection laser partially loaded with distributed Bragg reflector," *Jpn. J. Appl. Phys.*, vol. 17, no. 8, pp. 1439–1440, Aug. 1978.
- [52] Y. Sakakibara, K. Furuya, K. Utaka, and Y. Suematsu, "Single-mode oscillation under high-speed direct modulation in GaInAsP/InP integrated twin-guide lasers with distributed Bragg reflectors," *Electron. Lett.*, vol. 16, no. 12, p. 456, 1980.
- [53] K. Utaka, K. Kobayashi, K. Kishino, and Y. Suematsu, "1.5–1.6 μm GaInAsP/InP Integrated twin-guide lasers with first-order distributed Bragg reflectors," *Electron. Lett.*, vol. 16, no. 12, p. 455, 1980.
- [54] K. Utaka, K. Kobayashi, F. Koyama, Y. Abe, and Y. Suematsu, "Single-wavelength operation of 1.53 μm GaInAsP/InP buried-heterostructure integrated twin-guide laser with distributed Bragg reflector under direct modulation up to 1 GHz," *Electron. Lett.*, vol. 17, no. 11, p. 368, 1981.
- [55] K. Utaka, K. Kobayashi, and Y. Suematsu, "Lasing characteristics of 1.5 - 1.6 μm GaInAsP/InP integrated twin-guide lasers with first-order distributed Bragg reflectors," *IEEE J. Quantum Electron.*, vol. 17, no. 5, pp. 651–658, May 1981.
- [56] T. Tanbun-Ek, S. Arai, F. Koyama, K. Kishino, S. Yoshizawa, T. Watanabe, and Y. Suematsu, "Low threshold current CW operation of GaInAsP/InP buried heterostructure distributed Bragg-reflector integrated-twin-guide laser emitting at 1.5–1.6 μm ," *Electron. Lett.*, vol. 17, no. 25–26, p. 967, 1981.
- [57] K. Utaka, S. Akiba, K. Sakai, and Y. Matsushima, "Room-temperature CW operation of distributed-feedback buried-heterostructure InGaAsP/InP lasers

- emitting at 1.57 μm ,” *Electron. Lett.*, vol. 17, no. 25–26, p. 961, 1981.
- [58] T. Matsuoka, H. Nagai, Y. Itaya, Y. Noguchi, Y. Suzuki, and T. Ikegami, “CW operation of DFB-BH GaInAsP/InP lasers in 1.5 μm wavelength region,” *Electron. Lett.*, vol. 18, no. 1, p. 27, 1982.
- [59] K. Sekartedjo, N. Eda, K. Furuya, Y. Suematsu, F. Koyama, and T. Tanbun-Ek, “1.5 μm phase-shifted DFB lasers for single-mode operation,” *Electron. Lett.*, vol. 20, no. 2, p. 80, 1984.
- [60] J. P. van der Ziel, R. Dingle, R. C. Miller, W. Wiegmann, and W. A. Nordland, “Laser oscillation from quantum states in very thin GaAs–Al_{0.2}Ga_{0.8}As multilayer structures,” *Appl. Phys. Lett.*, vol. 26, no. 8, p. 463, Sep. 1975.
- [61] E. A. Rezek, N. Holonyak, B. A. Vojak, G. E. Stillman, J. A. Rossi, D. L. Keune, and J. D. Fairing, “LPE In_{1-x}Ga_xP_{1-z}As_z ($x=0.12$, $z=0.26$) DH laser with multiple thin-layer (<500 Å) active region,” *Appl. Phys. Lett.*, vol. 31, no. 4, p. 288, Aug. 1977.
- [62] G. C. Osbourn, “In_xGa_{1-x}As – In_yGa_{1-y}As strained-layer superlattices: A proposal for useful, new electronic materials,” *Phys. Rev. B*, vol. 27, no. 8, pp. 5126–5128, Apr. 1983.
- [63] A. R. Adams, “Band-structure engineering for low-threshold high-efficiency semiconductor lasers,” *Electron. Lett.*, vol. 22, no. 5, p. 249, 1986.
- [64] P. J. A. Thijs, L. F. Tiemeijer, P. I. Kuindersma, J. J. M. Binsma, and T. Van Dongen, “High-performance 1.5 μm wavelength InGaAs-InGaAsP strained quantum well lasers and amplifiers,” *IEEE J. Quantum Electron.*, vol. 27, no. 6, pp. 1426–1439, Jun. 1991.
- [65] A. Salhi, M. Alanzi, and B. Alonazi, “Effect of the quantum-well shape on the performance of InGaN-based light-emitting diodes emitting in the 400–500-nm range,” *J. Disp. Technol.*, vol. 11, no. 3, pp. 217–222, Mar. 2015.

- [66] Y.-H. Hsiao, M.-L. Tsai, and J.-H. He, "GaN-based multiple-quantum-well light-emitting diodes employing nanotechnology for photon management," *IEEE Trans. Ind. Appl.*, vol. 51, no. 2, pp. 1277–1283, Mar. 2015.
- [67] J. M. T. Huikari, E. A. Avrutin, B. S. Ryvkin, J. J. Nissinen, and J. T. Kostamovaara, "High-energy picosecond pulse generation by gain switching in asymmetric waveguide structure multiple quantum well lasers," *IEEE J. Sel. Top. Quantum Electron.*, vol. 21, no. 6, pp. 1–6, Nov. 2015.
- [68] A. Salhi and A. A. Al-Muhanna, "Self-consistent analysis of GaInNAsSb/GaSb quantum well lasers emitting at 2.3–3.3- μm -long wavelength," *IEEE J. Sel. Top. Quantum Electron.*, vol. 21, no. 6, pp. 1–6, Nov. 2015.
- [69] S. Sprengel, G. K. Veerabathran, F. Federer, A. Andrejew, and M.-C. Amann, "InP-based vertical-cavity surface-emitting lasers with type-II quantum wells," *IEEE J. Sel. Top. Quantum Electron.*, vol. 21, no. 6, pp. 1–10, Nov. 2015.
- [70] Y. Arakawa, "Multidimensional quantum well laser and temperature dependence of its threshold current," *Appl. Phys. Lett.*, vol. 40, no. 11, p. 939, Jun. 1982.
- [71] M. Asada, Y. Miyamoto, and Y. Suematsu, "Gain and the threshold of three-dimensional quantum-box lasers," *IEEE J. Quantum Electron.*, vol. 22, no. 9, pp. 1915–1921, Sep. 1986.
- [72] D. Leonard, M. Krishnamurthy, C. M. Reaves, S. P. Denbaars, and P. M. Petroff, "Direct formation of quantum-sized dots from uniform coherent islands of InGaAs on GaAs surfaces," *Appl. Phys. Lett.*, vol. 63, no. 23, p. 3203, Dec. 1993.
- [73] H. Hirayama, K. Matsunaga, M. Asada, and Y. Suematsu, "Lasing action of $\text{Ga}_{0.67}\text{In}_{0.33}\text{As}/\text{GaInAsP}/\text{InP}$ tensile-strained quantum-box laser," *Electron. Lett.*, vol. 30, no. 2, pp. 142–143, Jan. 1994.
- [74] K. Ohira, T. Murayama, S. Tamura, and S. Arai, "Low-threshold and high-

- efficiency operation of distributed reflector lasers with width-modulated wirelike active regions,” *IEEE J. Sel. Top. Quantum Electron.*, vol. 11, no. 5, pp. 1162–1168, Sep. 2005.
- [75] K. Otsubo, N. Hatori, M. Ishida, S. Okumura, T. Akiyama, Y. Nakata, H. Ebe, M. Sugawara, and Y. Arakawa, “Temperature-insensitive eye-opening under 10-Gb/s modulation of 1.3- μm p-doped quantum-dot lasers without current adjustments,” *Jpn. J. Appl. Phys.*, vol. 43, no. No. 8B, pp. L1124–L1126, Jul. 2004.
- [76] K. G. Wilcox, H. J. Khashi, A. H. Quarterman, O. J. Morris, V. Apostolopoulos, M. Henini, and A. C. Tropper, “Wetting-layer-pumped continuous-wave surface-emitting quantum-dot laser,” *IEEE Photon. Technol. Lett.*, vol. 24, no. 1, pp. 37–39, Jan. 2012.
- [77] M. Kasim, S. N. Elliott, A. B. Krysa, and P. M. Snowton, “Reducing thermal carrier spreading in InP quantum dot lasers,” *IEEE J. Sel. Top. Quantum Electron.*, vol. 21, no. 6, pp. 1–6, Nov. 2015.
- [78] P. Munnely, T. Heindel, M. M. Karow, S. Hofling, M. Kamp, C. Schneider, and S. Reitzenstein, “A pulsed nonclassical light source driven by an integrated electrically triggered quantum dot microlaser,” *IEEE J. Sel. Top. Quantum Electron.*, vol. 21, no. 6, pp. 1–9, Nov. 2015.
- [79] M. Gioannini, P. Bardella, and I. Montrosset, “Time-domain traveling-wave analysis of the multimode dynamics of quantum dot Fabry–Perot lasers,” *IEEE J. Sel. Top. Quantum Electron.*, vol. 21, no. 6, pp. 1–11, Nov. 2015.
- [80] Y. Suematsu and K. Utaka, “Distributed-reflector semiconductor laser with tunable and frequency modulation mechanism,” Japan Patent Appl. S-56–116683, opened Sep. 12, 1981, applied Feb. 20, 1980.
- [81] Y. Tohmori, Y. Suematsu, H. Tsushima, and S. Arai, “Wavelength tuning of

- GaInAsP/InP integrated laser with butt-jointed built-in distributed Bragg reflector,” *Electron. Lett.*, vol. 19, no. 17, p. 656, 1983.
- [82] S. Murata, I. Mito, and K. Kobayashi, “Over 720 GHz (5.8nm) frequency tuning by a 1.5 μm DBR laser with phase and Bragg wavelength control regions,” *Electron. Lett.*, vol. 23, no. 8, p. 403, 1987.
- [83] M.-C. Amann, S. Illek, C. Schanen, and W. Thulke, “Tunable twin-guide laser: A novel laser diode with improved tuning performance,” *Appl. Phys. Lett.*, vol. 54, no. 25, p. 2532, 1989.
- [84] M. Öberg, S. Nilsson, T. Klinga, and P. Ojala, “A three-electrode distributed Bragg reflector laser with 22 nm wavelength tuning range,” *IEEE Photon. Technol. Lett.*, vol. 3, no. 4, pp. 299–301, Apr. 1991.
- [85] J. Buus, M. Amann, and D. J. Blumenthal, *Tunable Laser Diodes and Related Optical Sources*. John Wiley & Sons, 2005.
- [86] V. Jayaraman, Z. M. Chuang, and L. A. Coldren, “Theory, design and performance of extended tuning range semiconductor lasers with sampled gratings,” *IEEE J. Quantum Electron.*, vol. 29, no. 6, pp. 1824–1834, Jun. 1993.
- [87] Y. Tohmori, Y. Yoshikuni, H. Ishii, F. Kano, T. Tamamura, Y. Kondo, and M. Yamamoto, “Broad-range wavelength-tunable superstructure grating (SSG) DBR lasers,” *IEEE J. Quantum Electron.*, vol. 29, no. 6, pp. 1817–1823, Jun. 1993.
- [88] L. A. Coldren, “Monolithic tunable diode lasers,” *IEEE J. Sel. Top. Quantum Electron.*, vol. 6, no. 6, pp. 988–999, Nov. 2000.
- [89] L. A. Coldren, G. A. Fish, Y. Akulova, J. S. Barton, L. Johansson, and C. W. Coldren, “Tunable semiconductor lasers: A tutorial,” in *J. Light. Technol.*, 2004, vol. 22, pp. 193–202.
- [90] L. Yu, D. Lu, B. Pan, L. Zhang, L. Guo, Z. Li, and L. J. Zhao, “Widely tunable

- narrow-linewidth lasers using self-injection DBR lasers,” *IEEE Photon. Technol. Lett.*, vol. 27, no. 1, pp. 50–53, Jan. 2015.
- [91] J. Zhao, H. Zhou, F. Liu, and Y. Yu, “Numerical analysis of phase noise characteristics of SGDBR lasers,” *IEEE J. Sel. Top. Quantum Electron.*, vol. 21, no. 6, pp. 1–9, Nov. 2015.
- [92] S. Yin, T. Chan, and W. I. Way, “100-km DWDM transmission of 56-Gb/s PAM4 per λ via tunable laser and 10-Gb/s InP MZM,” *IEEE Photon. Technol. Lett.*, vol. 27, no. 24, pp. 2531–2534, Dec. 2015.
- [93] M.-H. Shih, K.-S. Hsu, K. Lee, K.-T. Lai, C.-T. Lin, and P.-T. Lee, “Compact tunable laser with InGaAsP photonic crystal nanorods for C-band communication,” *IEEE J. Sel. Top. Quantum Electron.*, vol. 21, no. 6, pp. 1–5, Nov. 2015.
- [94] G. Tu, F. Dong, Y. Wang, B. Culshaw, Z. Zhang, T. Pang, H. Xia, and B. Wu, “Analysis of random noise and long-term drift for tunable diode laser absorption spectroscopy system at atmospheric pressure,” *IEEE Sens. J.*, vol. 15, no. 6, pp. 3535–3542, Jun. 2015.
- [95] F. Koyama, S. Kinoshita, and K. Iga, “Room temperature CW operation of GaAs vertical cavity surface emitting lasers,” *Trans. IEICE*, vol. B71, no. 11, pp. 1089–1090, 1988.
- [96] Y. H. Lee, J. L. Jewell, A. Scherer, S. L. McCall, J. P. Harbison, and L. T. Florez, “Room-temperature continuous-wave vertical-cavity single-quantum-well microlaser diodes,” *Electron. Lett.*, vol. 25, no. 20, p. 1377, 1989.
- [97] C. J. Chang-Hasnain, “Tunable VCSEL,” *IEEE J. Sel. Top. Quantum Electron.*, vol. 6, no. 6, pp. 978–987, Nov. 2000.
- [98] K. Iga, “Surface-emitting laser-its birth and generation of new optoelectronics field,” *IEEE J. Sel. Top. Quantum Electron.*, vol. 6, no. 6, pp. 1201–1215, Nov.

- 2000.
- [99] S. Kota Pavan, P. J. Decker, Y. Sun, R. Lingle, and S. E. Ralph, "Estimation of 25-Gbit/s VCSEL-MMF link penalties at 850 nm: temperature dependence," *J. Light. Technol.*, vol. 33, no. 1, pp. 109–116, Jan. 2015.
- [100] D. M. Kuchta, A. V. Rylyakov, C. L. Schow, J. E. Proesel, C. W. Baks, P. Westbergh, J. S. Gustavsson, and A. Larsson, "A 50 Gb/s NRZ modulated 850 nm VCSEL transmitter operating error free to 90 °C," *J. Light. Technol.*, vol. 33, no. 4, pp. 802–810, Feb. 2015.
- [101] C.-L. Ying, H.-H. Lu, C.-Y. Li, C.-Y. Lin, C.-Y. Lin, and P.-C. Peng, "A 20-km/60-Gb/s two-way PON based on directly modulated two-stage injection-locked 1.55- μm VCSEL transmitters and negative dispersion fibers," *IEEE Photonics J.*, vol. 7, no. 1, pp. 1–9, Feb. 2015.
- [102] J. Lavrencik, S. K. Pavan, D. K. Haupt, and S. E. Ralph, "Direct measurement of VCSEL transverse mode correlation and k_{mpn} ," *IEEE Photon. Technol. Lett.*, vol. 27, no. 19, pp. 2031–2034, Oct. 2015.
- [103] S. Paul, C. Gierl, J. Cesar, M. Malekizandi, B. Kogel, C. Neumeyr, M. Ortsiefer, and F. Kupfers, "10-Gb/s direct modulation of widely tunable 1550-nm MEMS VCSEL," *IEEE J. Sel. Top. Quantum Electron.*, vol. 21, no. 6, pp. 1–8, Nov. 2015.
- [104] F. J. Duarte, *Tunable Lasers Handbook*. Academic Press, 1995.
- [105] W. Demtröder, *Laser Spectroscopy: Basic Principle*. Springer, 2008.
- [106] J. R. Murray, L. J. Radziemski, R. W. Solarz, and J. A. Paisner, *Laser Spectroscopy and its Applications*. Marcel Dekker, 1987.
- [107] M. A. Akerman, F. J. Duarte, and L. W. Hillman, *Dye Laser Principles*. Academic Press, 1990.
- [108] "Compact Tunable Lasers: Changing the way you sense, measure & detect,"

- Newport Corporation.* [Online]. Available: www.newport.com/images/webDocuments-EN/images/19152.pdf. [Accessed: 09-Oct-2015].
- [109] S. W. S. Wang, *Frequency control of semiconductor lasers*, vol. 30. John Wiley & Sons, 1984.
- [110] J. Buus and E. J. Murphy, “Tunable lasers in optical networks,” *J. Light. Technol.*, vol. 24, no. 1, pp. 5–11, Jan. 2006.
- [111] “High performance tunable laser / TSL-510,” *Santec: The Photonics Pioneer*. [Online]. Available: <http://www.santec.com/jp/wp-content/uploads/TSL-510-C-E-v201005.pdf>. [Accessed: 09-Oct-2015].
- [112] J. Piprek, *Semiconductor Optoelectronic Devices: Introduction to Physics and Simulation*. Academic Press, 2003.
- [113] N. Bohr, “On the constitution of atoms and molecules, part I,” *Philos. Mag. Ser. 6*, vol. 26, no. 151, pp. 1–25, Jul. 1913.
- [114] L. A. Coldren, S. W. Corzine, and M. L. Masanovic, *Diode Lasers and Photonic Integrated Circuits*. John Wiley & Sons, 2012.
- [115] S. Adachi, *Properties of Aluminium Gallium Arsenide*. INSPEC, 1993.
- [116] R. Soref and J. Lorenzo, “All-silicon active and passive guided-wave components for $\lambda=1.3$ and $1.6 \mu\text{m}$,” *IEEE J. Quantum Electron.*, vol. 22, pp. 873–879, 1986.
- [117] S. L. Chuang, *Physics of Optoelectronic Devices*. Wiley, 1995.
- [118] Crosslight, “Publications.” [Online]. Available: <http://crosslight.com/publications/overview/>. [Accessed: 09-Oct-2015].
- [119] C. H. Henry, R. A. Logan, and K. A. Bertness, “Spectral dependence of the change in refractive index due to carrier injection in GaAs lasers,” *J. Appl. Phys.*, vol. 52, pp. 4457–4461, 1981.

- [120] Crosslight Software Inc., “A TCAD software for the simulation of semiconductor devices and processes.” PICS3D User Guide, 2010.
- [121] S. M. Sze, *Physics of Semiconductor Devices*. John Wiley & Sons, 1981.
- [122] C. Henry, “Theory of spontaneous emission noise in open resonators and its application to lasers and optical amplifiers,” *J. Light. Technol.*, vol. 4, 1986.
- [123] B. Tromborg, H. Olesen, and X. Pan, “Theory of linewidth for multielectrode laser diodes with spatially distributed noise sources,” *IEEE J. Quantum Electron.*, vol. 27, pp. 178–192, 1991.
- [124] Monash_University, “Professor Arthur Lowery.” [Online]. Available: <http://www.ecse.monash.edu.au/staff/lowery/>. [Accessed: 09-Oct-2015].
- [125] P. B. Johns and R. L. Beurle, “Numerical solution of 2-dimensional scattering problems using a transmission-line matrix,” *Proc. Inst. Electr. Eng.*, vol. 118, no. 9, p. 1203, 1971.
- [126] VPIPhotonics, “Publications.” [Online]. Available: www.vpiphotonics.com/Services/Downloads/DownloadArea/Publications/. [Accessed: 09-Oct-2015].
- [127] W. J. R. Hoefer, “The transmission-line matrix method - theory and applications,” *IEEE Trans. Microw. Theory Tech.*, vol. 33, no. 10, pp. 882–893, Oct. 1985.
- [128] A. J. Lowery, “New dynamic semiconductor laser model based on the transmission-line modelling method,” *IEE Proc. J Optoelectron.*, vol. 134, no. 5, p. 281, 1987.
- [129] VPIphotonics GmbH, “VPIcomponentMaker Photonic Circuits.” User’s Manual, 2015.
- [130] J. P. Weber, “Optimization of the carrier-induced effective index change in InGaAsP waveguides - application to tunable Bragg filters,” *IEEE J. Quantum*

- Electron.*, vol. 30, no. 8, pp. 1801–1816, 1994.
- [131] B. R. Bennett, R. A. Soref, and J. A. Del Alamo, “Carrier-induced change in refractive index of InP, GaAs, and InGaAsP,” *IEEE J. Quantum Electron.*, vol. 26, no. 1, pp. 113–122, 1990.
- [132] A. Tomita, “Free carrier effect on the refractive index change in quantum-well structures,” *IEEE J. Quantum Electron.*, vol. 30, no. 12, pp. 2798–2802, 1994.
- [133] H. Wenzel, G. Erbert, and P. M. Enders, “Improved theory of the refractive-index change in quantum-well lasers,” *IEEE J. Sel. Top. Quantum Electron.*, vol. 5, no. 3, pp. 637–642, 1999.
- [134] M. Yamaguchi, P. Delansay, and M. Kitamura, “Refractive index and loss changes produced by current injection in InGaAs(P)-InGaAsP multiple quantum-well (MQW) waveguides,” *IEEE J. Sel. Top. Quantum Electron.*, vol. 1, no. 2, pp. 408–415, Jun. 1995.
- [135] L. D. Westbrook, “Measurements of dg/dN and dn/dN and their dependence on photon energy in $\lambda=1.5\ \mu\text{m}$ InGaAsP laser diodes,” *IEE Proc. J Optoelectron.*, vol. 133, p. 135, 1986.
- [136] M. Okuda and K. Onaka, “Tunability of distributed Bragg-reflector laser by modulating refractive index in corrugated waveguide,” *Jpn. J. Appl. Phys.*, vol. 16, no. 8, pp. 1501–1502, Aug. 1977.
- [137] J. Manning, R. Olshansky, and C. Su, “The carrier-induced index change in AlGaAs and $1.3\ \mu\text{m}$ InGaAsP diode lasers,” *IEEE J. Quantum Electron.*, vol. 19, pp. 1525–1530, 1983.
- [138] S. Murata, A. Tomita, and A. Suzuki, “Influence of free carrier plasma effect on carrier-induced refractive index change for quantum-well lasers,” *IEEE Photon. Technol. Lett.*, vol. 5, no. 1, pp. 16–19, 1993.

- [139] J. E. Ehrlich, D. T. Neilson, and A. C. Walker, "Carrier-dependent nonlinearities and modulation in an InGaAs SQW waveguide," *IEEE J. Quantum Electron.*, vol. 29, no. 8, pp. 2319–2324, 1993.
- [140] J. Stohs, D. J. Bossert, D. J. Gallant, and S. R. J. Brueck, "Gain, refractive index change, and linewidth enhancement factor in broad-area GaAs and InGaAs quantum-well lasers," *IEEE J. Quantum Electron.*, vol. 37, no. 11, pp. 1449–1459, 2001.
- [141] S. Shin and C. B. Su, "Strong increase of the derivative of the carrier-induced index change of semiconductor lasers at low injected carrier density," *IEEE Photonics Technol. Lett.*, vol. 5, no. 9, pp. 981–983, Sep. 1993.
- [142] G. Schraud, G. Müller, L. Stoll, and U. Wolff, "Simple measurement of carrier induced refractive-index change in InGaAsP pin ridge waveguide structures," *Electron. Lett.*, vol. 27, no. 4, p. 297, Feb. 1991.
- [143] L. Dong, R. Zhang, D. Wang, S. Zhao, S. Jiang, Y. Yu, and S. Liu, "Modeling widely tunable sampled-grating DBR lasers using traveling-wave model with digital filter approach," *J. Light. Technol.*, vol. 27, no. 15, pp. 3181–3188, 2009.
- [144] L. Schneider, M. Pfeiffer, J. Piprek, A. Witzig, and B. Witzigmann, "Sampled-grating DBR lasers: calibrated 3D simulation of tuning characteristics," *Proc. SPIE*, 2005.
- [145] T. Shu and Y. Yu, "Modeling of tunable DBRs lasers based on transmission-line laser model," *J. Phys. Conf. Ser.*, vol. 276, p. 012088, Feb. 2011.
- [146] S. Adachi, *Physical Properties of III-V Semiconductor Compounds*. John Wiley & Sons, 1992.
- [147] H. X. Shi, D. A. Cohen, J. Barton, M. Majewski, L. A. Coldren, M. C. Larson, and G. A. Fish, "Dynamic range of widely tunable sampled-grating DBR lasers,"

- Electron. Lett.*, vol. 38, no. 4, p. 180, 2002.
- [148] B. Mason, G. A. Fish, S. P. DenBaars, and L. A. Coldren, "Widely tunable sampled grating DBR laser with integrated electroabsorption modulator," *IEEE Photon. Technol. Lett.*, vol. 11, pp. 638–640, 1999.
- [149] Y. A. Akulova, G. A. Fish, P. C. Koh, C. L. Schow, P. Kozodoy, A. P. Dahl, S. Nakagawa, M. C. Larson, M. P. Mack, T. A. Strand, C. W. Coldren, E. Hegblom, S. K. Penniman, T. Wipiejewski, and L. A. Coldren, "Widely tunable electroabsorption-modulated sampled-grating DBR laser transmitter," *IEEE J. Sel. Top. Quantum Electron.*, vol. 8, pp. 1349–1357, 2002.
- [150] S. Kim, Y. Chung, S. H. Oh, and M. H. Park, "Design and analysis of widely tunable sampled grating DFB laser diode integrated with sampled grating distributed Bragg reflector," *IEEE Photon. Technol. Lett.*, vol. 16, pp. 15–17, 2004.
- [151] S. L. Woodward, I. M. I. Habbab, T. L. Koch, and U. Koren, "The side-mode-suppression ratio of a tunable DBR laser," *IEEE Photon. Technol. Lett.*, vol. 2, pp. 854–856, 1990.
- [152] J. C. Cartledge and A. F. Elrefaie, "Threshold gain difference requirements for nearly single-longitudinal-mode lasers," *J. Light. Technol.*, vol. 8, pp. 704–715, 1990.
- [153] F. Koyama, Y. Suematsu, S. Arai, and T. Tawee, "1.5-1.6 μm GaInAsP/InP dynamic-single-mode (DSM) lasers with distributed Bragg reflector," *IEEE J. Quantum Electron.*, vol. 19, no. 6, pp. 1042–1051, 1983.
- [154] Y. Kotaki and H. Ishikawa, "Wavelength tunable DFB and DBR lasers for coherent optical fibre communications," *IEE Proc. J Optoelectron.*, vol. 138, no. 2, p. 171, 1991.

- [155] D. Delprat, L. Silvestre, A. Ougazzaden, F. Delorme, S. Slempek, and A. Ramdane, "Record tuning range of a 1.55 μm DBR laser realized by selective area growth," in *Proc. Int. InP & Rel. Mat. Conf.*, 1996, pp. 162–164.
- [156] D. Delprat, A. Ramdane, L. Silvestre, A. Ougazzaden, F. Delorme, and S. Slempek, "20-Gb/s integrated DBR laser-EA modulator by selective area growth for 1.55- μm WDM applications," *IEEE Photon. Technol. Lett.*, vol. 9, pp. 898–900, 1997.
- [157] V. I. Feies and I. Montrosset, "Design of two-section DBR laser operating at ITU frequencies only by grating current tuning," *J. Light. Technol.*, vol. 21, no. 6, pp. 1524–1530, 2003.
- [158] Y. Kotaki and H. Ishikawa, "Spectral characteristics of a three-section wavelength-tunable DBR laser," *IEEE J. Quantum Electron.*, vol. 25, no. 6, pp. 1340–1345, Jun. 1989.
- [159] N. P. Caponio, M. Goano, I. Maio, M. Meliga, G. P. Bava, G. Destefanis, and I. Montrosset, "Analysis and design criteria of three-section DBR tunable lasers," *IEEE J. Sel. Areas Commun.*, vol. 8, no. 6, pp. 1203–1213, 1990.
- [160] S. Sakano, A. Oka, and N. Chinone, "Wavelength-tunable three-electrode DBR laser with a thin-active layer in tuning regions," *IEEE Photon. Technol. Lett.*, vol. 3, no. 10, pp. 866–868, 1991.
- [161] S. L. Woodward, U. Koren, B. I. Miller, M. G. Young, M. A. Newkirk, and C. A. Burrus, "A DBR laser tunable by resistive heating," *IEEE Photon. Technol. Lett.*, vol. 4, no. 12, pp. 1330–1332, 1992.
- [162] A. Tsigopoulos, T. Spicopoulos, I. Orfanos, and S. Pantelis, "Wavelength tuning analysis and spectral characteristics of three-section DBR lasers," *IEEE J. Quantum Electron.*, vol. 28, no. 2, pp. 415–426, 1992.

- [163] T. Kameda, H. Mori, S. Onuki, T. Kikugawa, Y. Takahashi, F. Tsuchiya, and H. Nagai, "A DBR laser employing passive-section heaters, with 10.8 nm tuning range and 1.6 MHz linewidth," *IEEE Photon. Technol. Lett.*, vol. 5, no. 6, pp. 608–611, 1993.
- [164] A. A. M. Staring, J. J. M. Binsma, P. I. Kuindersma, E. J. Jansen, P. J. A. Thijs, T. van Dongen, and G. F. G. Depovere, "Wavelength-independent output power from an injection-tunable DBR laser," *IEEE Photon. Technol. Lett.*, vol. 6, no. 2, pp. 147–149, 1994.
- [165] M. Teshima, "Dynamic wavelength tuning characteristics of the 1.5- μm three-section DBR lasers: analysis and experiment," *IEEE J. Quantum Electron.*, vol. 31, pp. 1389–1400, 1995.
- [166] F. Delorme, G. Alibert, P. Boulet, S. Grosmaire, S. Slempek, and A. Ougazzaden, "High reliability of high-power and widely tunable 1.55- μm distributed Bragg reflector lasers for WDM applications," *IEEE J. Sel. Top. Quantum Electron.*, vol. 3, no. 2, pp. 607–614, 1997.
- [167] A. J. Ward, G. Busico, N. D. Whitbread, L. Ponnampalam, J. P. Duck, and D. J. Robbins, "Linewidth in widely tunable digital supermode distributed Bragg reflector lasers: Comparison between theory and measurement," *IEEE J. Quantum Electron.*, vol. 42, no. 11, pp. 1122–1127, 2006.
- [168] L. Ponnampalam, D. J. Robbins, A. J. Ward, N. D. Whitbread, J. P. Duck, G. Busico, and D. J. Bazley, "Equivalent performance in C- and L- bands of digital supermode distributed Bragg reflector lasers," *IEEE J. Quantum Electron.*, vol. 43, no. 9, pp. 798–803, Sep. 2007.
- [169] J. Zhao, S. Hu, Y. Tang, H. Zhao, and Y. Yu, "Widely tunable semiconductor laser based on digital concatenated grating with multiple phase shifts," *IEEE Photonics*

- J.*, vol. 5, no. 5, pp. 1502008–1502008, Oct. 2013.
- [170] J.-P. Engelstädter, B. Roycroft, F. H. Peters, and B. Corbett, “Design of tunable laser with interleaved sampled grating rear mirror,” *J. Light. Technol.*, vol. 28, no. 19, pp. 2830–2835, Oct. 2010.
- [171] F. Delorme, “Widely tunable 1.55- μm lasers for wavelength-division-multiplexed optical fiber communications,” *IEEE J. Quantum Electron.*, vol. 34, no. 9, pp. 1706–1716, 1998.
- [172] F. Delorme, G. Alibert, C. Ougier, S. Slemptes, and H. Nakajima, “Sampled-grating DBR lasers with 101 wavelengths over 44 nm and optimised power variation for WDM applications,” *Electron. Lett.*, vol. 34, no. 3, p. 279, 1998.
- [173] R. Todt, T. Jacke, R. Meyer, J. Adler, R. Laroy, G. Morthier, and M. C. Amann, “Sampled grating tunable twin-guide laser diodes with over 40-nm electronic tuning range,” *IEEE Photon. Technol. Lett.*, vol. 17, no. 12, pp. 2514–2516, 2005.
- [174] R. Todt, T. Jacke, R. Meyer, R. Laroy, G. Morthier, and M. C. Amann, “Widely tunable twin-guide laser diodes with sampled gratings: Design and performance,” *IEEE J. Sel. Top. Quantum Electron.*, vol. 13, no. 5, pp. 1095–1103, 2007.
- [175] H. Ishii, H. Tanobe, F. Kano, Y. Tohmori, Y. Kondo, and Y. Yoshikuni, “Quasicontinuous wavelength tuning in super-structure-grating (SSG) DBR lasers,” *IEEE J. Quantum Electron.*, vol. 32, no. 3, pp. 433–440, 1996.
- [176] H. Ishii, F. Kano, Y. Yoshikuni, and H. Yasaka, “Mode stabilization method for superstructure-grating DBR lasers,” *J. Light. Technol.*, vol. 16, no. 3, pp. 433–442, Mar. 1998.
- [177] G. Sarlet, G. Morthier, and R. Baets, “Control of widely tunable SSG-DBR lasers for dense wavelength division multiplexing,” *J. Light. Technol.*, vol. 18, no. 8, pp. 1128–1138, 2000.

- [178] M. Yamada, "Analysis of gain suppression in undoped injection lasers," *J. Appl. Phys.*, vol. 52, no. 4, p. 2653, 1981.
- [179] M. Yamada, H. Ishiguro, and H. Nagato, "Estimation of the intra-band relaxation time in undoped AlGaAs injection laser," *Jpn. J. Appl. Phys.*, vol. 19, pp. 135–142, 1980.
- [180] M. Asada and Y. Suematsu, "Density-matrix theory of semiconductor lasers with relaxation broadening model-gain and gain-suppression in semiconductor lasers," *IEEE J. Quantum Electron.*, vol. 21, no. 5, pp. 434–442, 1985.
- [181] M. Asada, A. Kameyama, and Y. Suematsu, "Gain and intervalence band absorption in quantum-well lasers," *IEEE J. Quantum Electron.*, vol. 20, no. 7, pp. 745–753, 1984.
- [182] E. Zielinski, H. Schweizer, S. Hausser, R. Stuber, M. Pilkuhn, and G. Weimann, "Systematics of laser operation in GaAs/AlGaAs multiquantum well heterostructures," *IEEE J. Quantum Electron.*, vol. 23, no. 6, pp. 969–976, Jun. 1987.
- [183] M. Takeshima, "Theory of the carrier-carrier and carrier-phonon interactions under double injection into undoped quantum wells and its application to a laser problem," *Phys. Rev. B*, vol. 36, no. 15, pp. 8082–8093, Nov. 1987.
- [184] M. Yamada, S. Ogita, M. Yamagishi, K. Tabata, and N. Nakaya, "Polarization-dependent gain in GaAs/AlGaAs multi-quantum-well lasers: theory and experiment," *Appl. Phys. Lett.*, vol. 45, pp. 324–325, 1984.
- [185] M. Asada, "Intraband relaxation effect on optical spectra," in *Quantum Well Lasers*, P. S. Zory Jr., Ed. San Diego, CA, USA: Academic, 1993.
- [186] F. Wooten, *Optical properties of solids*. San Diego, CA, USA: Academic, 1972.
- [187] M. Yamanishi, "Phase dampings of optical dipole moments and gain spectra in

- semiconductor lasers,” *IEEE J. Quantum Electron.*, vol. 23, no. 4, pp. 367–370, Apr. 1987.
- [188] S. R. Chinn, P. S. Zory, and A. R. Reisinger, “Model for GRIN-SCH-SQW diode lasers,” *IEEE J. Quantum Electron.*, vol. 24, pp. 2191–2214, 1988.
- [189] A. I. Kucharska and D. J. Robbins, “Lifetime broadening in GaAs-AlGaAs quantum well lasers,” *IEEE J. Quantum Electron.*, vol. 26, no. 3, pp. 443–448, Mar. 1990.
- [190] M. Asada, “Intraband relaxation time in quantum-well lasers,” *IEEE J. Quantum Electron.*, vol. 25, no. 9, pp. 2019–2026, 1989.
- [191] M. Yamada, S. Ogita, M. Yamagishi, and K. Tabata, “Anisotropy and broadening of optical gain in a GaAs/AlGaAs multiquantum-well laser,” *IEEE J. Quantum Electron.*, vol. 21, no. 6, pp. 640–645, 1985.
- [192] X. Pan, H. Olesen, and B. Tromborg, “Modulation characteristics of tunable DFB/DBR lasers with one or two passive tuning sections,” *IEEE J. Quantum Electron.*, vol. 25, no. 6, pp. 1254–1260, 1989.
- [193] C. M. Miller, “Intensity modulation and noise characterization of high-speed semiconductor lasers,” *IEEE LTS*, vol. 2, no. 2, pp. 44–50, May 1991.
- [194] L. M. Zhang and J. E. Carroll, “Enhanced AM and FM modulation response of complex coupled DFB lasers,” *IEEE Photon. Technol. Lett.*, vol. 5, no. 5, pp. 506–508, 1993.
- [195] T. Sphicopoulos, A. Anastassiadou, I. Orfanos, and C. Caroubalos, “Frequency modulation characteristics of three-section DBR lasers,” *IEE Proc. J Optoelectron.*, vol. 140, no. 3, pp. 201–205, 1993.
- [196] C. E. Zah, P. J. Delfyett, R. Bhat, C. Caneau, F. Favire, B. Pathak, P. S. D. Lin, A. S. Gozdz, N. C. Andreadakis, M. A. Koza, M. Z. Iqbal, H. Izadpanah, and T. P.

- Lee, "High speed performance of 1.5 μm compressive-strained multiquantum-well gain-coupled distributed-feedback lasers," *Electron. Lett.*, vol. 29, no. 10, p. 857, May 1993.
- [197] H. Olesen, B. Tromborg, X. Pan, and H. E. Lassen, "Stability and dynamic properties of multi-electrode laser diodes using a Green's function approach," *IEEE J. Quantum Electron.*, vol. 29, no. 8, 1993.
- [198] M. Öberg, O. Kjebon, S. Lourdudoss, S. Nilsson, L. Backbom, K. Streubel, and J. Wallin, "Increased modulation bandwidth up to 20 GHz of a detuned-loaded DBR laser," *IEEE Photon. Technol. Lett.*, vol. 6, no. 2, pp. 161–163, 1994.
- [199] A. Zatni and J. Le Bihan, "Analysis of FM and AM responses of a tunable three-electrode DBR laser diode," *IEEE J. Quantum Electron.*, vol. 31, no. 6, 1995.
- [200] H. Lu, T. Makino, and G. P. Li, "Dynamic properties of partly gain-coupled 1.55- μm DFB lasers," *IEEE J. Quantum Electron.*, vol. 31, no. 8, pp. 1443–1450, 1995.
- [201] H. Lu, C. Blaauw, B. Benyon, G. Ping Li, and T. Makino, "High-power and high-speed performance of 1.3- μm strained MQW gain-coupled DFB lasers," *IEEE J. Sel. Top. Quantum Electron.*, vol. 1, no. 2, pp. 375–381, Jun. 1995.
- [202] S. L. Lee, D. A. Tauber, V. Jayaraman, M. E. Heimbuch, L. A. Coldren, and J. E. Bowers, "Dynamic responses of widely tunable sampled grating DBR lasers," *IEEE Photon. Technol. Lett.*, vol. 8, no. 12, pp. 1597–1599, Dec. 1996.
- [203] M. Ferreira, "Frequency noise and modulation of a four-section DBR laser," *IEEE J. Quantum Electron.*, vol. 32, no. 5, pp. 851–858, 1996.
- [204] O. Kjebon, R. Schatz, S. Lourdudoss, S. Nilsson, B. Stålnacke, and L. Bäckbom, "30 GHz direct modulation bandwidth in detuned loaded InGaAsP DBR lasers at 1.55 μm wavelength," *Electron. Lett.*, vol. 33, no. 6, p. 488, 1997.
- [205] C. Y. Tsai, F. P. Shih, T. L. Sung, T. Y. Wu, C. H. Chen, and C. Y. Tsai, "A small-

- signal analysis of the modulation response of high-speed quantum-well lasers: Effects of spectral hole burning, carrier heating, and carrier diffusion-capture-escape,” *IEEE J. Quantum Electron.*, vol. 33, no. 11, pp. 2084–2096, 1997.
- [206] U. Feiste, “Optimization of modulation bandwidth in DBR lasers with detuned bragg reflectors,” *IEEE J. Quantum Electron.*, vol. 34, no. 12, pp. 2371–2379, 1998.
- [207] M. L. Majewski, J. Barton, L. A. Coldren, Y. Akulova, and M. C. Larson, “Direct intensity modulation in sampled-grating DBR lasers,” *IEEE Photon. Technol. Lett.*, vol. 14, no. 6, pp. 747–749, 2002.
- [208] J. Klamkin, J. M. Hutchinson, J. T. Getty, L. A. Johansson, E. J. Skogen, and L. A. Coldren, “High efficiency widely tunable SGDBR lasers for improved direct modulation performance,” *IEEE J. Sel. Top. Quantum Electron.*, vol. 11, no. 5, pp. 931–938, Sep. 2005.
- [209] L. Yu, H. Wang, D. Lu, S. Liang, C. Zhang, B. Pan, L. Zhang, and L. Zhao, “A widely-tunable directly-modulated DBR laser with high linearity,” *IEEE Photonics J.*, vol. 6, no. 4, pp. 1–1, 2014.

Appendix

In this Appendix the source code of the most basic files of the modeled three-section bulk TLD in PICS3D is given.

The my.mac file contains all the material parameters of the three-section bulk TLD

\$ my.mac file

\$ macro : inp

\$ [free-style]

\$ Bulk InP at 300K.

\$ Typical use:

\$ load_macro name=inp mater=#m

begin_macro inp

\$ Use the same type of velocity model as GaAs

material type=semicond band_valleys=(1 1) &&

el_vel_model=n.gaas hole_vel_model=beta

dielectric_constant value=12.56

electron_mass value=0.078

hole_mass value=0.588

band_gap value=1.347

affinity value=4.4

\$ From "GaInAsP alloy semiconductors" by Pearsall p. 203

electron_mobility variation=function

function(total_doping)

mu_max=0.52;

mu_min=0.04;

ref_dens=3.0d23;

alpha=0.42;

mu_min+(mu_max-mu_min)/(1+(total_doping/ref_dens

**alpha)

end_function

\$ From "properties of InP" by INSPEC.

hole_mobility variation=function

function(total_doping)

mu_max=0.017;

mu_min=0.001;

ref_dens=4.87d23;

alpha=0.62;

mu_min+(mu_max-mu_min)/(1+(total_doping/ref_dens)

**alpha)

end_function

beta_n value=2.

electron_sat_vel value=1.d5

beta_p value=1.

hole_sat_vel value=1.d5

norm_field value=4.e5

tau_energy value=1.d-13

lifetime_n value=1.e-7

lifetime_p value=1.e-7

radiative_recomb value=1.d-16

auger_n value=1.5d-41

auger_p value=1.5d-41

real_index value=3.167

```

absorption value=0.
thermal_kappa value=46.
end_macro inp

$
*****
$ macro ingaasp_active
$ [free-style]
$ Bulk In(1-x)Ga(x)As(y)P(1-y) lattice matched to InP at
$ 300K
$      Relation between x and y:
$      x=0.1894y/(0.4184-0.013y)
$ Typical use:
$ load_macro name= ingaasp_active var1=#y mater=#m
$ var_symbol1=y
$
*****
begin_macro ingaasp_active
material type=semicond band_valleys=(1 1) &&
  el_vel_model=n.gaas hole_vel_model=beta
dielectric_constant variation=function
function(y)
12.56 + 1.5 * y
end_function
electron_mass variation=function
function(y)
0.078 - 0.050 * y + 0.014 * y **2
end_function
hole_mass variation=function
function(y)
( 0.588 ** (3 / 2) + (0.12 - 0.069*y) ** (3 / 2) ) ** (2 / 3)
end_function
band_gap variation=function
function(y)
1.347 - 0.778*y + 0.149*y**2
end_function
affinity variation=function
function(y)
off=0.4;
eg=1.347 - 0.778*y + 0.149*y**2;
eg0=1.347;
4.4 + off*(eg0-eg)
end_function
max_electron_mob variation=function
function(y)
0.52 + 0.65*y
end_function
min_electron_mob value=0.04
electron_ref_dens value=3.0d23
alpha_n value=0.42
max_hole_mob value=0.017
min_hole_mob value=0.001
hole_ref_dens value=4.87d23
alpha_p value=0.62
norm_field variation=function
function(y)
4.e5 + 8.e5 * y
end_function
tau_energy value=1.e-13
beta_n value=2.
electron_sat_vel variation=function
function(y)
1.e5 - 0.225e5*y
end_function
beta_p value=1.
hole_sat_vel value=1.0e5
radiative_recomb value=2.d-16
auger_n value=1.75d-41
auger_p value=1.75d-41
lifetime_n value=1.e-8
lifetime_p value=1.e-8
real_index variation=function
function(y)
3.167 + 0.316*y

```

```

end_function
absorption value=0.
thermal_kappa value=46.
end_macro ingaasp_active

$
*****
$ macro ingaasp_passive
$ [free-style]
$ Bulk In(1-x)Ga(x)As(y)P(1-y) lattice matched to InP at
$ 300K
$      Relation between x and y:
$      x=0.1894y/(0.4184-0.013y)
$ Typical use:
$ load_macro name= ingaasp_passive var1=#y mater=#m
$ var_symbol1=y
$
*****

begin_macro ingaasp_passive
material type=semicond band_valleys=(1 1) &&
  el_vel_model=n.gaas hole_vel_model=beta
dielectric_constant variation=function
function(y)
12.56 + 1.5 * y
end_function
electron_mass variation=function
function(y)
0.078 - 0.050 * y +0.014 * y **2
end_function
hole_mass variation=function
function(y)
( 0.588 ** (3 / 2) + (0.12 - 0.069*y)** (3 / 2) ) ** (2 / 3)
end_function
band_gap variation=function
function(y)
1.347 - 0.778*y + 0.149*y**2

end_function
affinity variation=function
function(y)
off=0.4;
eg=1.347 - 0.778*y + 0.149*y**2;
eg0=1.347;
4.4 + off*(eg0-eg)
end_function
max_electron_mob variation=function
function(y)
0.52 + 0.65*y
end_function
min_electron_mob value=0.04
electron_ref_dens value=3.0d23
alpha_n value=0.42
max_hole_mob value=0.017
min_hole_mob value=0.001
hole_ref_dens value=4.87d23
alpha_p value=0.62
norm_field variation=function
function(y)
4.e5 + 8.e5 * y
end_function
tau_energy value=1.e-13
beta_n value=2.
electron_sat_vel variation=function
function(y)
1.e5 - 0.225e5*y
end_function
beta_p value=1.
hole_sat_vel value=1.0e5
radiative_recomb value=1.d-16
auger_n value=0.75d-41
auger_p value=0.75d-41
lifetime_n value=1.e-8
lifetime_p value=1.e-8
real_index variation=function

```

```

function(y)
3.167 + 0.316*y
end_function
absorption value=0.
thermal_kappa value=46.
end_macro ingaasp_passive

$*****
$ bulk In(1-xw)Ga(xw)As(yw)P(1-yw) lattice matched to InP
$ [free-style]
$ This can be considered a speccial case of quantum well
$ except that information regarding the barrier is not required.
$ Please note that for In(1-x)Ga(x)As(y)P(1-y) system, the
$ lattice matches to InP if x and y is related by
$  $x=0.1894*y/(0.4184-0.013*y)$ 
$ The band gap of lattice matched ingaasp is given by
$  $E_g=1.347-0.778*y+0.149*y**2$ 
$ There is no need to specify xw since it can be calculated
$ from yw
$ Typical use:
$ get_active_layer name=InGaAsP mater=#m var1=#yw
$ var_symbol1=yw
$*****

begin_active_layer InGaAsP
layer_type type=bulk valley_gamma=1 valley_l=4 &&
valley_hh=1 valley_lh=1
eg0_well variation=function
function(yw)
1.347 - 0.778*yw + 0.149*yw**2
end_function
lband_well variation=function
function(yw)
delega=0.28 ;
delein=1.1 ;
deleip=0.608 ;
delepp=-0.09 ;
xw=0.1894*yw/(0.4184-0.013*yw) ;
term1=(1.-xw)*yw*delein+(1.-xw)*(1.-yw)*deleip ;
term2=xw*yw*delega+xw*(1.-yw)*delepp ;
term1+term2
end_function
delta_so_well variation=function
function(yw)
xw=0.1894*yw/(0.4184-0.013*yw) ;
delga=0.34 ;
delin=0.43 ;
delip=0.10 ;
delgp=0.10 ;
term1=(1.-xw)*yw*delin+(1.-xw)*(1.-yw)*delip ;
term2=xw*yw*delga+xw*(1.-yw)*delgp ;
term1+term2
end_function
mass_gamma_well variation=function
function(yw)
emnga=0.064 ;
emnin=0.023 ;
emnip=0.08 ;
emngp=0.17 ;
xw=0.1894*yw/(0.4184-0.013*yw) ;
term1=(1.-xw)*yw*emnin+(1.-xw)*(1.-yw)*emnip ;
term2=xw*yw*emnga+xw*(1.-yw)*emngp ;
term1+term2
end_function
mass_l_well value=0.56
gamma_l_well variation=function
function(yw)
g1ga=6.85 ;
g1gp=4.1 ;
g1in=20.4 ;
g1ip=5.0 ;
xw=0.1894*yw/(0.4184-0.013*yw) ;
term1=(1.-xw)*yw*g1in+(1.-xw)*(1.-yw)*g1ip ;

```

```

term2=xw*yw*g1ga+xw*(1.-yw)*g1gp ;
term1+term2
end_function
gamma2_well variation=function
function(yw)
g2ga=2.1 ;
g2gp=0.49 ;
g2in=8.3 ;
g2ip=1.5 ;
xw=0.1894*yw/( 0.4184 -0.013*yw ) ;
term1=(1.-xw)*yw*g2in+(1.-xw)*(1.-yw)*g2ip ;
term2=xw*yw*g2ga+xw*(1.-yw)*g2gp ;
term1+term2
end_function
lattice_constant value=5.8688
end_active_layer InGaAsP
$*****

The active.layer file contains all the design parameters of the
active section of the three-section bulk TLD
$*****

$ active.layer file
begin_layer
use_macrofile macro1=my.mac
column column_num=1 w=1.5 mesh_num=2 r=1.0
bottom_contact column_num=1 from=0.0 to=1.5 &&
contact_num=1
layer_mater macro_name=inp column_num=1 &&
n_doping=1.e+24
layer d=1.5 n=38 r=0.8
layer_mater macro_name=ingaasp_active var1=0.492462
&& column_num=1 var_symbol1=y
layer d=0.05 n=34 r=0.9
layer_mater macro_name= ingaasp_active var1=0.84 &&
column_num=1 var_symbol1=y active_macro=InGaAsP
&& avar_symbol1=yw avar1=0.84
layer d=0.18 n=34 r=1.1

```

```

layer_mater macro_name= ingaasp_active var1=0.492462
&& column_num=1 var_symbol1=y
layer d=0.05 n=34 r=1.1
layer_mater macro_name=inp column_num=1 &&
p_doping=1.e+24
layer d=1.55 n=39 r=1.2
top_contact column_num=1 from=0.0 to=1.5 contact_num=2
end_layer
$*****

The phase.layer file contains all the design parameters of the
phase section of the three-section bulk TLD
$*****

$ phase.layer file
begin_layer
$ Make sure the program knows there is a segment before
$ this structure. The programs needs this information to
$ generate the material numbers correctly.
previous_layer file=active.layer
column column_num=1 w=1.5 mesh_num=2 r=1.0
bottom_contact column_num=1 from=0.0 to=1.5 &&
contact_num=1
layer_mater macro_name=inp column_num=1 &&
n_doping=1.e+24
layer d=1.35 n=38 r=0.8
$ Passive waveguide material declared to be "active" so that
$ interband optical model for index change can be used.
layer_mater macro_name= ingaasp_passive var1=0.745159
&& column_num=1 active_macro=InGaAsP &&
avar1=0.745159 && var_symbol1=y avar_symbol1=yw
layer d=0.58 n=39 r=1.0
layer_mater macro_name=inp column_num=1 &&
p_doping=1.e+24
layer d=1.4 n=39 r=1.2
top_contact column_num=1 from=0.0 to=1.5 contact_num=3
end_layer
$*****

```

The Bragg.layer file contains all the design parameters of the Bragg section of the three-section bulk TLD

```

$*****
$ Bragg.layer file
begin_layer
$ Make sure the program knows there is a segment before
$ this structure. The programs needs this information to
$ generate the material numbers correctly.
previous_layer file=phase.layer
column column_num=1 w=1.5 mesh_num=2 r=1.0
bottom_contact column_num=1 from=0.0 to=1.5 &&
contact_num=1
layer_mater macro_name=inp column_num=1 &&
n_doping=1.e+24
layer d=1.35 n=38 r=0.8
$ The grating structure is modeled as an embedded material
$ with active regions so that interband optical model for
$ index change can be used.
$ Passive waveguide material declared to be "active" so that
$ interband optical model for index change can
$ be used.
layer_mater macro_name= ingaasp_passive var1=0.7255159
&& active_macro=InGaAsP avar1=0.7255159 &&
column_num=1 embedded_structure=1 var_symbol1=y &&
avar_symbol1=yw
grating_compos column_num=1 &&
hi_macro_name=ingaasp_passive &&
hi_active_macro=InGaAsP &&
lo_macro_name=ingaasp_passive &&
lo_active_macro=InGaAsP d_high= 0.1 d_low= 0.1 &&
d_fall=0. d_rise=0. grating_order=1 hi_var_symbol1=y &&
hi_var1=0.745159 hi_avar_symbol1=yw &&
hi_avar1=0.745159 && lo_var_symbol1=y &&
lo_var1=0.695159 && lo_avar_symbol1=yw &&
lo_avar1=0.695159
layer d=0.2 n=39 r=0.9

```

```

layer_mater macro_name= ingaasp_passive var1=0.745159
&& column_num=1 active_macro=InGaAsP &&
avar1=0.745159 && var_symbol1=y avar_symbol1=yw
layer d=0.38 n=39 r=1.0
layer_mater macro_name=inp column_num=1 &&
p_doping=1.e+24
layer d=1.4 n=39 r=1.2
top_contact column_num=1 from=0.0 to=1.5 contact_num=4
end_layer
$*****

```

The active.gain file contains all the information for the gain spectrum of the active section of the three-section bulk TLD

```

$*****
$ active.gain file
begin_gain
use_macrofile macro1=my.mac
plot_data plot_device=postscript
$ Apply Lorentzian broadening lineshape function to gain
$ with intraband relaxation time  $\tau_m = 1$  ps, FC absorption
$ coefficient  $a_{FC} = 6 \times 10^{-23}$  m2 and IVBA coefficient
$  $a_{IVBA} = 6 \times 10^{-22}$  m2
active_reg broadening=lorentzian tau_scat=1e-12 a_scat=0
&& thickness=0.18 mater=3 ncarr_loss=6.e-23 &&
pcarr_loss=6.e-22
temperature temp=300
include file=active.mater
gain_wavel wavel_range=[1.4 1.6] conc_range=[5e23 5e24]
&& curve_number=20
sp.rate_wavel wavel_range=[1.4 1.6] &&
conc_range=[5e23 5e24] curve_number=20
index_wavel wavel_range=[1.4 1.6] &&
conc_range=[5e23 5e24] curve_number=20 &&
init_conc=1.5e24
current_conc conc_range=[1.4 1.6] data_point=30 &&
use_macro=yes fit_outfile=tmp.data
gain_density wavel_range=(1.4 1.6) conc_range=(5e23 5e24)

```

```

&& pn_ratio=1 data_point=30
gain_spon wavel_range=(1.4 1.6) conc_range=(5e23 5e24)
&& pn_ratio=1 data_point=30
end_gain
$*****

The phase.gain file contains all the information for the gain
spectrum of the phase section of the three-section bulk TLD
$*****

$ phase.gain file
begin_gain
use_macrofile macro1=my.mac
plot_data plot_device=postscript
$ Apply Lorentzian broadening lineshape function to gain
$ with intraband relaxation time  $\tau_{in} = 0.2$  ps, FC absorption
$ coefficient  $a_{FC} = 2 \times 10^{-23}$  m2 and IVBA coefficient
$  $a_{IVBA} = 2 \times 10^{-22}$  m2
active_reg broadening=lorentzian tau_sc=0.2e-12 a_sc=0
&& thickness=0.58 mater=6 ncarr_loss=2.e-23 &&
pcarr_loss=2.e-22
temperature temp=300
include file=phase.mater
gain_wavel wavel_range=[1.4 1.6] conc_range=[5e23 5e24]
&& curve_number=20
sp.rate_wavel wavel_range=[1.4 1.6] &&
conc_range=[5e23 5e24] curve_number=20
index_wavel wavel_range=[1.4 1.6] &&
conc_range=[5e23 5e24] curve_number=20 &&
init_conc=1.5e24
current_conc conc_range=[1.4 1.6] data_point=30 &&
use_macro=yes fit_outfile=tmp.data
gain_density wavel_range=(1.4 1.6) conc_range=(5e23 5e24)
&& pn_ratio=1 data_point=30
gain_spon wavel_range=(1.4 1.6) conc_range=(5e23 5e24)
&& pn_ratio=1 data_point=30
end_gain
$*****

```

```

The Bragg.gain file contains all the information for the gain
spectrum of the Bragg section of the three-section bulk TLD
$*****

$ Bragg.gain file
begin_gain
use_macrofile macro1=my.mac
plot_data plot_device=postscript
$ Apply Lorentzian broadening lineshape function to gain
$ with intraband relaxation time  $\tau_{in} = 0.2$  ps, FC absorption
$ coefficient  $a_{FC} = 2 \times 10^{-23}$  m2 and IVBA coefficient
$  $a_{IVBA} = 2 \times 10^{-22}$  m2
active_reg broadening=lorentzian tau_sc=0.2e-12 a_sc=0
&& thickness=0.2 mater=9 ncarr_loss=2.e-23 &&
pcarr_loss=2.e-22
active_reg broadening=lorentzian tau_sc=0.2e-12 a_sc=0
&& thickness=0.38 mater=10 ncarr_loss=2.e-23 &&
pcarr_loss=2.e-22
temperature temp=300
include file=Bragg.mater
gain_wavel wavel_range=[1.4 1.6] conc_range=[5e23 5e24]
&& curve_number=20
sp.rate_wavel wavel_range=[1.4 1.6] &&
conc_range=[5e23 5e24] curve_number=20
index_wavel wavel_range=[1.4 1.6] &&
conc_range=[5e23 5e24] curve_number=20 &&
init_conc=1.5e24
current_conc conc_range=[1.4 1.6] data_point=30 &&
use_macro=yes fit_outfile=tmp.data
gain_density wavel_range=(1.4 1.6) conc_range=(5e23 5e24)
&& pn_ratio=1 data_point=30
gain_spon wavel_range=(1.4 1.6) conc_range=(5e23 5e24)
&& pn_ratio=1 data_point=30
end_gain
$*****

```

The Bulk_TLD.sol file is where the main equation solver is used and the simulations are run.

\$*****

\$ Bulk_TLD.sol file

begin

use_macrofile macro1=my.mac

3d_solution_method 3d_flow=yes z_connect=no

z_structure uniform_length=400. zseg_num=1 zplanes=3

z_structure uniform_length=100. zseg_num=2 zplanes=2

z_structure uniform_length=300. zseg_num=3 zplanes=3

load_mesh mesh_inf=active.msh zseg_num=1

load_mesh mesh_inf=phase.msh zseg_num=2

load_mesh mesh_inf=Bragg.msh zseg_num=3

output sol_outf=TLD.out

begin_zmater zseg_num=1

include file=active.gain

include file=active.doping

end_zmater

begin_zmater zseg_num=2

include file=phase.gain

include file=phase.doping

end_zmater

begin_zmater zseg_num=3

include file=Bragg.gain

include file=Bragg.doping

end_zmater

\$ Waveguide settings

direct_eigen

init_wave backg_loss=500 boundary_type=(2 2 1 1) &&

init_wavel=1.554 wavel_range=(1.4, 1.6)

newton_par damping_step=10. var_tol=1.e-9 res_tol=1.e-9

full_ionization mater=1

full_ionization mater=2

full_ionization mater=3

full_ionization mater=4

full_ionization mater=5

full_ionization mater=6

full_ionization mater=7

full_ionization mater=8

full_ionization mater=9

full_ionization mater=10

full_ionization mater=11

\$ Activate contributions only from the FC plasma effect and

\$ the bandfilling effect to the effective refractive index

\$ change

index_model free-carrier=yes free_carr_passive=yes &&

use_l.w.e.factor=no l.w.e.factor=4 interband=yes &&

sample_mesh=no sample_point=200 linear_active=no &&

linear_passive=no

\$set_active_reg

\$ scanline = 1

equilibrium

rtgain_phase density=1.e24 zseg_num=1

rtgain_phase density=1.e24 zseg_num=2

rtgain_phase density=1.e24 zseg_num=3

newton_par damping_step=1. var_tol=1.e-4 res_tol=1.e-4

\$ Voltage bias on bottom electrode to avoid short-circuits

\$ between top electrodes

\$ scanline = 2

scan var=voltage_1 value_to=-0.3

\$ Initial current bias

\$ scanline = 3

scan var=current_2 value_to=-10.0e-3 &&

init_step=1e-5 min_step=1e-6 max_step=1.e-4 &&

auto_finish=rtgain auto_until=0.95 auto_condition=above

\$ Ramp up gain section to above threshold

\$ and start 3D c-RTG solver

\$ scanline = 4

scan var=current_2 value_to=-15.0e-3 &&

init_step=1e-5 min_step=1e-10 max_step=1.e-3 &&

solve_rtg=yes

\$ Tune device

\$ scanline = 5

newton_par damping_step=1. var_tol=1.e-3 res_tol=1.e-3

```
scan var=voltage_4 value_to=2.0 &&
var2=current_2 value2_to=-15.0e-3 &&
init_step=1e-6 min_step=1e-20 max_step=1.e-3 &&
print_step=0.1 solve_rtg=yes
add_mainmemory sparse_fill=1
end
begin_zsol
longitudinal ref_wavel=1.5505e-6 left_f_refl=0.3 &&
right_f_refl=1e-4
section length=4.e-4 sec_num=1 mesh_points=20
```

```
section length=1.e-4 sec_num=2 mesh_points=20
section length=3.e-4 sec_num=3 mesh_points=20
mode_srch adjust_range=no &&
wavel_xrange=[1.530e-6 1.553e-6] srch_sidemode=yes &&
sort_mode=total omega_xrange=45
end_zsol
$*****
```